

TOWARDS PRECISION TESTS OF GENERAL RELATIVITY
USING AN ATOM INTERFEROMETER

A DISSERTATION
SUBMITTED TO THE DEPARTMENT OF PHYSICS
AND THE COMMITTEE ON GRADUATE STUDIES
OF STANFORD UNIVERSITY
IN PARTIAL FULFILLMENT OF THE REQUIREMENTS
FOR THE DEGREE OF
DOCTOR OF PHILOSOPHY

Jason Hogan

June 2010

© 2010 by Jason Michael Hogan. All Rights Reserved.
Re-distributed by Stanford University under license with the author.



This work is licensed under a Creative Commons Attribution-
Noncommercial 3.0 United States License.
<http://creativecommons.org/licenses/by-nc/3.0/us/>

This dissertation is online at: <http://purl.stanford.edu/cf210zm6017>

I certify that I have read this dissertation and that, in my opinion, it is fully adequate in scope and quality as a dissertation for the degree of Doctor of Philosophy.

Mark Kasevich, Primary Adviser

I certify that I have read this dissertation and that, in my opinion, it is fully adequate in scope and quality as a dissertation for the degree of Doctor of Philosophy.

Savas Dimopoulos

I certify that I have read this dissertation and that, in my opinion, it is fully adequate in scope and quality as a dissertation for the degree of Doctor of Philosophy.

Philippe Bouyer

Approved for the Stanford University Committee on Graduate Studies.

Patricia J. Gumpert, Vice Provost Graduate Education

This signature page was generated electronically upon submission of this dissertation in electronic format. An original signed hard copy of the signature page is on file in University Archives.

Abstract

A 10-meter tall, dual-species atomic fountain gravimeter was designed and built for the purpose of testing the Equivalence Principle with freely-falling atoms. Once completed, the apparatus promises to be the most sensitive atom interferometer ever built, with a projected differential acceleration sensitivity of $10^{-15}g$. This phenomenal force sensitivity opens the door to exciting science applications which are reviewed, including setting new limits on the Equivalence Principle, measuring effects of General Relativity in a laboratory setting, and detecting gravitational waves.

Acknowledgements

First of all, thanks to my advisor Mark Kasevich for his years of guidance. Mark is exciting to work with because his ambitious ideas are always grounded in an unwavering experimental sense. I deeply respect his ability to maintain this difficult balance. Mark trusted me to lead the charge on this new project when I was just starting out, and for that opportunity I am very grateful.

It was exciting to watch what was initially ‘my project’ years ago evolve into something much bigger than one person. I am deeply indebted to the other members of the EP team: David Johnson, Susannah Dickerson, Alex Sugarbaker, Tim Kovachy and Sheng-wey Chiow. It is a privilege to work with such a talented and dedicated group of people.

At the start of this project, I leaned heavily on more experienced members of the group. Thanks to Yvan Sortais for patiently teaching me about lasers, and for showing me how to work in an atomic physics lab. Thanks as well to Peter Hommelhoff for always having time to answer my questions about cold atoms.

I also had the opportunity to collaborate closely with a number of talented theorists. Thanks to my theorist friends: Peter Graham, Surjeet Rajendran, Asimina Arvanitaki, and of course, Savas Dimopoulos. The EP project has benefited enormously from your hard work and insightful ideas. Thank you for teaching me how to think a little like a theorist, and for making me feel welcome in your group.

Finally, thank you to my family – Mike, Pat, Katie and Scott – for your constant support and unending enthusiasm for my work on this project.

Contents

Abstract	iv
Acknowledgements	v
1 Introduction	1
1.1 Equivalence Principle Tests	3
1.2 Motivation to Test the EP	5
1.3 Experiments Beyond the EP	8
1.3.1 Post-Newtonian Gravity	8
1.3.2 Gravitational Wave Detection	10
1.4 Organization of the thesis	11
2 Atom Interferometry	13
3 Phase shift determination	20
3.1 Phase shift formulae	20
3.2 Justification of phase shift formulae	21
4 Systematic Error Model	35
4.0.1 Gravity Inhomogeneities	40
4.0.2 Magnetic field inhomogeneities	42
4.1 Controlling potential systematic errors	44
4.1.1 Rotation of the Earth	44
4.1.2 Gravity gradients	47

4.1.3	Magnetic fields	49
5	Experimental Apparatus	51
5.1	Interferometer Region	51
5.1.1	Vacuum System	53
5.1.2	Bias Solenoid	56
5.1.3	Magnetic Shield Design	58
5.1.4	Characterizing the Magnetic Shield	61
5.1.5	Rotation Compensation System	66
5.2	Atom Source	68
5.2.1	Vacuum Chamber	71
5.2.2	Quadrupole Coils	74
5.2.3	2D and 3D MOT	76
5.3	Laser System	78
5.3.1	Dual Species Laser Cooling and Trapping Light	80
5.3.2	Atom Optics Light	87
5.3.3	Optimizing the optical lattice launch	95
5.4	Computer Control System	98
5.4.1	Stanford Timing Interface	99
5.4.2	FPGA Based Timing	103
6	General Relativistic Effects	105
6.1	General Relativistic Description of Atomic Interferometry	106
6.1.1	Dynamics of the Interferometer	108
6.1.2	Relativistic Phase Shift Formulae	113
6.2	GR Effects in the Earth's Gravitational Field	116
6.2.1	Interferometer Calculation in the Schwarzschild Metric	117
6.2.2	General Relativistic Effects and Interpretation	121
6.3	Measurement Strategies	128
6.3.1	Velocity Dependent Forces	129
6.3.2	Non-Linearity of Gravity	130
6.3.3	General Backgrounds	132

6.4	Other GR Effects?	138
6.4.1	Hubble Expansion (Vacuum Energy)	138
6.4.2	Lense-Thirring	140
6.4.3	Preferred Frame	143
6.5	Summary and Comparison	144
7	Detecting Gravitational Waves	146
7.1	Introduction	146
7.2	Atom Interferometry Sensitivity	148
7.3	Gravitational Wave Signal	151
7.3.1	Phase Shift Calculation	152
7.3.2	Results	155
7.4	Terrestrial Experiment	159
7.4.1	Experimental Setup	159
7.4.2	Backgrounds	165
7.5	Satellite Based Experiment	182
7.5.1	Experimental Setup	183
7.5.2	Backgrounds	191
7.5.3	Comparison with LISA	202
7.6	Gravitational Wave Sources	204
7.6.1	Compact Object Binaries	204
7.6.2	Stochastic Sources	206
7.7	Sensitivities	208
7.7.1	Binary Sources	208
7.7.2	Stochastic Gravitational Wave Backgrounds	214
7.8	Conclusion	220
7.8.1	Comparison with Previous Work	220
7.8.2	Summary	222
8	Conclusion	225

A Testing Atom and Neutron Neutrality	227
A.1 Introduction	227
A.2 Experimental Setup	228
A.3 Sensitivity	230
A.4 Systematics	231
B Gravity Inhomogeneities	235
B.1 Perturbation theory phase shifts	236
B.2 Transfer function for gravity inhomogeneities	237
B.3 Applications to specific interferometer configurations	243
B.3.1 Three pulse sequence	243
B.3.2 Four pulse sequence	245
B.4 Phase shift response for a discrete source spectrum	247
C Serrodyne Frequency Shifting	251
D Picosecond Optical Switching using NLTLs	259
Bibliography	266

List of Tables

4.1	Phase shift response for a single atom interferometer sequence.	38
4.2	Differential phase shift between ^{87}Rb and ^{85}Rb	39
4.3	Differential phase shift list with rotation compensation.	47
6.1	Phase shift terms arising from the full GR calculation for the PPN metric.	123
6.2	Origins of the phase shift terms arising from the full GR calculation for the PPN metric.	127
7.1	Calculated phase shift due to a gravitational wave.	156
7.2	Comparison of AGIS with LISA.	204
7.3	Summary of parameters chosen for GW sensitivity curves.	211
A.1	Estimated signal and systematic phase shifts for a proposed test of charge neutrality.	233

List of Figures

1.1	Projected $\alpha\text{-}\lambda$ limits to be set by our EP measurement.	7
2.1	Non-relativistic space-time diagram for a single atom.	15
2.2	Relativistically correct space-time diagram of a light pulse atom interferometer.	16
2.3	Two photon Raman transitions.	17
2.4	Two photon Bragg transitions.	17
3.1	The origin of separation phase.	31
4.1	Differential gravity response function between simultaneous ^{87}Rb and ^{85}Rb interferometers.	41
4.2	The power spectra of the local gravitational field, $\tilde{\delta g}_z$, for several example sources.	43
4.3	Differential magnetic field response function between simultaneous ^{87}Rb and ^{85}Rb interferometers.	45
5.1	Experimental apparatus.	52
5.2	The assembled support tower, vacuum tube and magnetic shield. . . .	55
5.3	Interferometer vacuum tube showing heat tape for bake-out.	57
5.4	Detail of one of the bias solenoid wire clamps.	59
5.5	Magnetic shield CAD model.	62
5.6	Three-layer magnetic shield segment.	63
5.7	Magnetometer shuttle system for characterizing the interferometer region magnetic field.	64

5.8	Measured magnetic field prior to shield installation.	65
5.9	Measured magnetic field after shield installation.	66
5.10	Rotation Compensation System	68
5.11	Octagon vacuum chamber	72
5.12	2D MOT vacuum chamber.	74
5.13	2D MOT and 3D MOT CAD Model.	76
5.14	2D MOT viewed along the axis of the atom beam.	77
5.15	Effect of the pusher beam on the ^{87}Rb MOT loading rate.	78
5.16	3D MOT loading curve for a dual species MOT.	79
5.17	Level structures and optical frequencies for a dual species MOT.	82
5.18	RF scheme for cooling and trapping both isotopes.	83
5.19	Optics setup for laser cooling light.	84
5.20	Laser setup for atom optics and optical lattice light.	90
5.21	Optics setup for the z -axis.	93
5.22	Theoretical atom loss fraction due to the lattice launch.	97
5.23	STI network architecture.	100
6.1	A relativistic space-time diagram of a light pulse atom interferometer.	107
6.2	Gravity inhomogeneity response function for various atom launch velocities.	136
7.1	Proposed setup for a terrestrial GW experiment	160
7.2	Overlapped interferometer sequences for high repetition rate.	163
7.3	Interferometer response to laser phase noise in a single $\frac{\pi}{2}$ pulse.	169
7.4	Interferometer response to a time varying g using a 10 km baseline.	172
7.5	Interferometer response to a time varying g using a 1 km baseline.	173
7.6	Space-time diagram of a double loop interferometer.	175
7.7	Space-time diagram of a triple loop interferometer.	177
7.8	Proposed setup for a satellite GW experiment.	182
7.9	Sensitivity curve to a gravitational wave of frequency f .	209
7.10	Projected sensitivities of the terrestrial experiments to GWs.	212
7.11	Projected sensitivities of the satellite experiments to GWs.	213

7.12	Projected sensitivity of the terrestrial experiments to stochastic GWs.	215
7.13	Projected sensitivity of the satellite experiments to stochastic GWs.	216
7.14	Possible new physics sources of stochastic gravitational waves.	219
A.1	Experimental setup for a test of charge neutrality.	228
A.2	Atom trajectories versus time in a proposed test of charge neutrality.	229
B.1	Atom trajectory for a $(\frac{\pi}{2}-\pi-\frac{\pi}{2})$ three pulse sequence.	244
B.2	Magnitude of the gravity transfer function for ^{87}Rb	245
B.3	Differential gravity transfer function for the EP measurement.	246
B.4	Atom trajectory for a $(\frac{\pi}{2}-\pi-\pi-\frac{\pi}{2})$ four pulse sequence.	247
B.5	EP differential gravity transfer function for a four pulse sequence.	248
C.1	Experimental setup for serrodyne modulation.	253
C.2	Optical spectrum with and without serrodyne modulation.	254
C.3	Serrodyne modulation efficiency.	255
C.4	Heterodyne spectra of push-pull frequency shift.	257
D.1	Experimental setup for a picosecond optical switch.	262
D.2	Picosecond switching using an MZI geometry.	264
D.3	Picosecond switching using a Sagnac geometry.	265

Chapter 1

Introduction

In addition to the Standard Model, Einstein’s theory of general relativity is one of the two cornerstones of modern physics. General relativity (GR) describes the force of gravity. In this regard it has so far been amazingly successful, elegantly describing all experiments and observations without a single adjustable parameter. As the weakest of the fundamental interactions, the effects of gravity only become significant on astrophysical or cosmological scales, and so gravity has been safely neglected in the arena of high-energy physics that is governed by the Standard Model. Although both these theories work well in their respective domains, their intersection presents serious fundamental problems, and the much sought after quantized theory of gravity continues to pose deep challenges. Thanks in part to this ongoing search for a unified ‘theory of everything,’ experimental searches for violations of GR are well motivated and are exciting avenues of current research.

Experimental tests of general relativity have gone through two major phases. The original tests of the perihelion precession and light bending were followed by a golden era from 1960 until today (see *e.g.*, [1]). These tests were in part motivated by alternatives to Einstein’s theory, such as Brans-Dicke, designed to incorporate Mach’s principle [2]. More recently, the cosmological constant problem suggests that our understanding of general relativity is incomplete, motivating a number of proposals for modifying gravity at large distances [3, 4, 5]. In addition, possible alternatives to the dark matter hypothesis have led to theories where gravity changes at slow

accelerations or galactic scales [6, 7, 8].

General relativity itself replaces a very successful theory of gravity – Newton’s law of universal gravitation – which accurately describes almost all gravitational phenomena known before the twentieth century (*e.g.*, the motion of planets in the solar system).¹ As such, many of the testable effects that can uniquely be attributed to GR appear as small corrections to the results of classical gravity. For example, GR accounts for an increased precession of the perihelion of the orbit of Mercury of only 43 arcseconds per century, less than 1% of the observed precession.[9] GR corrections are small for slowing moving bodies ($v \ll c$) in the presence of small gravitational potentials ($GM/Rc^2 \ll 1$), the conditions that define classical gravitation. Such conditions typically dominate in the laboratory environment, and to a somewhat lesser extent, in the solar system as well. The intrinsic smallness of many observable GR effects can make testing the theory itself a challenge, let alone looking for violations which are presumably even smaller.

To overcome this smallness, the obvious choice is to study systems with large velocities and strong gravitational potentials which are typical of astrophysical situations. This approach is necessarily limited to observational science that cannot be done in the lab. However, given a high enough experimental sensitivity, laboratory scale experiments may be an alternative to this paradigm. Laboratory based experiments have the advantage of being repeatable and highly reconfigurable as compared to astronomical observations. Certainly, laboratory tests of GR are not unknown, with perhaps the most famous being the Pound–Rebka experiment that measured the gravitational redshift.[10] Nevertheless, most GR tests have been observational in nature or have required launching satellites into orbit.²

In part, the work described here is an attempt to realize this paradigm of new and meaningful laboratory tests of general relativity. The primary tool we employ is precision light-pulse atom interferometry[11]. Light-pulse atom interferometers have already been used to make extremely accurate inertial force measurements in a variety of configurations, including gyroscopes [12], gradiometers [13, 14], and gravimeters

¹The anomalous precession of Mercury is an exception, with the deviation measured in 1859.

²Compared to satellite missions, being on the ground in a laboratory allows increased flexibility and likely decreased cost.

[15, 16]. For example, the local gravitational acceleration g of freely-falling Cs atoms was measured with an accuracy $\sim 10^{-9}g$ [15]. Gravity gradiometers have been used to suppress noise as well as many systematic errors that are present in absolute g measurements by comparing the acceleration of two displaced samples of atoms. A differential measurement of this kind was used to measure the Newtonian constant of gravity G with an accuracy of $\sim 3 \times 10^{-3}G$ [17].

Of the potential laboratory GR tests that we imagine performing with this technology, our primary focus so far is on a test of the Equivalence Principle (EP) using freely-falling atoms. Our EP experiment ambitiously aims to compare the gravitational accelerations of two co-located atoms of different species, in this case the isotopes of ^{85}Rb and ^{87}Rb , with a precision of $10^{-15}g$. The experimental apparatus described in this work has been designed with this EP test specifically in mind. However, we think that the technology and methods developed for the EP experiment – and likely even the apparatus itself – will be directly applicable to other atom interferometric tests of GR in the near future.

1.1 Equivalence Principle Tests

The Equivalence Principle has several forms, with varying degrees of universality. Here we experimentally consider a test of the Weak Equivalence Principle (WEP), which can be stated as follows: in the absence of all non-gravitational forces, the motion of a test body in a gravitational field in any local region of space-time is indistinguishable from its motion in a uniformly accelerated frame. This implies that the body’s inertial mass is equal to its gravitational mass, and that all bodies locally fall at the same rate under gravity, independent of their mass or composition. Here, ‘local’ has the specific meaning that the region must be small enough so that tidal forces are negligible. Also known as the Universality of Free Fall (UFF), the WEP is the least restrictive form of the EP. The more general Einstein Equivalence Principle (EEP) extends the concept of UFF, stating that the results of *any* (non-gravitational) experiment performed in a freely-falling inertial frame are independent of the position and velocity of the frame. For completeness, the Strong Equivalence Principle (SEP)

further extends the EEP to include gravitational experiments as well (e.g., situations with non-negligible gravitational binding energy, or Cavendish-type tests of gravity). Our EP experiment directly tests the UFF by comparing the free-fall motion of ^{85}Rb and ^{87}Rb atoms, and as such it is a WEP test.

To make the WEP test more concrete, the acceleration a of a test particle with inertial mass m_I and (passive) gravitational mass m_G is given by $m_Ia = m_Gg$. Then, according to the WEP, the ratio m_G/m_I must be the same for all objects in order to respect the UFF. Following the treatment by Will[18], violations of the WEP may be parameterized by decomposing the various contributions of the object's mass-energy. As the argument goes, an object's inertial mass consists of contributions from, for example, the rest mass of its constituent particles, electromagnetic and nuclear binding energy, and other (conceivably previously unknown) interactions. An EP violation will result if any of these interaction energies E_A couple to gravity in a different way than they contribute to the inertial mass-energy, resulting in $m_G = m_I + \sum_A \eta_A E_A/c^2$, where η_A quantifies the violation associated with each interaction. Note that since, according to GR, m_G is proportional to m_I in order to respect the UFF, all forms of energy couple to gravity with equal strength in GR and $\eta_A = 0$.

The results of EP experiments are typically expressed in terms of the Eötvös parameter

$$\eta = \frac{\Delta a}{\bar{a}} = 2 \frac{|a_1 - a_2|}{|a_1 + a_2|} \quad (1.1)$$

where Δa is the EP violating differential acceleration between the two test bodies and \bar{a} is their average acceleration [18]. In terms of the decomposed interaction energies, the Eötvös parameter becomes

$$\eta = \sum_A \eta_A \left(\frac{E_A^{(1)}}{m_I^{(1)}c^2} - \frac{E_A^{(2)}}{m_I^{(2)}c^2} \right) \quad (1.2)$$

Tests of the EP that constrain η set limits on the coupling strengths η_A of different types of interaction energies. The strengths of these limits depend on the details of the test masses and by how much they differ with respect to each type of interaction energy.

Currently, two conceptually different experiments set the best limits on the Equivalence Principle. Lunar Laser Ranging (LLR), which tests the EP by comparing the acceleration of the Earth and Moon as they fall toward the Sun, limits EP violation at $\eta = (-1.0 \pm 1.4) \times 10^{-13}$ [19]. Recently, the Eöt-Wash group has set a limit of $\eta = (0.3 \pm 1.8) \times 10^{-13}$ using an Earth-based torsion pendulum apparatus[20]. Several proposed satellite missions aim to improve on these limits by observing the motion of macroscopic test bodies in orbit around the Earth[21, 22].

Our effort to perform a ground-based EP test using individual atoms has a goal of measuring $\eta \sim 10^{-15}$. Instead of macroscopic test masses, we compare the simultaneous acceleration under gravity of freely-falling cold atom clouds of ^{87}Rb and ^{85}Rb . As described in more detail later, our motivation for using two isotopes of the same element rather than two completely different atoms is largely technical. Many potential noise sources and systematic errors are suppressed if the test masses have similar responses to external forces. Ideally, the two test particles should differ only in their mass; the isotopes of rubidium approach this standard as they share a similar electronic structure.

An EP test using freely-falling atoms has been performed previously[23, 15]. This experiment also compared the acceleration of ^{87}Rb and ^{85}Rb using atom interferometry and achieved $\eta = (1.2 \pm 1.7) \times 10^{-7}$. In this case, the atom interferometer was based on absorptive gratings made of standing waves of resonant light. Our experiment should significantly improve upon this initial result, due in part to substantially increased free-fall time, enhanced atom optics, and longer measurement integration time.

1.2 Motivation to Test the EP

Precision tests of the Equivalence Principle promise to provide insight into fundamental physics. Generally speaking, since the EP is one of the central axioms of general relativity, these experiments are powerful checks of gravity and can tightly constrain new theories. For example, EP experiments test for hypothetical fifth forces since many examples of new forces are EP-violating[24]. Any new force that is not proportional simply to the mass of the atoms but instead depends on the atomic species

or isotope is detectable in an EP experiment.

A common parameterization of new, gravity-modifying forces assumes a Yukawa-type interaction with a force carrier of mass m . The resulting modified gravitational potential energy between mass M_1 and M_2 is of the form $V(r) = -\frac{GM_1M_2}{r^2} \left(1 + \alpha e^{-r/\lambda}\right)$ where α is the strength of the new interaction relative to gravity and $\lambda = \frac{\hbar}{mc}$ is its range[24]. Our EP experiment, performed on the surface of the Earth, has maximal sensitivity to such EP violating forces that have a range greater than the Earth's radius ($\lambda > R_E$). Consequently, an infinite range force would be detectable by our experiment. For long range forces, the proposed experiment can detect forces as small as the acceleration sensitivity allows, or $\alpha \sim 10^{-15}$. As the range of the new force decreases below the Earth's radius, the sensitivity of the experiment decreases as $\alpha \sim 10^{-15} \left(\frac{R_E}{\lambda}\right)$ (with the overly simplistic assumption of uniform earth density) since the volume of source matter for the new Yukawa force scales as $\sim \lambda^3$ for $\lambda < R_E$. The sensitivity continues to follow this scaling down to a range of $\lambda \sim 10$ m, the rough size of the experiment, since below this scale the details of the local mass distribution become important.

It is important to emphasize that EP tests are only sensitive to differences in the strength α between two test masses. In this sense, the α - λ Yukawa force parameterization is closely related to the EP violating couplings that appear in Eq. 1.2. Indeed, in the infinite range limit ($\lambda \rightarrow \infty$), we have $\alpha = \eta_A E_A / m_I c^2$ for a particular coupling. Thus, the ratio $E_A / m_I c^2$ acts as the source charge for the new EP-violating force, and the resulting sensitivity of the measurement to the intrinsic violation η_A is suppressed by the source charge difference between the test masses.

Specific predictions for the α - λ constraints that can be inferred from a particular EP measurement are clearly model dependent since they must refer to specific source charge contributions of the two test bodies. As an example, Fig. 1.1 shows the projected limits that would be set by our EP experiment on new forces that couple to Baryon number (B), Baryon minus Lepton number (B - L), and to a light dilaton[27]. The large suppression factors come from the fact that ^{85}Rb and ^{87}Rb have similar couplings to these new forces and also roughly equal masses(see Eq. 1.2). Also shown in Fig. 1.1 are the current experimental limits on a force coupling to B that are set

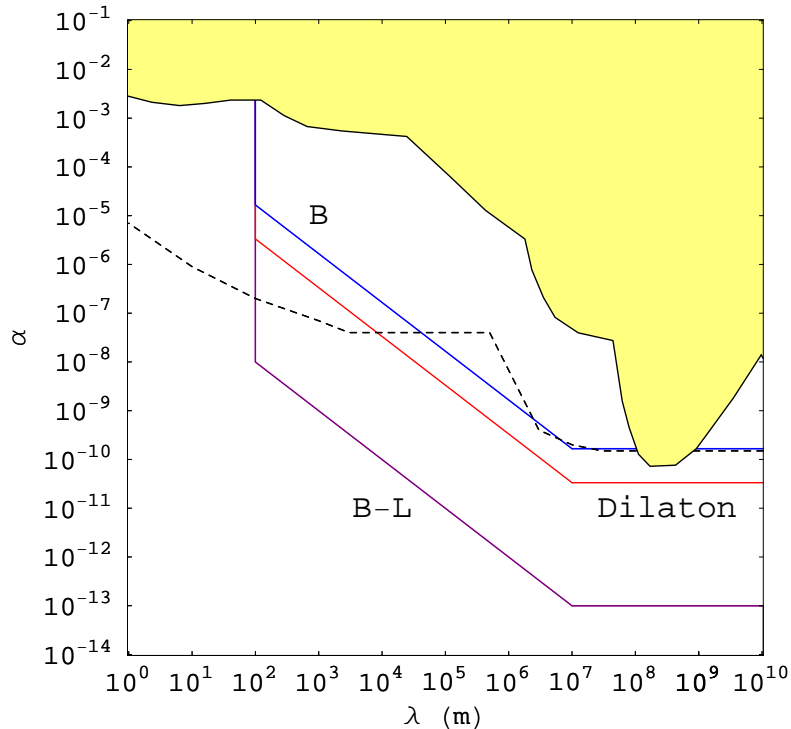


Figure 1.1: Projected limits to be set by the Equivalence Principle measurement. Limits are shown (labeled solid lines) for several possible new Yukawa forces arising from a coupling to Baryon number (B), Baryon minus Lepton number (B-L) and the dilaton. These assume a uniform Earth density. Previous limits are shown in solid (yellow) shading [25]. The dashed line is the current limit on a force coupling to B from an Equivalence Principle experiment using a realistic Earth model [26].

by another equivalence principle experiment[26]. This experimental result shows the difference that a realistic Earth model makes for the limits.

1.3 Experiments Beyond the EP

Our planned equivalence principle experiment is clearly an important test of one of the foundations of GR. However, since other theories of gravity can also respect the EP, the experiment does not test any unique GR predictions. In the near future, we foresee the possibility of applying atom interferometry to other gravity tests that do probe such effects. The technology developed for our EP experiment is directly applicable to this next generation of measurements.

1.3.1 Post-Newtonian Gravity

One exciting direction of research is to look for post-Newtonian gravitational effects in laboratory experiments. In the limit of weak gravity (such as on the surface of the Earth), gravity is nearly Newtonian and GR shows up as small perturbations to classical predictions. To calculate the effect of these GR corrections to Newtonian gravity on our atom interferometer, we need to rely on the metric governing the motion of the atoms and photons in the experiment. The parameterized post-Newtonian (PPN) expansion is a convenient formalism for this purpose that facilitates quantitative comparison between GR and other competing theories of gravity. Consider a Schwarzschild spacetime in the PPN expansion ($\hbar = c = 1$):

$$ds^2 = (1 + 2\phi + 2\beta\phi^2)dt^2 - (1 - 2\gamma\phi)dr^2 - r^2d\Omega^2 \quad (1.3)$$

where $\phi = -\frac{GM}{r}$ is the Earth's gravitational potential, and β and γ are PPN parameters. Combining the geodesic equations for the spatial \mathbf{x}^i ($i = 1, 2, 3$) and t , the coordinate acceleration of an atom in the frame of Eq. 1.3 (with $\mathbf{v} = \frac{d\mathbf{x}}{dt}$) is

$$\frac{d\mathbf{v}}{dt} = -\nabla(\phi + (\beta + \gamma)\phi^2) + \gamma(3(\mathbf{v} \cdot \hat{\mathbf{r}})^2 - 2\mathbf{v}^2)\nabla\phi + 2\mathbf{v}(\mathbf{v} \cdot \nabla\phi) \quad (1.4)$$

This illustrates two classes of leading GR corrections to the Newtonian force law ($\dot{\mathbf{v}} = -\nabla\phi \equiv \mathbf{g}$). The $\nabla\phi^2$ terms are related to the non-linear (non-Abelian) nature of gravity, indicating that gravitational energy gravitates through a three-graviton vertex. To see this, consider the relativistic gravitational acceleration in the limit of $\mathbf{v} = 0$:

$$\frac{d\mathbf{v}}{dt} = -\nabla(\phi + (\beta + \gamma)\phi^2). \quad (1.5)$$

Note that the divergence of the relativistic gravitational field $\dot{\mathbf{v}}$ given in Eq. 1.5 is nonzero because of the $\nabla\phi^2$ terms. Just as for an electric field, a nonzero divergence of the relativistic gravitational field implies a local source density ρ_G , in this case a local energy density, proportional to that divergence:

$$\rho_G \sim \nabla \cdot \frac{d\mathbf{v}}{dt} \sim \nabla \cdot \nabla\phi^2 = 2(\nabla\phi)^2 = 2\mathbf{g}^2 \quad (1.6)$$

(since $\mathbf{g} = -\nabla\phi$ and $\nabla^2\phi = 0$). So the local energy density here is proportional to the gravitational field squared, analogous to the energy density of the electric field $\rho_E \propto \mathbf{E}^2$. This gravitational field energy is the physical origin of the $\nabla\phi^2$ terms.

The second class of corrections present in Eq. 1.4 are velocity dependent forces related to the gravitation of the atom's kinetic energy. In GR, all types of energy and momentum gravitate. Thus, the kinetic energy associated with the relative motion of the atom with respect to the Earth modifies the effective gravitational field that the atom experiences.

The non-linear GR corrections are smaller than Newtonian gravity by a factor of $\phi \sim 7 \times 10^{-10}$, while the velocity dependent forces are smaller by $v^2 \sim 10^{-15}$ for typical atom velocities $v \sim (10 \text{ m/s})/c$. As shown in Chapter 6, the non-linear terms can only be measured through a gradient of the force produced and so are reduced by an additional factor of the ratio of the size of the experiment to the radius of the Earth, or $\frac{10\text{m}}{R_E} \approx 10^{-6}$ for a 10 m long experiment. Both effects are then $\sim 10^{-15}g$. This estimate is tantalizing because it is at the same level of sensitivity as our proposed EP apparatus, in principle permitting detection of these effects and their associated PPN parameters. Since alternative theories of gravity predict differing values for the PPN parameters in general, measurements of post-Newtonian corrections provide an

opportunity for strict tests of these theories.

1.3.2 Gravitational Wave Detection

In addition to laboratory tests, atom interferometry may prove to be a useful tool for observational science as well, specifically in the search for gravitational waves. Direct gravitational wave (GW) detection promises to open a new window into the Universe. Astrophysical objects such as black holes, neutron stars and white dwarf binaries which are difficult to observe electromagnetically are bright sources of gravitational radiation. GWs are unaffected by recombination and can probe the earliest epochs of the Universe. Since GW are generated by the most extreme astrophysics processes such as binary mergers, GW detection offers a way to probe general relativity in the strong gravity limit.

Laser interferometers (*e.g.* LIGO) have been at the forefront of GW astronomy. However, the sensitivity of current light interferometers at frequencies below ~ 40 Hz is severely limited by seismic noise. As described in Chapter 7, a gravity wave detector based on two atom interferometers operated in a gradiometer configuration could circumvent this limit, allowing for GW detection at lower frequencies. Conceptually, the atoms act as the inertial test masses of the sensor, analogous to the mirrors in a LIGO-like detector, with the advantage that the atoms are in free-fall and as a result are intrinsically highly decoupled from the noisy environment.³

The lower frequency range accessible to an atom interferometric GW sensor would be complementary to the range available to laser interferometers. In particular, the GW spectrum between 10^{-3} Hz and 10 Hz probes several exciting sources. The mergers of bright GW sources like white dwarf binaries, intermediate and massive black holes occur in this band. Moreover, compact solar mass binaries spend long times moving through this band before rapidly coalescing in LIGO’s band, increasing the population of the binaries in this band relative to the number accessible to LIGO. Also, the long lifetime of the compact binaries in this band increases the integration

³The remaining seismic coupling from the laser light can be greatly suppressed if the pair of interferometers is operated using the same light pulses; then this noise cancels as a common mode in the differential measurement.

time available to see them resulting in a significant enhancement in their detectability.

The 10^{-3} Hz – 10 Hz band is also interesting for stochastic GW searches [28]. The power spectra of GWs from violent events in the Universe at the TeV scale are typically peaked around 10^{-3} Hz – 10^{-1} Hz. Furthermore, the energy density Ω_{GW} in gravitational radiation produced by phenomena such as inflation is flat over several frequency decades. Consequently, the strain h of the GWs produced by these phenomena is significantly higher at lower frequencies. Since GW detectors respond to h , these sources can be more easily detected at lower frequencies. Atom interferometric GW detectors in the sub-Hertz band can thus provide a new astrophysical and cosmological probe.

1.4 Organization of the thesis

An overview of this thesis is as follows. Chapter 2 discusses the basics of atom interferometry and describes the general measurement sequence. Chapters 3 and 4 then deal with precision modeling of our dual species atom interferometer with the purpose of determining the systematic error budget. Chapter 3 begins with a review of the classical theory for calculating phase shifts in a light pulse atom interferometer. The material in Chapter 3 originally appeared in [29] and [30]. Chapter 4 goes on to apply this general result to our specific apparatus and then discusses the resulting experimental requirements. This chapter originally appeared in [30] and is work done in collaboration with David Johnson and Mark Kasevich.

Chapter 5 contains the technical description of the 10 m atomic fountain that we have built during the last six years for the purpose of testing the equivalence principle. I also discuss some of the design decisions that we made for addressing the systematic errors discussed in Chapter 4.

Chapters 6 and 7 consider the prospects for new measurements beyond the equivalence principle that rely on the technology and hardware of the 10 m apparatus. Chapter 6 discusses post-Newtonian effects and the measurement strategies required to extract them. In addition, I also present our formalism for calculating relativistically covariant phase shifts for an atom interferometer in an arbitrary space-time

metric. The work in Chapter 6 originally appeared in [29] and was done in collaboration with Savas Dimopoulos, Peter Graham, and Mark Kasevich. Finally, Chapter 7 is a study on the prospects for gravitational wave detection using atom interferometry, including a detailed review of many experimentally relevant backgrounds. This material first appeared in [31] and is work done in collaboration with Savas Dimopoulos, Peter Graham, Mark Kasevich, and Surjeet Rajendran.

Appendix A describes a proposed test of atom (and neutron) charge neutrality using a modified version of the EP apparatus described in Chapter 5. This work originally appeared in [32] and was done in collaboration with Asimina Arvanitaki, Savas Dimopoulos, Andrew Geraci, and Mark Kasevich. Appendix B contains an analysis of the sensitivity of an atom interferometer to gravity inhomogeneities. Appendix C describes the optical frequency shifting technique using serrodyne modulation that we developed for generating the laser frequencies for the dual species MOT. This material originally appeared in [33] and is work done in collaboration with David Johnson, Sheng-wei Chiow, and Mark Kasevich. Finally, Appendix D describes a proposal for picosecond optical switching using RF non-linear transmission lines, including a proof of concept implementation of the technique. The work in Appendix D was done in collaboration with David Johnson, Sheng-wei Chiow, and Mark Kasevich.

Chapter 2

Atom Interferometry

Atom interferometry can be used to measure accelerations precisely. In a light pulse atom interferometer, the atom is forced to follow a superposition of two spatially and temporally separated free-fall paths. This is accomplished by coherently splitting the atom wavefunction with a pulse of light that transfers momentum to a part of the atom. When the atom is later recombined, the resulting interference pattern depends on the relative phase accumulated along the two paths. This phase shift results from both the free-fall evolution of the quantum state along each path as well as from the local phase of the laser which is imprinted on the atom during each of the light pulses. Consequently, the phase shift is exquisitely sensitive to inertial forces present during the interferometer sequence, since it precisely compares the motion of the atom to the reference frame defined by the laser phase fronts. For our EP experiment, the goal sensitivity of the apparatus exceeds 10^{-14} m/s².[34]

A single measurement of acceleration in an atom interferometer consists of three steps: atom cloud preparation, interferometer pulse sequence, and detection. In the first step, the cold atom cloud is prepared. Using laser cooling and evaporative cooling techniques [35], a sub-microkelvin cloud of atoms is formed. Cold atom clouds are needed so that as many atoms as possible will travel along the desired trajectory and contribute to the signal. In addition, many potential systematic errors (see Section 4.1, and also Sections 7.4.2 and 7.5.2) are sensitive to the atom's initial conditions, so cooling can mitigate these unwanted effects. Here, evaporative cooling is preferred

since it yields the required tight control of the initial position and velocity of the cloud that cannot be achieved with laser cooling alone. At the end of the cooling procedure, the final cloud number density is kept low enough so that atom-atom interactions within the cloud are negligible (Section 6.3 contains a quantitative discussion of this point). This dilute ensemble of cold atoms is then launched with velocity v_L by transferring momentum from laser light. To avoid heating the cloud during launch, the photon recoil momenta should be transferred to the atoms coherently so that spontaneous emission is avoided. A promising way to implement such a launch is to accelerate the atoms using an optical lattice potential [36]. A detailed description of our lattice launch appears in Section 5.3.3.

In the second phase of the measurement, the atoms follow free-fall trajectories and the interferometry is performed. A sequence of laser pulses serve as beamsplitters and mirrors that coherently divide each atom's wavepacket and then later recombine it to produce the interference. Figure 2.1 is a space-time diagram illustrating this process for a single atom. The atom beamsplitter is implemented using a stimulated two-photon transition. In this process, laser light incident from the bottom of Fig. 6.1 with wavevector \mathbf{k}_1 is initially absorbed by the atom. Subsequently, laser light with wavevector \mathbf{k}_2 incident from the top stimulates the emission of a \mathbf{k}_2 -photon from the atom, resulting in a net momentum transfer of $\hbar\mathbf{k}_{\text{eff}} = \hbar\mathbf{k}_2 - \hbar\mathbf{k}_1 \approx 2\hbar\mathbf{k}_2$.

Note that the interferometer model depicted in Fig. 2.1 is sufficient for calculations in the non-relativistic limit, including the estimation of systematic errors in the equivalence principle apparatus. However, it ultimately break down when relativity becomes important since, for example, the model ignores the finite speed of light.¹ Figure 2.2 shows the relativistically correct interferometer diagram which accounts for the geodesic motion of both the atoms and the light. In Fig. 2.2, the two-photon atom optics are represented by the intersection of two counter-propagating photon paths at each interaction node. This relativistic model will be necessary for the treatment of GR effects that appears in Chapter 6.

There are several schemes for exchanging momentum between the atoms and the lasers. Figure 2.3(a) shows the case of a Raman transition in which the initial and

¹'Infinite speed' photons appear as vertical waves in Fig. 2.1

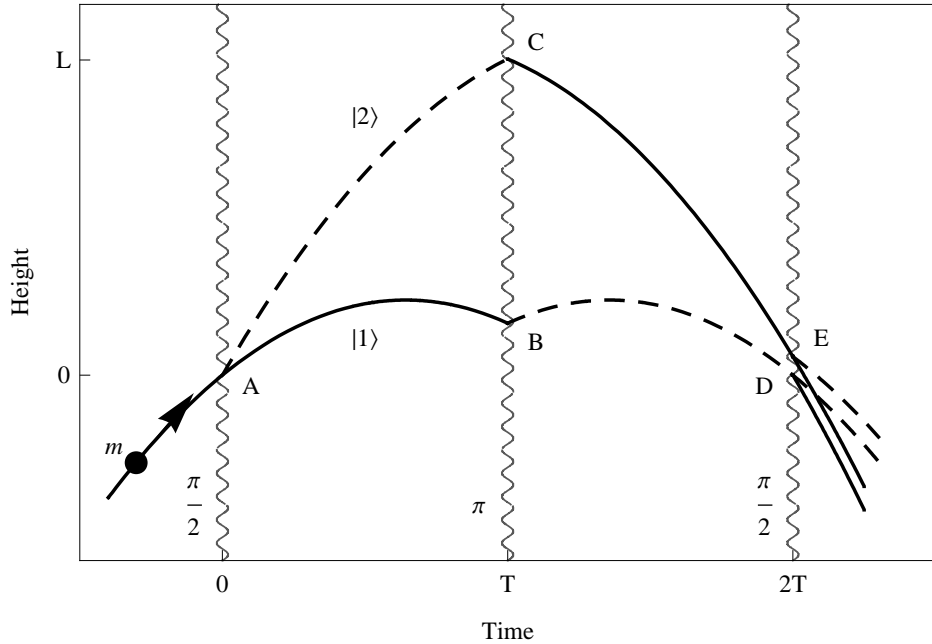


Figure 2.1: Non-relativistic space–time diagram for a single atom of mass m during the interferometer pulse sequence. The atom is launched with velocity v_z from the bottom of the vacuum system. At time $t = 0$, a $\frac{\pi}{2}$ (beamsplitter) pulse is applied to coherently divide the atom wavefunction. After a time T , a π (mirror) pulse is applied that reverses the relative velocity between the wavefunction components. A final $\frac{\pi}{2}$ (beamsplitter) pulse at time $2T$ results in interference between the two space–time paths. The interferometer phase shift is inferred by measuring the probability of detecting the atom in either state $|1\rangle$ (solid line) or state $|2\rangle$ (dashed line). Note that points D and E are in general spatially separated in the presence of non-uniform forces, leading to a separation phase shift.

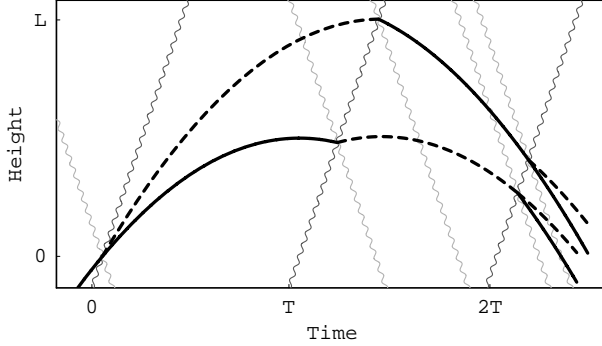


Figure 2.2: A relativistically correct version of a light pulse atom interferometer space-time diagram. The black curves indicate the geodesic motion of a single atom near the surface of the Earth. Laser light used to manipulate the atom is incident from above (light gray) and below (dark gray) and travels along null geodesics. The finite speed of the light has been exaggerated.

final states are different internal atomic energy levels. The light fields entangle the internal and external degrees of freedom of the atom, resulting in an energy level change and a momentum kick. As an alternative to this, it is also possible to use Bragg transitions in which momentum is transferred to the atom while the internal atomic energy level stays fixed (see Fig. 2.4). In both the Raman and Bragg scheme, the two lasers are far detuned from the optical transitions, resulting in a negligibly small occupancy of the excited state $|e\rangle$. This avoids spontaneous emission from the short-lived excited state. To satisfy the resonance condition for the desired two-photon process, the frequency difference between the two lasers is set equal to the atom's recoil kinetic energy (Bragg) plus any internal energy shift (Raman). While the laser light is on, the atom undergoes Rabi oscillations between states $|\mathbf{p}\rangle$ and $|\mathbf{p} + \hbar\mathbf{k}_{\text{eff}}\rangle$ (see Fig. 2.3(b)). A beamsplitter results when the laser pulse time is equal to a quarter of a Rabi period ($\frac{\pi}{2}$ pulse), and a mirror requires half a Rabi period (π pulse).

After the initial beamsplitter ($\frac{\pi}{2}$) pulse, the atom is in a superposition of states which differ in velocity by $\hbar\mathbf{k}_{\text{eff}}/m$. The resulting spatial separation of the halves of the atom is proportional to the interferometer's sensitivity to acceleration along the direction of \mathbf{k}_{eff} . After a time T , a mirror (π) pulse reverses the relative velocity of the

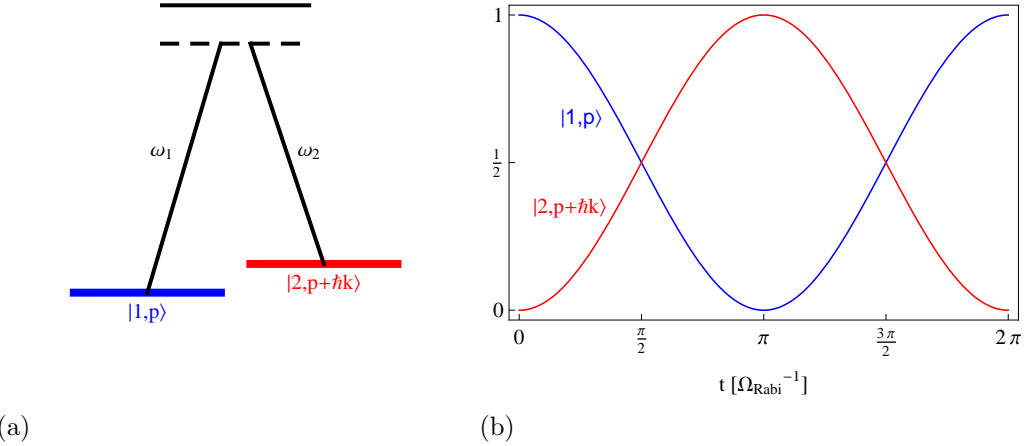


Figure 2.3: (a) Energy level diagram for a stimulated Raman transition between atomic states $|1\rangle$ and $|2\rangle$ through a virtual excited state using lasers of frequency ω_1 and ω_2 with propagation vectors \mathbf{k}_1 and \mathbf{k}_2 , respectively. (b) The probability that the atom is in states $|1\rangle$ and $|2\rangle$ in the presence of these lasers as a function of the time the lasers are on. A $\frac{\pi}{2}$ pulse is a beamsplitter since the atom ends up in a superposition of states $|1\rangle$ and $|2\rangle$ while a π pulse is a mirror since the atom's state is changed completely.

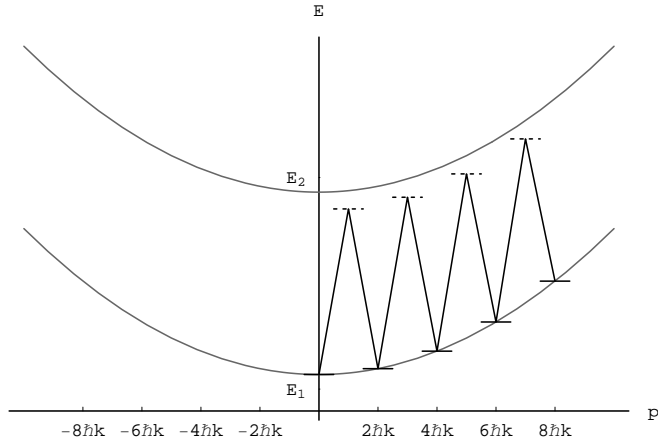


Figure 2.4: The atomic energy level diagram for a series of sequential two-photon Bragg transitions plotted as energy versus momentum. The horizontal lines indicate the states through which the atom is transitioned. The diagonal lines connecting the states represent the laser frequencies used in the transition. The result of this transition is to give the atom a large momentum.

two components of the atom, eventually leading to spatial overlap. To complete the sequence, a final beamsplitter pulse applied at time $2T$ interferes these overlapping components at the intersection point of the two paths. In this work we primarily consider this beamsplitter-mirror-beamsplitter $(\frac{\pi}{2} - \pi - \frac{\pi}{2})$ sequence [11], the simplest implementation of an accelerometer and the matter-wave analog of a Mach-Zender interferometer.

The third and final step of each acceleration measurement is atom detection. At the end of the interferometer sequence, each atom is in a superposition of the two output velocity states, as shown by the diverging paths at the top of Fig. 6.1. Since these two states differ in velocity by $\sim \hbar k_{\text{eff}}/m$, they spatially separate. After an appropriate drift time, the two paths can be separately resolved, and the populations are then measured by absorption imaging. These two final velocity states are directly analogous to the two output ports of a Mach-Zehnder light interferometer after the final recombining beamsplitter. As with a light interferometer, the probability that an atom will be found in a particular output port depends on the relative phase acquired along the two paths of the atom interferometer.

Recent atom interferometers have demonstrated sensor noise levels limited only by the quantum projection noise of the atoms (atom shot noise) [37, 38, 39]. Assuming a typical time-average atom flux of $n = 10^6$ atoms/s, the resulting phase sensitivity is $\sim 1/\sqrt{n} = 10^{-3}$ rad/ $\sqrt{\text{Hz}}$ and the ultimate phase uncertainty is $\sim 10^{-6}$ rad after 10^6 s of integration. This noise performance can potentially be improved by using entangled states instead of uncorrelated atom ensembles [40]. For a suitably entangled source, the Heisenberg limit is $\text{SNR} \sim n$, a factor of \sqrt{n} improvement. For $n \sim 10^6$ entangled atoms, the potential sensitivity improvement is 10^3 . Recent progress using these techniques may soon make improvements in signal-to-noise ratio (SNR) on the order of 10 to 100 realistic [41]. Of course, improvements in SNR may be easier to achieve simply with increased atom flux without using entanglement.

Another sensitivity improvement involves the use of more sophisticated atom optics. The acceleration sensitivity of the interferometer is proportional to the effective momentum $\hbar k_{\text{eff}}$ transferred to the atom during interactions with the laser. Both the Bragg and Raman schemes described above rely on a two-photon process for which

$\hbar k_{\text{eff}} = 2\hbar k$, but large momentum transfer (LMT) beamsplitters with up to $10\hbar k$ or perhaps $100\hbar k$ are possible [42]. Promising LMT beamsplitter candidates include optical lattice manipulations [36, 42, 43], sequences of Raman pulses [44] and multi-photon Bragg diffraction [45]. Figure 2.4 illustrates an example of an LMT process consisting of a series of sequential two-photon Bragg transitions as may be realized in an optical lattice[43]. As the atom accelerates, the resonance condition is maintained by increasing the frequency difference between the lasers.

Finally, consider the expected acceleration sensitivity our new atom interferometric gravimeter. Our dual isotope rubidium interferometer described in Chapter 5 takes advantage of an $L \approx 10$ m vacuum system which allows for a long interrogation time of $T = 1.34$ s [34, 30]. As Chapter 4 shows, the phase response of the interferometer to an acceleration g is $\phi_g = k_{\text{eff}} g T^2$. Using $10\hbar k$ LMT beamsplitters and shot-noise limited detection of $n = 10^6$ atoms/s for this apparatus results in a sensitivity of

$$\delta g = \left(\frac{\delta\phi}{\phi_g} \right) g = \frac{1/\sqrt{n}}{k_{\text{eff}} T^2} \approx \frac{1/\sqrt{10^6 \frac{\text{atoms}}{\text{s}}}}{(10 \times \frac{2\pi}{780 \text{ nm}})(1.34 \text{ s})^2} \sim 7 \times 10^{-13} \text{ } g/\sqrt{\text{Hz}} \quad (2.1)$$

which gives a precision of $\sim 10^{-15}g$ after a day of integration. In the most conservative case, constraining ourselves to conventional $2\hbar k$ atom optics leads to a precision of $< 10^{-15}g$ after ~ 1 month of integration. This estimate is based on realistic extrapolations from current performance levels, which are at $10^{-10}g$ [17].

Chapter 3

Phase shift determination

Here we review the theory for calculating the phase difference between the two halves of the atom at the end of the light-pulse atom interferometer pulse sequence. These results are well-known [46, 47, 30]. Other equivalent formalisms for this calculation exist as well (see, for example [48, 49]). The discussion of systematic errors in Chapter 4 relies on the formulae for the phase difference presented in Section 3.1. The proof of these formulae as well as a discussion of their range of validity is given in Section 3.2 but is not necessary for the rest of the thesis.

3.1 Phase shift formulae

The main result we will show is that the total phase difference $\Delta\phi_{\text{tot}}$ between the two paths of an atom interferometer may be written as the sum of three easily calculated components:

$$\Delta\phi_{\text{tot}} = \Delta\phi_{\text{propagation}} + \Delta\phi_{\text{separation}} + \Delta\phi_{\text{laser}}. \quad (3.1)$$

For this calculation we take $\hbar = c = 1$.

The propagation phase $\Delta\phi_{\text{propagation}}$ arises from the free-fall evolution of the atom between light pulses and is given by

$$\Delta\phi_{\text{propagation}} = \sum_{\text{upper}} \left(\int_{t_l}^{t_F} (L_c - E_i) dt \right) - \sum_{\text{lower}} \left(\int_{t_l}^{t_F} (L_c - E_i) dt \right) \quad (3.2)$$

where the sums are over all the path segments of the upper and lower arms of the interferometer, and L_c is the classical Lagrangian evaluated along the classical trajectory of each path segment. In addition to the classical action, Eq. (3.2) includes a contribution from the internal atomic energy level E_i . The initial and final times t_I and t_F for each path segment, as well as L_c and E_i , all depend on the path segment.

The laser phase $\Delta\phi_{\text{laser}}$ comes from the interaction of the atom with the laser field used to manipulate the wavefunction at each of the beamsplitters and mirrors in the interferometer. At each interaction point, the component of the state that changes momentum due to the light acquires the phase of the laser $\phi_L(t_0, \mathbf{x}_c(t_0)) = \mathbf{k} \cdot \mathbf{x}_c(t_0) - \omega t_0 + \phi$ evaluated at the classical point of the interaction:

$$\Delta\phi_{\text{laser}} = \left(\sum_j \pm \phi_L(t_j, \mathbf{x}_u(t_j)) \right)_{\text{upper}} - \left(\sum_j \pm \phi_L(t_j, \mathbf{x}_l(t_j)) \right)_{\text{lower}} \quad (3.3)$$

The sums are over all the interaction points at the times t_j , and $\mathbf{x}_u(t)$ and $\mathbf{x}_l(t)$ are the classical trajectories of the upper and lower arm of the interferometer, respectively. The sign of each term depends on whether the atom gains (+) or loses (−) momentum as a result of the interaction.

The separation phase $\Delta\phi_{\text{separation}}$ arises when the classical trajectories of the two arms of the interferometer do not exactly intersect at the final beamsplitter (see Fig. 3.1). For a separation between the upper and lower arms of $\Delta\mathbf{x} = \mathbf{x}_l - \mathbf{x}_u$, the resulting phase shift is

$$\Delta\phi_{\text{separation}} = \bar{\mathbf{p}} \cdot \Delta\mathbf{x} \quad (3.4)$$

where $\bar{\mathbf{p}}$ is the average classical canonical momentum of the atom after the final beamsplitter.

3.2 Justification of phase shift formulae

The interferometer calculation amounts to solving the Schrodinger equation with the following Hamiltonian:

$$\hat{H}_{\text{tot}} = \hat{H}_{\text{a}} + \hat{H}_{\text{ext}} + \hat{V}_{\text{int}}(\hat{\mathbf{x}}) \quad (3.5)$$

Here \hat{H}_a is the internal atomic structure Hamiltonian, \hat{H}_{ext} is the Hamiltonian for the atom's external degrees of freedom (center of mass position and momentum), and $\hat{V}_{\text{int}}(\hat{\mathbf{x}}) = -\hat{\mu} \cdot \mathbf{E}(\hat{\mathbf{x}})$ is the atom-light interaction, which we take to be the electric dipole Hamiltonian with $\hat{\mu}$ the dipole moment operator.

The calculation is naturally divided into a series of light pulses during which $\hat{V}_{\text{int}} \neq 0$, and the segments between light pulses during which $\hat{V}_{\text{int}} = 0$ and the atom is in free-fall. When the light is off, the atom's internal and external degrees of freedom are decoupled. The internal eigenstates satisfy

$$i\partial_t |A_i\rangle = \hat{H}_a |A_i\rangle = E_i |A_i\rangle \quad (3.6)$$

and we write the solution as $|A_i\rangle = |i\rangle e^{-iE_i(t-t_0)}$ with time-independent eigenstate $|i\rangle$ and energy level E_i .

For the external state solution $|\psi\rangle$, we initially consider $\hat{H}_{\text{ext}} = H(\hat{\mathbf{x}}, \hat{\mathbf{p}})$ to be an arbitrary function of the external position and momentum operators:

$$i\partial_t |\psi\rangle = H(\hat{\mathbf{x}}, \hat{\mathbf{p}}) |\psi\rangle. \quad (3.7)$$

It is now useful to introduce a Galilean transformation operator

$$\hat{G}_c \equiv \hat{G}(\mathbf{x}_c, \mathbf{p}_c, L_c) = e^{i \int L_c dt} e^{-i \hat{\mathbf{p}} \cdot \mathbf{x}_c} e^{i \mathbf{p}_c \cdot \hat{\mathbf{x}}} \quad (3.8)$$

which consists of momentum boost by \mathbf{p}_c , a position translation by \mathbf{x}_c , and a phase shift. We choose to write

$$|\psi\rangle = \hat{G}_c |\phi_{CM}\rangle. \quad (3.9)$$

We will show that for a large class of relevant Hamiltonians, if \mathbf{x}_c , \mathbf{p}_c , and L_c are taken to be the classical position, momentum and Lagrangian, respectively, then $|\phi_{CM}\rangle$ is a wavepacket with $\langle \hat{\mathbf{x}} \rangle = \langle \hat{\mathbf{p}} \rangle = 0$, and the dynamics of $|\phi_{CM}\rangle$ do not affect the phase shift result (i.e., $|\phi_{CM}\rangle$ is the center of mass frame wavefunction). However, for now we maintain generality and just treat \mathbf{x}_c , \mathbf{p}_c , and L_c as arbitrary functions of time.

Combining (3.7) and (3.9) results in

$$\begin{aligned} i\partial_t |\phi_{CM}\rangle &= \left\{ \hat{G}_c^\dagger H(\hat{\mathbf{x}}, \hat{\mathbf{p}}) \hat{G}_c - i\hat{G}_c^\dagger \partial_t \hat{G}_c \right\} |\phi_{CM}\rangle \\ &= \{H(\hat{\mathbf{x}} + \mathbf{x}_c, \hat{\mathbf{p}} + \mathbf{p}_c) + \dot{\mathbf{p}}_c \cdot \hat{\mathbf{x}} - (\hat{\mathbf{p}} + \mathbf{p}_c) \cdot \dot{\mathbf{x}}_c + L_c\} |\phi_{CM}\rangle \end{aligned} \quad (3.10)$$

where we used the following identities:

$$\begin{aligned} \hat{G}_c^\dagger \hat{\mathbf{x}} \hat{G}_c &= \hat{\mathbf{x}} + \mathbf{x}_c \\ \hat{G}_c^\dagger \hat{\mathbf{p}} \hat{G}_c &= \hat{\mathbf{p}} + \mathbf{p}_c \\ \hat{G}_c^\dagger H(\hat{\mathbf{x}}, \hat{\mathbf{p}}) \hat{G}_c &= H(\hat{\mathbf{x}} + \mathbf{x}_c, \hat{\mathbf{p}} + \mathbf{p}_c) \end{aligned} \quad (3.11)$$

Next, we Taylor expand $H(\hat{\mathbf{x}} + \mathbf{x}_c, \hat{\mathbf{p}} + \mathbf{p}_c)$ about \mathbf{x}_c and \mathbf{p}_c ,

$$H(\hat{\mathbf{x}} + \mathbf{x}_c, \hat{\mathbf{p}} + \mathbf{p}_c) = H(\mathbf{x}_c, \mathbf{p}_c) + \nabla_{\hat{\mathbf{x}}} H(\mathbf{x}_c, \mathbf{p}_c) \cdot \hat{\mathbf{x}} + \nabla_{\hat{\mathbf{p}}} H(\mathbf{x}_c, \mathbf{p}_c) \cdot \hat{\mathbf{p}} + \hat{H}_2 \quad (3.12)$$

where \hat{H}_2 contains all terms that are second order or higher in $\hat{\mathbf{x}}$ and $\hat{\mathbf{p}}$. (We will ultimately be allowed to neglect \hat{H}_2 in this calculation.) Inserting this expansion and grouping terms yields

$$i\partial_t |\phi_{CM}\rangle = \left\{ (H_c - \dot{\mathbf{x}}_c \cdot \mathbf{p}_c + L_c) + (\nabla_{\mathbf{x}_c} H_c + \dot{\mathbf{p}}_c) \cdot \hat{\mathbf{x}} + (\nabla_{\mathbf{p}_c} H_c - \dot{\mathbf{x}}_c) \cdot \hat{\mathbf{p}} + \hat{H}_2 \right\} |\phi_{CM}\rangle$$

where we have defined the classical Hamiltonian $H_c \equiv H(\mathbf{x}_c, \mathbf{p}_c)$. If we now let \mathbf{x}_c , \mathbf{p}_c , and L_c satisfy Hamilton's equations,

$$\begin{aligned} \dot{\mathbf{x}}_c &= \nabla_{\mathbf{p}_c} H_c \\ \dot{\mathbf{p}}_c &= -\nabla_{\mathbf{x}_c} H_c \\ L_c &= \dot{\mathbf{x}}_c \cdot \mathbf{p}_c - H_c \end{aligned} \quad (3.13)$$

with $\mathbf{p}_c \equiv \nabla_{\hat{\mathbf{x}}_c} L_c$ the classical canonical momentum, then $|\phi_{CM}\rangle$ must satisfy

$$i\partial_t |\phi_{CM}\rangle = \hat{H}_2 |\phi_{CM}\rangle \quad (3.14)$$

Next we show that it is possible to choose $|\phi_{CM}\rangle$ with $\langle \hat{x} \rangle = \langle \hat{p} \rangle = 0$ for a certain class of \hat{H}_2 , so that \mathbf{x}_c and \mathbf{p}_c completely describe the atom's classical center of mass trajectory. This is known as the semi-classical limit. Starting from Ehrenfest's theorem for the expectation values of $|\phi_{CM}\rangle$,

$$\partial_t \langle \hat{x}_i \rangle = i \left\langle \left[\hat{H}_2, \hat{x}_i \right] \right\rangle = \left\langle \partial_{\hat{p}_i} \hat{H}_2 \right\rangle \quad (3.15)$$

$$\partial_t \langle \hat{p}_i \rangle = i \left\langle \left[\hat{H}_2, \hat{p}_i \right] \right\rangle = - \left\langle \partial_{\hat{x}_i} \hat{H}_2 \right\rangle \quad (3.16)$$

and expanding about $\langle \hat{\mathbf{x}} \rangle$ and $\langle \hat{\mathbf{p}} \rangle$,

$$\begin{aligned} \partial_t \langle \hat{x}_i \rangle &= \left\langle \partial_{\hat{p}_i} \hat{H}_2 \Big|_{\langle \hat{\mathbf{x}} \rangle, \langle \hat{\mathbf{p}} \rangle} + \partial_{\hat{p}_j} \partial_{\hat{p}_i} \hat{H}_2 \Big|_{\langle \hat{\mathbf{x}} \rangle, \langle \hat{\mathbf{p}} \rangle} (\hat{p}_j - \langle \hat{p}_j \rangle) + \partial_{\hat{x}_j} \partial_{\hat{p}_i} \hat{H}_2 \Big|_{\langle \hat{\mathbf{x}} \rangle, \langle \hat{\mathbf{p}} \rangle} (\hat{x}_j - \langle \hat{x}_j \rangle) \right. \\ &\quad \left. + \frac{1}{2!} \partial_{\hat{p}_i} \partial_{\hat{p}_j} \partial_{\hat{p}_k} \hat{H}_2 \Big|_{\langle \hat{\mathbf{x}} \rangle, \langle \hat{\mathbf{p}} \rangle} (\hat{p}_j - \langle \hat{p}_j \rangle) (\hat{p}_k - \langle \hat{p}_k \rangle) + \dots \right\rangle \\ \partial_t \langle \hat{p}_i \rangle &= \left\langle \partial_{\hat{x}_i} \hat{H}_2 \Big|_{\langle \hat{\mathbf{x}} \rangle, \langle \hat{\mathbf{p}} \rangle} + \partial_{\hat{x}_j} \partial_{\hat{x}_i} \hat{H}_2 \Big|_{\langle \hat{\mathbf{x}} \rangle, \langle \hat{\mathbf{p}} \rangle} (\hat{x}_j - \langle \hat{x}_j \rangle) + \partial_{\hat{p}_j} \partial_{\hat{x}_i} \hat{H}_2 \Big|_{\langle \hat{\mathbf{x}} \rangle, \langle \hat{\mathbf{p}} \rangle} (\hat{p}_j - \langle \hat{p}_j \rangle) \right. \\ &\quad \left. + \frac{1}{2!} \partial_{\hat{x}_k} \partial_{\hat{x}_j} \partial_{\hat{x}_i} \hat{H}_2 \Big|_{\langle \hat{\mathbf{x}} \rangle, \langle \hat{\mathbf{p}} \rangle} (\hat{x}_j - \langle \hat{x}_j \rangle) (\hat{x}_k - \langle \hat{x}_k \rangle) + \dots \right\rangle \end{aligned}$$

we find the following:

$$\partial_t \langle \hat{x}_i \rangle = \partial_{\hat{p}_i} \hat{H}_2 \Big|_{\langle \hat{\mathbf{x}} \rangle, \langle \hat{\mathbf{p}} \rangle} + \frac{1}{2!} \partial_{\hat{p}_k} \partial_{\hat{p}_j} \partial_{\hat{p}_i} \hat{H}_2 \Big|_{\langle \hat{\mathbf{x}} \rangle, \langle \hat{\mathbf{p}} \rangle} \Delta p_{jk}^2 + \dots \quad (3.17)$$

$$\partial_t \langle \hat{p}_i \rangle = - \partial_{\hat{x}_i} \hat{H}_2 \Big|_{\langle \hat{\mathbf{x}} \rangle, \langle \hat{\mathbf{p}} \rangle} - \frac{1}{2!} \partial_{\hat{x}_k} \partial_{\hat{x}_j} \partial_{\hat{x}_i} \hat{H}_2 \Big|_{\langle \hat{\mathbf{x}} \rangle, \langle \hat{\mathbf{p}} \rangle} \Delta x_{jk}^2 + \dots \quad (3.18)$$

where $\Delta x_{jk}^2 \equiv \langle \hat{x}_j \hat{x}_k \rangle - \langle \hat{x}_j \rangle \langle \hat{x}_k \rangle$ and $\Delta p_{jk}^2 \equiv \langle \hat{p}_j \hat{p}_k \rangle - \langle \hat{p}_j \rangle \langle \hat{p}_k \rangle$ are measures of the wavepacket's width in phase space ¹. This shows that if \hat{H}_2 contains no terms higher than second order in $\hat{\mathbf{x}}$ and $\hat{\mathbf{p}}$, then Ehrenfest's theorem reduces to Hamilton's equations, and the expectation values follow the classical trajectories. Furthermore, this implies that we can choose $|\phi_{CM}\rangle$ to be the wavefunction in the atom's rest frame, since $\langle \hat{x} \rangle = \langle \hat{p} \rangle = 0$ is a valid solution to Eqs. (3.17) and (3.18) so long as all derivatives of \hat{H}_2 higher than second order vanish. In addition, even when this

¹In general, there will also be cross terms with phase space width such as $\langle \hat{x}_j \hat{p}_k \rangle - \langle \hat{x}_j \rangle \langle \hat{p}_k \rangle$.

condition is not strictly met, it is often possible to ignore the non-classical corrections to the trajectory so long as the phase space widths Δx_{jk} and Δp_{jk} are small compared to the relevant derivatives of \hat{H}_2 (i.e., the semi-classical approximation). For example, such corrections are present for an atom propagating in the non-uniform gravitational field g of the Earth for which $\partial_r \partial_r \partial_r \hat{H}_2 \sim \partial_r^2 g$. Assuming an atom wavepacket width $\Delta x \lesssim 1$ mm, the deviation from the classical trajectory is $\partial_t \langle \hat{p} \rangle \sim (\partial_r^2 g) \Delta x^2 \lesssim 10^{-20} g$, which is a negligibly small correction even in the context of the $\sim 10^{-15} g$ apparatus we describe below for testing the Equivalence Principle.

The complete solution for the external wavefunction requires a solution of Eq. (3.14) for $|\phi_{CM}\rangle$, but this is non-trivial for general \hat{H}_2 . In the simplified case where \hat{H}_2 is second order in $\hat{\mathbf{x}}$ and $\hat{\mathbf{p}}$, the exact expression for the propagator is known [50] and may be used to determine the phase acquired by $|\phi_{CM}\rangle$. However, this step is not necessary for our purpose, because for second order external Hamiltonians the operator \hat{H}_2 does not depend on either \mathbf{x}_c or \mathbf{p}_c . In this restricted case, the solution for the rest frame wavefunction $|\phi_{CM}\rangle$ does not depend on the atom's trajectory. Therefore, any additional phase evolution in $|\phi_{CM}\rangle$ must be the same for both arms of the interferometer and so does not contribute to the phase difference. This argument breaks down for more general \hat{H}_2 , as does the semi-classical description of the atom's motion, but the corrections will depend on the width of $|\phi_{CM}\rangle$ in phase space as shown in Eqs. (3.17) and (3.18). We ignore all such wavepacket-structure induced phase shifts in this analysis by assuming that the relevant moments $\{\Delta x_{jk}, \Delta p_{jk}, \dots\}$ are sufficiently small so that these corrections can be neglected. As shown above for the non-uniform ($\partial_r^2 g \neq 0$) gravitational field of the Earth, this condition is easily met in many experimentally relevant situations.

Finally, we can write the complete solution for the free propagation between the light pulses:

$$\langle \mathbf{x} | \psi, A_i \rangle = \langle \mathbf{x} | \hat{G}_c |\phi_{CM}\rangle |A_i\rangle = e^{i \int_{t_I}^{t_F} L_c dt} e^{i \mathbf{p}_c \cdot (\mathbf{x} - \mathbf{x}_c)} \phi_{CM}(\mathbf{x} - \mathbf{x}_c) |i\rangle e^{-i E_i (t_F - t_I)} \quad (3.19)$$

We see that this result takes the form of a traveling wave with de Broglie wavelength set by \mathbf{p}_c multiplied by an envelope function $\phi_{CM}(\mathbf{x})$, both of which move along the

classical path \mathbf{x}_c . Also, the wavepacket accumulates a propagation phase shift given by the classical action along this path, as well as an additional phase shift arising from the internal atomic energy:

$$\Delta\phi_{\text{propagation}} = \sum_{\text{upper}} \left(\int_{t_I}^{t_F} (L_c - E_i) dt \right) - \sum_{\text{lower}} \left(\int_{t_I}^{t_F} (L_c - E_i) dt \right) \quad (3.20)$$

where the sums are over all the path segments of the upper and lower arms of the interferometer, and t_I , t_F , L_c , and E_i all depend on the path.

Next, we consider the time evolution while the light is on and $\hat{V}_{\text{int}} \neq 0$. In this case, the atom's internal and external degrees of freedom are coupled by the electric dipole interaction, so we work in the interaction picture using the following state ansatz:

$$|\Psi\rangle = \int d\mathbf{p} \sum_i c_i(\mathbf{p}) |\psi_{\mathbf{p}}\rangle |A_i\rangle \quad (3.21)$$

where we have used the momentum space representation of $|\phi_{CM}\rangle$ and so $|\psi_{\mathbf{p}}\rangle \equiv \hat{G}_c e^{-i\hat{H}_2(t-t_0)} |\mathbf{p}\rangle$. Inserting this state into the Schrodinger equation gives the interaction picture equations,

$$\begin{aligned} i\partial_t |\Psi\rangle &= i \int d\mathbf{p} \sum_i \frac{\partial c_i(\mathbf{p})}{\partial t} |\psi_{\mathbf{p}}\rangle |A_i\rangle + \hat{H}_{\text{a}} |\Psi\rangle + \hat{H}_{\text{ext}} |\Psi\rangle = \hat{H}_{\text{tot}} |\Psi\rangle \\ \dot{c}_i(\mathbf{p}) &\equiv \frac{\partial c_i(\mathbf{p})}{\partial t} = \frac{1}{i} \int d\mathbf{p}' \sum_j c_j(\mathbf{p}') \langle A_i | \langle \psi_{\mathbf{p}} | \hat{V}_{\text{int}}(\hat{\mathbf{x}}) |\psi_{\mathbf{p}'}\rangle |A_j\rangle \end{aligned} \quad (3.22)$$

where we used (3.6) and (3.7) as well as the orthonormality of $|A_i\rangle$ and $|\psi_{\mathbf{p}}\rangle$. The interaction matrix element can be further simplified by substituting in $|\psi_{\mathbf{p}}\rangle$ and using identity (3.11):

$$\begin{aligned} \langle \psi_{\mathbf{p}} | \hat{V}_{\text{int}}(\hat{\mathbf{x}}) | \psi_{\mathbf{p}'}\rangle &= \langle \mathbf{p} | e^{i\hat{H}_2(t-t_0)} \hat{V}_{\text{int}}(\hat{\mathbf{x}} + \mathbf{x}_c) e^{-i\hat{H}_2(t-t_0)} | \mathbf{p}'\rangle \\ &= \langle \mathbf{p} | \hat{V}_{\text{int}}(\hat{\mathbf{x}} + \mathbf{x}_c) | \mathbf{p}'\rangle e^{i\left(\frac{\mathbf{p}^2}{2m} - \frac{\mathbf{p}'^2}{2m}\right)(t-t_0)} \end{aligned} \quad (3.23)$$

where we have made the simplifying approximation that $\hat{H}_2 \approx \frac{\hat{\mathbf{p}}^2}{2m}$. This approximation works well as long as the light pulse time $\tau \equiv t - t_0$ is short compared to the

time scale associated with the terms dropped from \hat{H}_2 . For example, for an atom in the gravitational field of Earth, this approximation ignores the contribution $m(\partial_r g)\hat{x}^2$ from the gravity gradient, which for an atom of size $\Delta x \approx 1$ mm leads to a frequency shift $\sim m(\partial_r g)\Delta x^2 \sim 1$ mHz. For a typical pulse time $\tau < 1$ ms, the resulting errors are $\lesssim 1$ μ rad and can usually be neglected. Generally, in this analysis we will assume the short pulse (small τ) limit and ignore all effects that depend on the finite length of the light pulse. These systematic effects can sometimes be important, but they are calculated elsewhere[51][52]. In the case of the ^{87}Rb - ^{85}Rb Equivalence Principle experiment we discuss below, such errors are common-mode suppressed in the differential signal because we use the same laser pulse to manipulate both atoms simultaneously.

As mentioned before, we typically use a two photon process for the atom optics (i.e., Raman or Bragg) in order to avoid transferring population to the short-lived excited state. However, from the point of view of the current analysis, these three-level systems can typically be reduced to effective two-level systems[53][54]. Since the resulting phase shift rules are identical, we will assume a two-level atom coupled to a single laser frequency to simplify the analysis. Assuming a single traveling wave excitation $\mathbf{E}(\hat{\mathbf{x}}) = \mathbf{E}_0 \cos(\mathbf{k} \cdot \hat{\mathbf{x}} - \omega t + \phi)$, Eq. (3.22) becomes

$$\dot{c}_i(\mathbf{p}) = \frac{1}{2i} \int d\mathbf{p}' \sum_j \Omega_{ij} c_j(\mathbf{p}') \langle \mathbf{p} | (e^{i(\mathbf{k} \cdot (\hat{\mathbf{x}} + \mathbf{x}_c) - \omega t + \phi)} + h.c.) | \mathbf{p}' \rangle e^{i \int_{t_0}^t \omega_{ij} + \frac{\mathbf{p}^2}{2m} - \frac{\mathbf{p}'^2}{2m} dt} \quad (3.24)$$

where the Rabi frequency is defined as $\Omega_{ij} \equiv \langle i | (-\hat{\mu} \cdot \mathbf{E}_0) | j \rangle$ and $\omega_{ij} \equiv E_i - E_j$. Now we insert the identity

$$\mathbf{k} \cdot (\hat{\mathbf{x}} + \mathbf{x}_c) - \omega t + \phi = \underbrace{\mathbf{k} \cdot \hat{\mathbf{x}}}_{\text{boost}} + \underbrace{(\mathbf{k} \cdot \mathbf{x}_c(t_0) - \omega t_0 + \phi)}_{\text{laser phase}} + \underbrace{\int_{t_0}^t (\mathbf{k} \cdot \dot{\mathbf{x}}_c - \omega) dt}_{\text{Doppler shift}} \quad (3.25)$$

into Eq. (3.24) and perform the integration over \mathbf{p}' using $\langle \mathbf{p} | e^{\pm i\mathbf{k} \cdot \hat{\mathbf{x}}} | \mathbf{p}' \rangle = \langle \mathbf{p} | \mathbf{p}' \pm \mathbf{k} \rangle$:

$$\begin{aligned}\dot{c}_i(\mathbf{p}) &= \frac{1}{2i} \sum_j \Omega_{ij} \left\{ c_j(\mathbf{p} - \mathbf{k}) e^{i\phi_L} e^{i \int_{t_0}^t (\omega_{ij} - \omega + \mathbf{k} \cdot \hat{\mathbf{x}}_c + \frac{\mathbf{k} \cdot \mathbf{p}}{m} - \frac{\mathbf{k}^2}{2m}) dt} \right. \\ &\quad \left. + c_j(\mathbf{p} + \mathbf{k}) e^{-i\phi_L} e^{-i \int_{t_0}^t (-\omega_{ij} - \omega + \mathbf{k} \cdot \hat{\mathbf{x}}_c + \frac{\mathbf{k} \cdot \mathbf{p}}{m} + \frac{\mathbf{k}^2}{2m}) dt} \right\} \end{aligned}\quad (3.26)$$

where we define the laser phase at point $\{t_0, \mathbf{x}_c(t_0)\}$ as $\phi_L \equiv \mathbf{k} \cdot \mathbf{x}_c(t_0) - \omega t_0 + \phi$. Finally, we impose the two-level constraint ($i = 1, 2$) and consider the coupling between $c_1(\mathbf{p})$ and $c_2(\mathbf{p} + \mathbf{k})$:

$$\begin{aligned}\dot{c}_1(\mathbf{p}) &= \frac{1}{2i} \Omega c_2(\mathbf{p} + \mathbf{k}) e^{-i\phi_L} e^{-i \int_{t_0}^t \Delta(\mathbf{p}) dt} \\ \dot{c}_2(\mathbf{p} + \mathbf{k}) &= \frac{1}{2i} \Omega^* c_1(\mathbf{p}) e^{i\phi_L} e^{i \int_{t_0}^t \Delta(\mathbf{p}) dt}\end{aligned}\quad (3.27)$$

Here the detuning is $\Delta(\mathbf{p}) \equiv \omega_0 - \omega + \mathbf{k} \cdot (\hat{\mathbf{x}}_c + \frac{\mathbf{p}}{m}) + \frac{\mathbf{k}^2}{2m}$, the Rabi frequency is $\Omega \equiv \Omega_{12} = (\Omega_{21})^*$, and $\omega_0 \equiv \omega_{21} > 0$. In arriving at Eqs. (3.27) we made the rotating wave approximation[55], dropping terms that oscillate at $(\omega_0 + \omega)$ compared to those oscillating at $(\omega_0 - \omega)$. Also, $\Omega_{ii} = 0$ since the $|A_i\rangle$ are eigenstates of parity and $\hat{\mu}$ is odd.

The general solution to (3.27) is

$$\begin{bmatrix} c_1(\mathbf{p}, t) \\ c_2(\mathbf{p} + \mathbf{k}, t) \end{bmatrix} = \begin{bmatrix} \Lambda_c(\mathbf{p}) e^{-\frac{i}{2} \Delta(\mathbf{p}) \tau} & -i \Lambda_s(\mathbf{p}) e^{-\frac{i}{2} \Delta(\mathbf{p}) \tau} e^{-i\phi_L} \\ -i \Lambda_s^*(\mathbf{p}) e^{\frac{i}{2} \Delta(\mathbf{p}) \tau} e^{i\phi_L} & \Lambda_c^*(\mathbf{p}) e^{\frac{i}{2} \Delta(\mathbf{p}) \tau} \end{bmatrix} \times \begin{bmatrix} c_1(\mathbf{p}, t_0) \\ c_2(\mathbf{p} + \mathbf{k}, t_0) \end{bmatrix} \quad (3.28)$$

$$\Lambda_c(\mathbf{p}) = \cos\left(\frac{1}{2} \sqrt{\Delta(\mathbf{p})^2 + |\Omega|^2} \tau\right) + i \frac{\Delta(\mathbf{p})}{\sqrt{\Delta(\mathbf{p})^2 + |\Omega|^2}} \sin\left(\frac{1}{2} \sqrt{\Delta(\mathbf{p})^2 + |\Omega|^2} \tau\right) \quad (3.29)$$

$$\Lambda_s(\mathbf{p}) = \frac{\Omega}{\sqrt{\Delta(\mathbf{p})^2 + |\Omega|^2}} \sin\left(\frac{1}{2} \sqrt{\Delta(\mathbf{p})^2 + |\Omega|^2} \tau\right) \quad (3.30)$$

In integrating (3.27) we applied the short pulse limit in the sense of $\mathbf{k} \cdot \ddot{\mathbf{x}}_c \tau^2 \ll 1$, ignoring changes of the atom's velocity during the pulse. For an atom falling in the gravitational field of the Earth, even for pulse times $\tau \sim 10 \mu\text{s}$ this term is $\sim k g \tau^2 \sim 10^{-2}$ rad which is non-negligible at our level of required precision. However, for pedagogical reasons we ignore this error here. Corrections due to the finite pulse time are suppressed in the proposed differential measurement between Rb isotopes since we use the same laser to simultaneously manipulate both species (see Section 5.3).

For simplicity, from now on we assume the light pulses are on resonance: $\Delta(0) = 0$. We also take the short pulse limit in the sense of $|\Delta(\mathbf{p}) - \Delta(0)| \tau \ll 1$ so that we can ignore all detuning systematics. This condition is automatically satisfied experimentally, since only the momentum states that fall within the Doppler width $\sim \tau^{-1}$ of the pulse will interact efficiently with the light.

$$\begin{bmatrix} c_1(\mathbf{p}, t) \\ c_2(\mathbf{p} + \mathbf{k}, t) \end{bmatrix} = \begin{bmatrix} \Lambda_c & -i\Lambda_s e^{-i\phi_L} \\ -i\Lambda_s^* e^{i\phi_L} & \Lambda_c \end{bmatrix} \begin{bmatrix} c_1(\mathbf{p}, t_0) \\ c_2(\mathbf{p} + \mathbf{k}, t_0) \end{bmatrix} \quad \Lambda_c = \cos \frac{|\Omega|\tau}{2} \quad \Lambda_s = \frac{\Omega}{|\Omega|} \sin \frac{|\Omega|\tau}{2} \quad (3.31)$$

In the case of a beamsplitter ($\frac{\pi}{2}$ pulse), we choose $|\Omega|\tau = \frac{\pi}{2}$, whereas for a mirror (π pulse) we set $|\Omega|\tau = \pi$:

$$\Lambda_{\pi/2} = \begin{bmatrix} \frac{1}{\sqrt{2}} & \frac{-i}{\sqrt{2}} e^{-i\phi_L} \\ \frac{-i}{\sqrt{2}} e^{i\phi_L} & \frac{1}{\sqrt{2}} \end{bmatrix} \quad \Lambda_\pi = \begin{bmatrix} 0 & -i e^{-i\phi_L} \\ -i e^{i\phi_L} & 0 \end{bmatrix} \quad (3.32)$$

These matrices encode the rules for the imprinting of the laser's phase on the atom: the component of the atom $c_1(\mathbf{p}, t_0)$ that gains momentum from the light (absorbs a photon) picks up a phase $+i\phi_L$, and the component of the atom $c_2(\mathbf{p} + \mathbf{k}, t_0)$ that loses momentum to the light (emits a photon) picks up a phase $-i\phi_L$. Symbolically,

$$|\mathbf{p}\rangle \rightarrow |\mathbf{p} + \mathbf{k}\rangle e^{i\phi_L} \quad (3.33)$$

$$|\mathbf{p} + \mathbf{k}\rangle \rightarrow |\mathbf{p}\rangle e^{-i\phi_L} \quad (3.34)$$

As a result, the total laser phase shift is

$$\Delta\phi_{\text{laser}} = \left(\sum_j \pm\phi_L(t_j, \mathbf{x}_u(t_j)) \right)_{\text{upper}} - \left(\sum_j \pm\phi_L(t_j, \mathbf{x}_l(t_j)) \right)_{\text{lower}} \quad (3.35)$$

where the sums are over all of the atom–laser interaction points $\{t_j, \mathbf{x}_u(t_j)\}$ and $\{t_j, \mathbf{x}_l(t_j)\}$ along the upper and lower arms, respectively, and the sign is determined by Eqs. (3.33) and (3.34).

The final contribution to $\Delta\phi_{\text{tot}}$ is the separation phase, $\Delta\phi_{\text{separation}}$. As shown in Fig. 3.1, this shift arises because the endpoints of the two arms of the interferometer need not coincide at the time of the final beamsplitter. To derive the expression for separation phase, we write the state of the atom at time $t = t_0 + \tau$ just after the final beamsplitter pulse as

$$|\Psi(t)\rangle = |\Psi_u(t)\rangle + |\Psi_l(t)\rangle \quad (3.36)$$

where $|\Psi_u(t)\rangle$ and $|\Psi_l(t)\rangle$ are the components of the final state that originate from the upper and lower arms, respectively. Just before the final beamsplitter pulse is applied, we write the state of each arm as

$$|\Psi_u(t_0)\rangle = \int d\mathbf{p} c_1(\mathbf{p}, t_0) \hat{G}_u(t_0) |\mathbf{p}\rangle |A_1\rangle e^{i\theta_u} \quad (3.37)$$

$$|\Psi_l(t_0)\rangle = \int d\mathbf{p} c_2(\mathbf{p}, t_0) \hat{G}_l(t_0) |\mathbf{p}\rangle |A_2\rangle e^{i\theta_l} \quad (3.38)$$

where $\hat{G}_u \equiv \hat{G}(\mathbf{x}_u, \mathbf{p}_u, L_u)$ and $\hat{G}_l \equiv \hat{G}(\mathbf{x}_l, \mathbf{p}_l, L_l)$ are the Galilean transformation operators for the upper and lower arm, respectively. These operators translate each wavepacket in phase space to the appropriate position (\mathbf{x}_u or \mathbf{x}_l) and momentum (\mathbf{p}_u or \mathbf{p}_l). Here we have assumed for clarity that prior to the final beamsplitter the upper and lower arms are in internal states $|A_1\rangle$ and $|A_2\rangle$ with amplitudes $c_1(\mathbf{p}, t_0)$ and $c_2(\mathbf{p}, t_0)$, respectively; identical results are obtained in the reversed case. We have also explicitly factored out the dynamical phases θ_u and θ_l accumulated along the upper and lower arms, respectively, which contain by definition all contributions to laser phase and propagation phase acquired prior to the final beamsplitter.

We write the wavefunction components after the beamsplitter in the form of Eq.

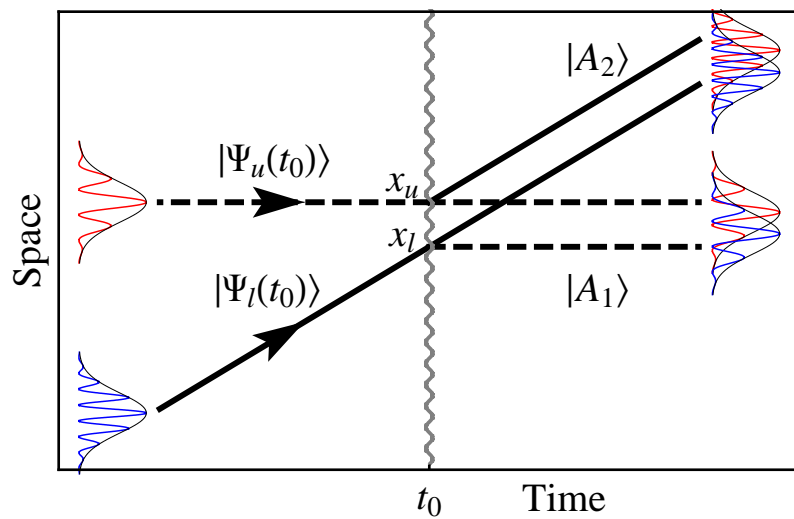


Figure 3.1: Separation Phase. This is a magnified view of the end of the interferometer which shows the upper and lower arms converging at the final beamsplitter at time t_0 , and the resulting interference. The dashed and solid lines designate the components of the wavefunction in internal states $|A_1\rangle$ and $|A_2\rangle$, respectively. After the beamsplitter, each output port consists of a superposition of wavepackets from the upper and lower arm. Any offset $\Delta\mathbf{x} = \mathbf{x}_l - \mathbf{x}_u$ between the centers of the wavepacket contributions to a given output port results in a separation phase shift.

(3.21):

$$|\Psi_u(t)\rangle = \int d\mathbf{p} \sum_i c_i^{(u)}(\mathbf{p}, t) \hat{G}_u |\mathbf{p}\rangle |A_i\rangle \quad (3.39)$$

$$|\Psi_l(t)\rangle = \int d\mathbf{p} \sum_i c_i^{(l)}(\mathbf{p}, t) \hat{G}_l |\mathbf{p}\rangle |A_i\rangle \quad (3.40)$$

where we invoked the short pulse limit so that $e^{-i\hat{H}_2\tau} \approx 1$. Next we time evolve the states using Eq. (3.31) assuming a perfect $\frac{\pi}{2}$ pulse and using the initial conditions given in Eqs. (3.37) and (3.38): namely, $c_1^{(u)}(\mathbf{p}, t_0) = c_1(\mathbf{p}, t_0)e^{i\theta_u}$ and $c_2^{(u)}(\mathbf{p}, t_0) = 0$ for the upper arm and $c_1^{(l)}(\mathbf{p}, t_0) = 0$ and $c_2^{(l)}(\mathbf{p}, t_0) = c_2(\mathbf{p}, t_0)e^{i\theta_l}$ for the lower arm.

$$|\Psi_u(t)\rangle = \int d\mathbf{p} c_1(\mathbf{p}, t_0) \left\{ \frac{1}{\sqrt{2}} \hat{G}_u |\mathbf{p}\rangle |A_1\rangle + \frac{-i}{\sqrt{2}} e^{i\phi_L(\mathbf{x}_u)} \hat{G}_u |\mathbf{p} + \mathbf{k}\rangle |A_2\rangle \right\} e^{i\theta_u} \quad (3.41)$$

$$|\Psi_l(t)\rangle = \int d\mathbf{p} c_2(\mathbf{p} + \mathbf{k}, t_0) \left\{ \frac{-i}{\sqrt{2}} e^{-i\phi_L(\mathbf{x}_l)} \hat{G}_l |\mathbf{p}\rangle |A_1\rangle + \frac{1}{\sqrt{2}} \hat{G}_l |\mathbf{p} + \mathbf{k}\rangle |A_2\rangle \right\} e^{i\theta_l} \quad (3.42)$$

We now project into position space and perform the \mathbf{p} integrals,

$$\langle \mathbf{x} | \Psi_u(t) \rangle = \frac{c_1(\mathbf{x} - \mathbf{x}_u, t_0)}{\sqrt{2}} \left\{ e^{i\mathbf{p}_u \cdot (\mathbf{x} - \mathbf{x}_u)} |A_1\rangle - i e^{i\phi_L(\mathbf{x}_u)} e^{i(\mathbf{p}_u + \mathbf{k}) \cdot (\mathbf{x} - \mathbf{x}_u)} |A_2\rangle \right\} e^{i\theta_u} \quad (3.43)$$

$$\langle \mathbf{x} | \Psi_l(t) \rangle = \frac{c_2(\mathbf{x} - \mathbf{x}_l, t_0)}{\sqrt{2}} \left\{ -i e^{-i\phi_L(\mathbf{x}_l)} e^{i(\mathbf{p}_l - \mathbf{k}) \cdot (\mathbf{x} - \mathbf{x}_l)} |A_1\rangle + e^{i\mathbf{p}_l \cdot (\mathbf{x} - \mathbf{x}_l)} |A_2\rangle \right\} e^{i\theta_l} \quad (3.44)$$

where we identified $c_i(\mathbf{x} - \mathbf{x}_c, t_0) = \int d\mathbf{p} \langle \mathbf{x} - \mathbf{x}_c | \mathbf{p} \rangle c_i(\mathbf{p}, t_0)$ as the Fourier transformed amplitudes. The resulting interference pattern in position space is therefore

$$\begin{aligned} \langle \mathbf{x} | \Psi(t) \rangle &= \langle \mathbf{x} | \Psi_u(t) \rangle + \langle \mathbf{x} | \Psi_l(t) \rangle \\ &= \frac{1}{\sqrt{2}} |A_1\rangle \left\{ c_1(\mathbf{x} - \mathbf{x}_u, t_0) e^{i\theta_u} e^{i\mathbf{p}_u \cdot (\mathbf{x} - \mathbf{x}_u)} - i c_2(\mathbf{x} - \mathbf{x}_l, t_0) e^{i\theta_l} e^{-i\phi_L(\mathbf{x}_l)} e^{i(\mathbf{p}_l - \mathbf{k}) \cdot (\mathbf{x} - \mathbf{x}_l)} \right\} \\ &\quad + \frac{1}{\sqrt{2}} |A_2\rangle \left\{ c_2(\mathbf{x} - \mathbf{x}_l, t_0) e^{i\theta_l} e^{i\mathbf{p}_l \cdot (\mathbf{x} - \mathbf{x}_l)} - i c_1(\mathbf{x} - \mathbf{x}_u, t_0) e^{i\theta_u} e^{i\phi_L(\mathbf{x}_u)} e^{i(\mathbf{p}_u + \mathbf{k}) \cdot (\mathbf{x} - \mathbf{x}_u)} \right\} \end{aligned}$$

The probability of finding the atom in either output port $|A_1\rangle$ or $|A_2\rangle$ is

$$|\langle A_1 | \langle \mathbf{x} | \Psi(t) \rangle|^2 = \frac{|c_1|^2 + |c_2|^2}{2} + \frac{1}{2} (i c_1 c_2^* e^{i\Delta\phi_1} + c.c.) \quad (3.45)$$

$$|\langle A_2 | \langle \mathbf{x} | \Psi(t) \rangle|^2 = \frac{|c_1|^2 + |c_2|^2}{2} - \frac{1}{2} (i c_1 c_2^* e^{i\Delta\phi_2} + c.c.) \quad (3.46)$$

with $c_1 \equiv c_1(\mathbf{x} - \mathbf{x}_u, t_0)$ and $c_2 \equiv c_2(\mathbf{x} - \mathbf{x}_l, t_0)$. For the total phase shift we find

$$\Delta\phi_1 \equiv \left\{ \theta_u + \mathbf{p}_u \cdot (\mathbf{x} - \mathbf{x}_u) \right\} - \left\{ \theta_l - \phi_L(\mathbf{x}_l) + (\mathbf{p}_l - \mathbf{k}) \cdot (\mathbf{x} - \mathbf{x}_l) \right\} \quad (3.47)$$

$$= \underbrace{\theta_u - (\theta_l - \phi_L(\mathbf{x}_l))}_{\Delta\phi_{\text{propagation},1}} + \underbrace{\bar{\mathbf{p}}_1 \cdot \Delta\mathbf{x}}_{\Delta\phi_{\text{separation},1}} + \Delta\mathbf{p} \cdot (\mathbf{x} - \bar{\mathbf{x}}) \quad (3.48)$$

and

$$\Delta\phi_2 \equiv \left\{ \theta_u + \phi_L(\mathbf{x}_u) + (\mathbf{p}_u + \mathbf{k}) \cdot (\mathbf{x} - \mathbf{x}_u) \right\} - \left\{ \theta_l + \mathbf{p}_l \cdot (\mathbf{x} - \mathbf{x}_l) \right\} \quad (3.49)$$

$$= \underbrace{(\theta_u + \phi_L(\mathbf{x}_u)) - \theta_l}_{\Delta\phi_{\text{propagation},2}} + \underbrace{\bar{\mathbf{p}}_2 \cdot \Delta\mathbf{x}}_{\Delta\phi_{\text{separation},2}} + \Delta\mathbf{p} \cdot (\mathbf{x} - \bar{\mathbf{x}}) \quad (3.50)$$

where $\bar{\mathbf{p}}_1 = \frac{\mathbf{p}_u + (\mathbf{p}_l - \mathbf{k})}{2}$ and $\bar{\mathbf{p}}_2 = \frac{(\mathbf{p}_u + \mathbf{k}) + \mathbf{p}_l}{2}$ are the average momenta in the $|A_1\rangle$ (slow) and $|A_2\rangle$ (fast) output ports, respectively. In general, the separation phase is

$$\Delta\phi_{\text{separation}} = \bar{\mathbf{p}} \cdot \Delta\mathbf{x} \quad (3.51)$$

which depends on the separation $\Delta\mathbf{x} \equiv \mathbf{x}_l - \mathbf{x}_u$ between the centers of the wavepackets from each arm as well as the average canonical momentum $\bar{\mathbf{p}}$ in the output port. We point out that even though the definitions (3.47) and (3.49) use the same sign convention as our previous expressions for laser (3.35) and propagation (3.20) phase in the sense of $()_{\text{upper}} - ()_{\text{lower}}$, the separation vector $\Delta\mathbf{x}$ is defined as $(\mathbf{x})_{\text{lower}} - (\mathbf{x})_{\text{upper}}$.

Notice that the phase shift expressions (3.48) and (3.50) contain a position dependent piece $\Delta\mathbf{p} \cdot (\mathbf{x} - \bar{\mathbf{x}})$, where $\bar{\mathbf{x}} \equiv \frac{\mathbf{x}_u + \mathbf{x}_l}{2}$ and $\Delta\mathbf{p} = (\mathbf{p}_u + \mathbf{k}) - \mathbf{p}_l = \mathbf{p}_u - (\mathbf{p}_l - \mathbf{k})$, owing to the fact that the contributions from each arm may have different momenta after the last beamsplitter. Typically this momentum difference is very small, so

the resulting phase variation has a wavelength that is large compared to the spatial extent of the wavefunction. Furthermore, this effect vanishes completely in the case of spatially averaged detection over a symmetric wavefunction.

Finally, we show that the total phase shifts $\Delta\phi_1$ and $\Delta\phi_2$ for the two output ports are actually equal, as required by conservation of probability. According to Eqs. (3.48) and (3.50), the contributions to the total phase differ in the following ways:

$$\begin{aligned} (\Delta\phi_{\text{propagation},1} + \Delta\phi_{\text{laser},1}) - (\Delta\phi_{\text{propagation},2} + \Delta\phi_{\text{laser},2}) &= \phi_L(\mathbf{x}_l) - \phi_L(\mathbf{x}_u) \\ &= \mathbf{k} \cdot (\mathbf{x}_l - \mathbf{x}_u) = \mathbf{k} \cdot \Delta\mathbf{x} \end{aligned}$$

$$\Delta\phi_{\text{separation},1} - \Delta\phi_{\text{separation},2} = \bar{\mathbf{p}}_1 \cdot \Delta\mathbf{x} - \bar{\mathbf{p}}_2 \cdot \Delta\mathbf{x} = -\mathbf{k} \cdot \Delta\mathbf{x}$$

Together these results imply that $\Delta\phi_1 = \Delta\phi_2$ and prove that the total interferometer phase shift $\Delta\phi_{\text{tot}}$ is independent of the output port.

The accuracy of the above formalism is dependent on the applicability of the aforementioned stationary phase approximation as well as the short pulse limit. The stationary phase approximation breaks down when the external Hamiltonian varies rapidly compared to the phase space width of the atom wavepacket. The short pulse limit requires that the atom's velocity not change appreciably during the duration of the atom-light interaction. Both approximations are justified to a large degree for a typical light pulse atom interferometer, but in the most extreme high precision applications such as we consider here, important corrections are present. However, we emphasize that these errors due to finite pulse duration and wavepacket size are well-known, previously established backgrounds.

Chapter 4

Systematic Error Model

An accurate test of the EP requires a thorough understanding of potential backgrounds. To reach the goal sensitivity, we must control spurious accelerations to $< 10^{-15}g$. Systematic errors at this level can arise from many sources, including gravity gradients, Earth's rotation, and electromagnetic forces. To calculate these contributions to the phase shift, we follow the prescription outlined in Chapter 3. We take the atom's Lagrangian in the lab frame to be

$$L = \frac{1}{2}m(\dot{\mathbf{r}} + \boldsymbol{\Omega} \times (\mathbf{r} + \mathbf{R}_e))^2 - m\phi(\mathbf{r} + \mathbf{R}_e) - \frac{1}{2}\alpha\mathbf{B}(\mathbf{r})^2 \quad (4.1)$$

where \mathbf{r} is the position of the atom in the lab frame, $\mathbf{R}_e = (0, 0, R_e)$ is the radius of the Earth, $\boldsymbol{\Omega} = (0, \Omega_y, \Omega_z)$ is the Earth's rotation rate, and $\phi(\mathbf{r})$ is the gravitational potential. In the chosen coordinate system, z is the vertical direction in the lab and $\boldsymbol{\Omega}$ lies in the y - z plane. We then expand ϕ in a Taylor series about \mathbf{R}_e ,

$$\phi(\mathbf{r} + \mathbf{R}_e) = - \left(\mathbf{g} \cdot \mathbf{r} + \frac{1}{2!}(T_{ij})r_i r_j + \frac{1}{3!}(Q_{ijk})r_i r_j r_k + \frac{1}{4!}(S_{ijkl})r_i r_j r_k r_l \right) \quad (4.2)$$

where Earth's gravity field is $\mathbf{g} \equiv -\nabla\phi(\mathbf{R}_e)$, the gravity gradient tensor is $T_{ij} \equiv \partial_j g_i$, the second gradient tensor is $Q_{ijk} \equiv \partial_k \partial_j g_i$, the third gradient tensor is $S_{ijkl} \equiv \partial_l \partial_k \partial_j g_i$, and repeated indices are summed over. Since $\hat{\mathbf{z}}$ is in the vertical direction in the lab we have that $\mathbf{g} = (0, 0, -g)$ and $g = 9.8 \text{ m/s}^2$. The interferometer follows a

fountain geometry which is approximately one-dimensional along the z -direction, so we only include Q_{zzz} and S_{zzzz} and safely ignore the other second and third gradient tensor terms. Likewise, in this analysis we assume that off-diagonal gradient tensor terms T_{ij} with $i \neq j$ are small and can be ignored (this is exactly true for a perfectly spherical Earth). The effects of higher-order moments of the gravitational field are treated separately using a perturbative calculation as described in Section 4.0.1.

Because magnetic fields can cause significant systematic errors, the atoms are prepared in one of the magnetic field insensitive clock states ($|m_F = 0\rangle$ states). The residual energy shift in a magnetic field \mathbf{B} is then $U_B = \frac{1}{2}\alpha\mathbf{B}^2$, where α is the second order Zeeman shift coefficient. We consider magnetic fields of the form

$$\mathbf{B}(\mathbf{r}) = \left(B_0 + \frac{\partial B}{\partial z} z \right) \hat{\mathbf{z}} \quad (4.3)$$

where B_0 is a constant bias magnetic field, and $\frac{\partial B}{\partial z}$ is the gradient of the background magnetic field. While this linear model is sufficient for slowly varying fields, in Section 4.0.2 we describe a perturbative calculation that can account for more complicated magnetic field spatial profiles.

We do not include additional electromagnetic forces in the Lagrangian as their accelerations are well below our systematic threshold. For neutral atoms, electric fields are generally not a concern since the atom's response is second order. Furthermore, electric fields are easily screened by the metallic vacuum chamber, leading to negligibly small phase shifts. Short range effects due to the Casimir [56] force or local patch potentials [57] are also negligible since the atoms are kept far (> 1 cm) from all surfaces throughout the experiment.

As explained in Section 3.2, we point out that the phase shift derived from Eq. 3.1 is only exactly correct for Lagrangians that are second order in position and velocity. When this is not true, as is the case in Eq. 4.1 when $Q_{ijk} \neq 0$ and $S_{ijkl} \neq 0$, the semiclassical formalism breaks down and there are quantum corrections to the phase shift. However, these corrections depend on the size of the atom wavepacket compared to the length scale of variation of the potential, and are typically negligible for wavepackets ~ 1 mm in size.

To analytically determine the trajectories $\mathbf{r}(t)$, we solve the Euler-Lagrange equations using a power series expansion in t :

$$r_i(t) = \sum_{n=0}^N a_{in}(t - t_0)^n \quad (i = 1, 2, 3) \quad (4.4)$$

The coefficients a_{in} are determined recursively after substitution into the equations of motion. This expansion converges quickly as long as $\Omega T \ll 1$ and $\left| \frac{r^n}{g} \frac{\partial^n g}{\partial r^n} \right| \ll 1$. For our apparatus with characteristic length $r \sim 10$ m and time $T \sim 1$ s these conditions are easily met, since $\Omega T \sim 10^{-4}$ rad and $\left| \frac{r^n}{g} \frac{\partial^n g}{\partial r^n} \right| \sim \left(\frac{r}{R_e} \right)^n \lesssim 10^{-6}$ assuming a spherical Earth. With these trajectories and the interferometer geometry shown in Fig. 2.1 we obtain the following expressions for the phase shift in the slow (state $|1\rangle$) output port:

$$\Delta\phi_{\text{propagation}} = \frac{1}{\hbar}((S_{AC} + S_{CE}) - (S_{AB} + S_{BD})) \quad (4.5)$$

$$\Delta\phi_{\text{laser}} = \phi_L(\mathbf{r}_A, 0) - \phi_L(\mathbf{r}_C, T) - \phi_L(\mathbf{r}_B, T) + \phi_L(\mathbf{r}_D, 2T) \quad (4.6)$$

$$\Delta\phi_{\text{separation}} = \frac{1}{2\hbar}(\mathbf{p}_D + \mathbf{p}_E) \cdot (\mathbf{r}_D - \mathbf{r}_E) \quad (4.7)$$

where S_{ij} is the classical action along the path segment between points \mathbf{r}_i and \mathbf{r}_j , and $\mathbf{p}_i = \partial_{\mathbf{r}}L(\mathbf{r}_i)$ is the classical canonical momentum at point \mathbf{r}_i after the final beamsplitter. The laser phase shift at each interaction point is

$$\phi_L(\mathbf{r}, t) = \mathbf{k}_{\text{eff}} \cdot \mathbf{r} - \omega_{\text{eff}} t + \phi_{\text{eff}} \quad (4.8)$$

where \mathbf{k}_{eff} , ω_{eff} , and ϕ_{eff} are the effective propagation vector, frequency and phase, respectively, for whatever atom–laser interaction is used to implement the atom optics. In the case of the stimulated two–photon processes mentioned earlier, $\mathbf{k}_{\text{eff}} = \mathbf{k}_2 - \mathbf{k}_1$, $\omega_{\text{eff}} = \omega_2 - \omega_1 = (k_2 - k_1)/c$, and $\phi_{\text{eff}} = \phi_2 - \phi_1$.

Using the above method, we computed the phase shift response for a single atom interferometer, and the results are shown in Table 4.1. The values of the experimental parameters used to generate this list are representative of the 8.8 m apparatus described previously. Many of these terms are common to both species, and in order

	Phase shift	Size (rad)	Fractional size
1	$-k_{\text{eff}}gT^2$	-2.85×10^8	1.00
2	$k_{\text{eff}}R_e\Omega_y^2T^2$	6.18×10^5	2.17×10^{-3}
3	$-k_{\text{eff}}T_{zz}v_zT^3$	1.58×10^3	5.54×10^{-6}
4	$\frac{7}{12}k_{\text{eff}}gT_{zz}T^4$	-9.21×10^2	3.23×10^{-6}
5	$-3k_{\text{eff}}v_z\Omega_y^2T^3$	-5.14	1.80×10^{-8}
6	$2k_{\text{eff}}v_x\Omega_yT^2$	3.35	1.18×10^{-8}
7	$\frac{7}{4}k_{\text{eff}}g\Omega_y^2T^4$	3.00	1.05×10^{-8}
8	$-\frac{7}{12}k_{\text{eff}}R_eT_{zz}\Omega_y^2T^4$	2.00	7.01×10^{-9}
9	$-\frac{\hbar k_{\text{eff}}^2}{2m}T_{zz}T^3$	7.05×10^{-1}	2.48×10^{-9}
10	$\frac{3}{4}k_{\text{eff}}gQ_{zzz}v_zT^5$	9.84×10^{-3}	3.46×10^{-11}
11	$-\frac{7}{12}k_{\text{eff}}Q_{zzz}v_z^2T^4$	-7.66×10^{-3}	2.69×10^{-11}
12	$-\frac{7}{4}k_{\text{eff}}R_e\Omega_y^4T^4$	-6.50×10^{-3}	2.28×10^{-11}
13	$-\frac{7}{4}k_{\text{eff}}R_e\Omega_y^2\Omega_z^2T^4$	-3.81×10^{-3}	1.34×10^{-11}
14	$-\frac{31}{120}k_{\text{eff}}g^2Q_{zzz}T^6$	-3.39×10^{-3}	1.19×10^{-11}
15	$-\frac{3\hbar k_{\text{eff}}^2}{2m}\Omega_y^2T^3$	-2.30×10^{-3}	8.06×10^{-12}
16	$\frac{1}{4}k_{\text{eff}}T_{zz}^2v_zT^5$	2.19×10^{-3}	7.68×10^{-12}
17	$-\frac{31}{360}k_{\text{eff}}gT_{zz}^2T^6$	-7.53×10^{-4}	2.65×10^{-12}
18	$3k_{\text{eff}}v_y\Omega_y\Omega_zT^3$	2.98×10^{-4}	1.05×10^{-12}
19	$-k_{\text{eff}}\Omega_y\Omega_zy_0T^2$	-7.41×10^{-5}	2.60×10^{-13}
20	$-\frac{3}{4}k_{\text{eff}}R_eQ_{zzz}v_z\Omega_y^2T^5$	-2.14×10^{-5}	7.50×10^{-14}
21	$\frac{31}{60}k_{\text{eff}}gR_eQ_{zzz}\Omega_y^2T^6$	1.47×10^{-5}	5.17×10^{-14}
22	$\frac{3}{2}k_{\text{eff}}T_{zz}v_z\Omega_y^2T^5$	-1.42×10^{-5}	5.00×10^{-14}
23	$-\frac{7}{6}k_{\text{eff}}T_{zz}v_x\Omega_yT^4$	1.08×10^{-5}	3.81×10^{-14}
24	$-2k_{\text{eff}}T_{xx}\Omega_yx_0T^3$	-6.92×10^{-6}	2.43×10^{-14}
25	$-\frac{7\hbar k_{\text{eff}}^2}{12m}Q_{zzz}v_zT^4$	-6.84×10^{-6}	2.40×10^{-14}
26	$-\frac{7}{6}k_{\text{eff}}T_{xx}v_x\Omega_yT^4$	-5.42×10^{-6}	1.90×10^{-14}
27	$-\frac{31}{60}k_{\text{eff}}gT_{zz}\Omega_y^2T^6$	4.90×10^{-6}	1.72×10^{-14}
28	$k_{\text{eff}}T_{xx}v_z\Omega_y^2T^5$	4.75×10^{-6}	1.67×10^{-14}
29	$\frac{3\hbar k_{\text{eff}}^2}{8m}gQ_{zzz}T^5$	4.40×10^{-6}	1.55×10^{-14}
30	$\frac{31}{360}k_{\text{eff}}R_eT_{zz}^2\Omega_y^2T^6$	1.63×10^{-6}	5.74×10^{-15}
31	$-\frac{31}{90}k_{\text{eff}}gT_{xx}\Omega_y^2T^6$	-1.63×10^{-6}	5.74×10^{-15}
32	$\frac{\hbar k_{\text{eff}}^2}{8m}T_{zz}^2T^5$	9.78×10^{-7}	3.43×10^{-15}
33	$-\frac{\hbar k_{\text{eff}}\alpha B_0(\partial_z B)T^2}{8m}$	-7.67×10^{-8}	2.69×10^{-16}
34	$\frac{31}{60}k_{\text{eff}}gS_{zzzz}v_z^2T^6$	-7.52×10^{-8}	2.64×10^{-16}
35	$-\frac{1}{4}k_{\text{eff}}S_{zzzz}v_z^3T^5$	3.64×10^{-8}	1.28×10^{-16}
36	$\frac{31}{72}k_{\text{eff}}T_{zz}Q_{zzz}v_z^2T^6$	-3.13×10^{-8}	1.10×10^{-16}

Table 4.1: Phase shift response for a single atom interferometer $\frac{\pi}{2} - \pi - \frac{\pi}{2}$ sequence given the Lagrangian in Eq. 4.1. Column 3 shows the fractional size of each term compared to the acceleration signal $k_{\text{eff}}gT^2$. All terms with fractional phase shift $> 10^{-16}$ are included. The numbers are for a ^{87}Rb interferometer with the following parameters: $k_{\text{eff}} = 2k = 2 \cdot \frac{2\pi}{780 \text{ nm}}$, $T_{zz} = -2g/R_e$, $T_{xx} = T_{yy} = g/R_e$, $Q_{zzz} = 6g/R_e^2$, $S_{zzzz} = -24g/R_e^3$, $R_e = 6.72 \times 10^6 \text{ m}$, $B_0 = 100 \text{ nT}$, and $\partial_z B = 0.1 \text{ nT/m}$. The Earth's rotation rate is given by $\Omega_y = \Omega \cos \theta_{\text{Lat}}$ and $\Omega_z = \Omega \sin \theta_{\text{Lat}}$ with $\Omega = 7.27 \times 10^{-5} \text{ rad/s}$ and $\theta_{\text{Lat}} = 37.4$ degrees North latitude. The initial position of the atom in the lab is taken as $\mathbf{r}(0) = (x_0, y_0, 0)$, with $x_0 = 1 \text{ mm}$ and $y_0 = 1 \text{ mm}$. The initial velocity is $\dot{\mathbf{r}}(0) = (v_x, v_y, v_z)$, with $v_x = 1 \text{ mm/s}$, $v_y = 1 \text{ mm/s}$, and $v_z = 13.2 \text{ m/s}$.

	Phase shift	Size (rad)	Fractional size
1	$-\frac{1}{2} \left(\frac{1}{m_{85}} - \frac{1}{m_{87}} \right) \hbar k_{\text{eff}}^2 T_{zz} T^3$	1.66×10^{-2}	5.83×10^{-11}
2	$2k_{\text{eff}} \delta v_x \Omega_y T^2$	3.35×10^{-3}	1.18×10^{-11}
3	$-k_{\text{eff}} T_{zz} \delta v_z T^3$	1.44×10^{-4}	5.05×10^{-12}
4	$-\frac{3}{2} \left(\frac{1}{m_{85}} - \frac{1}{m_{87}} \right) \hbar k_{\text{eff}}^2 \Omega_y^2 T^3$	-5.40×10^{-5}	1.90×10^{-13}
5	$-3k_{\text{eff}} \Omega_y^2 \delta v_z T^3$	-4.68×10^{-6}	1.64×10^{-14}
6	$-k_{\text{eff}} T_{zz} \delta z T^2$	8.93×10^{-7}	3.14×10^{-15}
7	$-k_{\text{eff}} \delta y \Omega_y \Omega_z T^2$	-7.41×10^{-7}	2.60×10^{-15}
8	$3k_{\text{eff}} \delta v_y \Omega_y \Omega_z T^3$	2.98×10^{-7}	1.05×10^{-15}
9	$-\frac{7}{12} \left(\frac{1}{m_{85}} - \frac{1}{m_{87}} \right) \hbar k_{\text{eff}}^2 Q_{zzz} v_z T^4$	-1.61×10^{-7}	5.65×10^{-16}
10	$\frac{3}{8} \left(\frac{1}{m_{85}} - \frac{1}{m_{87}} \right) \hbar k_{\text{eff}}^2 g Q_{zzz} T^5$	1.03×10^{-7}	3.63×10^{-16}
11	$-\left(\frac{\alpha_{85}}{m_{85}} - \frac{\alpha_{87}}{m_{87}} \right) \hbar k_{\text{eff}} B_0 (\partial_z B) T^2$	-9.94×10^{-8}	3.49×10^{-16}
12	$-2k_{\text{eff}} T_{xx} \delta x \Omega_y T^3$	-6.92×10^{-8}	2.43×10^{-16}

Table 4.2: Differential phase shift between ^{87}Rb and ^{85}Rb . To create the differential phase shift list we parameterized the launch kinematics with a differential velocity ($\delta v_x = 1 \mu\text{m/s}$, $\delta v_y = 1 \mu\text{m/s}$, $\delta v_z = 12 \mu\text{m/s}$) and position ($\delta x = 1 \mu\text{m}$, $\delta y = 1 \mu\text{m}$, $\delta z = 10 \text{ nm}$) between the centroids of the two isotope clouds. All other parameters are the same as in Table 4.1. Column 3 shows the fractional size of each term compared to the acceleration signal $k_{\text{eff}} g T^2$. We include all terms with a fractional phase shift $> 10^{-16}$.

obtain our $< 10^{-15}g$ sensitivity, we rely on their common mode cancellation. In Table 4.2 we compute the differential phase shift between a ^{87}Rb and a ^{85}Rb interferometer. The two species have different masses m and second order Zeeman coefficients α , as well as potentially different launch kinematics $\mathbf{r}(0)$ and $\dot{\mathbf{r}}(0)$. To create Table 4.2, we parameterized the launch kinematics with a differential velocity $\delta \mathbf{v} = (\delta v_x, \delta v_y, \delta v_z)$ and initial position $\delta \mathbf{r} = (\delta x, \delta y, \delta z)$ between the centroids of the two isotope clouds. Residual systematic phase errors are the result of differential accelerations that arise from gravity gradients, second gravity gradients, coriolis and centrifugal forces, and magnetic forces on the atoms.

As justified below, we expect to achieve experimental parameters that reduce the majority of the systematic errors below our experimental threshold. However, the first several terms in Table 4.2 are still too large. In order to further reduce these backgrounds, we can employ propagation reversal to suppress all terms $\propto k_{\text{eff}}^2$. This well-known technique entails reversing the laser propagation vector $\mathbf{k}_{\text{eff}} \rightarrow -\mathbf{k}_{\text{eff}}$ on

subsequent trials and then subtracting the two results [17]. This suppresses terms 1, 4, 9, and 10 by $\Delta k_{\text{eff}}/k_{\text{eff}}$, where Δk_{eff} is the error in k_{eff} made as a result of the reversal. Reducing these terms below our systematic threshold requires $\Delta k_{\text{eff}}/k_{\text{eff}} < 10^{-5}$. The main acceleration signal and all other terms linear in k_{eff} are not suppressed by this subtraction.

After propagation vector reversal, the last important background phase shifts arise from the differential coriolis and centrifugal acceleration between the isotopes (Table 4.2 terms 2, 5, 7, and 8), and from the Earth's gravity gradient (Table 4.2 terms 3 and 6). We discuss the techniques used to control these remaining systematics in Section 4.1.

4.0.1 Gravity Inhomogeneities

The Taylor series expansion of the gravitational potential (see Eq. 4.2) is a good approximation of the coarse structure of Earth's gravity on length scales of $\sim R_e$, the radius of the Earth. However, local gravity can also vary on much shorter length scales in a way that depends on the specific mass distribution surrounding the experiment, and these gravity inhomogeneities can result in spurious phase shifts. Since these inhomogeneities can be rapidly spatially varying, the Taylor series expansion is not well-suited for their description. Instead, we leverage the fact that these inhomogeneities are typically small in magnitude and solve for the induced phase shift using first-order perturbation theory [46]. This linearization allows us to make a Fourier decomposition of the phase shift response in terms of the spatial wavelengths of the local g -field. See Appendix B for a detailed treatment.

First, we assume a one-dimensional gravitational potential perturbation of the form $\delta\phi(z)$. The gravity field perturbation along the vertical (z) direction is defined as $\delta g_z(z) \equiv -\partial_z \delta\phi$ and may be written as

$$\delta g_z(z) = \int \tilde{\delta}g_z(\lambda) e^{\frac{i2\pi z}{\lambda}} d\lambda \quad (4.9)$$

where $\tilde{\delta}g_z(\lambda)$ is the Fourier component of a gravity perturbation with wavelength λ .

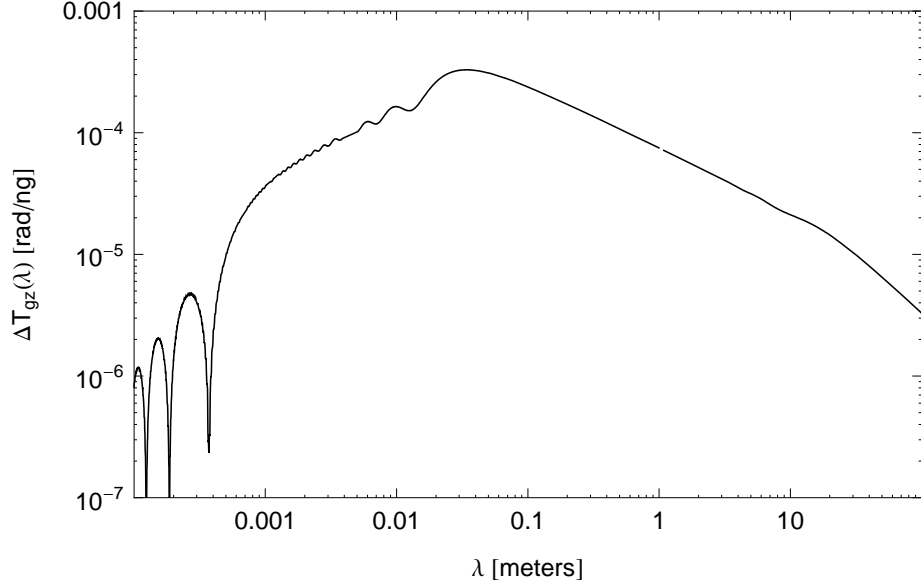


Figure 4.1: Differential gravity response function versus spatial wavelength λ between simultaneous ^{87}Rb and ^{85}Rb interferometers. Short wavelengths are averaged over by each individual interferometer, while long wavelength inhomogeneities cancel as a common-mode between the two species. This response curve assumes identical launch kinematics for the two isotopes.

The total phase shift due to gravity inhomogeneities summed over all wavelengths is

$$\Delta\phi_g = \int T_{gz}(\lambda)\tilde{\delta}g_z(\lambda)d\lambda \quad (4.10)$$

where $T_{gz}(\lambda)$ is the interferometer's gravity perturbation response function. Qualitatively, the response to short wavelengths is suppressed since the interferometer averages over variations that are smaller than its length [29]. The response is flat for wavelengths longer than the scale of the interferometer, and in the limit where $\lambda \sim R_e$ this analysis smoothly approaches the results of our Taylor series calculation described above.

For the ^{87}Rb - ^{85}Rb EP measurement, we are interested in the differential phase response between the isotopes. Figure 4.1 shows the differential response function

$\Delta T_{gz}(\lambda) \equiv |(T_{gz})_{87} - (T_{gz})_{85}|$ for gravity inhomogeneities. Once again, short wavelength variations are suppressed since each interferometer spatially averages over a ~ 10 m region. The peak response occurs at a length scale set by the spatial separation of the arms of a single interferometer $\Delta z = \frac{\hbar k_{\text{eff}}}{m} T \sim 16$ mm. Perfect differential cancellation between isotopes is not achieved because the spatial separation of the arms is mass dependent. Additionally, the long wavelength differential response is suppressed because the differences between the isotope trajectories are negligible when compared to variations with length scales much longer than Δz .

The differential response curve allows us to compute systematic errors arising from the specific gravity environment of our interferometer. Quantitative estimates of these effects requires knowledge of the local $\delta g_z(z)$, which may be obtained through a combination of modeling and characterization. The atom interferometer itself can be used as a precision gravimeter for mapping $\delta g_z(z)$ in situ. By varying the launch velocity, initial vertical position, and interrogation time T , the position of each gravity measurement can be controlled.

Figure 4.1 shows that the differential ^{87}Rb – ^{85}Rb interferometer is maximally sensitive to short wavelength ($\lambda \sim 1$ – 10 cm) gravitational inhomogeneities. To investigate the impact of local uneven mass distributions on the experiment, we compute the spectrum $\tilde{\delta g}_z(\lambda)$ of various sources at different distances from the interferometer. These results are shown in Fig. 4.2. When combined with our response function (Fig. 4.1), we see that for typical mass inhomogeneities, only those that are within a few centimeters of the interferometer can cause potentially significant systematic phase shifts. These nearby inhomogeneities result in phase errors of $\sim 10^{-6}$ rad, which is slightly above our target sensitivity. It will therefore be especially important for the EP measurement that we characterize the local g -field at the centimeter scale.

4.0.2 Magnetic field inhomogeneities

The linear expansion of \mathbf{B} in Eq. 4.3 approximates large scale variation of the magnetic field. However, local field inhomogeneities may exist on short length scales due

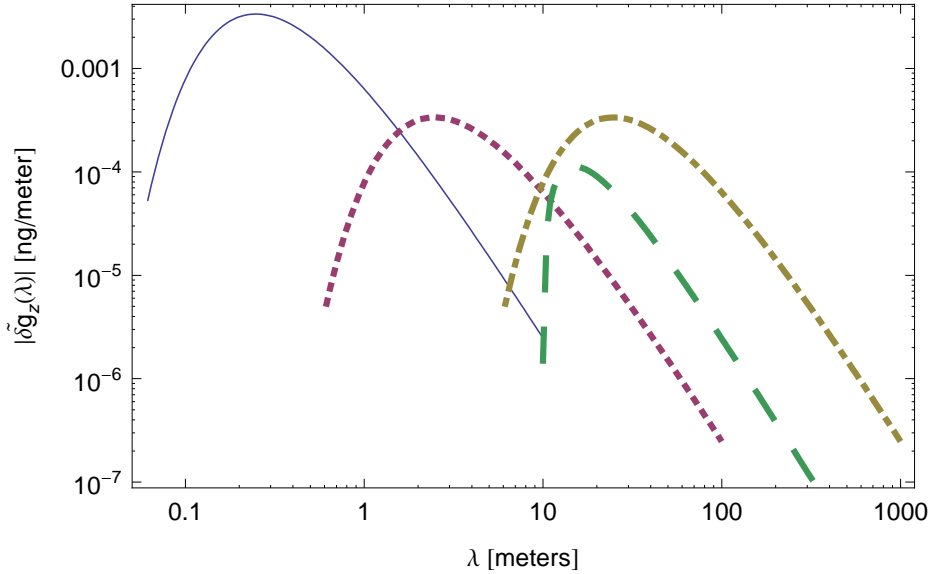


Figure 4.2: The magnitude power spectra of the local gravitational field, $\tilde{\delta g}_z$, for several example sources. The solid (blue) curve is a 10^{-2} kg point source, 10 cm from the center of the interferometer. Similarly, the dotted (purple) curve is a 1 kg source at 1 m and the dash-dotted (yellow) curve is 1000 kg at 10 m. The long-dashed (green) curve is a thin 10 m long rod of mass 10 kg, parallel to the interferometer, whose center is 1 m from the interferometer.

to the presence of nearby magnetic materials. These variations are not well approximated by a Taylor series expansion. Using the same procedure described above for gravity inhomogeneities, we write the local magnetic field as

$$B(z) = \int \tilde{B}_z(\lambda) e^{\frac{i2\pi z}{\lambda}} d\lambda \quad (4.11)$$

where $\tilde{B}_z(\lambda)$ is the Fourier component of a field perturbation with wavelength λ . The total phase shift from magnetic field inhomogeneities is

$$\Delta\phi_B = \int T_{Bz}(\lambda) \tilde{B}_z(\lambda) d\lambda \quad (4.12)$$

Here $T_{Bz}(\lambda)$ is the interferometer's magnetic inhomogeneity response function.

As with gravity above, we compute the differential response function $\Delta T_{Bz}(\lambda) \equiv |(T_{Bz})_{87} - (T_{Bz})_{85}|$ between ^{87}Rb and ^{85}Rb (see Fig. 4.3). The differential response arises because the isotopes have different second order Zeeman coefficients α , as well as different masses. This sensitivity curve drives our magnetic shield design requirements, as discussed in Section 4.1.3.

4.1 Controlling potential systematic errors

4.1.1 Rotation of the Earth

The largest systematic term in the phase shift expansion for a dual species differential interferometer after propagation reversal is due to the rotation of the Earth. Specifically, a differential acceleration due to the coriolis force occurs if the isotopes have different transverse velocities δv_x (Table 4.2, term 2). Reducing this phase shift below our systematic threshold would require $\delta v_x < 10^{-11}$ m/s, which is challenging. However, this specification can be relaxed by artificially making the rotation rate zero.

To a good approximation¹, the atoms are only affected by the Earth's rotation

¹The atoms are also weakly coupled electromagnetically and gravitationally to the local environment, which is fixed to the rotating Earth. These cross-couplings to rotation are generally not

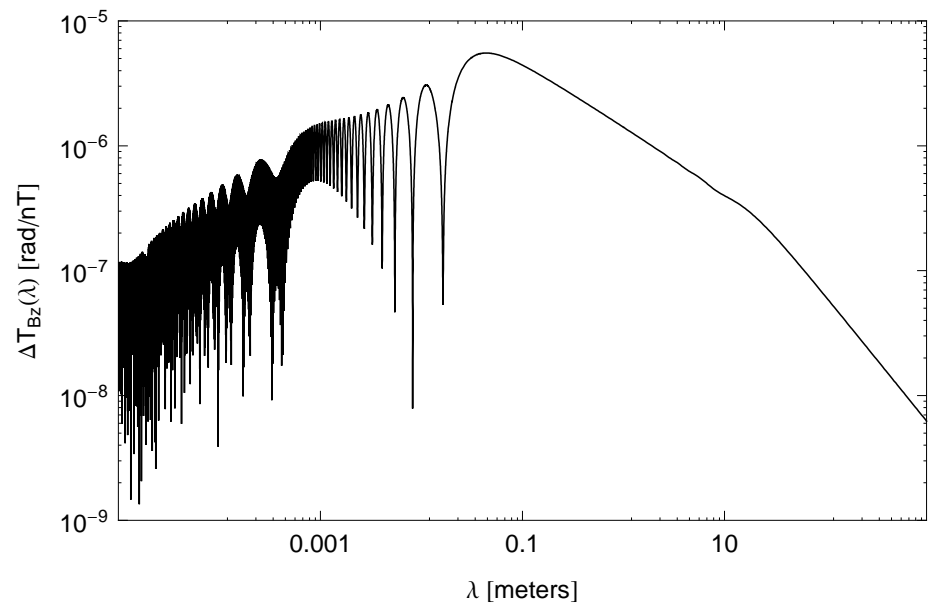


Figure 4.3: Differential magnetic field response function between simultaneous ^{87}Rb and ^{85}Rb interferometers. Short wavelengths are averaged over by each individual interferometer, while long wavelength inhomogeneities cancel as a common-mode between the two species. This response curve assumes identical launch kinematics for the two isotopes.

through their coupling to the laser, so the coriolis acceleration can be eliminated by rotating the laser in the opposite direction of the Earth's rotation. In order to calculate the effect of this rotation compensation, we performed the phase shift calculation using a rotating \mathbf{k}_{eff} . Following the work of [15], we use a retro-reflection configuration to deliver the laser beams \mathbf{k}_1 and \mathbf{k}_2 to the atoms. We rotate \mathbf{k}_{eff} by actuating the retro-reflection mirror. As a result, the incoming beam remains pointing along the z -direction and only the reflected beam rotates. With this configuration, \mathbf{k}_{eff} is given by

$$\mathbf{k}_{\text{eff}} = -2k\hat{\mathbf{n}}(\hat{\mathbf{n}} \cdot \hat{\mathbf{k}}) \quad (4.13)$$

where $\hat{\mathbf{n}}$ is the time-dependent unit normal vector of the retro-reflection mirror, and $\hat{\mathbf{k}}$ is a unit vector in the direction of the fixed delivery beam. Notice that the direction of \mathbf{k}_{eff} rotates as desired, but its length now depends on angle².

The resulting phase shift list appears in Table 4.3, with $\delta\Omega_y$ and $\delta\Omega_z$ the errors in the applied counter-rotation rate. Assuming a transverse velocity difference of $\delta v_x \sim 1 \mu\text{m/s}$, these rotation compensation errors must be kept below $10^{-5}\Omega_{\text{Earth}} \approx 1 \text{nrad/s}$. Methods for measuring angles with nanoradian precision have already been demonstrated [58]. In order to actuate the mirror at this level of precision we can use commercially available sub-nm accurate piezo-electric actuators along with active feedback.

Notice that not all rotation-related phase errors are removed by rotation compensation. Terms that arise from the differential centrifugal acceleration between the isotopes (e.g., Table 4.3 terms 3 and 4) are not suppressed. Physically, this is a consequence of the fact that the retro-reflection mirror that we use to change the laser's angle is displaced from the center of rotation of the Earth by R_e . Therefore, although we can compensate for the angle of the laser by counter-rotating, the retro-reflection mirror remains attached to the rotating Earth, leading to a centrifugal acceleration of

important because the dominant gravitational interaction with the Earth is spherically symmetric, and all electromagnetic interactions with the atom (e.g. with the applied magnetic bias field) are naturally small.

²This small change in magnitude of k_{eff} does not lead to any problematic phase errors in the interferometer since the total angle through which the laser rotates is only $\Delta\theta = 2\Omega_{\text{Earth}}T \sim 10^{-4} \text{ rad}$, and the effect is $\mathcal{O}(\Delta\theta^2)$.

	Phase shift	Size (rad)	Fractional size
1	$-\frac{1}{2} \left(\frac{1}{m_{85}} - \frac{1}{m_{87}} \right) \hbar k_{\text{eff}}^2 T_{zz} T^3$	1.66×10^{-2}	5.83×10^{-11}
2	$-k_{\text{eff}} T_{zz} \delta v_z T^3$	1.44×10^{-4}	5.05×10^{-12}
3	$-\frac{3}{2} \left(\frac{1}{m_{85}} - \frac{1}{m_{87}} \right) \hbar k_{\text{eff}}^2 \Omega_y^2 T^3$	-5.40×10^{-5}	1.90×10^{-13}
4	$-3k_{\text{eff}} \Omega_y^2 \delta v_z T^3$	-4.68×10^{-6}	1.64×10^{-14}
5	$-k_{\text{eff}} T_{zz} \delta z T^2$	8.93×10^{-7}	3.14×10^{-15}
6	$-\frac{7}{12} \left(\frac{1}{m_{85}} - \frac{1}{m_{87}} \right) \hbar k_{\text{eff}}^2 Q_{zzz} v_z T^4$	-1.61×10^{-7}	5.65×10^{-16}
7	$\frac{3}{8} \left(\frac{1}{m_{85}} - \frac{1}{m_{87}} \right) \hbar k_{\text{eff}}^2 Q_{zzz} g T^5$	1.03×10^{-7}	3.63×10^{-16}
8	$-\left(\frac{\alpha_{85}}{m_{85}} - \frac{\alpha_{87}}{m_{87}} \right) \hbar k_{\text{eff}} B_0 (\partial_z B) T^2$	-9.94×10^{-8}	3.49×10^{-16}
9	$k_{\text{eff}} T_{xx} \delta x \Omega_y T^3$	3.46×10^{-8}	1.22×10^{-16}
10	$-2k_{\text{eff}} \delta v_x \delta \Omega_y T^2$	-3.35×10^{-8}	1.18×10^{-16}

Table 4.3: Differential phase shift list with rotation compensation. Terms 1, 3, 6, and 7 will be suppressed by the propagation reversal technique described in Section 4.1.

the phase fronts. After propagation reversal, the only term of this type that is significant is $\sim k_{\text{eff}} \Omega_y^2 \delta v_z T^3$ (Table 4.3 term 4). However, this term is smaller than and has the same scaling with experimental control parameters as the gravity gradient phase shift (Table 4.3 term 2), so the constraints described in Section 4.1.2 to suppress the gravity gradient terms are sufficient to control this centrifugal term as well.

One potential obstacle in achieving the required transverse velocity constraint of $\delta v_x \sim 1 \mu\text{m/s}$ is the expected micro-motion the atoms experience in the TOP magnetic trap prior to launch [59]. Micro-motion orbital velocities in a tight TOP trap such as ours can approach $\sim 1 \text{ cm/s}$ in the transverse plane. Although the differential orbital velocities are suppressed by the ^{87}Rb – ^{85}Rb mass ratio, the resulting $\delta v_x \sim 100 \mu\text{m/s}$ is still too large. This problem can potentially be solved by adiabatically reducing the magnetic field gradient and increasing the rotating field frequency prior to launch.

4.1.2 Gravity gradients

The largest systematic background after rotation compensation is due to the gravity gradient along the vertical direction of the apparatus ($T_{zz} = \partial_z g_z$). Since gravity

is not uniform, the two isotopes experience a different average acceleration if their trajectories are not identical. This effect causes a differential phase shift proportional to the initial spatial separation and initial velocity difference between the isotopes (see Table 4.3, terms 2 and 5). Assuming a spherical Earth model, the gravity gradient felt by the atoms is $T_{zz} \sim 3 \times 10^{-16} g/\text{nm}$, which means that the initial vertical position difference between the isotopes δz must be $< 1 \text{ nm}$ and the initial vertical velocity difference δv_z must be $< 1 \text{ nm/s}$ in order to reduce the systematic phase shift beneath our threshold.

The experiment is designed to initially co-locate the two isotope clouds at the nm level by evaporative cooling both species in the same magnetic trap. For trapping, we use the state $|F = 2, m_F = 2\rangle$ for ^{87}Rb and $|F = 3, m_F = 3\rangle$ for ^{85}Rb since these states have the same magnetic moment.[60] The mass difference between the isotopes leads to a differential trap offset in the combined magnetic and gravitational potential given by

$$\Delta z_{\text{trap}} = \frac{g\Delta m}{\mu_B B''} \quad (4.14)$$

where Δm is the ^{87}Rb - ^{85}Rb mass difference, B'' is the magnetic field curvature of the trap, and μ_B is the Bohr magneton. Our TOP magnetic trap is designed to provide a field curvature $B'' \sim 4 \times 10^5 \text{ Gauss/cm}^2$ which reduces the trap offset to $\Delta z_{\text{trap}} \approx 10 \text{ nm}$. The resulting systematic error is $\sim 10^{-14} g$, but it can be subtracted during the analysis given a knowledge of Δz_{trap} at the $\sim 10\%$ level. This offset can be inferred from a measurement of the field curvature B'' of the trap (e.g., by measuring the trap oscillation frequency). The gravity gradient must also be known, but this can be characterized in situ by using the interferometer as a gradiometer [17].

Control of the gravity gradient phase shift (Table 4.3 term 2) requires that the differential launch velocity be $\delta v_z \leq 1 \text{ nm/s}$. Therefore we cannot employ standard launch techniques (e.g., moving molasses) since the velocity uncertainty is fundamentally limited by the photon recoil velocity $v_R \sim 6 \text{ mm/s}$ due to spontaneous emission. Instead, the atoms are launched using an accelerated optical lattice potential [36]. We launch the two species using the same far-detuned ($\sim 200\text{GHz}$) optical lattice, coherently transferring $\sim 2200\hbar k$ of momentum to each cloud. Because the two species

have different masses, they have different Bloch oscillation times $\tau_B = \frac{\hbar k_{\text{eff}}}{ma}$, where a is the lattice acceleration. As a result, after adiabatically ramping down the lattice potential, the two species are in different momentum eigenstates since they have absorbed a different number of photons. The differential velocity after launch is then

$$\delta v_L = \hbar k_{\text{eff}} \left(\frac{N_{85}}{m_{85}} - \frac{N_{87}}{m_{87}} \right) \quad (4.15)$$

where N_{85} and N_{87} are the number of photons transferred to ^{85}Rb and ^{87}Rb , respectively. We choose the integers $N_{85} = 2168$ and $N_{87} = 2219$ such that their ratio is as close to the isotope mass ratio as possible, resulting in $\delta v_L \sim 12 \mu\text{m/s}$. After launch, we can perform a velocity selective transition to pick out a common class from the overlapping distributions of the two isotopes, which at the expense of atom number could conceivably allow us to achieve our differential velocity constraint.

There are several additional ways to reduce the gravity gradient systematics beyond precise control of the launch kinematics. We can implement a 4-pulse sequence $(\frac{\pi}{2} - \pi - \pi - \frac{\pi}{2})$ which suppresses all phase shift terms $\propto T^3$ at the cost of an order one loss in acceleration sensitivity [48]. This eliminates the velocity dependent gravity gradient phase shifts but would still require that we maintain tight control over the initial differential vertical position between the isotope clouds. Secondly, we can potentially reduce the local gravity gradient T_{zz} by applying appropriate trim masses around the apparatus. It has been shown [29] that in principle a local mass distribution can effectively cancel the gravity gradient of the Earth for a 10 m-scale apparatus. Reducing T_{zz} by an order of magnitude would relax our initial position constraint to the level provided by the expected value of Δz_{trap} , thereby removing the requirement for subtraction during data analysis.

4.1.3 Magnetic fields

The magnetic field phase shift appearing in Table 4.3 (term 8) constrains the maximum allowed linear field gradient to $\partial_z B < 0.1 \text{ nT/meter}$. In the interferometer region, the measured gradient of the Earth's field is $\sim 3 \mu\text{T/m}$, and therefore we require a shielding ratio of at least $\sim 5 \times 10^4$. In addition to suppressing the field

gradient, the magnetic response function (see Fig. 4.3) indicates that the field must be uniform on length scales ~ 1 cm. Large magnetic shields with similar performance have been demonstrated [61]. The magnetic shielding for our interferometer region is provided by a three-layer concentric cylindrical shield made of high permeability material. To maintain a pristine magnetic environment, we use an aluminum vacuum chamber and non-magnetic materials inside the shielded region.

In order to verify the performance of the magnetic shield, we must characterize the field. As with gravity inhomogeneities, the atom interferometer can be used to map the local magnetic field *in situ*, in this case by using a magnetic field sensitive ($m_F \neq 0$) state [62].

Chapter 5

Experimental Apparatus

The apparatus can be conceptually divided into four parts: the interferometer region, where the inertial measurement is performed, the atom source, where the cold atom cloud is prepared, the laser system, which generates all the optical frequencies needed for the experiment, and the computer control system, which synchronizes the timing of the various electronics in the apparatus. Figure 5.1 shows a simplified layout of these subsystems.

5.1 Interferometer Region

From a science perspective, the interferometer region is the most important part of the apparatus. This is where the atom wavepackets are divided and later recombined after accruing the scientifically relevant phase shifts. As a result, this part of the apparatus must be a pristine environment where the atoms can freely fall without being subjected to any perturbations that could lead to systematic errors in the desired measurement.

The overall size of the interferometer region is an important design parameter as it sets the intrinsic acceleration sensitivity of a free-fall gravimeter $\Delta\phi = kgT^2$. As before, here T is the free-fall time of the atom. Since the length of the free-fall region must be at least $L = \frac{1}{2}gT^2$, the sensitivity of the gravimeter scales linearly with its length. We have exploited this scaling by building a 10 m-scale interferometer region.

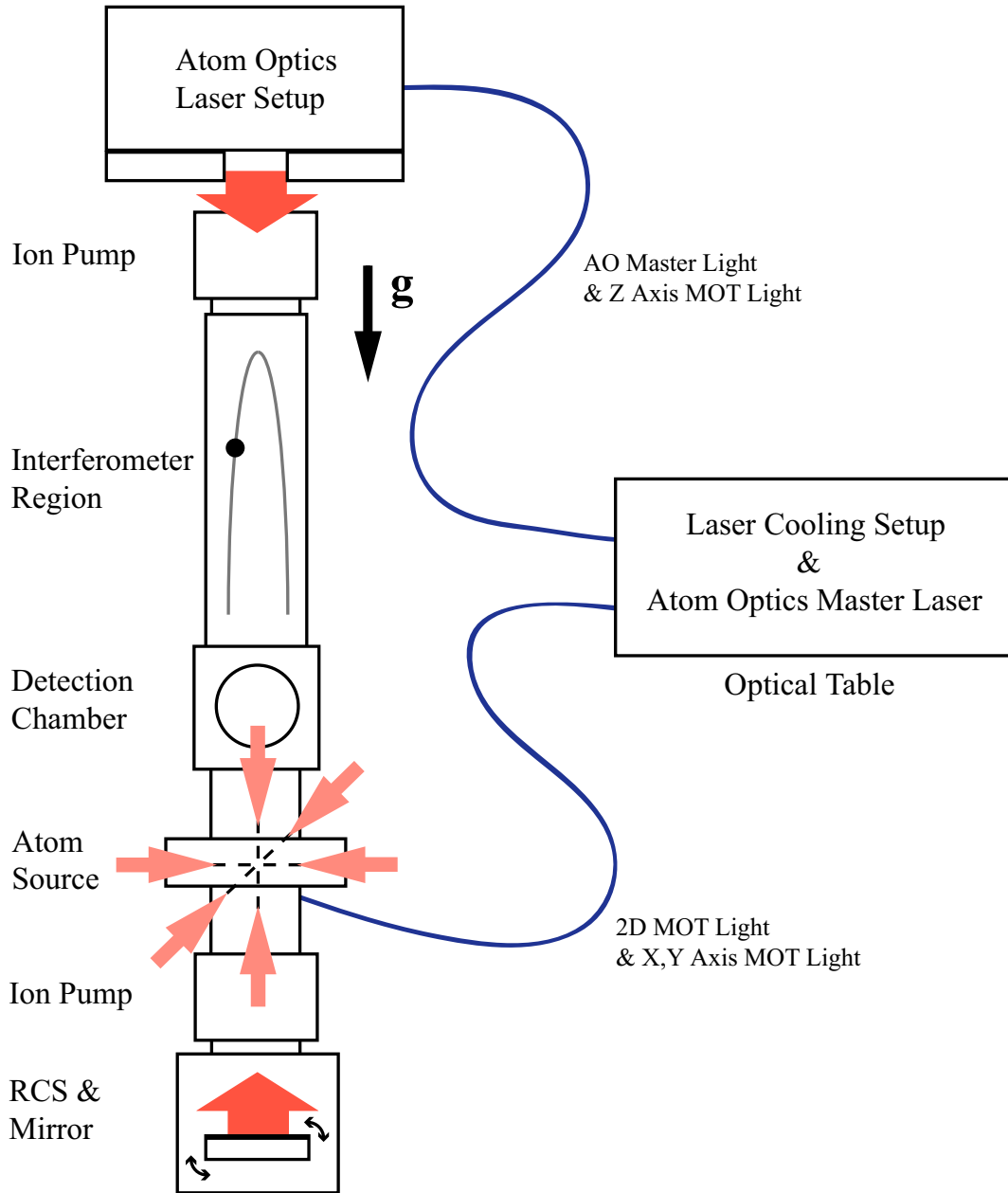


Figure 5.1: General layout of the experimental apparatus. Light is delivered from an optical table to the atom source and atom optics laser setup via optical fibers. The laser cooling light is represented by small arrows and the atom optics light is shown as large arrows. The Rotation Compensation System (RCS) includes the mirror used to retro-reflect the the z -axis light.

5.1.1 Vacuum System

The primary function of the interferometer region is to provide the necessary ultra-high vacuum (UHV) environment for the atoms. To avoid significant loss of atoms to collisions with residual background gas during the ~ 2 s free-fall time requires a mean collision time of $\tau \gtrsim 10$ s. This implies a background gas number density of $n < (\sigma \bar{v} \tau)^{-1} \approx 5 \times 10^7 \text{ cm}^{-3}$ and a pressure $p < 10^{-9} \text{ Torr}$.¹ For additional overhead, the design goal of the interferometer vacuum chamber was 10^{-10} Torr .

For a 1D atomic fountain gravimeter, the atom test masses ideally follow purely vertical trajectories, motivating our use of a cylindrical vacuum tube. The choice of diameter D of the tube reflects several competing considerations. Minimizing wavefront curvature errors from the interferometer beams motivates a larger D , since a larger gaussian beam waist implies a more uniform phase and intensity distribution over the extent of the atom cloud. In addition, from a vacuum pressure perspective, a larger diameter tube has a higher conductance ($C \propto D^3$), allowing for a lower base pressure throughout the tube for a given fixed pumping speed from the end. Since the apparatus itself can act as a source of detrimental gravity inhomogeneities, a larger D isolates the atoms more effectively from these effects. On the other hand, magnetic shielding considerations (see Section 5.1.3) strongly suggest a smaller D since this improves the theoretical transverse shielding factor. From a practical standpoint, the vacuum diameter D sets the innermost dimension of the apparatus and as such it determines the size (and cost) of all surrounding layers (e.g., the bias solenoid, bakeout components, magnetic shielding and support tower). We chose a tube with an inner diameter of 4.0 inches and outer diameter (OD) 5.0 inches.

To reach the target base pressure, the vacuum system was designed to be pumped by a pair of 300 L/s ion pumps attached to the ends of the tube. With this configuration and assuming uniform degassing, the worst pressure in the chamber will be at the midpoint of the tube. The theoretical conductance between one of the pumps and the midpoint of the chamber is $C_{\text{mid}} = (12.1 \text{ L/s}) \frac{(D/\text{cm})^3}{(L/2)/\text{cm}} \approx 30 \text{ L/s}$. The large ion pumps ensure that the effective pumping speed at the midpoint is only reduced

¹Assuming a background gas of N₂ at 300 Kelvin, $\bar{v} = 520 \text{ m/s}$ and the N₂-Rb cross section is $\sigma \approx 4 \times 10^{-18} \text{ m}^2$ [63].

to $S_{\text{eff}}/C_{\text{mid}} = 90\%$ of this conductance limit.

The interferometer region vacuum tube was manufactured out of aluminum. Aluminum was chosen because it is non-magnetic, whereas stainless steel can exhibit residual ferromagnetism. Since the vacuum cylinder is inside the magnetic shield and close to the atoms, its magnetic properties must be excellent. The vacuum tube consists of two approximately equal lengths of commercially available 5" OD aluminum pipe that were welded together to yield a final length of $L = 348$ inch ($L = 8.84$ m). The CF vacuum flanges welded to each end of the tube are bimetallic, consisting of an aluminum body with a stainless steel knife edge for sealing (Atlas Technologies). Since aluminum is typically too soft to be used in a CF knife edge seal, the bimetallic CF flanges give us the advantage of an aluminum chamber while still providing an uncompromised UHV connection to the other parts of the vacuum system.

The vacuum tube was installed vertically inside a 25 foot deep concrete-lined pit in our lab. The tube is supported by an elaborate tower made of aluminum extrusion (80/20) that is firmly anchored to the concrete walls of the pit as well as to the ceiling and to the floor (see Fig. 5.2). The vacuum tube is clamped to the tower at its ends using custom brackets that interface with the vacuum flanges. The tube is left unsupported along its length to allow for an unobstructed magnetic shield and bias solenoid. The upper support bracket provides only a radial constraint to allow for stress-free thermal expansion during bake-out cycles (the tube can expand in length by more than 1 inch). An aluminum mezzanine (the “work platform”) extends over the pit and surrounds the tower near the top of the vacuum system allowing access for personnel and a place to put equipment. Respecting the philosophy of keeping the area surrounding the interferometer region magnetically pristine, both the work platform and support tower are constructed using only non-magnetic hardware. However, the concrete walls of the pit likely contain carbon steel rebar which is magnetic.

To achieve the required base pressure, the chamber must be baked while under vacuum to accelerate the removal of residual gas adsorbed in its walls. The bake-out system consists of resistive heat tape wrapped around the vacuum cylinder covered by thermal insulation. The heat tape cords are 1" wide by 348" long ribbons, each



Figure 5.2: The assembled support tower, vacuum tube and magnetic shield. The pit and work platform are also visible.

capable of delivering over 1.5 kW of heat. For redundancy, four independent heat tape cords were wound around the cylindrical chamber in a non-overlapping helical pattern (two service the bottom half of the chamber and the other two the top). The heat tape is directly wound on the surface of the bias solenoid (mostly copper) which itself is in thermal contact with the vacuum chamber (see Fig. 5.3). Typically only two of the four heat tape cords were needed during a bake to reach the desired temperature. Thermal insulation was provided by a 1" thick layer of flexible mineral wool covered by a sheet of aluminized paper. During a bake, the temperature profile of the chamber was monitored by a set of 20 type E thermocouples uniformly placed along the length of the tube.² Part of the thermocouple wire bus is visible in Fig. 5.4. The typical target temperature range for a bake was 150 – 180 C. All of the materials used inside the thermal insulation are rated to at least 200 C.

5.1.2 Bias Solenoid

At the start of the interferometer sequence, the atom is prepared in well defined spin state magnetic sub-level $|F, m_F\rangle$ (typically $m_F = 0$ here for magnetic field insensitivity). During the interferometer free-fall it is important that this spin state remains unperturbed, or else spurious phase shifts and population of unwanted states may result. Stray magnetic fields can cause these undesirable changes to the state since the atom's spin will tend to align with the direction of the field. Applying a constant, known magnetic field in a well-defined direction can alleviate this problem as long as this bias field is much larger than residual stay fields. Of course, the bias field will also induce an unwanted phase shift on the atom, but this effect is known and can be characterized.³

The bias field is generated by a solenoid that is wound directly on the outside of the vacuum cylinder. The solenoid continues uninterrupted along the entire length of the vacuum tube from flange to flange, consisting of a single layer of 3005 ± 3 turns

²Type E thermocouples are considered non-magnetic.

³In fact, it can even cancel completely for symmetric interferometer configurations or in experiments that use differential measurement.

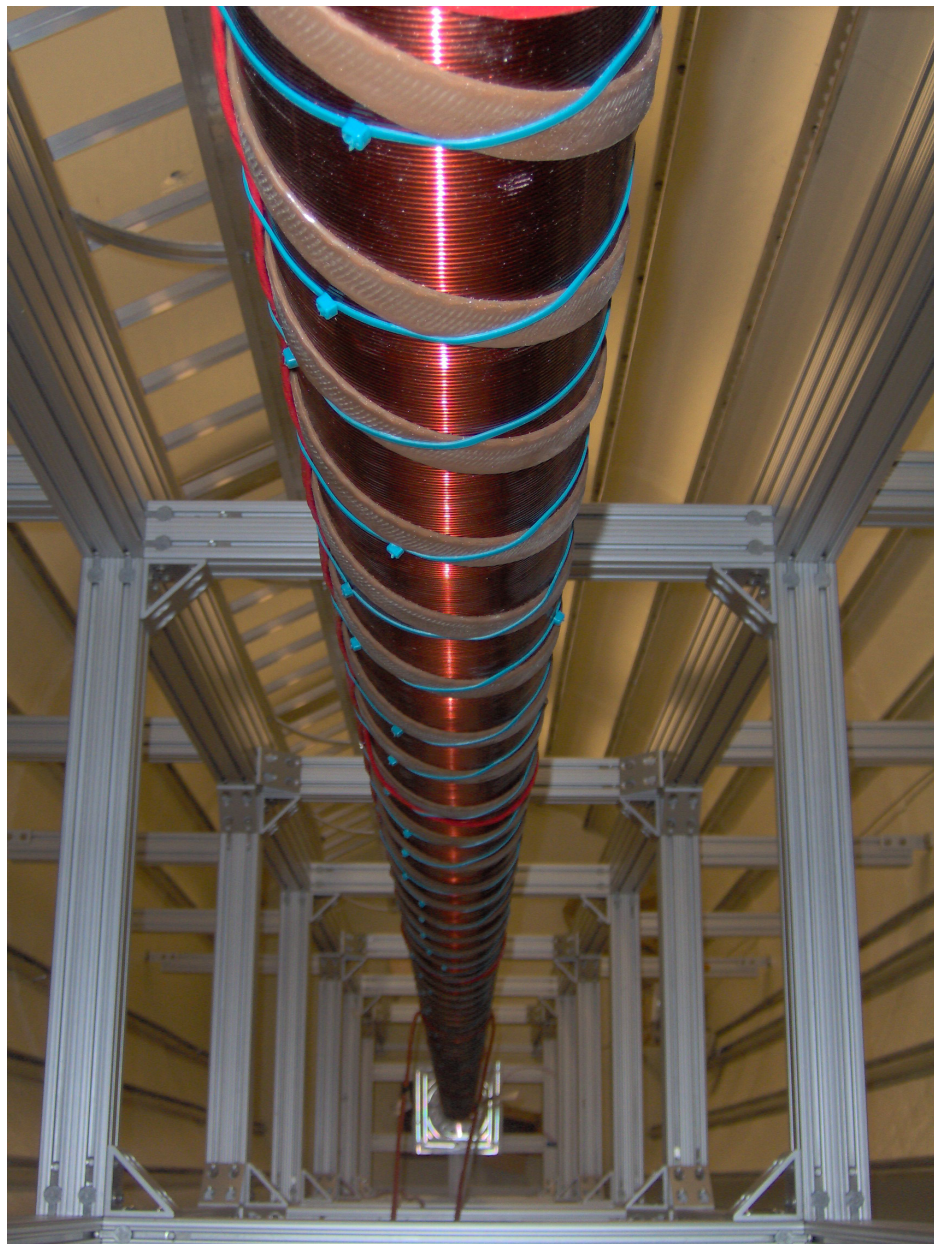


Figure 5.3: Interferometer vacuum tube showing heat tape for bake-out. Also visible is the bias solenoid (dark red insulated wire) which is wound on the outside of the vacuum cylinder.

(8.74 turns/in) of 0.125"-wide square cross-section copper wire with polyester-amide-imide film insulation (rated to 200 C). To avoid the need for a continuous spool of wire long enough, the full solenoid is made up of 11 independent coil segments that are wound end to end. Each solenoid is electrically independent and can have its own current supply. This configuration has the added benefit of increased tunability, as the currents in the individual segments can be adjusted to compensate for any residual field non-uniformities.

For the segmented solenoid, it is very important that gaps between segments be minimized. Even a gap the size of a single turn could lead to unacceptable field gradients. To minimize gaps, we developed a novel wire clamp to secure the ends of each segment. The clamp (see Fig. 5.4) is designed to capture both the end of one segment and the start of the next in such a way that the wire continues along the identical helical path from segment to segment. The only remaining discontinuity is a small ($\approx 0.125"$) circumferential gap that results from the finite radius of curvature of the two wires ends as they bend radially outward out of the clamp to connect to the current supply.

5.1.3 Magnetic Shield Design

The interferometer region must be magnetically shielded to protect the atoms from the effects of Earth's ambient magnetic field. The design goal for the residual field inside the shield was $< 10 \mu\text{G}$. For the magnetic fields we measured in the lab (see Fig. 5.8), this implies a required shielding ratio of $S_{\text{constant}} \approx \frac{500 \text{ mG}}{10 \mu\text{G}} = 5 \times 10^4$ for constant fields. As discussed in Chapter 4, avoiding spurious magnetic phase shifts requires precise control of not only the absolute value of the magnetic field, but also the magnetic field spatial gradient. Residual field gradients must be smaller than $3 \mu\text{G}/\text{m}$, implying a shielding ratio requirement of $S_{\text{gradient}} \approx \frac{30 \text{ mG/m}}{3 \mu\text{G}/\text{m}} = 1 \times 10^4$, assuming that the shield itself does not introduce any additional spatial variation in the field and simply reduces the observed Earth field gradients. Both of these specifications would be safely met by a shielding ratio of $S \geq 10^5$. In order to shield as much of the vacuum chamber as possible, a cylindrical shield geometry was natural.

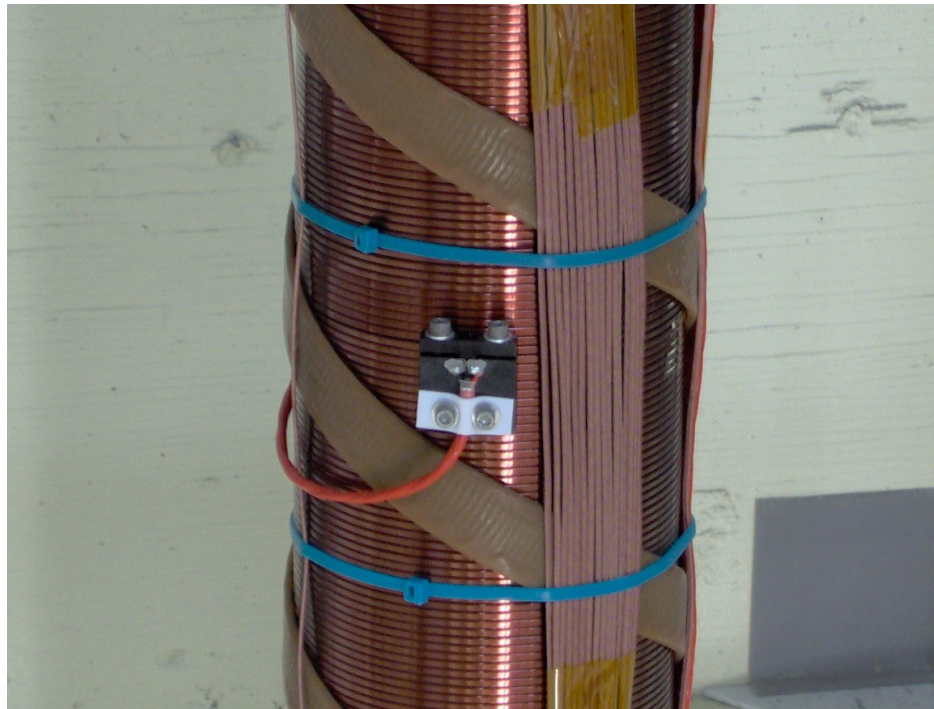


Figure 5.4: Detail of one of the wire clamps between segments of the bias solenoid. The clamp is attached at the joint between two solenoid segments. From this perspective, the wire from the end of the lower solenoid enters the clamp from the left, while the wire from the start of the upper solenoid enters the clamp from the right. A shielded, twisted pair cable (light red wire) is attached to the wire ends to deliver supply and return current to the upper and lower solenoid segments, respectively. Also visible is the heat tape helix (brown) and the thermocouple bus (brown wires running vertically).

The theoretical shielding ratio for an infinitely long multi-layer cylindrical shield is known analytically in the case of an applied field transverse to the cylinder axis.[64] Although this analysis will miss effects due to the finite length of the actual shield, it is still a useful design tool for predicting the transverse shielding ratio at the center of the shield (far from the ends). Specifically, we used Wills' formula [64] for a three-layer, infinitely long cylindrical shield. The layers of the shield have radii r_i ($i = \{1, 2, 3\}$ with $r_i < r_{i+1}$) and uniform material thickness t with relative permeability μ . In the limit that $r_i \gg t$ and $\mu \gg 1$ this formula becomes

$$S_3 = \frac{\mu t}{2r_1} \left(1 + \frac{r_1}{r_2} + \frac{r_1}{r_3} \right) + \frac{\mu^2 t^2}{4r_1 r_2} \left(1 - \frac{r_1^2}{r_2^2} + \frac{r_1 + r_2}{r_3} \left(1 - \frac{r_1 r_2}{r_3^2} \right) \right) \\ + \frac{\mu^3 t^3}{8r_1 r_2 r_3} \frac{(r_1^2 - r_2^2)(r_2^2 - r_3^2)}{r_2^2 r_3^2} \quad (5.1)$$

Under the more restrictive condition that $\mu \gg r_i/t \gg 1$, the cubic term dominates and the expression reduces to

$$S_3 \approx \frac{\mu^3 t^3}{8r_1 r_2 r_3} \frac{(r_1^2 - r_2^2)(r_2^2 - r_3^2)}{r_2^2 r_3^2} \quad \left(\frac{\mu t}{r_i} \gg 1 \right) \quad (5.2)$$

This result indicates that the transverse shielding ratio is generally better for shields with smaller radii, so we chose the smallest practical inner diameter for the innermost layer of the shield. It is also useful to examine Eq. 5.2 in the case where the shield layers are uniformly spaced by Δr :

$$S_{3,\Delta r} = \frac{t^3 \Delta r^2 \mu^3 (2r_1 + \Delta r)(2r_1 + 3\Delta r)}{8r_1 (r_1 + \Delta r)^3 (r_1 + 2\Delta r)^3} \quad (5.3)$$

For a fixed inner dimension r_1 and material thickness t this expression can be used to find the optimum layer separation to maximize the shielding ratio. The maximum occurs for a spacing of

$$\Delta r_{\max} \approx 0.567 r_1 \quad (5.4)$$

which for our shield inner layer radius of $r_1 = 3.625"$ implies a layer spacing of about 2 inches. Finally, the remaining design parameter for the shield is the material

thickness t . Since the shield performance is better for larger t , we chose the largest thickness we could, limited by cost.

The final shield design consists of three concentric cylindrical layers made of 0.050"-thick Amumetal (Amuneal Manufacturing Co.). Figure 5.5 is a CAD drawing of the shield design; Fig. 5.2 shows the shield after installation around the vacuum chamber. Assuming a conservative value of the permeability of Amumetal of $\mu = 2 \times 10^4$ and the design dimensions, the theoretical shielding ratio is $S_3 \simeq 2 \times 10^5$ based on Eq. 5.2. Although this result meets the design goal, it is important to keep in mind that the estimate ignores end effects and only applies to magnetic fields that are perpendicular to the cylinder axis.

To achieve the highest permeability, the Amumetal material must be hydrogen annealed. The annealing process should preferably be done only after all forming and welding is finished so as to avoid any degradation of the permeability due to mechanical and thermal stresses. Since the available annealing furnaces are of limited size, we were forced to divide each shield layer into a series of fifteen $\approx 24"$ -tall segments (see Fig. 5.6). These segments are held together with 4"-wide joining bands that extend 2" above and below each joint. Each joining band is welded to the segment below the joint and is attached to the segment above by a series of fasteners around the circumference of the band. In addition to joining the segments together mechanically, the bands are intended to prevent the magnetic field from leaking through the joints. It is therefore important that the bands fit as tightly as possible around the shield segments so as to closely approximate a continuous shield.

5.1.4 Characterizing the Magnetic Shield

In order to characterize the magnetic fields present in the vacuum chamber, we built a shuttle to move a precision fluxgate magnetometer (Applied Physics Systems model 540) along the length of the vacuum chamber (see Fig. 5.7). This shuttle is raised and lowered by a computer-controlled stepper motor via four cables. The magnetometer rides in a custom fabricated aluminum shuttle which is centered in the vacuum chamber by six delrin wheels. Only non-magnetic materials were used in the construction

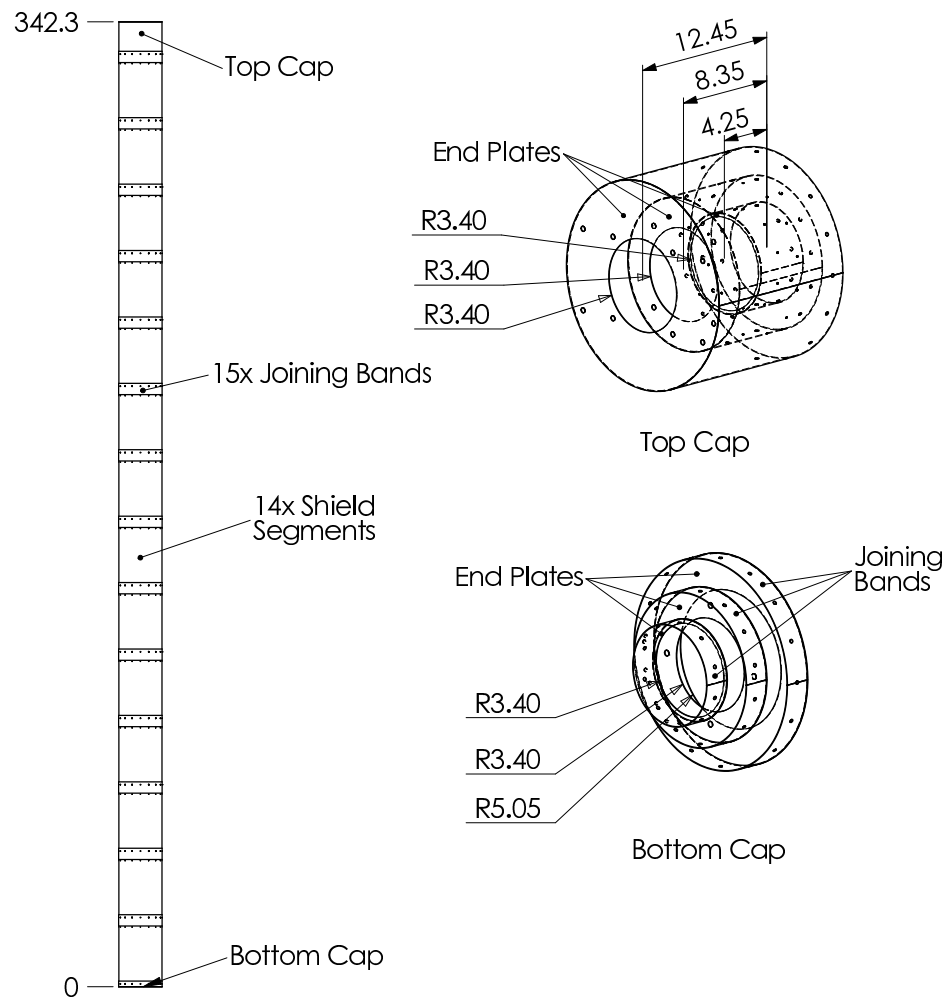


Figure 5.5: Magnetic shield CAD model. All dimensions are in inches.

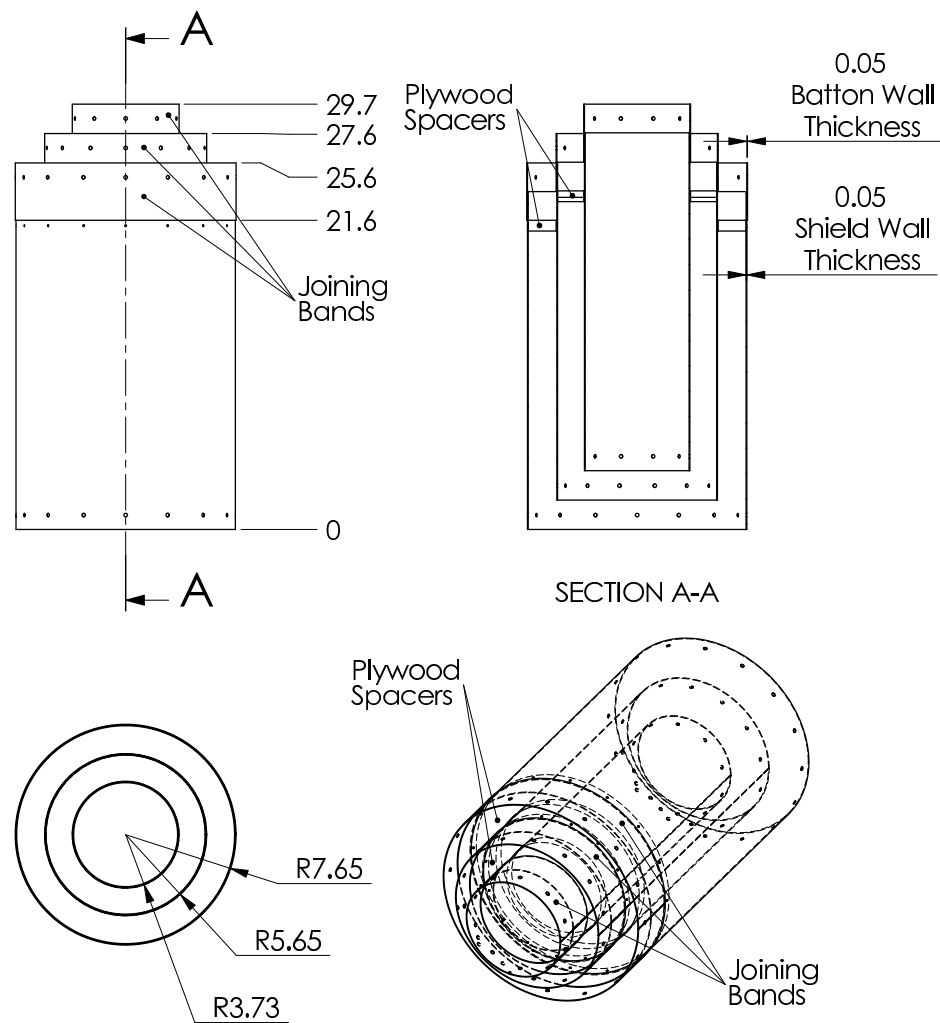


Figure 5.6: Three-layer magnetic shield segment. The complete shield consists of 14 identical three-layer segments plus two end caps. Each of the cylindrical segments have joining bands welded to one end which are used to connect the segments mechanically as well as magnetically. All dimensions are in inches.

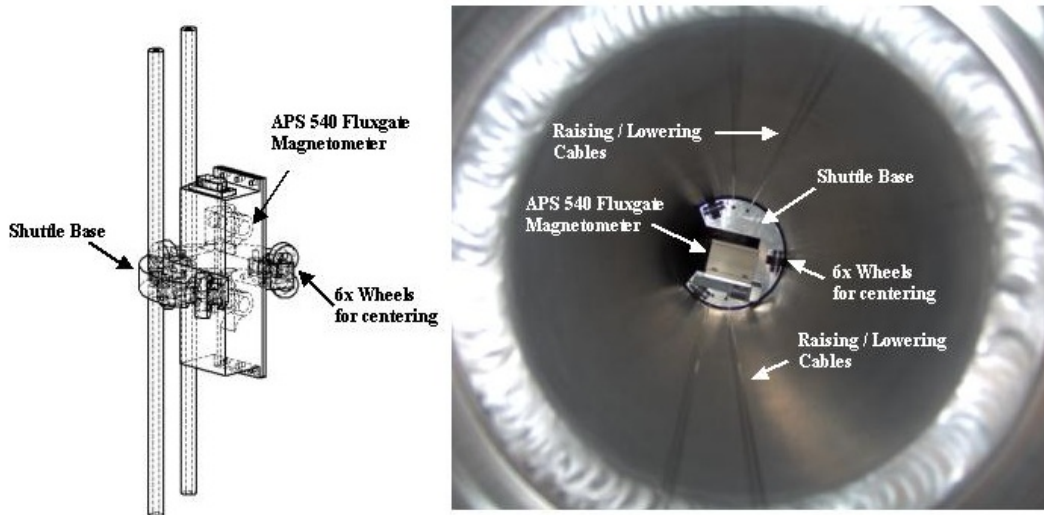


Figure 5.7: Magnetometer shuttle system for measuring the magnetic field inside the cylindrical vacuum chamber. We used an Applied Physics Systems model 540 fluxgate magnetometer to measure all three vector components of the magnetic field. The photograph on the right shows the inside of the vacuum chamber looking down. The shuttle can be seen suspended several feet below the top of the chamber.

of the shuttle system. A computer program moves the shuttle a small amount, records a data point, and repeats until the shuttle has traveled the full length of the vacuum chamber. At each measurement point, the computer records the position of the stepper motor and the three vector components of the magnetic field with a resolution of 0.5 mG. Data was taken at $\sim 0.15''$ intervals over the entire 348" vacuum chamber, corresponding to ~ 2300 data points per measurement. The position data is then post-processed to correct for non-linearities in the position of the shuttle that arise from cable stretching and uneven cable spooling (both $\sim 2\%$ corrections).

We measured the magnetic field inside the vacuum chamber before and after the installation of the shield. Figure 5.8 shows the initial field before shield installation. Notice that the vertical field component (B_z) is particularly large. This is a concern since a layered cylindrical geometry is more effective at shielding fields perpendicular to the cylinder axis. Vertical fields can penetrate the shield through the holes in each end cap.

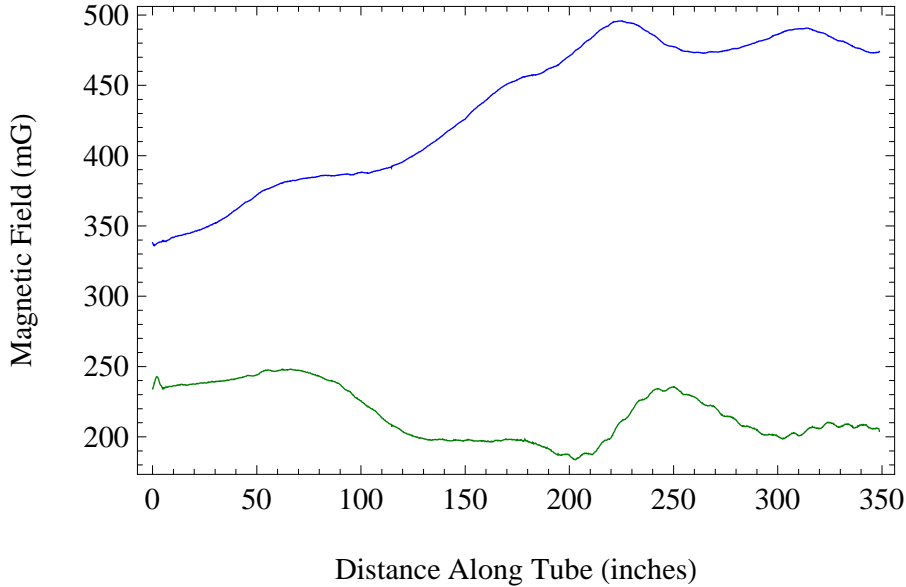


Figure 5.8: Magnetic field components B_z (blue) and B_r (green) before shield installation.

The magnetic field inside the vacuum chamber after shield installation is shown in Fig. 5.9. Although the effect of the shield is dramatic, the 13 prominent, ~ 100 mG spikes indicate that the shielding is not uniform along the length of the chamber. The locations of these spikes are consistent with the positions of the joints between the segments of the shield.

Evidently, the joining bands do not provide the desired continuity between segments. We hypothesize that the bands do not adequately carry the magnetic flux from segment to segment, but instead allow it to leak into the shielded region. A likely culprit is the presence of small, radial gaps that we observe between the joining bands and the shield segments. These gaps were noticed during the assembly of the shield, and are a result of fabrication tolerances. We speculate that closing these gaps could reduce the spikes in the field by eliminating the field leakage path. The work to repair this problem is ongoing.

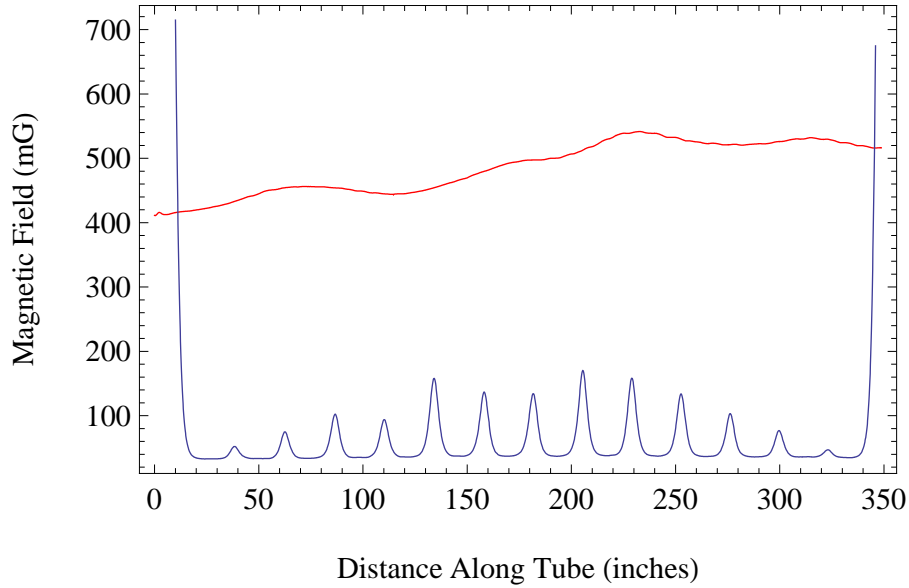


Figure 5.9: Magnetic field magnitude before shield installation (red) and after (blue).

5.1.5 Rotation Compensation System

As discussed in Section 4.1, the residual coriolis force systematic error can be minimized by actively rotating the retro-reflection mirror in the opposite direction of the Earth's rotation. Suppressing the coriolis systematic below the $10^{-15}g$ level requires that this servo system match the Earth's rotation rate at the level of $10^{-5}\Omega_{\text{Earth}} \approx 1 \text{ nrad/s}$. To achieve this, we designed a Rotation Compensation System (RCS) based on a set of three piezoelectric nanopositioners. The nanopositioner tripod (see Fig. 5.10(a)) supports a rigid 1" thick triangular aluminum mirror plate. The combined three degrees of freedom from the vertical actuators allows the mirror to be independently tilted about the x and y axes and also translated in the z direction. Each nanopositioner is capable of $30 \mu\text{m}$ of vertical travel with a resolution of 60 pm. Since the actuator attachment points on the mirror plate form an equilateral triangle inscribed in a 15 cm diameter circle, this linear translation yields an angular range of $267 \mu\text{rad}$ and an angular resolution of 0.5 nrad. This range is sufficient to compensate for the Earth's rotation angle during the interferometer time, which for the EP

apparatus is $2\Omega_{\text{Earth}}T \approx 200 \mu\text{rad}$.

To facilitate stable motion, the mirror plate is attached to the nanopositioner tripod via ball bearings using a minimum set of kinematic constraints.⁴ Three springs secure the mirror plate to these constraints. The mirror itself connects to the mirror plate using another set of minimum kinematic constraints. The lower surface of the mirror substrate has three machined holes that accept the ball bearing which interface with these kinematic constraints. In the case of the mirror to mirror plate connection, the nesting force for the constraints is provided by gravity alone.

The RCS design includes multiple ways to monitor the angle of the mirror as it is rotated. The nanopositioners are equipped with piezoresistive sensors that indicate the extension of each arm of the tripod, allowing the angle of the mirror to be inferred. These sensors have a noise floor of $2 \text{ pm}/\text{Hz}^{1/2}$ which implies an angle uncertainty of $20 \text{ prad}/\text{Hz}^{1/2}$. In order to measure the mirror angle directly, the mirror plate is designed with a large opening in the center so that laser light can be reflected off the bottom surface of the mirror. The mirror angle can be determined by measuring the deflection of this reflected beam using a position sensitive detector.[58]

To minimize wavefront distortion of the interferometer beams caused by propagation through vacuum viewports, the RCS is designed to be installed inside the same UHV chamber as the atom interferometer. As a result, the RCS must be UHV compatible down to 10^{-10} Torr. Figure 5.10(b) shows the assembled RCS vacuum chamber. The aluminum chamber is cylindrical with an endcap welded to the bottom. A 10" CF flange at the top of the chamber allows access for installation of the RCS. The three nanopositioners are anchored to the inside wall of the vacuum cylinder using vented fasteners for all blind tapped holes. UHV electrical feedthroughs are used to connect the nanopositioners to the control electronics. A vacuum viewport on the side of the chamber and a 45-degree mirror placed under the retro-reflection mirror allows optical access for measuring the mirror angle using the light deflection technique described above.

The RCS vacuum chamber is connected to the rest of the vacuum system via a

⁴This is the same set of constraints used in a traditional kinematic mirror mount: a sphere inside a trihedral hole (often substituted by a conical hole), a second sphere inside a V-groove, and a third sphere in contact with a plane.

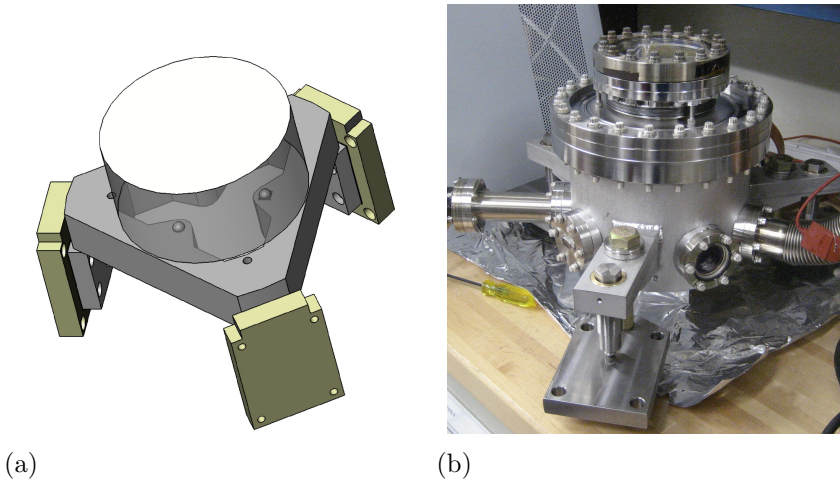


Figure 5.10: Rotation Compensation System. (a) CAD model of the RCS showing the mirror, the mirror plate, and the three nanopositioners. Two of the kinematic constraint ball bearings that connect the mirror to the mirror plate can be seen through the transparent mirror substrate. (b) Assembled RCS vacuum chamber. The chamber connects to the interferometer region vacuum system using a flexible bellows. Here the bellows is shown blanketed off during the initial vacuum test.

flexible bellows. This allows the RCS chamber to be articulated with respect to the interferometer region so that the angle of the retro-reflection mirror can be coarsely aligned. The chamber is anchored to the ground by three tabs that are welded to the outside of the RCS. Each tab has an anchor bolt and a counterposing adjustable set screw so that its height can be changed. In addition to allowing coarse adjustment, the bellows also help decouple the retro-reflection mirror from vibrational noise.

5.2 Atom Source

The atom source is responsible for preparing the cold atom ensembles before they get sent into the interferometer region. Since every experiment cycle begins with the atom source, the primary goal here is to provide as many usable atoms as possible in a short time so that the repetition rate of the apparatus remains high. Here “usable” typically refers to the velocity distribution of the atom ensemble, although

their number density can also be important.

An upper bound on the acceptable ensemble temperature for a free-fall gravimeter is set by the expansion rate of the cloud during the measurement. For an atom ensemble with a velocity spread on the order of the recoil velocity ($v_r = \hbar k/m \approx 6$ mm/s for rubidium), the final cloud diameter after falling for ~ 2.7 s inside the interferometer region is approximately 3 cm. Since the vacuum chamber diameter is 10 cm, the atoms transverse velocity spread must be no larger than this or a significant number of atoms will be lost to collisions with the walls. The atom cloud temperature should therefore be less than the recoil temperature $T_r = mv_r^2/k_B = 360$ nK.

In addition to the above practical limit, the velocity spread is also tightly constrained by a number of systematic effects discussed in Chapter 4, such as magnetic and gravitational inhomogeneities as well as coriolis and centrifugal forces. Generally speaking, systematic errors associated with the kinematic properties of the ensemble are due to uncontrolled offsets in the mean \bar{x} of the distribution (*e.g.*, the average velocity) not the standard deviation σ_x (*e.g.*, temperature). However, the uncertainty of the mean is $\delta\bar{x} = \sigma_x/\sqrt{N}$ for an ensemble of N atoms, so the width of the distribution does limit how well such uncontrolled offsets can be eliminated. In other words, the need to control systematic errors can dictate how narrow a distribution is required to suppress such spurious offsets. For example, an ensemble of 10^6 atoms of ^{87}Rb with temperature T_r has a velocity spread (standard deviation) of $\sigma_v = 6$ mm/s, so the uncertainty of the average velocity of the cloud is $\delta\bar{v} = 6$ $\mu\text{m/s}$, meaning that the average velocity will vary by this amount across repeated trials.⁵ Since we estimate that launch velocity control better than 1 $\mu\text{m/s}$ will be required for a 10^{-15}g EP test (see Chapter 4), this implies the need for a sub-recoil temperature (≈ 10 nK) atom cloud.

All of the estimates of the kinematic requirements of the atom source point towards ensembles that are colder than can be achieved with standard laser cooling alone. Although sub-Doppler, polarization gradient cooling can yield temperatures of a few

⁵Stochastic variation of the mean of a kinematic variable can also in principle be a source of random noise in the experiment if the variable in question couples to the interferometer response. However, in that case the noise contribution will (trivially) end up being negligible whenever the associated systematic error is successfully suppressed.

T_r , this is still at least an order of magnitude too hot. Certainly, laser cooling below the recoil temperature has been demonstrated[65, 66, 67], although these schemes are sometimes complex. Alternatively, evaporative cooling provides a robust, well-tested path to sub-recoil temperatures as it is used to produce Bose-Einstein condensates (BEC). Although a BEC is likely problematic for use in precision atom interferometry due to large number densities which can lead to undesirable collisional phase shifts (see Section 6.3.3), evaporative cooling can still be used to provide significant phase space compression while stopping short of BEC. In order to explore the full parameter space of atom interferometry using an evaporatively cooled source, our design goal was to build an atom source capable of reaching BEC.

To achieve BEC, we pursued two well-known trap designs: a time-averaged orbiting potential (TOP) trap and an optically plugged trap (OPT). Both traps are similar in that they are based on magnetic trapping in a spherical quadrupole field with high spatial gradients. This field is convenient since it is the same configuration used for the MOT. Of course, the problem with the quadrupole field for trapping cold atoms is that the magnetic field at the center of the trap is zero, resulting in significant atom losses due to Majorana spin flips. This occurs because the spin state of the atom does not adiabatically stay aligned with the magnetic field as the atom passes through the region near the trap center where the field is small.

A TOP trap avoids Majorana losses by applying a rotating bias field that shifts the zero of the field away from where the atoms are.[68] As long as the bias field rotates faster than the atom oscillation frequency in the trap, atoms can never reach the moving field zero, and instead their motion is governed by the time-average of the magnetic potential. As a result, near the center of this effective potential there is always a sufficiently large magnetic field to avoid spin flip losses.

An alternative solution, the OPT trap, avoids Majorana losses through the addition of a conservative optical potential at the trap center. Light that is detuned to the blue of an atomic transition results in a positive AC Stark shift of the atom's energy level, causing the atom to be repelled from regions of high intensity. As long as this light is sufficiently far detuned, the associated photon scattering rate will be highly suppressed and the light force will be conservative with negligible heating. Therefore,

a focused beam of blue-detuned light at the center of the quadrupole field can act as a barrier to prevent spin-flip losses.

5.2.1 Vacuum Chamber

The atom source vacuum system is composed of three custom-designed stainless steel sub-chambers. First, the ‘3D MOT chamber’ is the centerpiece of the atom source because it is where the atoms are cooled and trapped in a MOT and subsequently evaporatively cooled. Next, the ‘2D MOT chamber’ is a smaller auxiliary chamber where we make the 2D MOT which serves as the cold atom beam responsible for loading atoms into the 3D MOT. Finally, the ‘detection chamber’ is an auxiliary chamber with large viewports for optical access that can be used for imaging the atom cloud at the end of an interferometer sequence.

All of the vacuum viewports are custom synthetic fused silica windows that are attached to the steel using soft-metal Indalloy seals. We use the same technique described in [69]. The seals are made from a (97.5%) lead alloy called Indalloy 165. The motivation for using this sealing material (rather than indium) is that the Indalloy seals can be baked above 200 C. Each sealing gasket is formed from a loop of Indalloy solder with the ends melted together. The gaskets are then pre-compressed using a custom jig. A different jig was used for each type of widow to form gaskets of the appropriate dimensions. The Indalloy gaskets require a smooth surface on the vacuum chamber in order to form a seal, so all the viewport sealing surfaces were machined flat. To assemble a viewport, gaskets were placed on both surfaces of the window (one as a seal and the other as a “pad”) and clamps were installed to provide the required sealing force.

The layout of the 3D MOT chamber is based on a cylindrical octagon design, with several modifications to allow for tight integration of the magnetic coils. Both the inner and outer surfaces of the chamber are nominally cylindrical, with the outer surface having eight facets for CF ports that are arranged as a 6.67"-wide octagon. Figure 5.11(a) shows the newly machined octagon chamber prior to brazing to the rest of the chamber. The symmetry axis of the octagon chamber is oriented vertically,

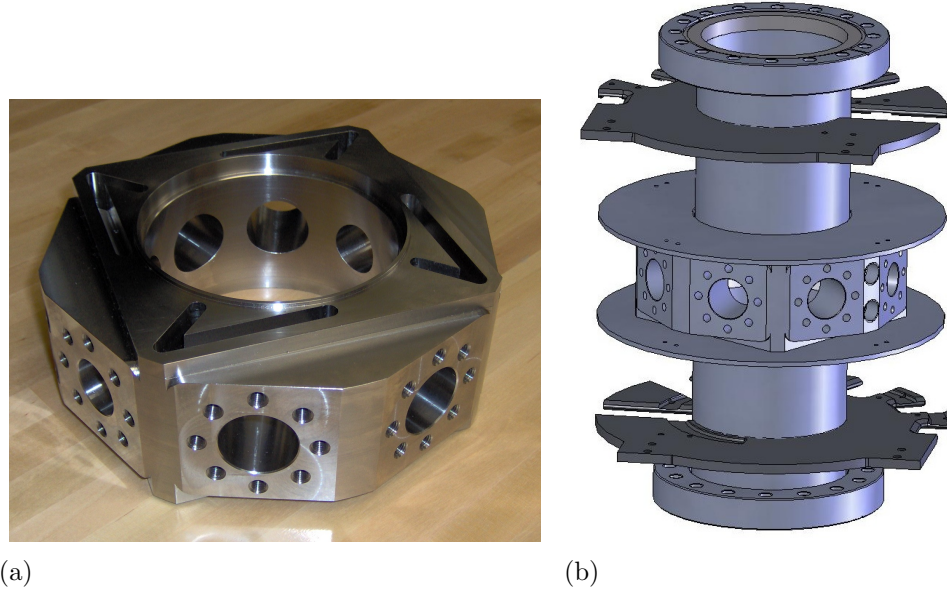


Figure 5.11: (a) Octagon vacuum chamber prior to brazing. The eight 2.125" CF ports are machined flat (no knife edge) to allow for soft metal seals to custom viewports. 4" long sections of vacuum tube attached to 6" CF flanges were brazed onto the top and bottom of the octagon for connecting to the rest of the system. The slots that appear on the top surface of the chamber are for water cooling. Plates were brazed onto the top and bottom of the chamber to form a closed circuit for the water. (b) CAD model of the completed 3D MOT chamber including winding guides for the quadrupole coils. The coils occupy the annular regions above and below the octagon. The numerous slots in the winding guides allow access to the inner layers of the coil for the purpose of water cooling.

so the eight 2.125" CF ports on the octagon facets provide optical access in the horizontal plane. Note that these ports have the bolt pattern of a 2.125" CF flange, but their sealing surfaces are all machined flat (no knife edge) for attaching viewports using Indalloy seals. To allow for large interferometer laser beams along the vertical direction, the minimum inner diameter of the chamber is 3.81" (same as the ID of a standard 6" CF flange).

In addition to the ports in the horizontal plane, the top and bottom surfaces of the chamber are fitted with 4"-long sections of vacuum tube that terminate with 6" CF flanges for connection to other parts of the vacuum system. With the addition

of integrated winding guides, these extension tubes serve as the hub of the main quadrupole magnetic coils which are wound directly onto the chamber. The CAD model of the complete 3D MOT vacuum chamber including winding guides appears in Fig. 5.11(b).

The coils that produce the rotating bias field for the TOP trap need to be placed as closely as possible to the center of the atom trap to minimize the amount of dissipated power at the required field strength. Four rectangular reliefs for these TOP coils were cut into the outer wall of the octagon chamber so that each of the four coils encircles two of the 2.125" viewports.

The TOP coils are in direct thermal contact with the vacuum chamber. Since at full power they each dissipate $> 1 \text{ kW}$ due to resistive losses, the coils can cause detrimental heating of the chamber. In addition, we found that at the operating frequency of $\sim 1 \text{ kHz}$ there is substantial inductive coupling to the steel chamber (eddy current damping), presumably leading to heating as well. Heating can adversely affect a UHV chamber since the temperature strongly affects the outgassing rate. To compensate for both resistive and inductive heating, the octagon chamber has integrated water cooling. Between its inner and outer surfaces, the chamber is mostly hollow and serves as a water manifold (see Fig. 5.11(a)).

The 2D MOT chamber is a simple rectangular design which is dominated by four large, rectangular viewports (see Fig. 5.12). These viewports allow for large aspect ratio 2D MOT laser beams. Several smaller 1.33" CF ports located near the back end of the chamber are included for vacuum pump connections and as a place to attach the rubidium source. A 2.125" circular viewport on the back surface of the chamber provides optical access along the 2D MOT atom beam propagation direction. A right angle fused silica prism with a protected gold mirror coating is bonded to the front surface of the inside of the chamber. This mirror gives optical access in the opposite direction of the 2D MOT atom beam propagation. A small hole drilled through center of this prism allows the 2D MOT beam to exit the chamber and propagate to the 3D MOT. Since the 2D MOT chamber is designed to run as a Rb vapor cell at $\sim 10^{-5} \text{ Torr}$, it is connected to the UHV 3D MOT chamber by a low conductance tube (diameter 3 mm, length 5 cm) which acts as a differential pump. The differential

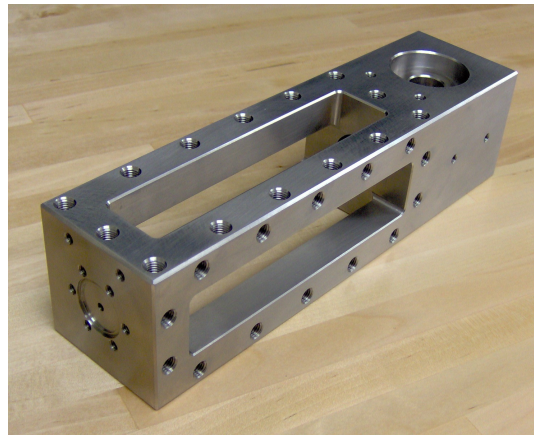


Figure 5.12: 2D MOT vacuum chamber. The long rectangular windows are for the 2D MOT beams. The atoms exit out of the small hole in the front of the chamber which attaches to the 3D MOT. Three 1.33" CF flanges were welded to the circular pockets near the back of the chamber.

pumping tube is made of graphite (an alkali getter) to help minimize Rb pressure in the 3D MOT region.

Approximately five grams of rubidium⁶ are stored in a small auxiliary chamber ('Rb chamber') attached to one rear port of the 2D MOT chamber. Rubidium was initially moved into the Rb chamber from a commercially available ampoule by transferring under vacuum to a cold point. The Rb is located between two all-metal valves that serve as a vacuum interlock during Rb transfers.

The detection chamber is based on a modified commercially available 6" CF cube. Four of the six CF sealing surfaces are machined flat to allow for Indalloy-sealed viewports. The viewports have a 4" clear aperture to maximize optical access for atom detection.

5.2.2 Quadrupole Coils

The quadrupole magnetic field for the MOT and the magnetic trap is generated by a pair of high power coils arranged in an anti-Helmholtz configuration. While the

⁶Natural isotope concentrations are 72% ⁸⁵Rb, 28% ⁸⁷Rb.

field gradient requirements for the MOT are modest (~ 15 G/cm), the magnetic trap requires much larger gradients for efficient evaporative cooling. In part, the collision rate (and hence, re-thermalization time) of atoms in a magnetic trap is determined by the trap frequency since this sets how quickly atoms move through the trap volume. The trap frequency is just $\omega = \sqrt{k/m}$, where the curvature k for a TOP trap in the radial direction is $k = \mu(\nabla B)^2/2B_{\text{rot}}$. Typical trap frequencies for ^{87}Rb ($\mu \sim 2\pi\hbar \cdot 0.70$ MHz/G) are

$$\omega_{\text{TOP}}/2\pi = 60 \text{ Hz} \left(\frac{\nabla B}{300 \text{ G/cm}} \right) \sqrt{\frac{10 \text{ G}}{B_{\text{rot}}}} \quad (5.5)$$

which shows that large field gradients are required to reach trapping frequencies larger than ~ 10 Hz. The design goal for our quadrupole gradient was 300 G/cm.

One complication of our vacuum system design already alluded to in Section 5.1.1 is the large inner diameter. The system must have a large clear aperture along the z -direction to allow for large diameter laser beams for the interferometer light. This makes it more challenging to achieve high field gradients, since for a coil pair satisfying the Helmholtz condition,⁷ the field gradient is $\nabla B \sim \mu_0 I/R^2$ for coil radius R and current I . For this reason, our quadrupole coils must have many loops and require high current, resulting in significant resistivity heating.

Our quadrupole coil pair is designed to produce a radial field gradient of $\nabla B = (0.95 \text{ Gauss/cm/A}) \cdot I$. The coils have an inner radius of 2" and consist of 12 radial layers of 0.195"-thick square cross-section copper conductor with heavy build dacron glass insulation. The coils have a minimum axial separation of 3" and are each 16 axial layers tall, resulting in a total of $12 \times 16 = 192$ turns for each coil. The measured series resistance of the coil pair is $r_{\text{quad}} = 0.18 \Omega$, resulting in a Joule heating rate of $I^2 r_{\text{quad}} \sim 16$ kW. To dissipate this heat, the copper conductor used to wind the coil is hollow (0.100" ID), allowing cooling water to flow through it. In order to increase the flow rate of cooling water, we subdivided each coil into six sub-coils. Each sub-coil is an independent water manifold, so although the 12 coil segments are in series electrically, we are able to put them in parallel for water cooling.

⁷A coil pair satisfying the Helmholtz condition has the coil radius equal to the coil separation.

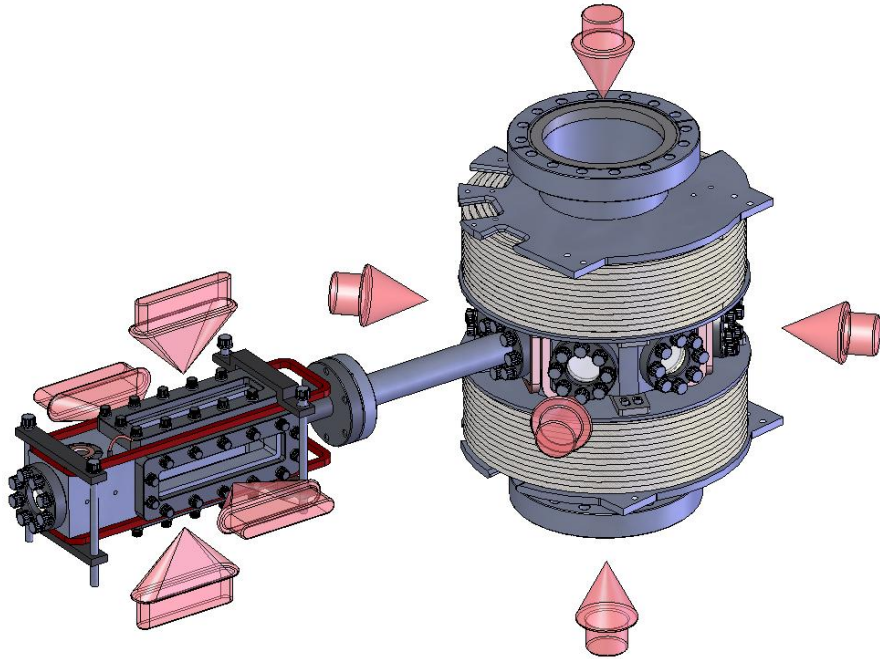


Figure 5.13: 2D MOT and 3D MOT CAD Model. The quadrupole coils appear above and below the octagon chamber and the TOP coils can be seen around the octagon windows.

Subdividing the coils substantially improves the water flow rate. Still, we require an input pressure of ~ 200 psi to the water cooling manifolds in order to maintain enough flow to adequately cool the coils at full power. This requires a booster pump to increase the input pressure above the ~ 80 psi available from the building's process cooling water. We use a Goulds 10 GPM booster pump for this purpose.

5.2.3 2D and 3D MOT

The rectangular viewports on the 2D MOT are attached to the steel chamber using a hybrid sealing technique. Indalloy seals alone resulted in residual leaks, so in addition to the Indalloy seal we also used a vacuum compatible epoxy to attach the viewports.[70] A thin layer of epoxy was applied between the chamber and an Indalloy



Figure 5.14: 2D MOT viewed along the axis of the atom beam. The bright spot in the center of the crossed beams is the 2D MOT.

gasket; likewise, a second layer of epoxy was applied between the glass window and the Indalloy gasket. Care was taken to avoid dripping any epoxy which could lead to unintentional bonds between the two epoxy layers. With this technique, the epoxy forms the vacuum seal, and the Indalloy gasket acts as a compliant element which can thermally expand during bake-out. This arrangement avoids stressing the glass which would occur if it were directly bonded to the chamber with epoxy.

Figure 5.14 shows the operational 2D MOT. To increase the atom flux, we also added a ‘pusher’ beam directed along the longitudinal axis of the 2D MOT as was done in [71]. The pusher significantly improves the usually 2D MOT flux as determined

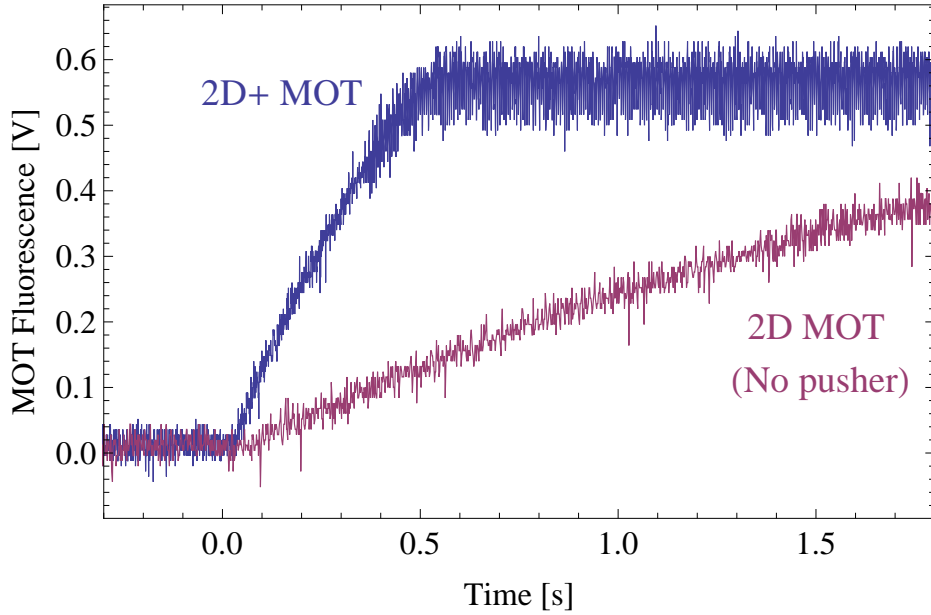


Figure 5.15: Effect of the pusher beam on the ^{87}Rb MOT loading rate. The upper curve (blue) shows the 3D MOT fluorescence versus time with a longitudinal pusher beam added to the 2D MOT (a 2D+ MOT). The lower curve is the same 3D MOT loading trace with the pusher beam blocked.

by the 3D MOT loading rate. Figure 5.15 is a comparison of the 3D MOT loading rate with and without the pusher beam. In this case the pusher increases the loading rate by a factor of ~ 5 .

Figure 5.16 shows the loading curve for the dual species 3D MOT. Each species can be loaded independently by blocking the seed light for the other species (see Section 5.3.1), and the atom number ratio between the two is easily adjustable.

5.3 Laser System

We built two conceptually distinct laser systems: the laser cooling light and the atom optics light. The laser cooling optics setup generates all light frequencies that are required to cool, trap and image the two isotopes Rb. Due to hyperfine structure differences, the two isotopes have unique frequency requirements for these tasks; this

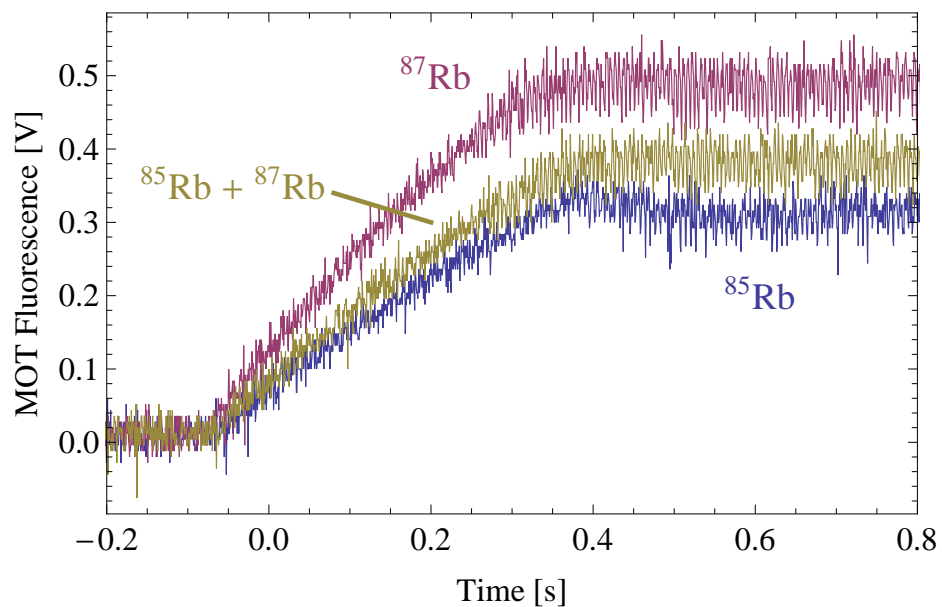


Figure 5.16: 3D MOT loading curves for ^{85}Rb (blue), ^{87}Rb (red), and a dual species MOT (yellow). Each trace shows 3D MOT fluorescence measured by a photodiode versus time. The individual species curves were taken by simply blocking the seed light into TA₂ of the opposite species.

doubles the number of required frequencies compared to a single species experiment. The atom optics laser system provides the light for implementing the atom interferometer beamsplitters as well as for optical lattice manipulations. Both of these applications use two-photon transitions (either Raman or Bragg) with light frequencies that are chosen to be far detuned from all single photon resonances. As a result, the atom optics laser system can simultaneously address both isotopes using the same light frequencies. In addition to simplifying the design of the atom optics system, the use of common laser light for both isotopes during the interferometer can significantly suppress laser-related noise and systematic errors.

5.3.1 Dual Species Laser Cooling and Trapping Light

Making the dual species MOT requires four different laser frequencies, two for each species. Doppler cooling requires light detuned slightly red of an atomic transition so that an atom moving opposite to the light propagation direction sees a Doppler shift which brings the light closer to resonance. As a result, atoms experience an enhanced scattering force from light propagating opposite their velocity direction, leading to damping. For the MOT to work, the atomic states used for cooling must form a closed cycling transition, allowing the atom to undergo many repeated scattering events without pumping to another state that does not interact with the light. The transitions $F = 3 \rightarrow F' = 4$ in ^{85}Rb and $F = 2 \rightarrow F' = 3$ in ^{87}Rb very nearly meet this condition. However, there is a small probability that the cooling light will cause an off-resonant excitation $F = 3 \rightarrow F' = 3$ in ^{85}Rb (or $F = 2 \rightarrow F' = 2$ in ^{87}Rb). These off-resonant excitations can subsequently lead to decays that put the atom in the lower hyperfine ground state ($F = 2$ for ^{85}Rb and $F = 1$ for ^{87}Rb), which is not part of the cycling transition. To eliminate this loss channel, a second laser frequency, called repump, is used to pump atoms that end up in the dark lower hyperfine state back into the cycling transition.

Figure 5.17 shows the hyperfine level structure and the four laser frequencies required for the dual species MOT. The cooling light frequencies ν_{c85} and ν_{c87} are detuned from the cooling transition by a variable amount δ_{85} and δ_{87} for ^{85}Rb and

^{87}Rb , respectively. During the loading and initial cooling phase of the MOT, the detuning is typically set at $\sim 2\Gamma \approx 10$ MHz where Γ is the natural linewidth.

Light used to make the MOT must have its frequency stabilized to better than $\Gamma \sim 6$ MHz. This requires that the lasers be frequency locked to an atomic reference. To simplify the cooling laser setup, we use a single master laser that is frequency locked to rubidium. The master laser is a Newport Vortex external cavity diode laser (ECDL) with a short term linewidth < 1 MHz. All of the cooling and repump frequencies are derived from this master light using frequency shifting techniques, eliminating the need for multiple laser locks.

The master laser frequency is chosen at a convenient location to facilitate the generation of the four other frequencies. This is accomplished with an offset locking technique. Master light is double-passed through an AOM (see Fig. 5.19) resulting in a redshift of $\Delta\nu_{\text{AOM}}$. This shifted light is then locked to the $3' \rightarrow 4'$ crossover resonance of ^{85}Rb using saturation absorption spectroscopy. As a result, the master laser is locked $\Delta\nu_{\text{AOM}}$ to the blue of the lock point (See Fig. 5.18).

The optics layout for generating the saturation spectroscopy error signal used to frequency lock the laser appears in Fig. 5.19. Probe light is first sent through a phase modulator (ϕM_1) where 10 MHz sidebands are added before being sent through a rubidium reference cell. In order to achieve a Doppler-free spectroscopy signal, a pump beam also passes through the same reference cell counter-propagating with respect to the probe so that only a narrow (natural linewidth-wide) velocity class is simultaneously resonant.

After being acquired by a photodetector, the error signal is demodulated with a mixer and then sent into a PID control circuit. The feedback signal is then applied to the current modulation input of the Vortex. To account for low frequency drifts given the finite tuning range of the current modulation input, a low-passed copy of the feedback signal is amplified and then applied to the laser's piezo input to adjust its cavity length. This combination of a fast current loop and a slow piezo loop results in a tight laser lock that is capable of compensating for large drifts. However, over very long times (> 1 hour), the low frequency integrator that adjusts the piezo ultimately reaches its voltage limit. To avoid losing lock, a third, computer-based

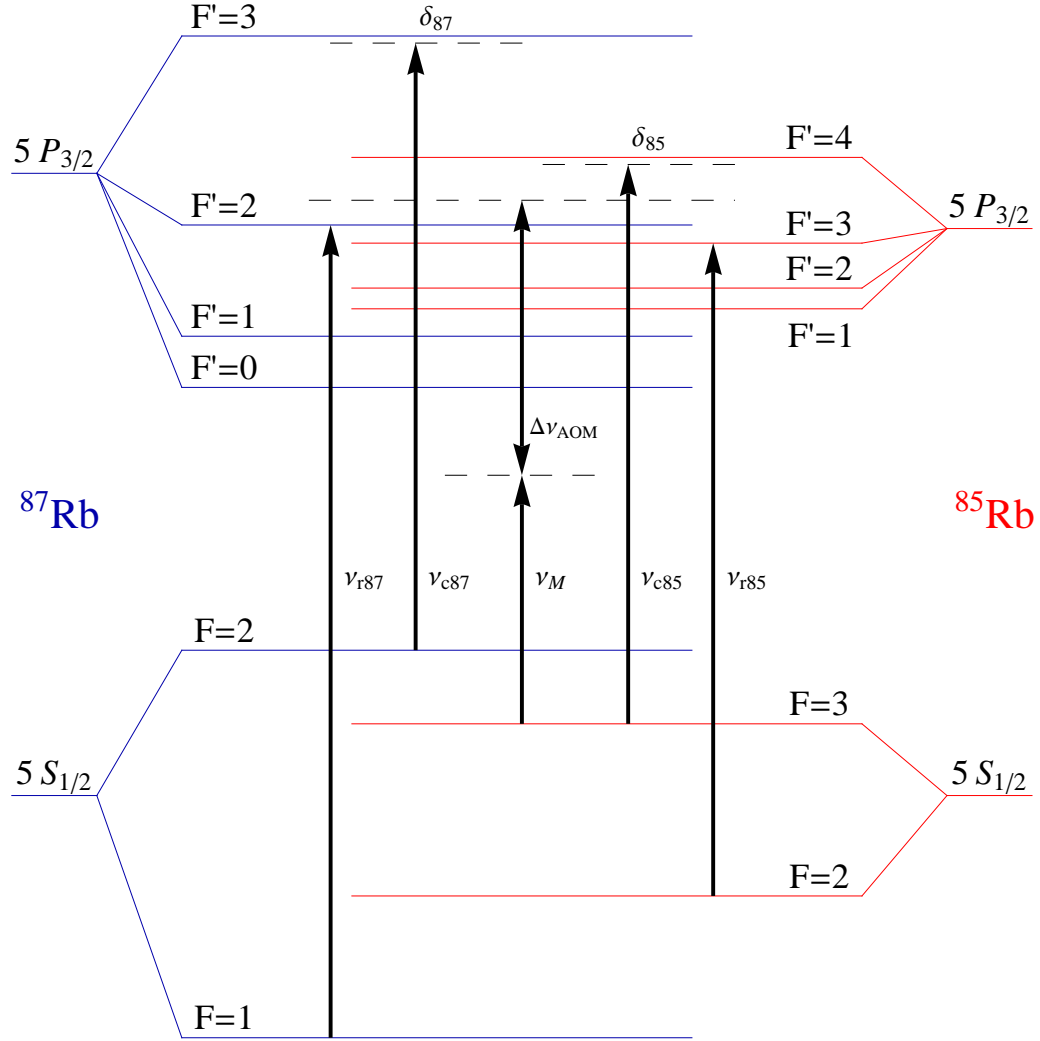


Figure 5.17: Level structures and optical frequencies for cooling and trapping both isotopes. The master laser ν_M is offset locked by $\Delta\nu_{\text{AOM}}$ from the $3' \rightarrow 4'$ crossover resonance of ^{85}Rb . The cooling and repump transitions are shown for both species, with the subscript c denoting cooling and r repump. The cooling light is detuned from resonance by δ_{85} and δ_{87} for ^{85}Rb and ^{87}Rb , respectively. Note that the hyperfine splittings of the $5P_{3/2}$ manifolds are exaggerated by a factor of 80 with respect to the $5S_{1/2}$ manifolds for the sake of readability. The optical transitions $5S_{1/2} \rightarrow 5P_{3/2}$ are not drawn to scale.

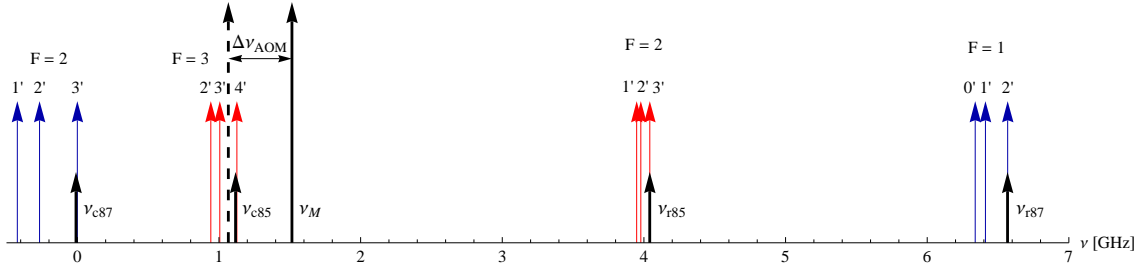


Figure 5.18: RF scheme for cooling and trapping both isotopes. The lock point is the $3' \rightarrow 4'$ crossover resonance of ^{85}Rb and is shown as a dashed arrow. The master laser ν_M sits $\Delta\nu_{\text{AOM}}$ to the blue of the lock point. Light to address the cooling and repump transitions is then generated by putting sidebands on the master laser using phase modulators.

feedback loop operates in parallel. This outer loop monitors the voltage level of the slow piezo feedback loop with a 1 s update rate. If this voltage gets too close to the edge of the piezo circuit's limits, the computer issues a GPIB command to the Vortex which coarsely adjusts the piezo's DC value such that the feedback circuit is brought back into range. With all three loops in place, the laser can stay locked for days at a time.

The narrow line-width master laser does not output enough power to generate all the required cooling light, so we use a master oscillator, power amplifier (MOPA) arrangement. A tapered amplifier (TA₁ in Fig. 5.19) is seeded by the master and provides up to 15 dB of optical gain. This yields several hundred milliwatts of power for ~ 10 mW of seed light which is then divided up for the lock and several phase modulators. Before being used, the output of TA₁ is sent through a single-mode optical fiber (SMF₁ in Fig. 5.19) to cleanup its spatial mode and to help decouple the alignment of the rest of the setup from the pointing stability of the TA.

The TA modules are based around 500 mW tapered amplifier chips from Eagleyard Photonics that have gain profiles centered around 780 nm. The C-mount style chips are mounted in custom copper housings that act as both mechanical anchors and thermal heat sinks. Thermal contact with the housing is facilitated by a soft indium foil pad placed between the chip and the housing which deforms to fit both

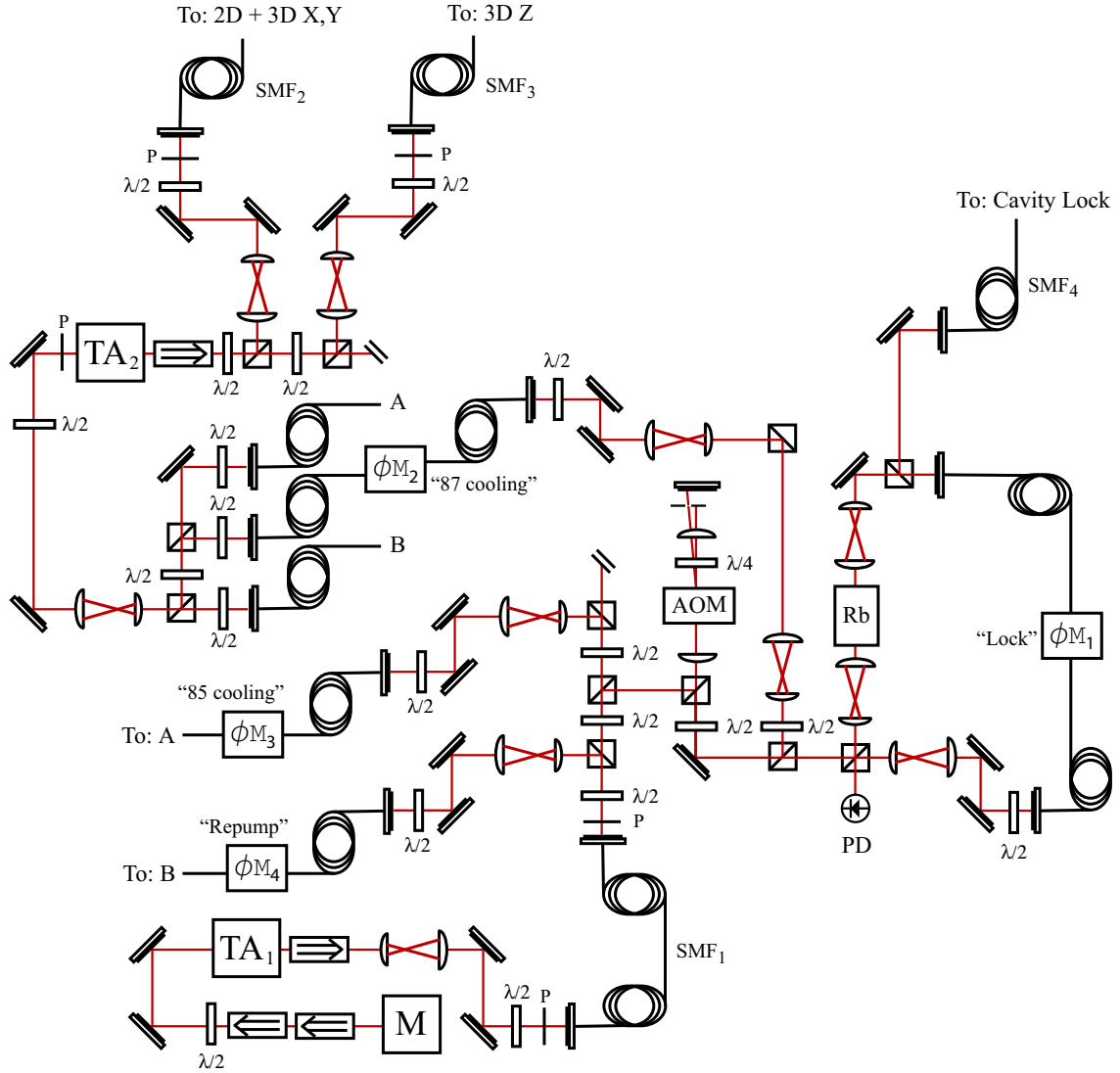


Figure 5.19: Optics setup for generating laser cooling and trapping light for both isotopes. The ECDL master laser is labeled M and the tapered amplifiers are labeled TA_i . SMF_i designates a single-mode fiber. PD is a photo detector. Half waveplates and quarter waveplates are labeled $\lambda/2$ and $\lambda/4$, respectively. P indicates an absorptive polarizer (Polarcor). All beamsplitter cubes are polarizing. The fiber phase modulators are labeled as ϕM_i . In two places, marked A and B , the fibers are drawn with a break for the purpose of clarity. Rb is the rubidium vapor cell used for the saturation absorption spectroscopy laser lock system. AOM is an acousto-optic modulator that gives a double-pass frequency shift of $\Delta\nu_{AOM}$.

surfaces. For stable amplitude and frequency operation, the TAs benefit from a precision low-noise current source and active temperature control. A thermistor embedded in the copper housing in conjunction with a thermoelectric cooler (TEC) monitors and stabilizes the temperature of the housing using PI feedback. The copper housing is mounted to a water cooled aluminum block so that the heat pumped by the TEC can be efficiently removed. Master seed light is injected into the TA via an $f = 2$ mm lens. To optimize the coupling into the TA, the lens is mounted inside a 100 threads/inch lens tube which attaches to the copper housing, allowing for fine adjustment of the focus. An identical lens setup collimates the diverging output mode of the TA, and then finally a cylindrical lens corrects for astigmatism.

We generate the cooling and repump light frequencies by putting sidebands on the amplified master light using fiber-based electro-optic traveling wave phase modulators (Photline Technologies, NIR-MPX850-LN08). These broadband fiber modulations (labeled as ϕM_i in Fig. 5.19) have a microwave bandwidth of 8 GHz, allowing sidebands on the master ν_M to reach to any of the rubidium D2 transitions. To minimize the number of independent modulators, we generate both repump frequencies ν_{r85} and ν_{r87} with a single modulator ϕM_4 by choosing its modulation frequency $\Delta\nu_4$ equal to the isotope splitting:

$$\Delta\nu_4 = \nu_{1 \rightarrow 2'}^{(87)} - \nu_{2 \rightarrow 3'}^{(85)} \approx 2.526 \text{ GHz} \quad (5.6)$$

Furthermore, by special choice of the master laser offset frequency $\Delta\nu_{\text{AOM}} = 449$ MHz, we arrange for the master laser to be exactly $\Delta\nu_4$ to the red of the ${}^{85}\text{Rb}$ repump frequency $\nu_{2 \rightarrow 3'}^{(85)}$. As a result, the output of modulator ϕM_4 has its first order sideband at $\nu_{r85} = \nu_M + \Delta\nu_4 = \nu_{2 \rightarrow 3'}^{(85)}$ and its second order sideband at $\nu_{r87} = \nu_M + 2\Delta\nu_4 = \nu_{1 \rightarrow 2'}^{(87)}$, both of which are resonant with the respective repump transitions of the two isotopes. For sinusoidal modulation of the form $\sin(\nu_M t + \beta \sin(\Delta\nu_4 t))$, the first and second order sidebands have equal magnitude at a modulation depth of $\beta \approx 2.6$. Since the fiber modulators have very small $V_\pi \approx 5$ Volts, $\beta = 2.6$ is experimentally accessible with a modest power requirement of $(5V)^2/(50 \Omega) = 0.5$ W. Therefore, experimentally we can get roughly equal power in the two repump sidebands using

a single fiber modulator driven with a single RF modulation frequency. The dual species loading rate results in Fig. 5.16 use this frequency generation scheme.

In some experiments, where only a single isotope MOT is required, we used slightly different settings for the offset lock frequency and repump fiber modulator shift. When generating a single species ^{87}Rb MOT, we operated with a master offset of $\Delta\nu'_{\text{AOM}} = 388$ MHz and a repump modulation of $\Delta\nu'_4 = 2568$ MHz. The second order sideband from the modulator is then resonant with the ^{87}Rb repump transition. However, the ^{85}Rb repump transition is not resonate with these modulation parameters.

Although the phase modulator approach to generating the MOT frequencies has the advantage of minimizing the number of independent laser locks, one disadvantage is the inefficiency of phase modulation due to the presence of many undesired sidebands. Sinusoidal phase modulation results in a spectrum consisting of an infinite series of positive and negative sidebands:

$$\sin(\nu t + \beta \sin(\Delta\nu t)) = \sum_{n=-\infty}^{\infty} J_n(\beta) \sin((\nu + n\Delta\nu)t) \quad (5.7)$$

Our application calls for a pure frequency shift of light from ν_M to one of the MOT transitions. Thus, only a single sideband is desired, and the rest of the sidebands in Eq. 5.7 are wasted at best and could excite unanticipated atomic transitions at worse. To avoid these problems, we use a serrodyne modulation technique instead of sinusoidal modulation (see Appendix C). By driving a phase modulator with a sawtooth waveform generated by a non-linear transmission line (NLTL), most of the power ends up in the desired sideband, with the other sidebands suppressed by typically 5 to 10 dB.

Spurious sideband suppression is particularly important for the cooling light frequencies ν_{r85} and ν_{r87} because they represent most of the power in the MOT. Ideally, undesired sidebands should be kept at least an order of magnitude smaller than the cooling light amplitude so that most of the power delivered to the MOT is at a useful frequency. To generate the ^{87}Rb cooling frequency ν_{r87} , we use serrodyne modulation with a Picosecond Pulse Labs model 7113-110 NLTL. This NLTL operates best at drive frequencies near 1 GHz and degrades quickly for frequencies above

1.2 GHz. Since the cooling transition is 1515 MHz to the red of the master ν_M but only 1066 MHz to the red of the AOM-shifted offset lock point $\nu_M - \Delta\nu_{\text{AOM}}$, it is advantageous to use the AOM-shifted light instead of the master light as the carrier for generating ν_{r87} . As shown in Fig. 5.19, light from after the AOM double-pass is sent through fiber modulator ϕM_2 where it is frequency shifted by $\Delta\nu_2 = (-1066 \text{ MHz} + \delta_{87})$ using serrodyne modulation.⁸ With this scheme, residual spurious sidebands are reduced to smaller than 5% of the power of the ⁸⁷Rb cooling sideband.

We use voltage controlled oscillators (VCOs) to drive the high frequency ($> 1 \text{ GHz}$) modulators. The VCOs are from the Analog Devices ADF4360 series. Each ADF4360 chip is an integrated package that includes several VCOs and a phase locked loop (PLL) which servos the VCO frequency to a reference signal. The ADF4360 circuit accepts a 10 MHz reference which is digitally multiplied to reach the GHz operating frequency of the VCO. The output frequency of the VCO can be adjusted by hundreds of MHz simply by changing the digital multiplier via a serial communication interface. The ⁸⁷Rb cooling sideband $\Delta\nu_2$ and the repump modulation frequency $\Delta\nu_4$ are both generated by ADF4360 chips.

5.3.2 Atom Optics Light

Compared to the laser cooling laser system, the light used to manipulate the atoms during the interferometer sequence must satisfy much more stringent requirements. These include enhanced frequency and phase stability, polarization purity, intensity stability and wavefront uniformity. In addition, the atom optics laser system is responsible for generating the accelerating optical lattice potential needed for launching the atoms along their fountain trajectories. This application demands flexible, continuous frequency tunability, and puts tight constraints on the minimum beam intensity and detuning.

First of all, consider the necessary frequency control. The atom interferometer beamsplitters and the optical lattice are both based on two-photon transitions.

⁸ $\delta_{87} < 0$ then corresponds to light that is red detuned from the cooling transition.

These include Raman transitions, which change the atom's internal hyperfine state in addition to changing its momentum, and Bragg transitions, which only change the momentum while leaving the internal state unchanged.⁹ In either case, the transitions require two laser frequencies to drive a stimulated two-photon process, and these frequencies are chosen to be far detuned from the single photon resonance so that single photon transitions are greatly suppressed. From energy conservation, the two-photon resonance condition using light with propagation vectors \mathbf{k}_1 and \mathbf{k}_2 and frequencies ω_1 and ω_2 is given by

$$\omega_1 - \omega_2 = \underbrace{(\omega_f^a - \omega_i^a)}_{\text{Internal state}} + \underbrace{\mathbf{k}_{\text{eff}} \cdot \mathbf{v}}_{\text{Doppler shift}} + \underbrace{\frac{\hbar \mathbf{k}_{\text{eff}}^2}{2m}}_{\text{Recoil shift}} \quad (5.8)$$

where $\hbar\omega_i^a$ and $\hbar\omega_f^a$ are respectively the initial and final internal atomic state energies, \mathbf{v} is the atom's initial velocity, and $\mathbf{k}_{\text{eff}} \equiv \mathbf{k}_1 - \mathbf{k}_2$ is the effective propagation vector of the transition. For counter-propagating beams, $\mathbf{k}_{\text{eff}} \approx 2\mathbf{k}_1$ since $|\omega_1 - \omega_2| \ll c|\mathbf{k}_1|$. Note that the recoil shift for ⁸⁷Rb is approximately 15 kHz while the energy level difference between the hyperfine ground states is 6.8 GHz. For a Bragg transition, $\omega_i^a = \omega_f^a$, so Eq. 5.8 requires that the frequency difference between the two lasers be 15 kHz for an atom initially at rest. The equivalent Raman transition requires an additional 6.8 GHz of shift to account for the internal energy difference of the states. Additionally, as the atom falls for time $2T$, its velocity will change by $2gT \approx 26$ m/s, which corresponds to a Doppler shift of 68 MHz. The laser frequency difference must be adjusted to account for this shift.

The atom optics laser system needs to have sufficient frequency agility to satisfy Eq. 5.8 for both Raman and Bragg transitions over the entire range of atom velocities. This requires continuous tuning of the frequency difference over a range of 68 MHz. As shown in Fig. 5.20, a set of three double-passed AOMs are used to perform these frequency shifts. Each AOM is used to generate a different laser frequency:

$$\nu_i = \nu_{\text{ao}} + \delta\nu_i \quad (i = 1, 2, 3) \quad (5.9)$$

⁹An optical lattice acceleration can be thought of as a sequence of temporally overlapped Bragg transitions.

Here $\delta\nu_i$ is the frequency shift imparted by AOM_i in Fig. 5.20 and ν_{ao} is the carrier frequency for the atom optics system which is sent into the AOMs. The use of three AOMs (instead of two) is more flexible as it allows for simultaneously two independent resonant pairs to be sent to the atoms. Since each pair of beams can be used to satisfy a different resonant condition, this setup can simultaneously induce Bragg (or Raman) transitions for two different atom velocities. This flexibility is needed for more sophisticated large momentum transfer (LMT) atom optics, as well as for simultaneous conjugate interferometers.

The optical lattice launch puts additional demands on the frequency agility of the system. During the lattice launch, the atoms must be accelerated from $v = 0$ to $v = gT = 13.2$ m/s over a distance of ~ 10 cm, corresponding to an acceleration of $a = 88g$. In order for the lattice to continuously satisfy Eq. 5.8, the frequency difference between the lattice beams must be swept at a rate $\alpha/2\pi = 2ka/2\pi \approx 2.2$ MHz/ms for a time of 15 ms. We can generate this type of chirped frequency by driving the AOMs with a direct digital synthesis (DDS) board.

For a Raman transition, a frequency shift of 6.835 GHz for ^{87}Rb or 3.036 GHz for ^{85}Rb must be added to one beam as well. This is accomplished with a broadband fiber phase modulator. As shown in Fig. 5.20, the 0th-order (undeflected) light out of AOM_3 is picked off and then sent through fiber modulator ϕM_5 before being returned along the same path. When driving a Raman transition, AOM_3 is left off and ϕM_5 adds the appropriate microwave sideband to compensate for the hyperfine splitting in Eq. 5.8. During Bragg transitions, AOM_3 is used instead and the 0th-order beam path is blocked with a mechanical shutter.

Next, the intensity of the atom optics laser beams should be as large as possible for a number of reasons. The two-photon effective Rabi frequency Ω_{eff} is a good figure of merit for both the interferometer pulses and the optical lattice, and it scales with the intensity of the two beams as $\Omega_{\text{eff}} \propto \sqrt{I_1}\sqrt{I_2}$. For the interferometer sequence specifically, there are systematic errors associated with the finite duration $\tau \sim \Omega_{\text{eff}}^{-1}$ of the beamsplitter pulses that are greatly suppressed in the short pulse limit. Additionally, N -photon LMT beamsplitters require a time $\sim N/\Omega_{\text{eff}}$ to complete, motivating high Rabi frequency and high intensity. Likewise, Ω_{eff} determines the optical lattice

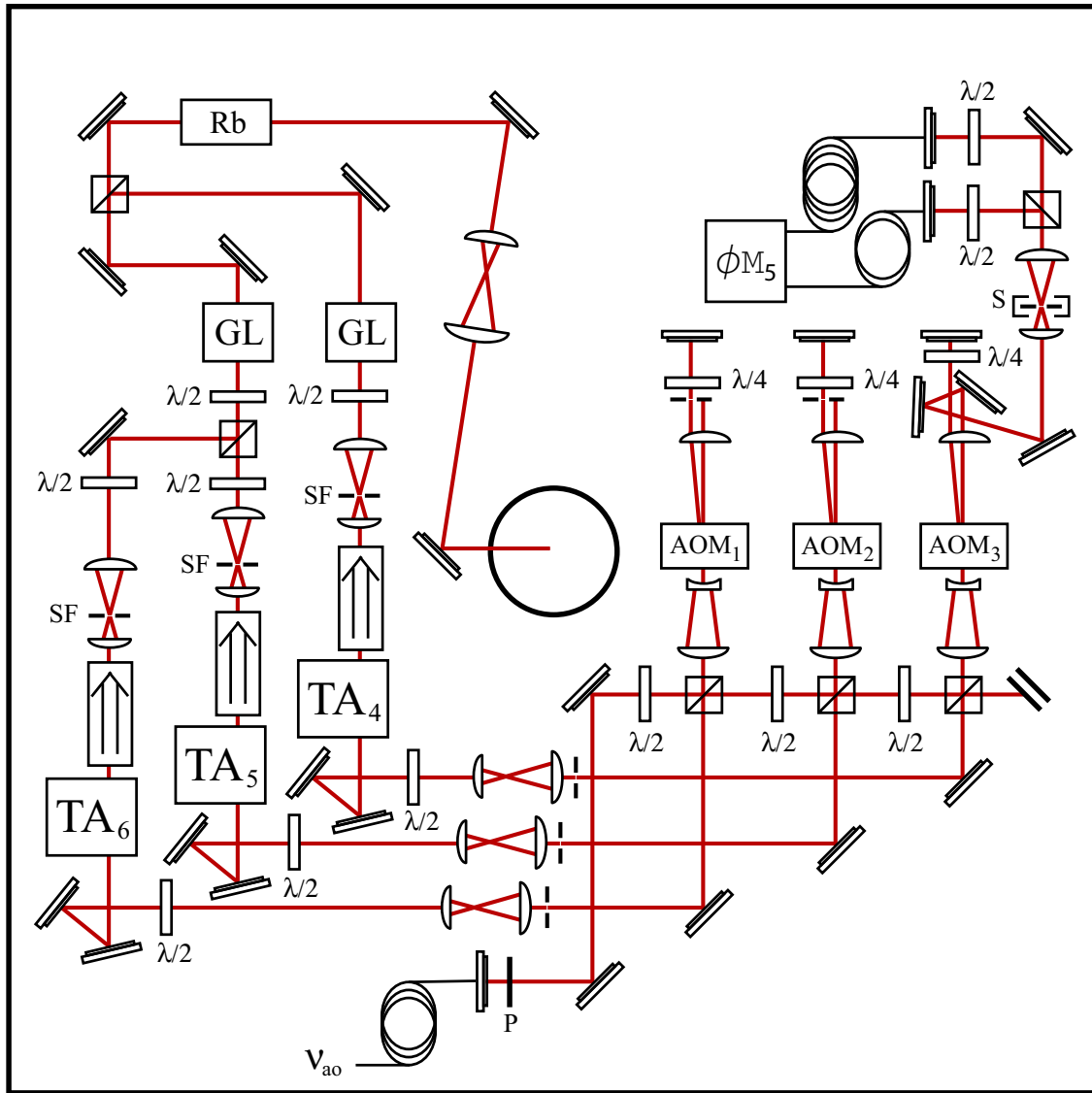


Figure 5.20: Laser setup for generating atom optics light and optical lattice light. Tapered amplifiers are labeled TA_i . Half waveplates and quarter waveplates are labeled $\lambda/2$ and $\lambda/4$, respectively. P indicates an absorptive polarizer (PolarcorTM) and **GL** is a Glan Laser prism polarizer. All beamsplitter cubes are polarizing. ϕM_4 is a fiber phase modulator for generating Raman sidebands. **Rb** is the rubidium vapor cell used to filter resonant ASE. AOM_i are the acousto-optic modulators used for frequency control of the Bragg beams.

depth, and a larger lattice depth allows for a faster acceleration during the launch.

On the other hand, spatial mode concerns place restrictions on the minimum beam diameter, limiting its intensity. Since the wavefronts of a Gaussian beam are in general curved, the finite size of the beams results in a nonuniform transverse spatial phase which gets imprinted on the atoms during the interferometer. This can lead to systematic errors if the atoms follow different trajectories. To avoid this, the beam diameter should be large compared to the spatial extent of the atom cloud so that the atoms stay near the center of the beam where the phase is mostly flat. A related constraint is that the interferometer beams must remain collimated over the length of the interferometer. In this case, the Rayleigh range must satisfy $z_R \gg 10$ m so that the intensity and phase profile stay uniform over the entire interferometer region.

To compensate for the beam diameter constraints, the atom optics lasers must be high power. Figure 5.20 shows the set of three TAs that we use to amplify the frequency shifted light from the AOMs. These TA assemblies are similar to those described in section 5.3.1 with the important exception that the diodes can deliver 1 W average power. Each TA is responsible for amplifying one of the AOM outputs, so nominally only one frequency is sent into each TA. This avoids the possibility of nonlinear mixing between competing frequencies inside the TA which could potentially add unwanted sidebands to the light.

The spatial mode of the interferometer light is very important because it determines the spatial phase that the light pulses imprint on the atom cloud. Therefore each TA is sent through its own pinhole spatial filter. After the beams are combined, the final beam is sent through an additional pinhole before being sent to the atoms.

The polarization of the atom optics laser beams must be chosen to satisfy the appropriate selection rules for the two-photon transitions. Consider atom optics beams incident along the z-direction with $\mathbf{k}_{\text{eff}} = k_{\text{eff}}\hat{\mathbf{z}}$. In this basis, the allowed light polarizations are linearly polarized along either $\hat{\mathbf{x}}$ or $\hat{\mathbf{y}}$ and circularly polarized with either right handed $\hat{\sigma}_+ = \frac{-1}{\sqrt{2}}(\hat{\mathbf{x}} + i\hat{\mathbf{y}})$ or left handed $\hat{\sigma}_- = \frac{1}{\sqrt{2}}(\hat{\mathbf{x}} - i\hat{\mathbf{y}})$ rotation. Let the polarization vectors of the two beams be denoted by $\hat{\epsilon}_1$ and $\hat{\epsilon}_2$. Note that for first-order magnetic field insensitivity, the interferometer uses the $m_F = 0$ states, so the required two-photon coupling is of the form $|F_i, m_F = 0\rangle \leftrightarrow |F_f, m_F = 0\rangle$, where

$|F_f - F_i| = 1$ for Raman and is zero for Bragg. The allowed polarizations for driving a Bragg transition of this type are $(\hat{\epsilon}_1, \hat{\epsilon}_2) = (\hat{x}, \hat{x})$, $(\hat{\epsilon}_1, \hat{\epsilon}_2) = (\hat{y}, \hat{y})$, $(\hat{\epsilon}_1, \hat{\epsilon}_2) = (\hat{\sigma}_+, \hat{\sigma}_+)$, and $(\hat{\epsilon}_1, \hat{\epsilon}_2) = (\hat{\sigma}_-, \hat{\sigma}_-)$. Likewise, for a $m_F = 0$, $\Delta m_F = 0$ Raman transition the allowed polarizations are $(\hat{\epsilon}_1, \hat{\epsilon}_2) = (\hat{x}, \hat{y})$, $(\hat{\epsilon}_1, \hat{\epsilon}_2) = (\hat{y}, \hat{x})$, $(\hat{\epsilon}_1, \hat{\epsilon}_2) = (\hat{\sigma}_+, \hat{\sigma}_+)$, and $(\hat{\epsilon}_1, \hat{\epsilon}_2) = (\hat{\sigma}_-, \hat{\sigma}_-)$. Notice that the polarization requirements for Raman and Bragg are incompatible in the case of linearly polarized light since Raman requires $\text{lin} \perp \text{lin}$ and Bragg requires $\text{lin} \parallel \text{lin}$. However, both types of transitions may be driven using the same circularly polarized light, so we use this polarization to maintain flexibility.

We use a retro-reflection beam configuration to deliver the atom optics beams. Figure 5.21 shows the final stage of the z -axis optics setup with the waveplates responsible for generating the $(\hat{\epsilon}_1, \hat{\epsilon}_2) = (\hat{\sigma}_+, \hat{\sigma}_+)$ polarization states for the counterpropagating beams \mathbf{k}_1 and \mathbf{k}_2 . Previously, the two beams were overlapped with perpendicular polarizations on a PBS (see Fig. 5.20, after the GL polarizers). The overlapped beams are sent through a quarter waveplate, producing $\hat{\sigma}_+$ and $\hat{\sigma}_-$ beams propagating down towards the interferometer region. Both beams are retro-reflected where they pass through another quarter waveplate which reverses the handedness of the polarization. As a result, there are two counter-propagating pairs of beams that have the right polarizations to drive either Raman or Bragg transitions. The degeneracy between these two sets is broken by the generally non-zero velocity of the atoms, which shifts the resonance condition (Eq. 5.8) in a way that depends on the direction of \mathbf{k}_{eff} .

Using two quarter waveplates in this fashion has the added benefit that it can be used to produce the correct polarization for a MOT along the z -direction. Optical access constraints that arise from the long interferometer region make it necessary for the z -axis MOT beams to co-propagate along the interferometer beam axis. With this scheme, the z -axis MOT light is amplified by a TA in Fig. 5.20 before being sent to the interferometer region where the waveplates shown in Fig. 5.21 produce the counter-propagating $\hat{\sigma}_+ - \hat{\sigma}_-$ pair.

Imperfect polarization purity of the atom optics light can limit the transfer efficiency of the interferometer pulses into the desired state. A small polarization error of the form $\hat{\epsilon}_1 = \hat{\sigma}_+ + \epsilon \hat{\sigma}_-$ (with $\epsilon \ll 1$) can couple transitions such as

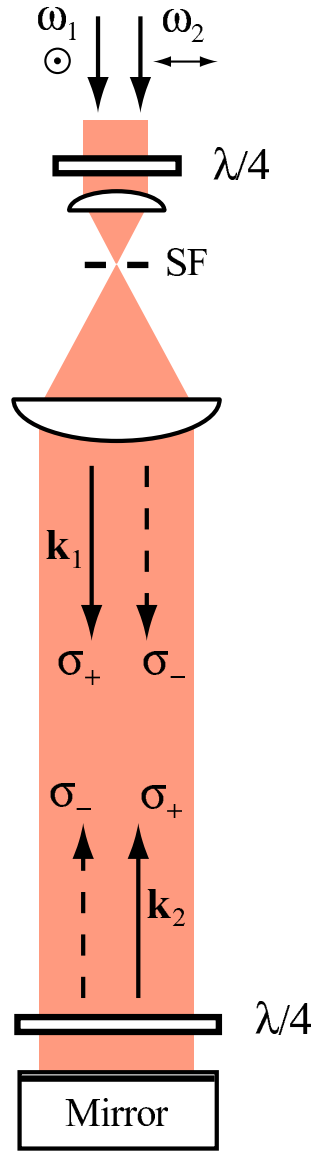


Figure 5.21: Optics setup for the z -axis. The two frequencies of atom optics light ω_1 and ω_2 are delivered to the top of the interferometer region with perpendicular linear polarizations. A $\lambda/4$ converts the polarization into circular σ_+ and σ_- . A second $\lambda/4$ ensures that the pair of counter-propagating beams \mathbf{k}_1 and \mathbf{k}_2 (solid arrows) have the correct polarization for driving either Raman or Bragg transitions. Another pair of beams (dotted arrows) have the correct polarization, but their frequency difference will not be resonant as long as the atom velocity is non-zero. SF is a pinhole spatial filter.

$|F_i, m_F = 0\rangle \leftrightarrow |F_f, m_F = \pm 2\rangle$. This pollutes the interferometer with population in unwanted states with a probability of $P_{m_F=\pm 2} = \sin^2(\epsilon\Omega_{\text{eff}}\tau/2) \sim \pi^2\epsilon^2/16$, assuming a $\pi/2$ -pulse. Since the $m \neq 0$ states are more sensitive to magnetic field phase shifts, the presence of population in these states can lead to magnetic field systematic errors. Aside from this, such undesired transitions represent a loss of interferometer contrast and therefore sensitivity. As shown in Fig. 5.20, each interferometer beam is sent through a Glan Laser (GL) prism polarizer before the beams are overlapped and sent to the interferometer region. The GL polarizers have a specified intensity extinction ratio of $10^5 : 1$, in principle allowing for electric field polarization purity $\epsilon \sim \sqrt{10^{-5}}$ when properly aligned.¹⁰

The wavefront quality of the atom optics beams in the interferometer region is important because non-uniformities in the transverse phase of the laser result in systematic errors due to the imperfect overlap of the isotope trajectories. The local laser phase gets imprinted on the atom during each interferometer pulse, and so the atom optics laser phase fronts should be as spatially uniform as possible in order to relax the overlap requirements of the isotope trajectories. As indicated by Eq. 4.8, it is actually the relative phase $\phi_2 - \phi_1$ that gets imprinted on the atom. As a result, the most relevant wavefront distortions are those induced by any optical elements that are not shared by the two counterpropagating beams \mathbf{k}_1 and \mathbf{k}_2 .

The retro-reflection geometry (see Fig. 5.21) is beneficial with regard to wavefront distortion because the number of non-common elements is minimized. As Fig. 5.21 indicates, the two beams are sent through the same pinhole spatial filter prior to entering the interferometer region in an attempt to produce the same initial transverse mode. However, the upward-propagating \mathbf{k}_2 beam passes through the bottom $\lambda/4$ waveplate twice and reflects off the bottom mirror before interacting with the atoms, whereas the downward-propagating \mathbf{k}_1 beam does not. Therefore, distortions from the bottom waveplate and mirror must be minimized. In addition, the final collimation lens after the spatial filter is an important element because of the potential ill effects of spherical aberration. Spherical aberration can result in significant phase ripple in

¹⁰During alignment, a third GL prism can be used as an analyzer to verify the extinction ratio and perpendicularity of the other two GL prisms.

the near field of the lens. Also, a spherically aberrated beam evolves into different transverse phase profiles for the two different propagation distances from the lens.

5.3.3 Optimizing the optical lattice launch

The detuning Δ of the atom optics light carrier frequency ν_{ao} from the single photon resonance has important repercussions on the efficiency of the lattice launch. In the limit of small lattice depth, the lattice acceleration may be thought of as a sequence of adiabatic passages between momentum states $|p + 2n\hbar k\rangle \rightarrow |p + 2(n+1)\hbar k\rangle$ up to the desired launch velocity. Each such pair of states is coupled by a two-photon Bragg transition. These transitions sequentially come into resonance as the lattice beams' frequency difference is swept according to $\delta\omega(t) = \alpha t$, where α is the frequency sweep rate. However, there are two atom loss mechanisms to contend with during the launch: spontaneous emission and Landau-Zener tunneling.

First of all, there is always a non-zero single-photon excitation rate which leads to spontaneous emission loss. If an atom undergoes a spontaneous emission cycle during the launch then it will be lost from the lattice and will not end up in the correct initial momentum state for the interferometer. This loss rate depends on the sum of the single photon scattering rates from the two beams:

$$R_{\text{sp}} = R_{\text{sp}}^{(1)} + R_{\text{sp}}^{(2)} = \Gamma \frac{I/I_{\text{sat}}}{1 + (2\Delta/\Gamma)^2} \quad (5.10)$$

where $I = I_1 \sim I_2$ is the light intensity (taken to be equal for both beams), Γ is the atomic linewidth and I_{sat} is the saturation intensity for the transition. Since the total fraction of atoms lost during the launch is $f_{\text{sp}} = R_{\text{sp}}\delta t_L$ for launch time δt_L , minimizing the spontaneous emission loss rate relies on increasing the detuning, decreasing the intensity, and decreasing the launch time.

Next, Landau-Zener (LZ) tunneling losses arise due to non-adiabatic transitions that occur when the lattice acceleration is too large for a given lattice depth. This effect may be understood classically as the acceleration at which atoms that are nominally trapped in the lattice periodic potential are forced to slide out of their original lattice site. Although, in the classical case, this only can happen when the

acceleration-induced pseudoforce is large enough to eliminate the potential energy minima of the lattice, quantum mechanical tunneling through a finite barrier results in LZ losses even at lower accelerations.

Quantitative predictions of the loss rate require a slightly more sophisticated model of lattice acceleration than the earlier, small lattice depth, description. Atoms that are initially loaded into the lattice by adiabatically increasing the lattice depth will end up occupying the lowest energy eigenstate of the lattice potential. These eigenstates (the Bloch states) form an energy band structure $E_{n,q}$, labeled by band number n and quasimomentum q . The bands are periodic with quasimomentum, with each Brillouin zone having width $2\hbar k$. As the lattice is accelerated, the atom's energy adiabatically follows the lowest band. At the edge of each Brillouin zone, the atom must pass through an avoided crossing which can result in a non-adiabatic transition to the first excited band and subsequent loss from the lattice. Thus, the LZ loss rate is set by the probability for an atom to make such a diabatic transition which is given by

$$P_{\text{LZ}} = \exp\left[-\frac{\pi}{2} \frac{\Omega_{\text{bg}}^2}{\alpha}\right] \quad (5.11)$$

where $\hbar\Omega_{\text{bg}}$ is the band gap energy at the avoided crossing. In order to launch an atom with a final velocity v_L , the atom must pass through $N = mv_L/2\hbar k$ avoided crossings, and so the fraction of atoms lost due to LZ tunneling is $f_{\text{LZ}} = 1 - (1 - P_{\text{LZ}})^N$. For lattice depth not too large, the band gap may be approximated as

$$\Omega_{\text{bg}} \approx \Omega_{\text{eff}} = \frac{\Omega_1 \Omega_2}{2\Delta} = \frac{\Gamma}{2} \frac{(I/I_{\text{sat}})}{(2\Delta/\Gamma)} \quad (5.12)$$

where here once again $I = I_1 \sim I_2$. The exact band gap can be easily calculated numerically by solving for the lattice band structure. However, Eq. 5.12 will suffice for the purposes of discussing the relevant scalings since Ω_{bg} strictly increases with Ω_{eff} . From these results it is clear that minimizing LZ losses requires a large band gap and a slow acceleration, implying the need for high intensity, small detuning, and a long launch time δt_L . Since these scaling are exactly the opposite of those for minimizing spontaneous emission losses, we must find a compromise solution that optimizes the

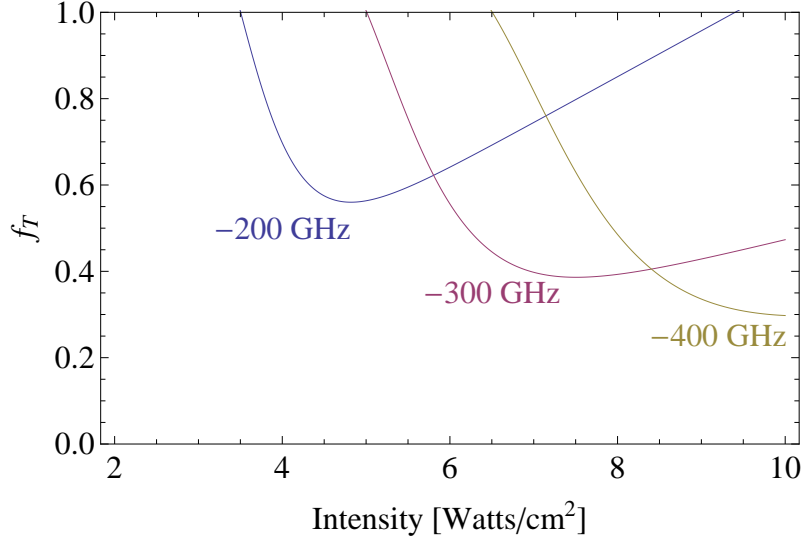


Figure 5.22: Theoretical atom loss fraction due to the lattice launch. f_T is the fraction of ^{87}Rb atoms lost due to spontaneous emission and LZ tunneling as a function of the single beam intensity. Each curve shows a different carrier detuning Δ . The launch kinematic parameters are $v_L = 13.2 \text{ m/s}$ and $d_L = 10 \text{ cm}$, corresponding to a lattice acceleration of $88g$ and atom momentum change of $2238\hbar k$. The results assume a retro-reflected lattice beam geometry, so the spontaneous emission rate is larger than Eq. 5.10 by a factor of two.

combined loss rate. Note that the kinematic degrees of freedom of the launch are already constrained by other considerations. The choice of a particular launch velocity v_L determines the number of two-photon transitions N and also constrains the acceleration rate since $\alpha\delta t_L = 2kv_L$. The final constraint on the acceleration time δt_L comes from our restriction that the launch must occur within a fixed distance $d_L = \frac{1}{2}\frac{\alpha}{2k}\delta t_L^2$. Thus, the only free parameters available for the optimization are the laser detuning and intensity.

Figure 5.22 shows the total theoretical loss fraction $f_T = f_{\text{sp}} + f_{\text{LZ}}$ including both spontaneous emission and LZ tunneling as a function of lattice laser power. Each curve is for a different detuning Δ , and the launch kinematics are for the experimentally relevant launch velocity of $v_L = 13.2 \text{ m/s}$ and launch distance of $d_L = 10 \text{ cm}$. Note that LZ losses are dominant at low intensity and spontaneous emission takes

over at high intensity, so the best operating point occurs at intermediate intensity when both effects are comparable. We chose a detuning of $\delta/2\pi = -200$ GHz, implying an optimal operating point of about 4.8 W/cm^2 and a predicted loss fraction of 56%.

5.4 Computer Control System

The various subsystems of the apparatus are controlled by a sophisticated computer system that must fulfill a number of requirements. As described in Chapter 2, each experimental cycle consists of a series of steps during which the atoms are prepared, manipulated, and then detected. To accumulate statistics, this cycle must be repeated many times with minimal interruption. Furthermore, the specific details of the cycle must be flexible and reconfigurable in order to cope with the continuously evolving apparatus, as well as to allow for systematic scans of experimental control parameters. Finally, as a result of the spatial extent of the apparatus, the hardware is controlled by multiple computers which must be synchronized.

From a computer control perspective, an experimental cycle consists of a series of time-ordered events that occur on the various input and output channels of the apparatus. Each event is defined by three parameters: the absolute time of the event, the channel on which it occurs, and the value that the channel assumes. The hardware channels themselves are very diverse, including digital outputs, analog voltage inputs and outputs, function generator outputs, and CCD camera inputs. Regardless of these differences, at the highest level our computer control system treats each hardware channel in the same way, resulting in a set of abstract channels that all accept events in the form (time, channel, value) as described above. Working within this event-based abstraction, the computer control system conceptually performs two distinct tasks. The first step is to accept a list of human-readable events from the user and to parse this list, producing a set of low-level, channel-specific events. The second step is to synchronize the playback of these parsed events on the hardware channels. This powerful abstraction greatly simplifies the experimental cycle description by hiding all of the details of the specific hardware channels.

The large scale of the apparatus motivates the use of a network of computers, each responsible for controlling a local subset of the hardware. Specifically, the atom source is at the bottom of the interferometer region, 10 m below the atom optics laser system, and the laser cooling light is generated on a optics table in another room, ~ 15 m away. Each of these subsystems has its own associated electronics and computer I/O interface requirements which are naturally handled locally. Using different computers for the control of each subsystem, rather than a single central computer, has the advantages of decreasing the computational load on any one computer and also minimizing cable lengths. Consequently, the multiple computers need to be synchronized during event playback, and in addition they must be able to receive communication containing the list of events to be played.

5.4.1 Stanford Timing Interface

To coordinate the control of the various computers in the apparatus, we wrote software that allows for communication between the computers over the local area network (LAN). This software infrastructure, which implements the network communication, timing cycle event parsing, and general apparatus control system, we refer to as the Stanford Timing Interface (STI).

The STI network architecture consists of a central server and a set of devices that are controlled by the server. Each device provides a number of channels that can accept timing events as described above. These channels correspond to local hardware channels that the device is capable of controlling. In addition, the server communicates with an independent console application. The console provides a user interface for defining timing cycle events, and displays the status of the apparatus during event playback. Multiple consoles can simultaneously connect to the server, allowing multiple users to monitor the apparatus; however only one console is in control at a given time. The network architecture is shown schematically in Fig. 5.23.

At the highest level, STI provides a scripting language for defining the experiment's timing cycle. This language is implemented as a custom extension library

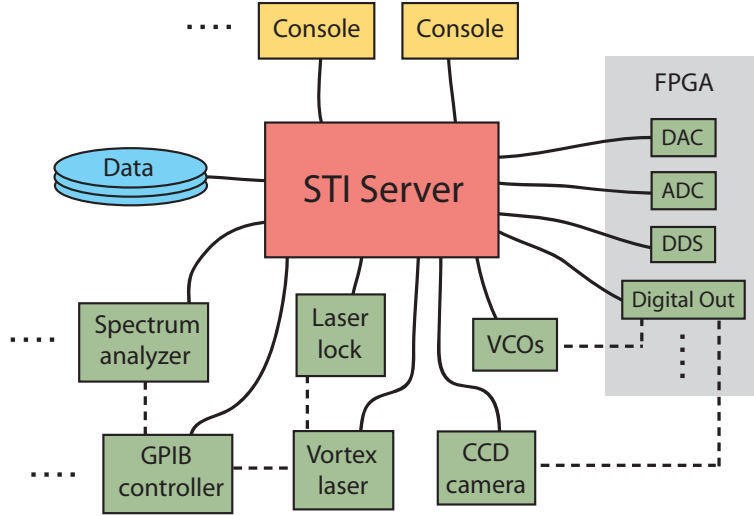


Figure 5.23: STI network architecture. The STI server controls a flexible collection of devices, a subset of which are shown here (green). The server in turn is controlled by the user via the console. The hardware for certain timing-critical devices is controlled by the FPGA system, shown here in gray (see Section 5.4.2). Inter-device communication is indicated by the dashed lines connecting some devices.

of the Python programming language called STIPy (written in C++). The STIPy library contains a small number of STI-specific Python functions that allow the user to define timing events as well as to specify STI devices and channels. In addition, all valid Python code is allowed. A timing file written using the STIPy library completely defines all the events in an experimental cycle, and thus it serves as the documentation record of the cycle.

For communication between computers over the network, STI uses CORBA middleware.¹¹ As a result, STI supports a heterogeneous computer environment consisting of multiple computers, operating systems and programming languages. The STI server is implemented in C++ using an open source CORBA implementation called omniORB. Likewise, the STI devices are also implemented in C++ using omniORB. Lastly, the client is implemented in Java and relies on Java's built-in CORBA

¹¹The Common Object Request Broker Architecture (CORBA) is a standard that enables remote procedure calls (RPCs) between multiple computers which are both programming language and operating system independent.

implementation.

As the center of our computer control architecture, the STI server has many diverse responsibilities. First of all, the server communicates with all the devices in the apparatus. The server-device communication scheme is general in the sense that the server does not have any a priori information about the devices that connect to it. Instead, each new device that connects to the server is responsible for transmitting all required information about itself to the server. For example, newly connected devices present the server with the set of available channels that they provide. This general communication interface allows new devices to be added to the apparatus without modifying the server, and it means that the server can treat all devices the same way.

The server is also responsible for parsing the STIPy timing definition scripts. This is accomplished by an embedded Python parser that loads the STIPy package. When the server receives a timing definition file from the console, it is first parsed by Python, resulting in a list of all the requested timing events. This list is then divided up into sublists for the devices connected to the server based on the channels of the parsed events. The server then transmits the event lists to the respective devices.

In order to communicate with the server, each STI device implements a generic device interface. This interface defines a set of common functions that all devices must have in order to receive and playback timing events. Although the server relies on this general interface in order to transfer events to the devices, the details of each device's implementation are necessarily device-specific. Since the server only has access to the high-level channel description of each device, all of the low-level, hardware-specific functionality associated with event playback is determined by the device itself. Therefore, during the second stage of event parsing, after the high-level events are transmitted from the server to each device, the events are converted into device-specific events which can be played on the actual hardware. Specifically, it is at this stage that the ‘value’ field specified for the channel in the timing file is interpreted and converted into the appropriate low-level command. For this reason, the allowed data types permitted for the ‘value’ field of an event are generic; each device defines its own specific value field format based on the requirements of its

channels.¹²

An STI device may also define a list of attributes that can affect the device's functionality. Attributes are generic string parameters that have a specific meaning only for the device in question. For example, a device that is capable of operating in more than one user-selectable mode can use an attribute to control this setting. Device attributes are stored locally and can be changed by the server in response to a user command issued through the console. The attributes interface operates independently of the timing event system, as attributes cannot be changed at specific times. However, since the behavior of a device is dependent on the state of its attributes, the values of all attributes are recorded in order to provide complete documentation for each event playback cycle.

Since devices control a specific set of hardware channels, the implementation of a device must run on a computer than has direct hardware access to the relevant channels. Typically, each device is implemented as a separate program, but multiple devices can also run in the same program.

In addition to communication with the server, STI devices can communicate directly with each other. This allows for more advanced, abstract devices that can use other devices as resources, or that can cooperate to allow for more complicated behavior. The other devices that a device communicates with are referred to as partner devices. Devices can play events on their partners' channels and are able to change their partners' attributes.

Inter-device communication is facilitated by the server. When devices register with the server, they declare a list of required partner devices. When these required partners become available on the network, the server gives the device the necessary network references to allow inter-device communication. Once the device has received the network reference to a partner device, it can directly interact with the partner, bypassing the server. All the network reference lists are kept current by the server as different devices connect and disconnect from the network.

Each experiment cycle must be thoroughly documented so that the data can

¹²As a result, the server, client and the STIPy library are all completely general, without any device-specific data formats or keywords.

be meaningfully analyzed later. The STI server automatically generates XML-based documentation after every cycle finishes playback. The documentation consists of the timing file used to generate the timing events, the list of registered devices including all device attributes, and also the time that the cycle was run. In addition, the XML documentation contains the results of any measurements made during the sequence, as well as links to auxiliary data files (e.g., camera images).

The STI console provides the user interface for the entire computer control system. From within the console, the user can edit, save, and parse timing files. When the user parses a particular timing file, the console submits the file to the server where the parsing actually occurs. The console receives and displays the results of parsing, including the detailed event list or any parsing errors that occurred. Event playback can then be initiated by the user via the console. During event playback, the server monitors the progress of each device and reports the system status back to the console.

The console also displays a generic user interface for each of the devices registered with the server. This interface can be used to check a device's status, modify its attributes, or run individual events on its channels.

Often, the same experimental cycle must be run multiple times, possibly with slight modifications in order to scan some experimental parameter. This type of behavior is supported through the sequence interface. Specifically, the console accepts an additional Python script which can be used to generate a list of experiment cycles, each with different parameters if necessary. Then, during playback, the server plays each cycle in the sequence, re-parsing the timing file each time using the specific parameters indicated for that cycle. In this way, the system can automatically collect multiple cycles worth of data without requiring any additional input from the user.

5.4.2 FPGA Based Timing

The timing accuracy of the software-based timing control system described above is typically limited to the millisecond level due to network latency and operating system task switching. As a result, the timing critical parts of the experiment require

a hardware-based timing system. We developed a custom FPGA-based timing system which provides the precision timing of a hardware system while maintaining the flexibility of software.¹³

The FPGA main board we use is a custom embedded system based around an Axis ETRAX FS microprocessor and a Xilinx Spartan-3 FPGA. The onboard microprocessor has a number of direct lines to the FPGA to facilitate loading firmware as well as checking the the FPGA's status. The FPGA clock period is set at 10 ns, resulting in timing jitter at the nanosecond level.

The main board has eight sockets that accept smaller, task-specific daughter boards. Each socket has a 32 pin connector which provides direct logic connections between the FPGA and the daughter board. Available daughter boards include a 2 channel, 3 MHz analog input board, a 2 channel, 10 MHz analog output board, a 40 channel, 1 MHz analog output board, a 4 channel, 250 MHz direct digital synthesis (DDS) board, and a 24 channel, 100 MHz digital input/output board. Any of these board types can be used in any of the eight daughter board slots, depending on the I/O demands of the apparatus.¹⁴

Each FPGA daughter board has its own associated STI device. These STI devices run on the ETRAX embedded system and are responsible for parsing timing events that are received from the server. The high-level events from the server are converted into machine words that can be read by the FPGA. Each FPGA event consists of two words: a 32 bit time and a 32 bit value.¹⁵ The firmware associated with each daughter board can interpret these value words in order to produce the appropriate IC-level timing sequence necessary to operate the hardware.

Each event is loaded from memory by the FPGA in time order. During playback, the FPGA compares its internal counter to the time value of the next event, and when these times are equal it plays the event on the associated daughter board. The STI device software monitors the status of the playback by querying a memory address linked to the daughter board's event counter, and reports back to the server when playback is complete.

¹³A field-programmable gate array (FPGA) is a reconfigurable integrated circuit.

¹⁴The slow 40 channel analog output board takes up two adjacent daughter slots.

¹⁵The DDS board is the exception and requires a 32 bit time plus two 32 bit values per event.

Chapter 6

General Relativistic Effects

In a previous paper [34] we discussed the possibility of testing general relativity with atom interferometry. We found that many relativistic effects will be large enough to be seen in the upcoming generation of experiments, such as with EP apparatus described in Chapter 5. In this chapter we give the details of the framework for calculating the effects of general relativity in an atom interferometer. We then apply this to an interferometer in the Earth’s gravitational field with the motivation of using the high precision of atom interferometry to test general relativity in a laboratory experiment. The ability to find GR effects in an atom interferometer is more widely applicable as well. In particular we consider other effects such as the Lense-Thirring effect. Further, in Chapter 7 we apply this technique to find the effect of a gravitational wave.[72, 31]

We will also discuss a few ideas for strategies to measure several of these GR effects in the lab. We do not attempt to prove that such experiments are feasible, since this would require a very detailed analysis of the many relevant backgrounds. Instead, we give a few arguments why the most important backgrounds may be controllable. We wish mainly to motivate a more careful consideration of these experiments, given the interest in laboratory tests of general relativity.

An attempt was made to make the different sections of this chapter as independent as possible. Section 6.1 will describe our method for finding the final phase shift in an atom interferometer in any space-time in general relativity. Section 6.2.1 will

specialize this discussion to the Schwarzschild metric for application to an atom interferometer in a weak gravitational field such as the Earth's. Section 6.2.2 will give our results for the GR effects in an atom interferometer near the Earth and discuss their physical origin in general relativity. Section 6.3 will discuss a few ideas for measuring these GR terms in an actual experiment. Section 6.4 will discuss other applications of this work including using atom interferometry to measure the Lense-Thirring effect and the expansion of the universe.

6.1 General Relativistic Description of Atomic Interferometry

We are interested in the leading order effects of general relativity in an atom interferometer. Chapter 3 described our non-relativistic calculation. Here we build on the results of that chapter to create a formalism which treats the entire calculation in a relativistic manner. It is very difficult to solve for the quantum mechanical evolution of the atom in a general metric background. Thus, we will use the semi-classical approximation method outlined for the non-relativistic calculation. This method can be used in relativity, with some minor modifications, since in general relativity the concept of potential is replaced by the least action principle.

As described in Chapter 2, the atoms follow free-fall trajectories during which a sequence of laser pulses serve as beamsplitters and mirrors that coherently divide each atom's wavepacket and then later recombine it to produce the interference. Figure 6.1 is a relativistically correct space-time diagram illustrating this process for a single atom. As before, the atom beamsplitter is implemented using a stimulated two-photon transition. In this process, laser light incident from the right of Fig. 6.1 with wavevector \mathbf{k}_1 is initially absorbed by the atom. Subsequently, laser light with wavevector \mathbf{k}_2 incident from the left stimulates the emission of a \mathbf{k}_2 -photon from the atom, resulting in a net momentum transfer of $\hbar\mathbf{k}_{\text{eff}} = \hbar\mathbf{k}_2 - \hbar\mathbf{k}_1 \approx 2\hbar\mathbf{k}_2$. These two-photon atom optics are represented in Fig. 6.1 by the intersection of two counter-propagating photon paths at each interaction node.

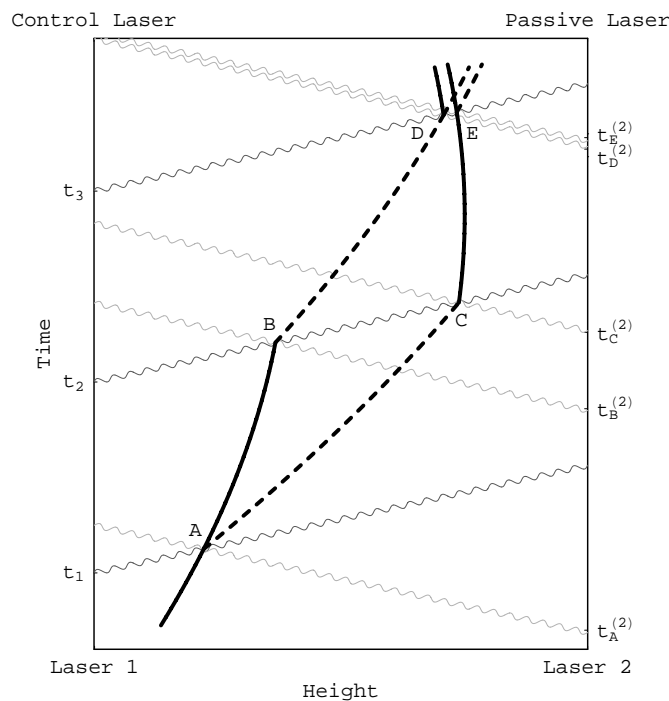


Figure 6.1: A relativistic space-time diagram of a light pulse atom interferometer. The black lines indicate the motion of a single atom. Laser light used to manipulate the atom is incident from above (light gray) and below (dark gray) and travels along null geodesics. Here the lasers' world-lines are taken to be the two vertical lines on the left and right edges of the graph.

In brief, the calculation method is as follows. Using the prescription in Section 3.1, the free propagation of the atoms and the light in Figure 6.1 is treated non-quantum mechanically. Thus, both the laser pulses and the atoms are taken to move along geodesics of the space-time. The description of the atom-light interaction is taken from non-relativistic quantum mechanics, but must be described in a covariant manner as will be discussed below. Finally, the total resulting phase shift must be a coordinate invariant. Further, to understand the result it is necessary to write it in terms of the physical variables of the problem as measured by an experiment, thus removing any coordinate dependence from the answer.

Our objective is to calculate the leading order general relativistic effects in order to explore interesting and possibly measurable signals. In order to simplify the calculation, many sub-leading order effects will be dropped including effects due to the finite pulse time of the lasers, AC Stark shifts, and the errors in the semi-classical approximation due to the finite size of the atom's wavefunction. All these may give important backgrounds but they can be and have been calculated easily in the non-relativistic formalism. We are interested in the largest effects that arise due to general relativity and so we can ignore all these effects.

We will consider an atom interferometer in a background space-time with metric $g_{\mu\nu}$. The proper time for a particle in this space-time is then given by $d\tau^2 = g_{\mu\nu}dx^\mu dx^\nu$. We will take $\hbar = c = 1$.

6.1.1 Dynamics of the Interferometer

The trajectories of the atoms and the laser pulses are found by solving the geodesic equation

$$\frac{d^2x^\mu}{d\tau^2} + \Gamma_{\alpha\beta}^\mu \frac{dx^\alpha}{d\tau} \frac{dx^\beta}{d\tau} = 0, \quad (6.1)$$

where Γ is the affine connection and Greek indices run 0 to 3. In order to compute the leading order GR effects we will calculate the phase shift using the approximations explained in Section 7.2, for which it is sufficient to find the motion of the center of the atomic wavefunction. Of course, there are corrections to this semi-classical (or stationary phase) approximation due to the finite size of the atomic wavefunction

which have been discussed in Section 3. However, the leading order GR effects are just large enough to be experimentally measured and therefore these corrections to our GR results are negligible and will be ignored. The interferometer is then defined by the initial space-time position and velocity of the atom before the first beamsplitter pulse, and by the starting positions of the three laser pulses which define the interferometer, the beamsplitter-mirror-beamsplitter sequence. Once these are given, the rest of the interferometer is found by calculating the intersection of the geodesics as shown in Fig. 6.1. We assume atomic transitions only occur when the atom is simultaneously in the presence of both laser beams. We will assume that for every atom-light interaction point, the right laser is always turned on sufficiently far before the left laser so that the atom is already in the presence of the light from the right laser when the light from the left laser hits it. Thus the atomic transitions will always occur when the light from the left laser reaches the atom. This choice makes a small but potentially measurable effect that will be discussed below. We will call the left laser the ‘control laser’, because its timing determines the timing of the interferometer and the right laser the ‘passive laser’.

The intersection of the initial beamsplitter pulse (from the control laser) and the initial atomic trajectory defines point A. After the first beamsplitter interaction, the half of the atom which is not affected by the light travels on to B along the same trajectory. The half of the atom which is affected travels on a new trajectory originating from point A but with a new velocity which is a function of the incoming momenta of the atom and the light pulse as will be described below. The two halves then travel to B and C respectively, which are defined by the intersections with the mirror pulse. At B, the atom gets a kick from the light in the same way as before. At C, it loses momentum via stimulated emission. These halves then travel on to D and E respectively, where they interact with the final beamsplitter and interference is assumed to occur as described above. The relativistic calculation of the final phase shift is described below. Thus, given the initial conditions for the atom and laser pulses, the interferometer can be calculated in a fully covariant manner.

We must now give a coordinate invariant description of these initial conditions. This means they must be written in terms of the physical variables measured by the

experimentalist. For all the calculations described here we will consider the laser to be at a fixed spatial coordinate location, \vec{x}_L . As we will see, for all the metrics we consider, we will choose coordinates such that this is a suitable model for the laser. The initial beamsplitter pulse then defines the start of the interferometer and should be considered to be at an arbitrary time coordinate, t_1 (unless the experimenter somehow has independent knowledge of the metric). The mirror pulse is then taken to leave the laser at \vec{x}_L a time T later as measured on the laser's clock. Similarly, a time T later on the laser's clock the final beamsplitter pulse is emitted from the laser. The laser's proper time is given by

$$T = \int d\tau = \int_{t_1}^{t_2} \sqrt{g_{00}} dt = \int_{t_2}^{t_3} \sqrt{g_{00}} dt. \quad (6.2)$$

Solving these two equations for t_2 and t_3 yields the time-coordinates at which the mirror and final beamsplitter pulses originate from the laser. This then defines the three laser pulses in a coordinate invariant way. The atom's initial position may be changed depending on the application and thus it is harder to give a single, relativistic description of it. One natural way to define it is to take the atom to begin at the same position as the laser (and thus at a well-defined time on the laser's clock), and then to travel for a certain amount of time (again on the laser's clock) before the first beamsplitter pulse is emitted. This defines the initial position in a relativistically invariant manner. The atom's initial velocity can also be defined in several ways. For example, it could be taken as the radar ranging velocity that the laser sees. Where it is relevant, we will usually consider it to be the more experimentally realistic velocity that would result from getting some large number of momentum kicks from the laser. Once the initial conditions for the atom interferometer have been defined in a coordinate invariant manner, we can calculate the entire interferometer sequence.

The atom-light interaction can most easily be thought about in a local Lorentz frame, x' , (LLF) of the atom (essentially Riemann normal coordinates). This is a choice of coordinates such that the atom is at rest at the origin of these coordinates and space-time is locally flat near the atom. Specifically, in the LLF the metric is

locally flat with vanishing first derivatives at the position of the atom so that

$$\Gamma_{\alpha'\beta'}^{\mu'} \Big|_{x'=0} = 0 \quad (6.3)$$

and near the origin (the position of the atom)

$$g_{\mu'\nu'}(x') = \eta_{\mu'\nu'} + \mathcal{O}(x'^2), \quad (6.4)$$

where η is the flat metric. In these coordinates, the leading order effects of the interaction with the light on the atom are just the non-relativistic quantum mechanical rules given in Section 7.2. So in this frame the spatial momentum of the atom after the transition is equal to the sum of the spatial momenta of the atom before the transition and the incoming light which causes the transition, namely

$$m_{\text{in}} \frac{dx'^i_{\text{atom}}}{d\tau} \Big|_{\text{after}} = m_{\text{fi}} \frac{dx'^i_{\text{atom}}}{d\tau} \Big|_{\text{before}} + \frac{dx'^i_{\text{light}}}{d\lambda} \quad (\text{in LLF}) \quad (6.5)$$

where $i = 1, 2, 3$, m_{in} and m_{fi} are the rest masses of the atom before and after the atomic transition, and λ is the affine parameter for the laser's null geodesic (the analogue of τ in Eq. (6.1) but with different units). Typically $m_{\text{in}} = m_{\text{fi}} \pm \omega_a$ where ω_a is the frequency difference between the initial and final (internal) atomic states that are coupled by the laser interaction¹. Note that in the case of a multi-photon transition (e.g., the two-photon transitions shown in Fig. 6.1) the photon momentum $\frac{dx'^i_{\text{light}}}{d\lambda}$ in Eq. (6.5) must be replaced by the sum of the momenta of all photons that contribute to the transition. Since the metric deviates slightly from flat, there are small corrections due to the tidal effects of gravity over the size Δx of the atomic wavefunction which are $\mathcal{O}(R\Delta x^2)$, where R represents the Riemann curvature tensor. Thus any effects of gravity are suppressed by the size of the atomic wavefunction, so even the leading order Newtonian contributions to Riemann can be neglected during the atom-light interaction (see the discussion of the semi-classical approximation in

¹In the case of a two-photon Raman transition, ω_a is typically the hyperfine splitting of the ground state of an alkali atom ($\omega_a \approx 2\pi \times 6.8$ GHz for ^{87}Rb). For a Bragg transition, $\omega_a = 0$ since the initial and final internal states are the same.

Sec. 3.2). For a description of transforming coordinates to the LLF see [73].

To find these spatial momenta in the LLF (x') it is necessary to know them in the main coordinate system (x) being used and then transform them to the LLF. The atom's spatial momenta are simply determined from its geodesic and proper time coordinate τ . However, a light ray travels on the same geodesic no matter what its momentum is. We must then know the correct affine parameterization, $x_{\text{light}}^\mu(\lambda)$, of the null geodesic such that $\frac{dx_{\text{light}}^i}{d\lambda}$ is actually the spatial momentum and not just proportional to it. This is determined by the initial conditions for the laser pulse. However, we cannot simply take the spatial momentum $\left.\frac{dx_{\text{light}}^i}{d\lambda}\right|_{x_L}$ of the laser pulse at emission to be equal to k^i , the laser's wavevector, because the coordinates x^i do not necessarily have any physical meaning and so such a choice would be coordinate dependent. We must instead write our answers only in terms of physical variables; in this case we must use the k which an observer would measure the laser to have. For definiteness we will assume the laser's frequency is measured by an observer at the same position x_L as the laser and not moving with respect to it. Then this defines

$$\left. \left(g_{\mu\nu} U^\mu \frac{dx_{\text{light}}^\nu}{d\lambda} \right) \right|_{x_L} \equiv \omega = k \quad (6.6)$$

where ω is the frequency of the laser and $U^\mu = \frac{dx_{\text{obs}}^\mu}{d\tau}$ is the four-velocity of the observer. This equation implicitly defines the λ such that our observer sitting on the laser (in the laser's LLF) measures the emitted pulses to have the proper frequency ω . This pulse is then propagated to the atom in the main coordinate system of the problem (x). When the light reaches the atom, its momentum is transformed to the atom's LLF (x') in order to find the momentum transferred to the atom. Eq. (6.6) is critical as it modifies the result for the GR corrections at leading order as we will see explicitly below.

Note that this rule (Eq. (6.5)) of adding the momenta only applies in the LLF, and there is in fact some ambiguity about which LLF to use: the rest frame of the atom before or after the interaction. This ambiguity implies relativistic corrections to the recoil velocity that are $\mathcal{O}(v_r^2)$, thus changing the atom's velocity at $\mathcal{O}(v_r^3)$. This is far too small to be visible in the experiments we are considering; however if it

becomes necessary to compute such corrections, the formalism given here would have to be adapted.

We have now completely determined the dynamics of the interferometer in a fully relativistic framework. Importantly, the initial conditions have been given in terms of physical variables of the problem and so there is no coordinate dependence left. All that remains is to determine the rules for calculating the final phase difference in general relativity.

6.1.2 Relativistic Phase Shift Formulae

The propagation phase is proportional to the integral of the Lagrangian, i.e., the action. In general relativity, the action for a particle moving in a background space-time is the length of its world-line, $S = \int m d\tau$, where the mass m of the particle is irrelevant for the equations of motion but is inserted so that the Lagrangian reduces to the normal non-relativistic Lagrangian in the appropriate limit. Since $S = \int L dt$, the Lagrangian is $L = m \frac{d\tau}{dt}$. To demonstrate that this reduces to the expected Lagrangian in a weak gravitational field, insert the Schwarzschild metric (Eq. (6.13)) and take a post-Newtonian expansion in ϕ and $\vec{v}^i \equiv \frac{d\vec{x}^i}{d\tau}$. Then $L = m - \frac{1}{2}m\vec{v}^2 + m\phi + \mathcal{O}(v^4, \phi^2, v^2\phi)$ as expected. By analogy with the non-relativistic formula in Section 7.2, the general relativistic action is the propagation phase

$$\phi_{\text{propagation}} = \int L dt = \int m d\tau = \int p_\mu dx^\mu \quad (6.7)$$

where $p^\mu \equiv m \frac{dx^\mu}{d\tau}$ is the particle's momentum. The last equality follows from $p_\mu dx^\mu = mg_{\mu\nu} \frac{dx^\mu}{d\tau} dx^\nu = m \frac{d\tau}{dt} d\tau$. Notice that this is the opposite sign convention from the non-relativistic expression for propagation phase from Section 7.2.

The separation phase follows essentially from the formula outlined in Section 7.2 applied in the LLF. The separation phase in the LLF is $\bar{E}\Delta t' - \vec{p} \cdot \Delta \vec{x}'$. We then employ the standard trick, to write the formula in this frame as a coordinate invariant

$$\phi_{\text{separation}} = \int_E^D \bar{p}_{\mu'} dx'^{\mu'} \sim \bar{E}\Delta t' - \vec{p} \cdot \Delta \vec{x}' \quad (6.8)$$

where the integral is taken along the null geodesic connecting points E and D (the final beamsplitter pulse from laser 1). Since this is a coordinate invariant and is true in the Local Lorentz Frame (x'), it is then valid in all frames. Then in any coordinate system (x) the separation phase is

$$\phi_{\text{separation}} = \int_E^D \bar{p}_\mu dx^\mu. \quad (6.9)$$

Here \bar{p}^μ is the average momentum of the two halves of the atom at points D and E

$$\bar{p}^\mu = \frac{1}{2} \left(m_o \left. \frac{dx^\mu}{d\tau} \right|_D + m_o \left. \frac{dx^\mu}{d\tau} \right|_E \right) \quad (6.10)$$

and the momenta are evaluated at points D and E after the final beamsplitter pulse and in the same output port (either slow, $|A_1\rangle$, or fast, $|A_2\rangle$, whichever is being used to compute the final phase shift; see Fig. 3.1). Here m_o is the mass of the atom in the chosen output port. The small coordinate ambiguities in this formula are negligible for every metric considered, as will be shown below. As is clear from the formulas, the separation phase (6.9) can be thought of as the last piece of propagation phase (6.7). The term $\bar{E}\Delta t$ is then roughly the phase acquired by bringing the half of the atom that transitioned earlier at the second beamsplitter up to the same time as the second half of the atom, so they can interfere. We have chosen to define the separation phase along the null geodesic which is the final beamsplitter pulse because this is the first hypersurface on which interference can be considered to have occurred. Of course, since quantum mechanics is linear, we can choose any later hypersurface, add the two halves of the atom's wavefunction and calculate a separation phase then (of course we would also need the correct rule for propagating the atoms forward after the final beamsplitter). In other words, in order to find the total phase shift, the atom's wavefunction can be evaluated at any point in space-time after the final beamsplitter pulse. For example, the number of atoms in each output port is often measured with a detection laser pulse. This would correspond to a final null geodesic which is equivalently good for calculating the final phase shift.

As shown in Section 7.2, the laser phase imparted to the atom during a beam-splitter or mirror pulse is the phase of the light at the interaction point. Since this applies in the LLF and is also a coordinate invariant statement, it can be applied in any frame. A null geodesic is a line of constant phase for the laser since e.g. it is the world-line in space-time that a crest of the laser pulse follows. Thus the light's phase at an interaction point is the same as its phase at the time of emission of that light pulse from the laser. For example, the laser phase of the pulse from laser 1, the control laser, at point A is just the phase of laser 1 at time t_1 in Fig. 6.1. The total laser phase shift is then the sum of the laser phases from each laser over all the interaction points. For example, in the slow output port, the total laser phase is

$$\Delta\phi_{\text{laser}}^{\text{slow}} = \phi_{L1}(t_1) - 2\phi_{L1}(t_2) + \phi_{L1}(t_3) - \phi_{L2}(t_A^{(2)}) + \phi_{L2}(t_B^{(2)}) + \phi_{L2}(t_C^{(2)}) - \phi_{L2}(t_D^{(2)}) \quad (6.11)$$

where $\phi_{Li}(t)$ means the phase of laser i at time t . Because we have assumed that laser 2 is always on ², the transition points are defined by the intersection of the atom's geodesic with the light pulse from laser 1. Of course, the interaction takes some small amount of time, but we assume that the phase of the laser at the beginning of the interaction is the one imparted because the corrections to this approximation are typically small and do not affect the leading order GR result (see the discussion of the short pulse limit in Section 3.2). Thus the phase which laser 2 imprints on the atom is the phase of the light from laser 2 (the passive laser) which is passing the atom at the first instant of the interaction as set by laser 1 (the control laser). Finding this phase requires determining the time that this part of the light left laser 2, which we label $t_A^{(2)}, t_B^{(2)}$, etc. We will usually assume that the phase of laser i is just its frequency (as defined by Eq. (6.6)) times its proper time $\phi_{Li}(t) = \omega_i \tau_{Li}(t)$. For a time independent metric this is also $\phi_{Li}(t) = \omega_i \sqrt{g_{00}} t$. So in this case, the contributions to laser phase from laser 1, the control laser, completely cancel.

We now have rules for finding the final phase shift in an atom interferometer,

$$\Delta\phi_{\text{tot}} = \Delta\phi_{\text{propagation}} + \Delta\phi_{\text{separation}} + \Delta\phi_{\text{laser}} \quad (6.12)$$

²In fact, all we have assumed is that laser 2 is turned on well before laser 1, so that the interaction points are determined by the timing of laser 1.

in general relativity.

It can be seen that this formula is independent of the output port used to calculate the phase. The propagation phase does not depend on output port. Laser phase depends on output port since in the slow output port it includes the phase of the laser at point D, while in the fast output port it includes the phase of the laser at point E. As can be seen from Figure 6.1, this is a difference of $\sim \omega (t_E^{(2)} - t_D^{(2)})$ where ω is the frequency of laser 2. The separation phase also differs between ports because the momentum used in Eq. (6.9) is the average momentum of the relevant component of the atom's state after the final beamsplitter pulse. In the fast output port this momentum is $\sim mv_r \approx k_{\text{eff}}$ larger than in the slow output port. So the difference in separation phase between the fast and the slow output port is $\sim k_{\text{eff}}(x_E - x_D) \approx 2\omega(x_E - x_D)$, since $k_{\text{eff}} \approx 2\omega$ for a two-photon transition. But $x_E - x_D \approx t_E - t_D$ since points D and E lie on a null geodesic, and as a result we find that $x_E - x_D \approx \frac{1}{2}(t_E^{(2)} - t_D^{(2)})$. Therefore, the difference in the separation phase between the two output ports is exactly compensated by the change in the laser phase, and Eq. (6.12) is independent of which output port is used.

6.2 GR Effects in the Earth's Gravitational Field

The methods of the previous section can be used to find the effects of general relativity in an atom interferometer in the Earth's gravitational field. The space-time can be modeled with the Schwarzschild metric

$$ds^2 = (1 + 2\phi) dt^2 - \frac{1}{1 + 2\phi} dr^2 - r^2 d\Omega^2 \quad (6.13)$$

where $\phi = -\frac{GM}{r}$ is the gravitational potential. For simplicity, in this section the rotation of the Earth is neglected. It will not modify the GR effects given here, and the possibility of measuring relativistic effects associated with that rotation will be considered in Section 6.4.2. Of course, this rotation will contribute non-relativistic terms that can be backgrounds, which can easily be calculated using simpler, non-relativistic methods. Because the Earth's gravitational field is weak, $\phi \sim 10^{-9}$ at the

surface, we can take a post-Newtonian expansion in ϕ . In order to study effects beyond GR as well, we will calculate the phase shift in the parameterized post-Newtonian (PPN) expansion of the Schwarzschild metric

$$ds^2 = (1 + 2\phi + 2\beta\phi^2)dt^2 - (1 - 2\gamma\phi)dr^2 - r^2d\Omega^2. \quad (6.14)$$

Here β and γ parameterize modifications of general relativity and $\beta = \gamma = 1$ gives normal GR. For the results presented in this section we will generally be considering this PPN expansion of the Schwarzschild metric, though there is little difference in a weak gravitational field. Section 6.2.1 contains the details of the phase shift calculation for this metric. In Section 6.2.2 we present the results of this calculation and explain their physical significance. It can be read without the previous Section 6.2.1.

6.2.1 Interferometer Calculation in the Schwarzschild Metric

The geodesic equation (6.1) for the metric (6.14) cannot in general be solved exactly. We approximate the solution using a power series solution in τ . By varying the order of the series, we ensure that we use a sufficiently high order to include all measurably large terms in the final phase shift. For simplicity, we present first the approximate solutions using the metric (6.13) for a radial geodesic:

$$r(\tau) = r_0 + v_{r0}\tau - \frac{\eta}{2}(\partial_r\phi(r_0))\tau^2 - \frac{\eta}{6}v_{r0}(\partial_r^2\phi(r_0))\tau^3 + \mathcal{O}(\tau^4) \quad (6.15)$$

$$\begin{aligned} t(\tau) = t_0 + & \frac{\sqrt{v_{r0}^2 + \eta + 2\eta\phi(r_0)}}{1 + 2\phi(r_0)}\tau - \frac{v_{r0}\sqrt{v_{r0}^2 + \eta + 2\eta\phi(r_0)}\partial_r\phi(r_0)}{(1 + 2\phi(r_0))^2}\tau^2 \\ & + \frac{\sqrt{v_{r0}^2 + \eta + 2\eta\phi(r_0)}((4v_{r0}^2 + \eta + 2\eta\phi(r_0))\partial_r\phi(r_0)^2 - v_{r0}^2(1 + 2\phi(r_0))\partial_r^2\phi(r_0))\tau^3}{3(1 + 2\phi(r_0))^3} \\ & + \mathcal{O}(\tau^4) \end{aligned} \quad (6.16)$$

where $\eta = g_{\mu\nu}\frac{dx^\mu}{d\tau}\frac{dx^\nu}{d\tau}$ is 0 for null geodesics and 1 for time-like geodesics. Note that these are roughly the normal parabolic paths with some relativistic corrections. Also, light rays do ‘bend’ under gravity, but in these coordinates that effect shows up in

the equation for $t(\tau)$ only. In these solutions, the potential ϕ has effectively been expanded around r_0 , making this approximation better the closer the paths are to r_0 or, roughly, the smaller τ is. The scale this is to be compared to is the radius of the Earth, R_E , as this determines the size of the higher r derivatives of ϕ . Since the atom travels a distance much smaller than R_E , this approximation works very well here. The paths in the PPN metric (6.14) are

$$\begin{aligned} r(\tau) = & r_0 + v_{r0}\tau \\ & + \frac{(v_{r0}^2(1-\gamma) + \eta + 2(v_{r0}^2(\beta - 2\gamma) + \beta\eta)\phi(r_0) - 6v_{r0}^2\beta\gamma\phi(r_0)^2)\partial_r\phi(r_0)}{2(-1 + 2\gamma\phi(r_0))(1 + 2\phi(r_0) + 2\beta\phi(r_0)^2)}\tau^2 \\ & + \frac{v_{r0}}{6} \left(\frac{v_{r0}^2(2\gamma - 1) - \eta - 2(v_{r0}^2(\beta - 3\gamma) + \beta\eta)\phi(r_0) + 8v_{r0}^2\beta\gamma\phi(r_0)^2}{(1 - 2\gamma\phi(r_0))^2(1 + 2\phi(r_0) + 2\beta\phi(r_0)^2)} 2\gamma\partial_r\phi(r_0)^2 \right. \\ & + \frac{2(v_{r0}^2 + \eta - 2v_{r0}^2\gamma\phi(r_0))}{(1 - 2\gamma\phi(r_0))^2(1 + 2\phi(r_0) + 2\beta\phi(r_0)^2)^2} \left\{ 2 - \beta - \gamma + 6(\beta - \gamma)\phi(r_0) \right. \\ & \left. + 6\beta(\beta - 3\gamma)\phi(r_0)^2 - 16\beta^2\gamma\phi(r_0)^3 \right\} \partial_r\phi(r_0)^2 + \frac{v_{r0}^2\gamma\partial_r^2\phi(r_0)}{1 - 2\gamma\phi(r_0)} \\ & \left. - \frac{(1 + 2\beta\phi(r_0))(v_{r0}^2 + \eta - 2v_{r0}^2\gamma\phi(r_0))\partial_r^2\phi(r_0)}{(1 - 2\gamma\phi(r_0))(1 + 2\phi(r_0) + 2\beta\phi(r_0)^2)} \right) \tau^3 + \mathcal{O}(\tau^4) \end{aligned} \quad (6.17)$$

$$\begin{aligned} t(\tau) = & t_0 + \sqrt{\frac{v_{r0}^2 + \eta - 2v_{r0}^2\gamma\phi(r_0)}{1 + 2\phi(r_0) + 2\beta\phi(r_0)^2}} \left\{ \tau - \frac{v_{r0}(1 + 2\beta\phi(r_0))\partial_r\phi(r_0)}{1 + 2\phi(r_0) + 2\beta\phi(r_0)^2}\tau^2 \right. \\ & - \left((((v_{r0}^2(5 - 2\beta - \gamma) + \eta + 2(v_{r0}^2(2\beta\eta - 6\gamma + \beta(8 + \gamma)))\phi(r_0) \right. \\ & + 2\beta(v_{r0}^2(8\beta - 19\gamma) + 2\beta\eta)\phi(r_0)^2 - 36v_{r0}^2\beta^2\gamma\phi(r_0)^3)\partial_r\phi(r_0)^2 \\ & \left. - v_{r0}^2(1 - 2\gamma\phi(r_0))(1 + 2(1 + \beta)\phi(r_0) + 6\beta\phi(r_0)^2 + 4\beta^2\phi(r_0)^3)\partial_r^2\phi(r_0))\tau^3 \right) / \\ & \left. \left(3((-1 + 2\gamma\phi(r_0))(1 + 2\phi(r_0) + 2\beta\phi(r_0)^2)^2) \right) \right\} + \mathcal{O}(\tau^4) \end{aligned} \quad (6.18)$$

These geodesics are calculated on a computer with a symbolic algebra package and so can easily be found to higher orders. We present here the results up to third order to illustrate the method without overcomplicating the equations.

Theoretically, the intersection points of the laser pulses with the atom geodesics

can now be found as discussed above. However, these geodesics are too complicated to solve exactly so we must make two approximations. First, the equations are solved self-consistently only to the order in τ to which the entire calculation is done. In practice this means, for example, inverting the series to find $\tau(t)$ which can then be plugged in to $x(\tau)$ to give $x(t)$ for the atom. An analogous procedure is used to find $x(t)$ for the light. The atom and light coordinate trajectories are then equated and solved perturbatively order by order in t . Second, we must still expand in the variables which are small in order to simplify the results sufficiently so that they remain tractable. The correct way to do this expansion that keeps only relevant terms and avoids an “order of limits” problem is to Taylor expand in all the variables simultaneously, taking into account their relative sizes. Specifically, let ϵ signify 10^{-1} and plug in $\epsilon^9 \phi$ for ϕ everywhere (since $\phi \sim 10^{-9}$), and similarly for the other dimensionless variables: $v_L \sim 10^{-7}$, $\frac{k_{\text{eff}}}{m} \sim v_r \sim 10^{-10}$, $\frac{\omega_a}{m} \sim 10^{-15}$, $\frac{R_E}{T} \sim 10^{-2}$, and $mT \sim 10^{26}$. Since the corrections to the parabolic paths are small, we have a few large terms at low orders which give easily solved equations and then very many small corrections. So we can Taylor expand all our results in ϵ and keep only terms which are large enough to possibly affect the final answer. For the intersection points, we usually keep any terms which are $\gtrsim 10^{-30} R_E$. We vary this order to make sure we haven’t neglected any relevant terms in the final phase shift. The entire calculation is done on a computer using a symbolic algebra package.

We take each laser to be at a fixed coordinate location because the lasers are assumed to be fixed to the Earth. Note that this is not a geodesic. A fixed radial coordinate implies a fixed physical position since this is a static, time-independent metric. Effects such as time variations in the Earth’s gravitational field or oscillations of the laser platform which cause the laser’s effective coordinate location (or the whole metric) to vary are very small and so will affect the leading order GR signal at an unmeasurable level. Of course, depending on the phenomenological characteristics of the signal being searched for, such effects crossed into the zeroth order Newtonian signal could be relevant backgrounds. They can then be calculated simply in a non-relativistic fashion. For now we ignore them since we are interested in calculating the effects of general relativity. In Section 6.3 we consider measuring these GR signals

and there we discuss the relevant backgrounds.

The rest of the calculation will be illustrated using metric (6.14). The interferometer is defined, as shown above, by the initial positions and momenta of the laser pulses and the atom. For simplicity, and because it illustrates all the effects we will be interested in, we make the following choices. The lasers will be at positions $r = r_{L_1}$ and r_{L_2} with frequencies ω_1 and ω_2 , with laser 2 above laser 1. We will take the usual definitions $k_{\text{eff}} = \omega_1 + \omega_2$ and $\omega_{\text{eff}} = \omega_1 - \omega_2$. The pulses from laser 1 will originate at $t_1 = 0$, $t_2 = \frac{T}{\sqrt{1+2\phi(r_{L_1})+2\beta\phi(r_{L_1})^2}}$, and $t_3 = 2t_2$. Following the prescription given in Eq. (6.6) for referencing the light momenta, an observer at the laser has coordinate velocity

$$U^\mu = \frac{dx_{\text{obs}}^\mu}{d\tau} = \left(\frac{dt_{\text{obs}}}{d\tau}, \frac{dx_{\text{obs}}}{d\tau} \right) = \left(\frac{1}{\sqrt{1+2\phi(r_{L_1})+2\beta\phi(r_{L_1})^2}}, 0 \right) \quad (6.19)$$

giving an initial light momentum for the pulses from laser 1 of

$$\begin{aligned} \frac{dx_{\text{light}}^\mu}{d\lambda} &= \left(\frac{dt_{\text{light}}}{d\lambda}, \frac{dx_{\text{light}}}{d\lambda} \right) \\ &= \omega_1 \left(1 + \phi(r_{L_1}) + \frac{3}{2}\phi(r_{L_1})^2 - \beta\phi(r_{L_1})^2, 1 - \gamma\phi(r_{L_1}) + \frac{3}{2}\gamma^2\phi(r_{L_1})^2 \right). \end{aligned} \quad (6.20)$$

This is close to (ω_1, ω_1) but with small GR corrections. These corrections will modify the GR effects in the final answer at leading order and so they must be included.

We will take the atom to be initially at $r = r_{L_1}$ at $t = 0$. For now we leave all expressions in terms of the unphysical coordinate launch velocity, $v_L = \frac{dr}{dt}$. We show below that this makes no important difference to the final phase shift and it keeps the expressions simpler. The geodesics and intersections can now all be found as explained in Section 6.1.

As one example, we describe the calculation of intersection point C. The initial velocity of the fast half of the atom at point A is found by adding the light momentum to the atom's initial momentum as described above. For the atom-light interaction

at A, the coordinate transformations to the LLF take a vector V^μ to

$$V_{\text{LLF}}^{\mu'} = b_\nu^{\mu'} V^\nu \quad (6.21)$$

with

$$b_0^0 = \sqrt{(1 + v_L^2 + 2v_L^2\gamma\phi(r_{L_1})) (1 - 2\phi(r_{L_1}) + 2\beta\phi(r_{L_1})^2)} \quad (6.22)$$

$$b_1^0 = -v_L(1 + 2\gamma\phi(r_{L_1})) \quad (6.23)$$

$$b_0^1 = v_L \sqrt{(1 + 2\gamma\phi(r_{L_1})) (1 - 2\phi(r_{L_1}) + 2\beta\phi(r_{L_1})^2)} \quad (6.24)$$

$$b_1^1 = -\sqrt{(1 + 2\gamma\phi(r_{L_1})) (1 + v_L^2 + 2v_L^2\gamma\phi(r_{L_1}))} \quad (6.25)$$

The velocity of the half of the atom going from A to C in the main coordinate system (metric (6.14)) is then

$$\left. \frac{dr}{d\tau} \right|_A = v_L + \frac{k_{\text{eff}}}{m} \left(1 + v_L^2 - \frac{\omega_a}{m} - \gamma \partial_r \phi(r_{L_1}) + \frac{3}{2} \gamma^2 \partial_r \phi(r_{L_1})^2 \right) + \frac{k_{\text{eff}}^2 v_L}{2m^2} - v_L \frac{\omega_{\text{eff}}}{m} \quad (6.26)$$

which is roughly $v_L + v_r$ with relativistic corrections. Intersecting the atom and light geodesics using the approximations described above gives point C. The expressions for the coordinates are very long and so are not shown. Of course, they are roughly just $r_C \approx r_{L_1} + (v_L + \frac{k_{\text{eff}}}{m}) T$ and $t_C \approx T$ as they would be in the non-relativistic case.

Computing the laser phase requires finding the times $t_A^{(2)}, t_B^{(2)}$, etc (see (6.11)) by dropping null geodesics from these intersection points to the second laser at r_{L_2} .

The entire calculation is done on a computer using a symbolic algebra package (Mathematica) so all Taylor series orders, initial conditions and such can be changed easily. The calculation was written for a general metric so the same code is used to calculate the phase shift for several different metrics including (6.13) and (6.14).

6.2.2 General Relativistic Effects and Interpretation

We present here the results of the calculation of the phase shift in an atom interferometer placed in a weak gravitational field such as the Earth's. The physical origins of the important terms in the phase shift will be discussed, focusing on the GR terms

and their interpretation.

To summarize the variables we are using, T is the interrogation time between pulses on the laser's clock, ω_i is the frequency of laser i , $k_{\text{eff}} \equiv \omega_1 + \omega_2$, $\omega_{\text{eff}} \equiv \omega_1 - \omega_2$, ω_a is the frequency of the atomic transition between states 1 and 2 of the atom (see Figure 2.3(a)), m is the rest mass of the atom in the lower ground state, v_L is the atom's launch velocity in the radial (vertical) direction, r_{L_i} is the position of laser i , $\phi(r)$ is the local gravitational potential (for a perfect Schwarzschild metric $\phi(r) = -\frac{GM}{r}$), $g = -\nabla\phi$, β and γ are PPN parameters in the metric, and $c = \hbar = 1$. We present the results for the final phase shift for metric (6.14) in Table 6.1. The phase shift has been expanded into a sum of terms and we have grouped terms that have the same scalings with experimental control parameters. Table 6.1 also displays the results of a non-relativistic (NR) calculation for the phase shift in a gravitational potential (see Section 7.2 for a description of the NR calculation). Note that we have kept the laser frequencies the same for all three pulses, though in a real experiment these would have to be tuned to keep the transitions on resonance in order to compensate for the Doppler shift due to the atom's acceleration under gravity³.

To understand the GR effects underlying some of these phases, recall that, roughly, the atom interferometer is sensitive to accelerations. The following discussion will be highly coordinate dependent and not rigorous, but its only purpose is to gain some intuition for the GR effects we find. Combining the geodesic equations (6.1) for the spatial \vec{x}^i ($i = 1, 2, 3$) and t , the coordinate acceleration of an atom in the frame of Eq. (6.14) is

$$\frac{d\vec{v}}{dt} = -\vec{\nabla}(\phi + (\beta + \gamma)\phi^2) + \gamma(3(\vec{v} \cdot \hat{r})^2 - 2\vec{v}^2)\vec{\nabla}\phi + 2\vec{v}(\vec{v} \cdot \vec{\nabla}\phi) \quad (6.27)$$

with $\vec{v} = \frac{d\vec{x}}{dt}$ for this equation only. The acceleration is approximately that from Newtonian gravity, $-\vec{\nabla}\phi$, but with leading order GR corrections. These corrections fall into two classes, both of which will interest us.

The $\nabla\phi^2$ terms are related to the non-linear nature of gravity, the fact that a

³Without such compensation, the transfer efficiency of the beamsplitter and mirror pulses would be prohibitively small.

	GR Phase Shift	Size (rad)	Interpretation	NR Phase Shift
1.	$-k_{\text{eff}}gT^2$	$3. \times 10^8$	Newtonian gravity	$-k_{\text{eff}}gT^2$
2.	$-k_{\text{eff}}(\partial_r g)v_LT^3$	$-2. \times 10^3$	1st gradient	$-k_{\text{eff}}(\partial_r g)v_LT^3$
3.	$-\frac{7}{12}k_{\text{eff}}(\partial_r g)gT^4$	$9. \times 10^2$		$-\frac{7}{12}k_{\text{eff}}(\partial_r g)gT^4$
4.	$-3k_{\text{eff}}g^2T^3$	$-4. \times 10^1$	finite speed of light and	
5.	$-3k_{\text{eff}}gv_LT^2$	$4. \times 10^1$	Doppler shift corrections	
6.	$-\frac{k_{\text{eff}}^2}{2m}(\partial_r g)T^3$	$-7. \times 10^{-1}$	1st gradient recoil	$-\frac{k_{\text{eff}}^2}{2m}(\partial_r g)T^3$
7.	$(\omega_{\text{eff}} - \omega_a)gT^2$	$-4. \times 10^{-1}$	detuning	
8.	$(2 - 2\beta - \gamma)k_{\text{eff}}g\phi T^2$	$-2. \times 10^{-1}$	GR (non-linearity)	
9.	$-\frac{3k_{\text{eff}}^2}{2m}gT^2$	$2. \times 10^{-2}$		
10.	$-\frac{7}{12}k_{\text{eff}}v_L^2(\partial_r^2 g)T^4$	$8. \times 10^{-3}$	2nd gradient	$-\frac{7}{12}k_{\text{eff}}v_L^2(\partial_r^2 g)T^4$
11.	$-\frac{35}{4}k_{\text{eff}}(\partial_r g)gv_LT^4$	$6. \times 10^{-4}$		
12.	$-4k_{\text{eff}}(\partial_r g)v_L^2T^3$	$-3. \times 10^{-4}$		
13.	$2\omega_a g^2T^3$	$2. \times 10^{-4}$		
14.	$2\omega_a gv_LT^2$	$-2. \times 10^{-4}$		
15.	$-\frac{7k_{\text{eff}}^2}{12m}v_L(\partial_r^2 g)T^4$	$7. \times 10^{-6}$	2nd gradient recoil	$-\frac{7k_{\text{eff}}^2}{12m}v_L(\partial_r^2 g)T^4$
16.	$-12k_{\text{eff}}^2v_LT^3$	$-7. \times 10^{-6}$		
17.	$-7k_{\text{eff}}g^3T^4$	$4. \times 10^{-6}$		
18.	$-5k_{\text{eff}}gv_L^2T^2$	$3. \times 10^{-6}$	GR (\vec{v} -dependent force)	
19.	$(2 - 2\beta - \gamma)k_{\text{eff}}\partial_r(g\phi)v_LT^3$	$2. \times 10^{-6}$	GR 1st gradient	
20.	$\frac{7}{12}(4 - 4\beta - 3\gamma)k_{\text{eff}}\phi(\partial_r g)gT^4$	$-2. \times 10^{-6}$	GR	
21.	$(\omega_{\text{eff}} - \omega_a)(\partial_r g)v_LT^3$	$2. \times 10^{-6}$		
22.	$\frac{7}{12}(\omega_{\text{eff}} - \omega_a)(\partial_r g)gT^4$	$-1. \times 10^{-6}$		
23.	$-\frac{7}{12}(2 - 2\beta - \gamma)k_{\text{eff}}g^3T^4$	$-3. \times 10^{-7}$	GR	
24.	$-\frac{7k_{\text{eff}}^2}{2m}(\partial_r g)v_LT^3$	$-2. \times 10^{-7}$		
25.	$-\frac{27k_{\text{eff}}^2}{8m}(\partial_r g)gT^4$	$2. \times 10^{-7}$		
26.	$\frac{k_{\text{eff}}\omega_a}{m}gT^2$	$-1. \times 10^{-7}$		
27.	$6(2 - 2\beta - \gamma)k_{\text{eff}}\phi g^2T^3$	$5. \times 10^{-8}$	GR	
28.	$3(\omega_{\text{eff}} - \omega_a)g^2T^3$	$4. \times 10^{-8}$		
29.	$3(\omega_{\text{eff}} - \omega_a)gv_LT^2$	$-4. \times 10^{-8}$		
30.	$6(1 - \beta)k_{\text{eff}}\phi gv_LT^2$	$3. \times 10^{-8}$	GR	

Table 6.1: A list of all the terms above a certain size in the phase shift from the full GR calculation for metric (6.14), along with their numerical size in radians and an interpretation. The NR phase shift column shows the results of a completely non-relativistic phase shift calculation for comparison. The sizes of the terms assume the initial design, sensitive to accelerations $\sim 10^{-15}g$, which has $L = 9$ m, $T = 1.3$ s, $v_L = 13 \frac{\text{m}}{\text{s}}$, $k_{\text{eff}} = 2 \frac{2\pi}{780 \text{ nm}}$, $\omega_a = 6.8$ GHz, and $m = 81$ GeV (for ^{87}Rb). All detuning terms assume $\omega_{\text{eff}} - \omega_a = 1$ kHz. Note that there is some ambiguity in how some of the terms are grouped since by definition $g = -\partial_r\phi$.

gravitational field seems to source itself in general relativity. This could also be called the non-Abelian nature of gravity since gravitational energy gravitates through a three-graviton vertex. To see that this is the origin of the $\nabla\phi^2$ terms, note that, because of these terms, the divergence of the gravitational field given in Eq. (6.27) is nonzero (here by gravitational field we mean $\vec{g} \equiv \frac{d\vec{v}}{dt}$ from Eq. (6.27)). Just as for an electric field, a nonzero divergence of the gravitational field implies a local source density (in general relativity this means a local energy density) that is proportional to that divergence. So Eq. (6.27) implies that there is a local energy density in free space proportional to $\nabla \cdot \vec{g} \propto \nabla \cdot \nabla\phi^2 = 2(\nabla\phi)^2$. But note that to leading order $\nabla\phi \approx \vec{g}$ so that $\nabla \cdot \vec{g} \propto \vec{g}^2$. In other words, the local energy density is proportional to the field squared, exactly as expected from the electric field analogy. This energy is then the source of the $\nabla\phi^2$ terms. The non-linearity of gravity is parametrized in the standard way by the PPN parameter β .

The other terms in Eq. (6.27) proportional to $\vec{v}^2\nabla\phi$ are velocity dependent forces. These terms are related to the gravitation of the atom's kinetic energy (or the kinetic energy of the source mass in the frame where the atom is stationary and the source is moving), since all energy, not just mass, gravitates in general relativity.

The non-linear GR corrections in Eq. (6.27) are smaller than Newtonian gravity by a factor of $\phi \sim 10^{-9}$, while the velocity dependent force terms are smaller by $v^2 \sim 10^{-15}$ for the atom velocities we are considering. We will see that the non-linear terms can only be measured through a gradient of the force produced and so are reduced by an additional factor of $\frac{10m}{R_{\text{Earth}}} \approx 10^{-6}$ for a 10m long experiment. Both effects are then $\sim 10^{-15}g$.

These effects can be seen in the total phase shift in the interferometer. Table 6.1 presents the answer for the total phase shift as found by the relativistic calculation outlined above. It lists all the terms in the total phase shift large enough to be measured by the initial apparatus. Effectively, the local gravitational acceleration is expressed as a Taylor series in the height above the Earth's surface. The first phase shift in Table 6.1 represents the effect of the leading order (constant) piece of the local acceleration while the 2nd and 10th terms are the next gradients in the Taylor series. Notice that even the second gradient of the gravitational field is relevant for

this interferometer. The terms in this list that have been measured agree with the results of previous experiments. The largest two phase shifts due to the first two terms in the Taylor expansion of the local g field were known and measured several times (e.g. [11, 15]). The 4th and 5th terms arise from the second order Doppler shift of the laser's frequency as seen by the moving atom. These Doppler shift and finite speed of light corrections (terms 4 and 5) were known and measured to cancel each other in a ‘symmetric’ interferometer [74]. The 7th term is proportional to the two-photon detuning between the difference in the two lasers’ frequencies, ω_{eff} , and the resonant frequency of the atomic transition, ω_a . In any practical experiment this detuning is kept quite small and this term will be negligible. The terms proportional to ω_a and ω_{eff} almost cancel since the lasers’ frequencies are usually chosen to be on resonance with the atomic transition and so could never have been measured given the precision of previous interferometers. These terms were not previously known because their calculation requires a fully relativistic calculation. The recoil shift $\frac{k_{\text{eff}}^2}{m} T^3 \partial_r g$ was known and measured [75, 76].

The 8th, 18th through 20th, 23rd, 27th, and 30th terms arise only from GR and are not present in the results of our Newtonian calculation. The 8th and 19th terms arise in part from the non-linear nature of gravity. This is clear since they look like the analogue of kgT^2 and the 1st gradient terms but with g replaced by the part of the acceleration coming from the non-linearity of gravity, $g\phi$ in Eq. (6.27). Similarly the 18th term arises in part from the velocity dependent forces in Eq. (6.27) since it appears to be an acceleration $\sim gv_L^2$. Note that of course the acceleration from these velocity dependent forces is actually proportional to the integrated effects along the entire trajectory of the atom. However, this is obscured by the expansion we are taking, and so we just see the largest term, $\propto v_L^2$, with terms proportional to the other velocities v_r , gT and so on, farther down the list. In fact, for every term $\propto v_L$, we expect and see a term with v_L replaced by gT also on the list, since the velocity changes over the course of the interferometer by roughly this amount.

We now address the fact that we have left the phase shift in Table 6.1 in terms of the unphysical (coordinate-dependent) launch velocity. This is the only coordinate dependent variable in Table 6.1; all others (k_{eff} , T , etc.) have coordinate invariant

definitions. Ultimately, in any real experiment the experimenter determines how to measure the launch velocity, and this gives the physical, coordinate-invariant definition. On this point, different experiments will surely vary, so here we assume a simple prescription but leave Table 6.1 in the general form in terms of v_L , which should allow any prescription to be applied. We assume that the atom is launched by the lasers using n_L photon kicks (Raman or Bragg transitions). The experimental definition of the physical launch velocity will then be $v_p = n_L \frac{k_{\text{eff}}}{m}$. Note that n_L , k_{eff} , and m all have physical, coordinate-independent definitions. Repeating the normal atom-light interaction calculation (Eq. (6.5) and ensuing discussion) n_L times then gives the relation

$$v_L \approx v_p \left(1 - \gamma\phi - \frac{\omega_a}{m} (1 - \gamma\phi) - \frac{n_L - 1}{2} \frac{\omega_{\text{eff}}}{m} (1 - \gamma\phi) \right) \quad (6.28)$$

with higher order terms dropped. It is not surprising that there are higher order GR corrections when the coordinate launch velocity is written in terms of a physically measurable parameter. Here we are only interested in this if it changes the GR effects we seek to measure, for example by changing the dependence on the PPN parameters. It is clear that substituting Eq. (6.28) into the phase shift in Table 6.1 will not affect the two GR terms we are most interested in, 8 and 18. It can affect other GR terms at the level of 10^{-6} rad and below, but it cannot remove totally the dependence on the PPN parameters of GR terms 8 and 18, and so it does not qualitatively change their interpretation.

The origin of some of the largest terms in the phase shift list highlights important differences between a relativistic calculation and a non-relativistic one. From Table 6.2 we see that frequently the contributions to a given term in the phase shift lift from the propagation and separation phases cancel, and so the term can be considered to come from laser phase. There is even a term in the propagation and separation phases that is larger than kgT^2 which cancels. Note that this term is $k_{\text{eff}}cT^3(\partial_r g)$ if we do not take $c = 1$. Many of the terms in propagation and separation phase can be considered to arise from the fact that, in a relativistic calculation, the endpoints of the interferometer (points D and E in Fig. 6.1) are not simultaneous. This has a large effect because the phase of the atom evolves at a rate proportional to its mass

	Parameter Dependence	Total Phase Shift Coefficient	Propagation Phase Coefficient	Separation Phase Coefficient	Laser Phase Coefficient	Size (rad)
1.	$k_{\text{eff}}T^3(\partial_r g)$	0	1	-1	0	4×10^{10}
2.	$k_{\text{eff}}gT^2$	-1	-1	1	-1	3×10^8
3.	$\omega_{\text{eff}}gT^2$	1	2	-2	1	3×10^3
4.	$\omega_a gT^2$	-1	-1	0	0	3×10^3
5.	$k_{\text{eff}}(\partial_r g)T^3v_L$	-1	2	-2	-1	2×10^3
6.	$k_{\text{eff}}(\partial_r g)\phi T^3$	0	$2\gamma + 2\beta - 2$	$-2\gamma - 2\beta + 2$	0	3×10^1
7.	$k_{\text{eff}}gT^2v_L$	-3	-5	5	-3	1×10^1
8.	$k_{\text{eff}}g\phi T^2$	$2 - 2\beta - \gamma$	$2 - 2\beta - \gamma$	$-2 + 2\beta + \gamma$	$2 - 2\beta - \gamma$	2×10^{-1}
9.	$k_{\text{eff}}g^2T^3v_L$	-12	-17	17	-12	7×10^{-6}
10.	$k_{\text{eff}}\partial_r(g\phi)T^3v_L$	$2 - 2\beta - \gamma$	$-4 + 4\beta + 2\gamma$	$4 - 4\beta - 2\gamma$	$2 - 2\beta - \gamma$	2×10^{-6}
11.	$k_{\text{eff}}gT^2v_L^2$	-5	-9	9	-5	5×10^{-7}

Table 6.2: A breakdown of some of the terms in the phase shift, Table 6.1, list by origin. The sizes are given for the coefficient of the term in the total phase shift. Note that there is some ambiguity in dividing terms 9 and 10 since by definition $g = -\partial_r\phi$.

m , as follows from the separation phase formula (6.9). In other words, the Compton wavelength measures separation in time just as the de Broglie wavelength does in space.

It is interesting to consider an atom interferometer with only a single laser driving the atomic transitions directly between two levels, instead of the normal two-photon transition through a virtual intermediate level. In this case, there is no passive laser and the laser phase is zero, as mentioned in Section 6.1.2. This means that the $k_{\text{eff}}gT^2$ term is removed as are most of the k_{eff} terms. However we must now have the two atomic levels spaced by an energy which is roughly the frequency of a laser, so $\omega_a \sim k$, instead of ω_{eff} . After doing such a single laser calculation we find that the largest term in the phase shift is $\omega_a gT^2$, which is roughly the same size as kgT^2 . This phase shift now comes from propagation phase instead of laser phase, as would be guessed from Table 6.2. This term arises because the rest mass of the atom is different in the two atomic states. This means that the dominant phase shift does not depend on the laser frequency and is instead set by the intrinsic structure of the atom. In the normal non-relativistic calculation there is only the $k_{\text{eff}}gT^2$ term which comes from laser phase (not from propagation phase), and there is no $\omega_a gT^2$ term at all. So the non-relativistic single laser calculation gets the origin of the major part of the phase

shift wrong, and it gives an answer which is off by the amount the laser frequency ω is detuned from resonance ω_a .

The term $-5k_{\text{eff}}gT^2v_L^2$ (term 18) receives contributions from the velocity-dependent forces in Eq. (6.27), but its coefficient is independent of γ . There are two canceling contributions to this term coming from the γ terms in the force law for the atom and the photon. Note that the γ terms in the equation of motion for the light are not suppressed by any small velocity factors (since $c = 1$), so they are just as large as the ‘normal’ Newtonian gravity term (this is the origin of the famous factor of 2 in the equation for the bending of light by the sun). This phase shift term thus measures both the effect of gravity on light and the velocity-dependent force on the atom. If we put a different parameter, δ_{light} , in front of the ϕ in the component g_{00} of the metric governing the motion of the light and redo the entire calculation, this term becomes $(4 + \delta_{\text{light}} + \gamma_{\text{light}} - \gamma_{\text{atom}})k_{\text{eff}}gT^2v_L^2$, where the γ ’s are the PPN parameters in the metrics for the light and the atom. This term then tests a matter-light principle of equivalence, namely that they both feel the same metric. A new force may well couple to light and matter in a different manner than gravity and so may be testable in this way.

6.3 Measurement Strategies

In this section we consider several ideas for measuring GR or beyond GR effects using atom interferometry. Possible measurement strategies are discussed for testing the Principle of Equivalence (PoE) and measuring the effects of the velocity dependent forces arising from GR, the non-linear nature of gravity, and the bending of light in a gravitational field. We have discussed some of these ideas in a previous paper [34] but here we give a few more thoughts. Our main motivation is to describe some phenomenological differences between the GR effects we have calculated and classical, non-relativistic effects in order to show that these GR effects are not coordinate artifacts, and are possibly distinguishable from Newtonian gravity and other backgrounds. We do not claim to have proven that every conceivable background is under control. Instead we only wish to argue that it may be possible to test GR in the lab

using this technology, and so it is well worth trying to design experiments to do so.

In general we consider a ~ 10 m long interferometer with $T \sim 1$ s and $\sim 10^6$ atoms cooled and launched per shot, resulting in a final phase sensitivity of $\sim 10^{-6}$ rad after about 10^6 shots. This implies sensitivity above atom shot noise of $10^{-15}g$ where g is the acceleration due to gravity on Earth. As we have seen, this is enough to start measuring GR effects in the lab. Of course, there are many possible improvements to this technology, and the potentially achievable sensitivities (at least above shot noise) were discussed in [34].

6.3.1 Velocity Dependent Forces

In order to measure the GR effects of the ‘velocity dependent forces’ and the gravitational effect on the laser light, we must pick out the phase shift term with the v_L^2 scaling. The basic idea is that it is very difficult for classical gravity to mimic the effect of a true velocity dependent force. Again we will consider a differential measurement between simultaneous atom interferometers since this aids greatly in the control of many backgrounds. Here we consider two atom interferometers with differing launch velocities in order to select the velocity dependent term we are looking for. This will naturally cancel many phase shifts, including the leading order one from gravity, $k_{\text{eff}}gT^2$. Of course, there are still several possible background terms that are larger than the signal and scale with launch velocity. These include terms coming from the Earth’s gravity gradient, $k_{\text{eff}}(\partial_r g)T^3v_L$, the effect of the doppler shift of the laser as seen by the moving atom, $k_{\text{eff}}gT^2v_L$, and the effect of the Earth’s rotation, $k_{\text{eff}}v_L\Omega^2T^3$, where Ω is the component of the Earth’s rotation rate perpendicular to the launch velocity [47]. Magnetic fields do not induce velocity dependent phase shifts when the internal atomic state remains unchanged, as in a Bragg beamsplitter. All of these background terms, although much larger than our signal, scale differently with v_L and T than our signal. There are no terms which scale as $v_L^2T^2$; this is a unique sign of GR. Varying these around the typical values ($v_L = 13\frac{\text{m}}{\text{s}}$ and $T = 1.3$ s) then allows the GR term to be picked out from the backgrounds with a sensitivity limited only by the atom shot noise. It is crucial for this fit that v_L can be known

experimentally very precisely (better than the ratio of the background to the signal). This is possible since the launch velocity is precisely linked to laser frequencies (see the discussion of physical velocity and Eq. (6.28)) which can be known extremely well.

Additionally, in case backgrounds do become a problem, it is possible to reduce the measured size of the background terms even before this fit. Because the GR term scales as $(v_L T)^2$, there is no loss in the signal by going to the regime where the launch velocity is large. In this regime, the atom's velocity is roughly constant over the length L of the interferometer and $L = v_L T$. If v_L and T are then always scaled inversely so that L is fixed, then the signal does not change but all the background terms do. Further, by taking v_L large, all the background terms are suppressed by at least one power of v_L because they all have more powers of T than of v_L . For example, the gravity gradient term becomes $k_{\text{eff}}(\partial_r g) \frac{L^3}{v_L^2}$. Thus, the sizes of the phase shifts from these backgrounds can be directly reduced even before data analysis.

6.3.2 Non-Linearity of Gravity

To measure the terms which arise from the non-linearity of gravity, it may help to run three simultaneous atomic gradiometers along three mutually orthogonal axes in a ‘divergence configuration’. Such a configuration effectively measures the divergence of the local gravitational field, which must be zero in Newtonian gravity outside the source mass. This should then allow the non-linear GR effect, $k_{\text{eff}}g\phi T^2$, to be picked out. In particular, the atoms can be launched along a single, large (e.g. 10 m) vertical axis. Then three perpendicular atom interferometers can be run along this same axis using three perpendicular sets of lasers. Thus the atoms can be split vertically or in either horizontal direction to make the three perpendicular atom interferometers. Yet all three interferometers are in essentially the same position, separated only by the much smaller $v_r T \sim 1$ cm.

One question which arises is the extent to which the three laser axes can be made mutually orthogonal, since they must be perpendicular to one part in 10^9 (since on the Earth $\phi \sim 10^{-9}$) in order to reduce the Earth's gravity gradient below the

GR signal. Methods for measuring angles with nanoradian precision have already been demonstrated, albeit for angles much smaller than 90 degrees [77]. It may also be possible to geometrically construct laser axes which are perpendicular to very high accuracy by using the ability to accurately measure distances with a laser interferometer.

It is also possible to ameliorate the requirement on the perpendicularity of the laser axes by reducing the local gravity gradient with an appropriately constructed local mass distribution. We will show that it is possible to reduce the gravity gradient along all three perpendicular axes by $\mathcal{O}(1)$ of its natural size on the Earth. With such a construction, the three gravity gradients can then be measured by the atom interferometer itself. It should then be possible to make minor modifications to the mass distribution to cancel the gravity gradients with increasing precision, without an exact knowledge of the angles of the atom interferometers. Every order of magnitude reduction in the size of the local gravity gradient reduces the requirement on perpendicularity of the laser axes by an order of magnitude. Since the atom interferometer can measure gravity gradients very precisely, it may be possible to align the lasers to sufficient accuracy without a complicated alignment mechanism.

Now we must show that the Earth's gravity gradients in all three directions (i.e. $\partial_x \vec{g}_x$, $\partial_y \vec{g}_y$, and $\partial_z \vec{g}_z$) can be cancelled to $\mathcal{O}(1)$. If the z -axis runs perpendicularly to the local surface of the Earth at the point in question, then $\vec{g}_z \approx -\frac{GM_{\text{Earth}}}{R_{\text{Earth}}^2}$ ⁴ is negative and the gradient $\partial_z \vec{g}_z \approx -2\frac{\vec{g}_z}{R_{\text{Earth}}}$ is positive. Adding more mass on the z -axis either completely above or completely below the atom interferometer will only add a positive quantity to $\partial_z \vec{g}_z$, thus increasing the gravity gradient. Therefore we must add mass around the atom interferometer. As a proof of principle, take a sphere of mass centered on the point in question with a cylindrical hole along the z -axis (the atom interferometer apparatus would be placed in this hole). Assuming the radius of the cylinder is small compared with the radius of the sphere, the Newtonian gravitational field due to the sphere inside itself has a derivative with an opposite sign compared to the Earth's gradient: $\partial_z \vec{g}_z = -\frac{4}{3}\pi G\rho_{\text{sphere}}$. Since in vacuum the divergence is zero in Newtonian gravity ($\partial_x \vec{g}_x + \partial_y \vec{g}_y + \partial_z \vec{g}_z = 0$) and there is a

⁴Of course there are small corrections due to the fact that the Earth is not perfectly spherical.

rotational symmetry about the z -axis, the other two components of the sphere's gravity gradient are $\partial_x \vec{g}_x = \partial_y \vec{g}_y = -\frac{1}{2} \partial_z \vec{g}_z$. With an appropriate choice of ρ_{sphere} then, the Earth's gravity gradient can be cancelled off. Notice that the sphere cancelled the z -component of the Earth's gradient while the cylindrical hole cancelled the x - and y -components, since in the infinite limit the cylinder only has x - and y -components of acceleration.

6.3.3 General Backgrounds

One possible background to any measurement made with an atom interferometer arises from the interaction of the atoms with ambient electromagnetic fields. The electric fields present in any realistic setup are too small to give detectable phase shifts as they are easily screened. Surface effects such as the Casimir interaction are negligible as the atoms are kept far from all surfaces. Only ambient magnetic fields can give large enough phase shifts to be potential backgrounds. An atom responds strongly to a background magnetic field, so we usually consider a magnetically shielded interferometer. Ambient magnetic fields can be shielded down to the nT level (see for example [78]) which leads to appropriately small phase shifts. The atoms are prepared in a magnetically insensitive, $m = 0$, state and so the energy shifts that arise are second order in the magnetic field, $\Delta E = \frac{1}{2} \alpha B^2$ where α is the second order Zeeman coefficient of the state. Since the internal levels of the atom can have different values of α , magnetic phase shifts are generally smaller when the internal state is fixed, as is the case in an interferometer that uses Bragg transitions. Systematic phase shifts can then only result from spatial variations in the field:

$$\Delta\phi \approx -k_{\text{eff}} \frac{\alpha}{m} B_0 \frac{\partial \delta B}{\partial z} T^2$$

where $B = B_0 + \delta B$, $B_0 \sim 100$ nT is the constant bias magnetic field and δB is a small field perturbation. Variations of $\delta B \sim 1$ nT over the length of the interferometer give negligible phase shifts for a ^{87}Rb apparatus. The above formula generally holds for field perturbations that vary on length scales that are long compared to the interferometer arm splitting. In the opposite limit, the interferometer averages over

perturbations with wavelengths that are small compared to the overall interferometer length. This spatial averaging behavior also occurs for short wavelength gravity perturbations, as we describe in more detail below.

Another potential background in the interferometer arises from atom-atom collisions within the atom cloud. For ^{87}Rb , the frequency shift of the atomic state $|F = 2, m_F = 0\rangle$ due to atom-atom collisions is

$$\delta\nu \approx (-0.9 \text{ mHz}) \left(\frac{n}{10^9 \text{ cm}^{-3}} \right) \sqrt{\frac{\tau}{1 \mu\text{K}}}$$

for a cloud of number density n and temperature τ [79, 80]. Unlike in atomic clocks, phase errors due to this effect in a $\frac{\pi}{2}-\pi-\frac{\pi}{2}$ pulse sequence atom interferometer implemented using Bragg atom optics are the result of unequal densities between the two arms. Nominally, the upper and lower arms of the interferometer have the same atom number density, but an imperfect initial beamsplitter can cause an asymmetry between the arms, resulting in a phase shift

$$\delta\phi_{\text{collision}} = 4\pi\delta\nu T \approx (1.1 \times 10^{-2} \text{ rad}) \left(\frac{n}{10^9 \text{ cm}^{-3}} \right) \sqrt{\frac{\tau}{1 \mu\text{K}}} \left(\frac{T}{1 \text{ s}} \right) \left(\frac{\Delta n}{n} \right)$$

for a density difference Δn . This represents an upper bound on the atom-atom phase shift, since in reality the cloud density decreases in time during the experiment due to ballistic expansion⁵. Making the conservative assumption that the density difference can be controlled at the level of $\frac{\Delta n}{n} \sim 10^{-2}$ implies a phase error of $\sim 10^{-4}$ rad. However, this systematic offset is not a concern for many of the experiments we consider since it is expected to cancel as a result of our differential measurement strategies. This cancellation relies on the condition that the density does not depend on any of the other control parameters in the experiment, an assumption that must be verified experimentally⁶.

An additional tool that may be useful for reducing backgrounds and picking out

⁵This result does not apply to an interferometer that uses Raman atom optics, since in that case the time evolution of the density leads to the main effect.

⁶This cancellation does not occur in the case of the Equivalence Principle measurement, since the two isotopes have different atom-atom interaction strengths.

the signal terms is the possibility of running the atom interferometer with different pulse sequences. While the $\frac{\pi}{2}$ - π - $\frac{\pi}{2}$ sequence is an accelerometer, more complicated sequences can be used which suppress accelerations and leave the gravity gradients, or vice versa. In general, either T^2 or T^3 terms, or both, can be removed by a suitable choice of pulse sequence [48, 81]. This can remove most of the relevant backgrounds to the velocity-dependent force measurement since they scale with higher powers of T . These different pulse sequences improve the ability to pick out a term that scales in a particular way with the control parameters.

Finally, it is possible that small gravitational ‘anomalies’ due to local masses may be a background. In fact, only the small wavelength variations in the local g field can be a relevant background for these experiments. Perturbations to local g at wavelengths larger than the rough size of the experiment (e.g. 10 m) are well described by the Taylor series expansion that we have assumed for the Earth’s field. Since these perturbations are naturally small compared to the Earth’s field, the differential measurement strategies discussed above for the Principle of Equivalence, velocity dependent force, and non-linearity of gravity measurements will remove these long wavelength perturbations in exactly the same way as they removed the Earth’s field.

Short wavelength perturbations in the local gravitational field can be relevant. Luckily, the atom interferometer naturally averages over these perturbations because of its spatial length. In the limit that the gravity inhomogeneities are small, the atom interferometer response may be linearized (See Appendix B). We write the total phase shift due to gravity anomalies along the vertical (z) direction summed over all wavelengths λ as

$$\Delta\phi_g = \int T_{gz}(\lambda)\tilde{\delta}g_z(\lambda)d\lambda \quad (6.29)$$

where $T_{gz}(\lambda)$ is the interferometer’s gravity perturbation response function and the gravitational field at a position z in the interferometer is

$$\delta g_z(z) = \int \tilde{\delta}g_z(\lambda)e^{\frac{i2\pi z}{\lambda}}d\lambda, \quad (6.30)$$

where $\tilde{\delta}g_z(\lambda)$ is the Fourier component of a gravity perturbation with wavelength λ . Figure 6.2 shows the response of an atom interferometer in the example 10 m

configuration to perturbations in the local g field of wavelength λ . The top curve is for the atom interferometer run in the ‘symmetric’ configuration where the atoms are launched from the bottom of the interferometer region with exactly the right velocity to stop at the top, $v_L = gT$ and the first and last beamsplitter pulses happen when the atom is at the bottom on its way up and on its way down, respectively. The next lower curve assumes the atom is dropped from rest at the top. The next two curves assume the atom is launched downwards from the top with velocities $1\frac{\text{m}}{\text{s}}$ and $10\frac{\text{m}}{\text{s}}$, respectively. As expected, the atom interferometer always averages down the perturbations on scales below its size, here $10m$. If the atom is launched so that its velocity is never zero then the suppression is much bigger at shorter lengths. For the lower two curves, the phase falls off as λ^2 , as compared with λ for the case in which the atom comes to rest during the interferometer. Roughly, the more uniform the atoms’ velocity, the larger the reduction that comes from averaging over the small scale gravity perturbations. This is a very useful tool for reducing backgrounds from local masses. It also scales favorably with the length of the interferometer, since a longer interferometer suppresses larger distance scales, leading to an even greater suppression at short distances.

The differential measurement strategies suppress the longer wavelength contributions. In fact, at very long wavelengths there is no difference between what we have called a ‘perturbation’ and the previously included part of Earth’s gravitational field. The differential measurement strategies were designed to allow us to control systematics arising from the Earth’s gravitational field. For the proposed Principle of Equivalence measurement, atom clouds of the two isotopes are separated by less than $1\mu\text{m}$. This provides a large suppression to longer wavelength gravitational perturbations. Similarly, in the divergence strategy measurement (see Section 6.3.2) the three atom interferometers are separated by ~ 1 cm. For wavelengths longer than this scale the divergence measurement looks like a true divergence (instead of a finite difference approximation to the derivative) and so the longer wavelength gravitational modes are suppressed. As discussed above, the velocity dependent force measurement benefits greatly from the ability to launch the atoms with a large initial velocity to suppress all Newtonian gravitational effects without suppressing the GR signal. This

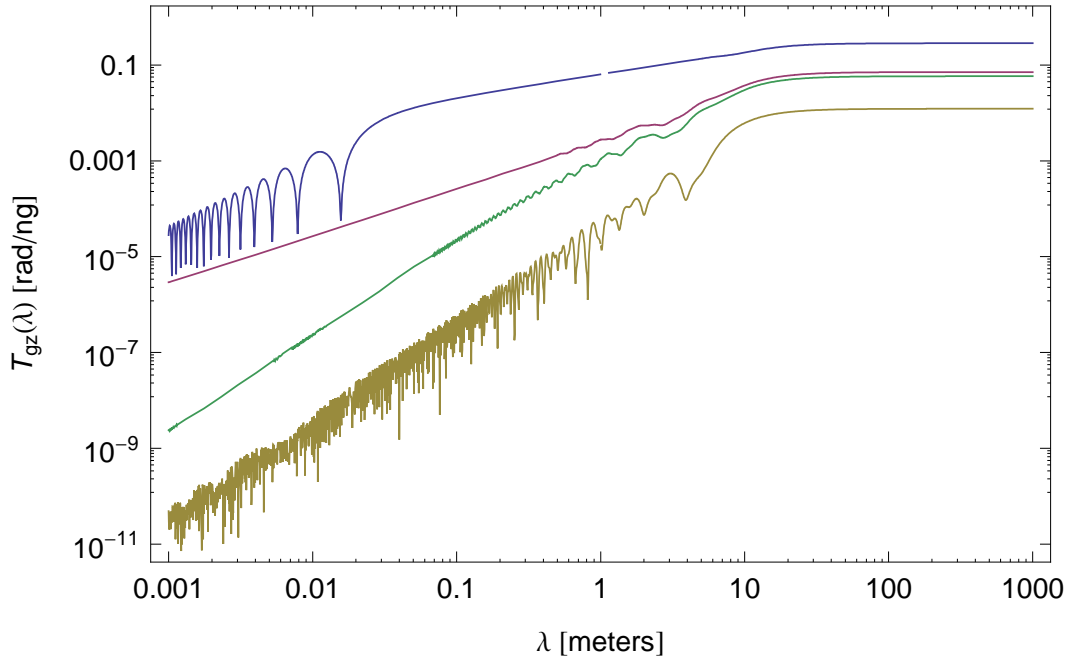


Figure 6.2: The response function, T_{gz} , as defined in Eq. (6.29). It gives the phase shift response of the atom interferometer to a Fourier component of the local gravitational field with wavelength λ and amplitude $10^{-9}g_{\text{Earth}}$. All curves assume the example 10 m atom interferometer. The top curve assumes it is run in a ‘symmetric’ configuration (see text), the next lower curve assumes the atoms are dropped from rest at the top of the device and the following two curves assume a downward launch velocity of $1 \frac{\text{m}}{\text{s}}$ and $10 \frac{\text{m}}{\text{s}}$ respectively.

suppression of all wavelengths can be seen by comparing the lowest two curves in Figure 6.2. The lowest curve has a larger launch velocity and is therefore suppressed at all wavelengths as expected.

If we know the magnitude of the perturbation in the local gravitational field, we can compute the phase shift induced in an interferometer from Eq. (6.29). This implies some constraints on the mass and distance of nearby objects that must be taken into account when designing an actual experiment. Fig. 4.2 displays $\tilde{\delta}g_z(\lambda)$ for several example sources. Each source is taken to be some perpendicular distance from the center of the atom interferometer. We have always plotted the magnitude of the Fourier transforms in Figures 6.2 and 4.2 (i.e. we have taken the sum in quadrature of the sine and cosine components). An object that is farther away than its size looks like a point mass. Its gravitational field has a Fourier transform, $\tilde{\delta}g_z(\lambda)$, that is sharply peaked around its distance from the interferometer. An object that is large compared to its distance (represented by the rod in Figure 4.2) produces a $\tilde{\delta}g_z(\lambda)$ that is sharply peaked around the object's size. This analysis allows us to predict the expected size of local gravitational perturbations as a function of wavelength.

The differential response curve allows us to compute systematic errors arising from the specific gravity environment of our interferometer. Quantitative estimates of these effects requires knowledge of the local $\delta g_z(z)$, which may be obtained through a combination of modelling and characterization. The atom interferometer itself can be used as a precision gravimeter for mapping $\delta g_z(z)$ in situ. By varying the interrogation time T , a local gravity measurement can be made over a small spatial region. Many such measurements in different positions can be made by varying the launch velocity and time of the initial beamsplitter, resulting in a measurement of $\delta g_z(z)$.

The interferometer's response to the short wavelength modes can be quite suppressed as in Fig. 6.2. Additionally, the amplitudes of the gravitational perturbations can be kept small as in Fig. 4.2. Further, depending, to some extent, on the nature of the gravitational source, the phase shifts due to these local gravitational anomalies are unlikely to vary at order one with the control parameters used in the experiment, or to vary at order one from shot to shot. This leads to a further suppression, since a truly constant phase shift would not be a background to many of these proposed

experiments. Thus, it seems possible to reduce the background phase shifts due to local gravitational effects below the required 10^{-6} rad level.

There are, of course, many details we have not addressed here that are important for a real experiment. Here we have given our ideas for ways of distinguishing the main GR effects of the Earth's gravitational field from the relevant backgrounds. These effects are found to be possibly phenomenologically distinguishable from Newtonian gravity and other backgrounds, and are thus true GR (or beyond GR) effects, indescribable in a Newtonian model. We have tried to motivate why these or similar experiments may be possible, but we have not proven that they will work in the full detail necessary for a real experiment. We just wish to motivate future work.

6.4 Other GR Effects?

6.4.1 Hubble Expansion (Vacuum Energy)

The cosmological expansion of the universe can be described by the metric

$$ds^2 = dt^2 - e^{2Ht} d\vec{x}^2 \quad (6.31)$$

where H is the Hubble constant. Using the geodesic equation (6.1), a particle moving in this metric has an acceleration

$$\frac{d^2\vec{x}}{d\tau^2} = 2H \frac{d\vec{x}}{d\tau} \frac{dt}{d\tau} \approx 2Hv. \quad (6.32)$$

For laboratory atomic velocities this would be $\sim 10^{-18}g$, large enough to be very interesting compared to the initial sensitivity of the interferometer under construction $\sim 10^{-15}g$. We would like to consider whether it is then possible to measure the expansion rate of the universe in an atom interferometer. Since the local neighborhood has collapsed gravitationally, the normal cosmological expansion of the metric is presumably not occurring inside the solar system. However, a true cosmological constant would necessarily be present everywhere and must therefore affect the metric locally. We will loosely model the local effects of the vacuum energy using metric (6.31) (to

include the effects of local mass a McVittie metric [82] should really be used), but it must be remembered that H will then presumably refer only to the contribution of the vacuum energy.

Unfortunately, this is just an artificial, coordinate acceleration, not the physical acceleration that would be measured by any experiment. A calculation of the acceleration that would be measured in an actual experiment, either an observer using radar-ranging to determine the atom's position or using an atom interferometer, shows that the physically observable accelerations are of $\mathcal{O}(H^2)$.

Another way to see an effect linear in H is to consider two observers on geodesics of (6.31) which are at constant \vec{x} positions. The spatial distance (defined by integrating only the spatial terms in the metric at a fixed time) between these observers is $e^{Ht}\Delta\vec{x}$ and so it would appear that there is a relative velocity of $\mathcal{O}(H\Delta x)$. In fact a radar-ranging calculation of the distance or velocity shows essentially the same thing. This is not a surprise, since this is in fact just the normal observation of Hubble's law for the expansion of the universe. Such observers represent galaxies, which are measured to recede from each other at velocities of order H . However we cannot create a similar laboratory version of this experiment in order to measure the Hubble constant (really vacuum energy) without starting the atom with an initial velocity of $\mathcal{O}(H)$, which defeats the purpose. The galaxies naturally have such velocities, and so tend to mark the cosmological expansion, due to the action of the $\mathcal{O}(H^2)$ acceleration acting for the age of the universe H^{-1} .

More generally, it seems there cannot be effects linear in H , at least in ‘normal’ variables such as position, velocity, or acceleration, in any experiment we can set up. Without access to observers in some special reference frame such as the galaxies provide, any experiment will be free-falling in the cosmological expansion. By the Principle of Equivalence, such an experiment will then see a metric that is locally flat with corrections proportional to the Riemann curvature. But this is $R \propto H^2$ (all components are either 0, $-H^2$, or $\pm H^2 e^{2Ht}$). This is very similar to transforming Eq. (6.31) to the static patch

$$ds^2 = (1 - H^2 r^2) dt^2 - \frac{1}{1 - H^2 r^2} dr^2 - r^2 d\Omega^2. \quad (6.33)$$

In these coordinates it is clear that all accelerations (all Christoffel symbols), the Reimann curvature and other similar quantities will be $\mathcal{O}(H^2)$. Of course, the argument that in a LLF the answer will just be proportional to the curvature and therefore to H^2 misses the important point that the Reimann tensor (at least in either of the coordinates (6.31) or (6.33)) still has coordinate dependence, and therefore cannot actually be observable. This problem highlights the importance of working entirely in physical variables, as we stressed for the atom interferometer in Section 6.1.

The expansion of the universe is occasionally proposed as an explanation for the Pioneer Anomaly [83] which is an anomalous acceleration of the Pioneer spacecrafts of order H . Radar ranging the Pioneer is quite similar in spirit to the atom interferometer, which can be thought of as laser ranging the atom to find its acceleration. Thus, similar arguments apply to this case as well, and the Pioneer anomaly cannot be explained within general relativity as being due to the cosmological expansion.

Intuitively, it is impossible to observe effects linear in Hubble in a local experiment because of the equivalence principle. Essentially, everything in the experiment is ‘falling’ together in the expansion of the universe. Similarly, it is impossible to detect (at leading order) the acceleration toward the dark matter of the galaxy. Only the gradient of this force is detectable, and this is too small to be measured. However, violations of the equivalence principle could in principle lead to observable effects both for the expansion of the universe and dark matter. These would probably be suppressed by a small factor which is the extent to which the equivalence principle is known to be valid.

6.4.2 Lense-Thirring

The Lense-Thirring effect is a gravitomagnetic effect due to the rotation of a source mass. It is difficult to measure and has been searched for in several experiments [84, 85, 86, 87, 88] but no undisputed, conclusive measurements exist yet to better than $\mathcal{O}(1)$. Given the success of atom interferometers used as gyroscopes, it seems worthwhile to consider whether gravitomagnetic effects could be measured in an atom interferometer. To understand the effect, the metric outside a spinning body can be

written as [73]

$$ds^2 = (-1 - 2\phi - 2\phi^2 - 2\psi) dt^2 + (1 - 2\phi) d\vec{x}^2 + 2\vec{\zeta} \cdot d\vec{x} dt \quad (6.34)$$

Using this in the geodesic equations (6.1) gives the coordinate acceleration as

$$\frac{d\vec{v}}{dt} = -\nabla(\phi + 2\phi^2 + \psi) - \frac{d\vec{\zeta}}{dt} + \vec{v} \times (\nabla \times \vec{\zeta}) + 3\vec{v} \frac{d\phi}{dt} + 4\vec{v}(\vec{v} \cdot \nabla)\phi - \vec{v}^2 \nabla\phi \quad (6.35)$$

where $\vec{v} = \frac{d\vec{x}}{dt}$. The terms proportional to $\vec{\zeta}$ give the gravitomagnetic terms we are interested in. Outside a spinning, spherical body with angular momentum $\vec{J} \propto MR^2\vec{\Omega}$

$$\vec{\zeta}(\vec{x}) = \frac{2G}{r^3} (\vec{x} \times \vec{J}). \quad (6.36)$$

The relevant acceleration of a test body caused by this effect is then

$$a_{LT} = \vec{v} \times (\nabla \times \vec{\zeta}) \sim \frac{GMR_E^2\Omega v}{r^3}. \quad (6.37)$$

Near the Earth's surface, using the launch velocity $v \sim 10^{-7}$, the highest this acceleration can be is $a_{LT} \sim 10^{-13}g$, which is certainly above the planned sensitivity of upcoming interferometers [34]. Though we have not done a full GR calculation as outlined above, following the usual guess the phase shift is $ka_{LT}T^2 \sim 10^{-4}\text{rad}$. Unfortunately, this phase shift scales very similarly with control parameters as the phase shift due to the Coriolis effect (assuming an Earth-bound atom interferometer). The Coriolis effect gives a phase shift

$$\vec{k} \cdot \vec{a}_C T^2 \sim \vec{k} \cdot (\vec{\Omega} \times \vec{v}_L) T^2. \quad (6.38)$$

On the Earth this acceleration is $\sim 10^{-4}g$. Then, by (6.37), the Lense-Thirring effect is roughly a factor of ϕ smaller than Coriolis in magnitude: $a_{LT} \sim \phi a_C \sim 10^{-9}a_C$. Further, they scale the same way with the control parameters k , v_L , and T , although their directions and dependencies on the directions of the vectors involved, \vec{v}_L , \vec{x} , and $\vec{\Omega}$, are different. This means the Lense-Thirring effect cannot be directly

measured beneath the much larger Coriolis background. However, the Coriolis effect is a kinematical effect and is thus qualitatively different from the dynamical Lense-Thirring effect which depends on the rotation of the source mass itself and not just of the laboratory in which the experiment is being performed. For one thing, it means that the Lense-Thirring effect depends on the distance to the source mass and not just the angular velocity. Our idea to measure the Lense-Thirring effect in an atom interferometer exploits this difference to isolate the effect from the much larger Coriolis background.

To subtract off the Coriolis background, we can use a differential measurement between two simultaneous interferometers that measure a different Lense-Thirring acceleration but the same Coriolis acceleration. Our idea for accomplishing this is to have the two interferometers differ in only one control parameter, their height above the Earth's surface. This gives the same Coriolis force, up to the level that the other control parameters can be made equal between the two interferometers (note that time variations are not relevant here so long as the two interferometers remain identical in everything but height). However there are constraints on how identical the two interferometers can be. One of the most important is the need to make the launch velocities equal to high precision, since the Coriolis force scales directly with v_L . One idea for doing this is a common launch of a single cloud that is subsequently split into two at differing heights. This limits how far apart the interferometers can be. We will take a height difference of 1 m as an optimistic but not unreasonable guess. Then the size the Lense-Thirring effect that can be measured is reduced by a gradient factor to $a_{LT} \frac{1 \text{ m}}{R_E} \sim 10^{-19}$. This is roughly a factor of 10^4 below the initial sensitivity we are considering. As mentioned in Section 7.2, there are many possibilities for improving this sensitivity by orders of magnitude. However this number seemed challenging enough that we have not pursued this idea further (we are explicitly not considering tying an atom interferometer to a telescope in a Gravity Probe B (GPB)-like configuration, since that has already been proposed [88]). It is also possible that there are better ideas for isolating Lense-Thirring from the Coriolis backgrounds that would allow a measurement, since the Lense-Thirring effect is naturally quite large compared to the sensitivities of upcoming atom interferometers. This is left to future

work.

6.4.3 Preferred Frame

There are many possible modified theories of gravity beyond those parametrized by the PPN parameters β and γ in metric (6.14). As one example, the PPN formalism includes eight other parameters that parametrize the possible metric modifications of general relativity [1, 18]. There are many other, non-metric, theories as well. The full PPN metric [1, 18] would still fall under the calculation method outlined above.

We have not performed the full calculation to see what other effects from the PPN metric would be present in an atom interferometer, but we can easily guess one. Often, the new effects introduced by the full PPN metric can usefully be thought of as preferred frame or location effects, usually called violations of Lorentz invariance. Such effects have been pursued before as modulations of the local acceleration in an accelerometer on the Earth's surface with periods of a day, a year, and so on [1, 18, 89, 16]. While the atom interferometer can yield an impressive increase in sensitivity over the accelerometers used to do the previous searches (and has already led to improved limits [16]), the previous experiments were ultimately limited by geophysical uncertainties. Thus, it is not clear that an increase in accelerometer sensitivity would lead to an improved ability to search for such Lorentz violating effects without an equally improved geophysical model. Of course, the atom interferometer is much more than just an accelerometer, as attested to by the many control parameters and measurement strategies employing simultaneous differential measurements outlined above. Further, there may be signals from these PPN and Lorentz violating effects that are more than just modulations of the local acceleration. We cannot exclude the possibility that there are novel search techniques that would allow atom interferometers to provide stringent tests of Lorentz violating theories, but we leave such considerations to future work.

6.5 Summary and Comparison

Relativistic effects in interferometry have been discussed before in several contexts [90, 91, 92, 93, 94]. None of these discussed specific, viable experiments for the post-Newtonian relativistic effects we have considered. Mostly, they focus on calculation methods instead of specific laboratory experiments. These methods are not applicable to our experimental setup.

In [91], general discussion and motivation was given for considering the effects of general relativity on devices such as atom or neutron interferometers. Relativistic calculations for a certain type of interferometer were given in [92, 93] and were used to give a rough estimate of the phase shift that might arise in a setup similar to neutron interferometry. While it is possible that a similar estimate could be given for the atom interferometer, it would miss most of the important effects since their analysis does not take into account the laser pulses which actually form a light-pulse atom interferometer like the ones we consider here. None of these calculations can be applied directly to the atom interferometer for several reasons, including the lack of description of the laser pulses and the difficulty of solving the necessary equations for the full atom interferometer sequence in a general metric background. Essentially, these calculations only have what we call propagation phase. Further, this phase is not calculated along the trajectories that are relevant for light-pulse atom interferometry. The measurements suggested in these papers are also quite different from the our proposals.

Atom interferometry is considered in [94] as a way to measure space-time curvature, which is essentially the leading order effect of (Newtonian) gravity. We are interested in measuring the post-Newtonian corrections. We are thus led to consider a specific setup in which the effect of the laser pulses and the platform on which the laser rests is crucial and must be taken into account. The formalism given in [90] does not give the final phase shift for the general relativistic effects we are interested in, though some of the effects are mentioned. We cannot use this calculation because the equations become too difficult to solve when all the post-Newtonian terms are kept to the order which is necessary given the precision of the experiment. Further,

the effect of gravity on the laser pulses that serve as our beamsplitters and mirrors is not taken into account, and thus a relativistic prescription for the atom-light interaction is not included. Thus, in order to have a fully relativistic, coordinate-invariant calculation, we use our semi-classical method for calculating the phase shift in the interferometer. Additionally, in order to simplify the calculations, many of these previous papers worked in the linearized gravity approximation where the metric is expanded as $g_{\mu\nu} \approx \eta_{\mu\nu} + h_{\mu\nu}$. This cannot yield a correct result for the non-linear effects in general relativity.

We build and expand upon this previous work by considering a specific experimental scenario for a light pulse atom interferometer, in which the GR effects can be calculated in a fully relativistic framework. This includes important effects such as a relativistic treatment of the laser pulses forming the beamsplitters and mirrors which accounts for the influence of gravity on the propagation of the light, as well as changes to the phase shift formulas. This framework is able to go beyond linearized gravity to reveal the effect of the non-linearity of gravity on an atomic interferometer. This requires calculating phase shifts for terms in the Hamiltonian higher than quadratic order. We also consider several specific experimental strategies for testing general relativity in an atom interferometer.

Chapter 7

Detecting Gravitational Waves

7.1 Introduction

Gravitational waves offer a rich, unexplored source of information about the universe [95, 28]. Many phenomena can only be explored with gravitational, not electromagnetic, radiation. These include accepted sources such as white dwarf, neutron star, or black hole binaries whose observation could provide useful data on astrophysics and general relativity. It has even been proposed that these compact binaries could be used as standard sirens to determine astronomical distances and possibly the expansion rate of the universe more precisely [96]. Gravitational waves could also be one of the only ways to learn about the early universe before the surface of last scattering. There are many speculative cosmological sources including inflation and reheating, early universe phase transitions, and cosmic strings. For all these applications, it is important to be able to observe gravitational waves as broadly and over as large a range of frequencies and amplitudes as possible.

Here we expand on a previous article [72], giving the details of our proposal for an Atomic Gravitational wave Interferometric Sensor (AGIS). We develop proposals for two experiments, one terrestrial, the other satellite-based. We will see that, at least in the configurations proposed here, it is primarily useful for observing gravitational waves with frequencies between about 10^{-3} Hz and 10 Hz. In particular, the terrestrial experiment is sensitive to gravitational waves with frequencies $\sim 1 - 10$ Hz, below

the range of any other terrestrial gravitational wave detector. This arises in part from the vast reduction in systematics available with atom interferometers but impossible with laser interferometers. The satellite-based experiment will have peak sensitivity to gravitational waves in the $\sim 10^{-3} - 1$ Hz band. The use of atomic interferometry also leads to a natural reduction in many systematic backgrounds, allowing such an experiment to reach sensitivities comparable to and perhaps better than LISA's with reduced engineering requirements.

The ability to detect gravitational waves in such a low frequency band greatly affects the potential sources. Binary stars live much longer and are more numerous at these frequencies than in the higher band around 100 Hz where they are about to merge. Stochastic gravitational waves from cosmological sources can also be easier to detect at these low frequencies. These sources are usually best described in terms of the fractional energy density, Ω_{GW} , that they produce in gravitational waves. The energy density of a gravitational wave scales quadratically with frequency (as $\rho_{\text{GW}} \sim h^2 f^2 M_{\text{pl}}^2$). Thus, a type of source that produces a given energy density is easier to detect at lower frequencies because the amplitude of the gravitational wave is higher. This makes low frequency experiments particularly useful for observing cosmological sources of gravitational waves.

There are several exciting proposed and existing experiments to search for gravitational waves including broadband laser interferometers such as LIGO and LISA, resonant bar detectors [97, 98], and microwave cavity detectors [99]. Searching for gravitational waves with atomic interferometry is motivated by the rapid advance of this technology in recent years. Atom interferometers have been used for many high precision applications including atomic clocks [100], metrology, gyroscopes [12], gradiometers [13], and gravimeters [15]. We consider the use of such previously demonstrated technology to achieve the sensitivity needed to observe gravitational waves. Further, we consider technological advances in atom interferometry that are currently being explored, including the apparatus described in Chapter 5, and the possible impact these will have on the search for gravitational waves.

The different sections of this chapter are as independent as possible. Section 7.2 discusses current atom interferometry sensitivity levels, as well as what we anticipate

will be feasible in the near future. In Section 7.3 we calculate the gravitational wave signal in an atom interferometer. In section 7.4 we discuss an experimental configuration for observing this signal on the earth and the relevant backgrounds. In section 7.5 we give the setup and backgrounds for a satellite-based experiment. In section 7.6 we give a brief summary of the astrophysical and cosmological sources of gravitational waves that are relevant for such experiments. In section 7.7 we give a description of the projected sensitivities of the earth- and space-based experiments. In Section 7.8 we compare this work with previous ideas on atom interferometry and gravitational waves and summarize our findings.

7.2 Atom Interferometry Sensitivity

We propose to search for gravitational waves using light pulse atom interferometry. As described in Chapters 2 and 3, the phase shift in an atom interferometer is exquisitely sensitive to inertial forces present during the interferometer sequence, since it precisely compares the motion of the atom to the reference frame defined by the laser phase fronts. Equivalently, the atom interferometer phase shift can be viewed as a clock comparison between the time kept by the laser's phase evolution and the atom's own internal clock. Sensitivity to gravitational waves may be understood as arising from this time comparison, since the presence of space-time strain changes the light travel time between the atom and the laser.

To explore the potential reach of AI-based gravitational wave detectors, we consider progressive phase sensitivities that are likely to be feasible in the near future. Recent atom interferometers have already demonstrated sensor noise levels limited only by the quantum projection noise of the atoms (atom shot noise) [37, 38, 39]. For a typical time-average atom flux of $n = 10^6$ atoms/s, the resulting phase sensitivity is $\sim 1/\sqrt{n} = 10^{-3}$ rad/ $\sqrt{\text{Hz}}$. For example, modern light pulse atom interferometers of the type considered here achieve an atom flux at this level by periodically launching $\sim 10^6$ atoms per shot at a repetition rate of ~ 1 Hz. For our most aggressive terrestrial proposal, we assume quantum projection noise-limited detection of 10^8 atoms per shot at a repetition rate of 10 Hz, implying a phase sensitivity of

3×10^{-5} rad/ $\sqrt{\text{Hz}}$. In the satellite-based proposal we assume 10^8 atoms per shot with a 1 Hz repetition rate, yielding 10^{-4} rad/ $\sqrt{\text{Hz}}$.

Cold atom clouds with 10^8 to 10^{10} atoms are readily produced using modern laser cooling techniques [101]. However, the challenges in this application are to cool to the required narrow velocity distribution and to do so in a short enough time to support a high repetition rate. As discussed in Sections 7.4.2 and 7.5.2, suppression of velocity-dependent backgrounds requires RMS velocity widths as small as ~ 100 $\mu\text{m}/\text{s}$, corresponding to 1D cloud temperatures of ~ 100 pK. The required ~ 100 $\mu\text{m}/\text{s}$ wide cloud could conceivably be extracted from a very large ($\gtrsim 10^{10}$ atoms) μK -temperature thermal cloud by applying a highly velocity-selective cut¹, or by using evaporative cooling techniques. In either case, low densities are desirable to mitigate possible systematic noise sources associated with cold collisions.

The repetition rate required for each proposal is a function of the gravitational wave signal frequency range that the experiment probes. On earth, a 10 Hz repetition rate is necessary to avoid under-sampling signals in the target frequency band of $\sim 1 - 10$ Hz. The satellite experiment we consider is sensitive to the $\sim 10^{-3} - 1$ Hz band, so a 1 Hz rate is sufficient. However, in both cases, multiple interferometers must be overlapped in time since the duration of a single interferometer sequence ($T \sim 1$ s for earth, ~ 100 s for space) exceeds the time between shots. Section 7.5.1 discusses the logistics of simultaneously manipulating a series of temporally overlapping interferometers and describes the implications for atom detection.

Sensor noise performance can potentially be improved by using squeezed atom states instead of uncorrelated thermal atom ensembles [40]. For a suitably entangled source, the Heisenberg limit is $\text{SNR} \sim n$, a factor of \sqrt{n} improvement. For $n \sim 10^6$ entangled atoms, the potential sensitivity improvement is 10^3 . Recent progress using these techniques may soon make improvements in SNR on the order of 10 to 100 realistic [41]. Even squeezing by factor of 10 can potentially relax the atom number

¹Such a cut may be implemented using a Doppler sensitive two-photon transition. This technique results in a narrow velocity distribution along the longitudinal direction without reducing the velocity width in the directions transverse to the cut. Ensembles such as these which are only cold along a single dimension can still be useful for suppressing certain systematics (e.g. gravity gradients). See Sections 7.4.2 and 7.5.2 for specific velocity width requirements.

requirements by 10^2 .

Another sensitivity improvement involves the use of more sophisticated atom optics. The phase sensitivity to gravitational waves is proportional to the effective momentum $\hbar k_{\text{eff}}$ transferred to the atom during interactions with the laser. Both the Bragg and Raman schemes described above rely on a two-photon process for which [44] $\hbar k_{\text{eff}} = 2\hbar k$, but large momentum transfer (LMT) beamsplitters with up to $10\hbar k$ or perhaps $100\hbar k$ are possible [45]. Promising LMT beamsplitter candidates include optical lattice manipulations [36], sequences of Raman pulses [44] and multiphoton Bragg diffraction [45]. Figure 2.4 illustrates an example of an LMT process consisting of a series of sequential two-photon Bragg transitions as may be realized in an optical lattice. As the atom accelerates, the resonance condition is maintained by increasing the frequency difference between the lasers.

Finally, we consider the acceleration sensitivity of the atom interferometer gravitational wave detectors proposed here. The intrinsic sensitivity of the atom interferometer to inertial forces makes it necessary to tightly constrain many time-dependent perturbing accelerations, since background acceleration inputs in the relevant frequency band cannot be distinguished from the gravitational wave signal of interest. The theoretical maximum acceleration sensitivity of the apparatus follows from the shot-noise limited phase sensitivity discussed above, combined with the well-known acceleration response of the atom interferometer, $\phi = k_{\text{eff}}aT^2$:

$$\frac{\delta a}{a} = \frac{\delta\phi}{\phi} \sim \frac{1/\text{SNR}}{k_{\text{eff}}aT^2} = \left(\frac{1}{k_{\text{eff}}aT^2\sqrt{n}} \right) \tau^{-1/2} \quad (7.1)$$

where the total signal-to-noise ratio is $\text{SNR} \sim \sqrt{n\tau}$ for a detected atom flux of n atoms per second during an averaging time τ . For the terrestrial apparatus we propose, the resulting sensitivity in terms of the gravitational acceleration g of the earth is $4 \times 10^{-16} \left(\frac{1}{T} \right)^2 \left(\frac{1000k}{k_{\text{eff}}} \right) \left(\frac{10^9 \text{atoms/s}}{n} \right)^{\frac{1}{2}} g/\sqrt{\text{Hz}}$. Likewise, in the satellite experiment the acceleration sensitivity is $1 \times 10^{-18} \left(\frac{100}{T} \right)^2 \left(\frac{100k}{k_{\text{eff}}} \right) \left(\frac{10^8 \text{atoms/s}}{n} \right)^{\frac{1}{2}} g/\sqrt{\text{Hz}}$. The sum of all perturbing acceleration noise sources must be kept below these levels in order for the apparatus to reach its theoretical noise limit. Sections 7.4.2 and 7.5.2 identify

many of these potential backgrounds and discusses the requirements necessary to control them.

7.3 Gravitational Wave Signal

In this section we will discuss the details of the calculation of the phase shift in an atom interferometer due to a passing gravitational wave. This calculation follows the method for a relativistic calculation discussed in [34, 29]. The method itself will not be reviewed here, only its application to a gravitational wave and the properties of the resultant phase shift will be discussed. For the rest of the paper, only the answer from this calculation is necessary. We will see that the signal of a gravitational wave in the interferometer is an oscillatory phase shift with frequency equal to the gravitational wave's frequency that scales with the length between the laser and the atom interferometer.

Intuitively the atom interferometer can be thought of as precisely comparing the time kept by the laser's clock (the laser's phase), and the time kept by the atom's clock (the atom's phase). A passing gravitational wave changes the normal flat space relation between these two clocks by a factor proportional to the distance between them. This change oscillates in time with the frequency of the gravitational wave. This is the signal that can be looked for with an atom interferometer. Equivalently, the atom interferometer can be thought of as a way of laser ranging the atom's motion to precisely measure its acceleration. Calculating the acceleration that would be seen by laser ranging a test mass some distance away in the metric of the gravitational wave (7.2) shows a similar oscillatory acceleration in time, and this is the signal of a gravitational wave in an atom interferometer. This radar ranging calculation gives essentially the same answer as the full atom interferometer calculation in this case.

7.3.1 Phase Shift Calculation

For the full atom interferometer calculation we will consider the following metric for a plane gravitational wave traveling in the z -direction

$$ds^2 = dt^2 - (1 + h \sin(\omega(t-z) + \phi_0)) dx^2 - (1 - h \sin(\omega(t-z) + \phi_0)) dy^2 - dz^2 \quad (7.2)$$

where ω is the frequency of the wave, h is its dimensionless strain, and ϕ_0 is an arbitrary initial phase. Note that this metric is only approximate, valid to linear order in h . This choice of coordinates for the gravitational wave is known as the “+” polarization in the TT gauge. For simplicity, we will consider a 1-dimensional atom interferometer with its axis along the x -direction. An orientation for the interferometer along the x - or y -axes gives a maximal signal amplitude, while along the z -axis gives zero signal.

We will work throughout only to linear order in h and up to quadratic order in all velocities. These approximations are easily good enough since even the largest gravitational waves we will consider have $h \sim 10^{-18}$ and the atomic velocities in our experiment are at most $v \sim 10^{-7}$. For simplicity we take $\hbar = c = 1$.

The total phase shift in the interferometer is the sum of three parts: the propagation phase, the laser interaction phase, and the final wavepacket separation phase. The usual formulae for these must be modified in GR to be coordinate invariants. Our calculation has been discussed in detail in [29]. Here we will only briefly summarize how to apply that formalism to a gravitational wave metric. The space-time paths of the atoms and lasers are geodesics of Eqn. 7.2. The propagation phase is

$$\phi_{\text{propagation}} = \int L dt = \int m ds \quad (7.3)$$

where L is the Lagrangian and the integral is along the atom’s geodesic. The separation phase is taken as

$$\phi_{\text{separation}} = \int \bar{p}_\mu dx^\mu \sim \bar{E} \Delta t - \vec{\bar{p}} \cdot \Delta \vec{x} \quad (7.4)$$

where, for coordinate independence, the integral is over the null geodesic connecting

the classical endpoints of the two arms of the interferometer, and \bar{p} is the average of the classical 4-momenta of the two arms after the third pulse. The laser phase shift due to interaction with the light is the constant phase of the light along its null geodesic, which is its phase at the time it leaves the laser.

We will make use of the fact that the laser phase in the atom interferometer comes entirely from the second laser, the ‘passive laser’, which is taken to be always on so it does not affect the timing of the interferometer. Instead the first laser, the ‘control laser’, defines the time at which the atom-light interaction vertices occur. For a more complete discussion of this point, see Section 3 of [29].

In practice, we will consider the atom interferometer to be 1-dimensional so that the atoms and light move only in the x -direction and remain at a constant $y = z = 0$. This is not an exact solution of the geodesic equation for metric (7.2). In the full solution the atoms and light are forced to move slightly in the z -direction because of the z in g_{xx} . However the amplitude of this motion is proportional to h which will mean that it only has effects on the calculation at $\mathcal{O}(h^2)$. This was shown by a full interferometer calculation in two dimensions. It can also be understood intuitively since all displacements, velocities, and accelerations in the second dimension are $\mathcal{O}(h)$. The separation phase is then $\phi_{\text{separation}} \sim p_z \Delta x_z \sim \mathcal{O}(h^2)$. The extra z piece of propagation phase is $\sim g_{zz} \Delta z^2 \sim \mathcal{O}(h^2)$. Changes to the calculated x and t coordinates and to g_{xx} will also be $\mathcal{O}(h^2)$ so propagation phase is only affected at this level by the motion in the z direction. Finally, if the laser phase fronts are flat in the z dimension as they travel in the x direction then there will be no effect of the displacement in the z direction. However the phase fronts cannot be made perfectly flat and so there will be an $\mathcal{O}(h)$ effect of the displacement in the z direction times the amount of bending of the laser phase fronts. This is clearly much smaller than the leading $\mathcal{O}(h)$ signal from the gravitational wave and so we will ignore it since we are primarily interested in calculating the signal.

The lasers will be taken to be at the origin and at spatial position $(D, 0, 0)$. We can make this choice because a fixed spatial coordinate location is a geodesic of metric (7.2). Without loss of generality, we take the initial position of the atom to lie on the null geodesic originating from the origin (the first beamsplitter pulse) with $x = x_A$.

Of course, this means that x_A is not a physically measurable variable but is instead a coordinate dependent choice. The results are still fully correct in terms of x_A and the interpretation will also be clear because the coordinate dependence only enters at $\mathcal{O}(h)$. Since, as we will see, the leading order piece of the signal being computed is $\mathcal{O}(h)$, this ambiguity can only have an $\mathcal{O}(h^2)$ effect on the answer. We can ignore this and consider x_A to be the physical length between the atom's initial position and the laser, by any reasonable definition of this length. Similar reasoning allows us to define the initial launch velocity of the atoms at x_A as the coordinate velocity $v_L \equiv \frac{dx}{d\tau}|_{\text{initial}}$. The ability to ignore the $\mathcal{O}(h)$ corrections to the coordinate expressions for quantities such as the initial position and velocity of the atoms relies on the fact that this is a null experiment so the leading order piece of the phase shift is proportional to h .

With the choices above we find the geodesics of metric (7.2) are given as functions of the proper time τ by

$$x(\tau) = x_0 + v_{x0}\tau + h \left(-\frac{v_{x0} \cos(\phi_0 + t_0\omega)}{\sqrt{\eta + v_{x0}^2}\omega} + \frac{v_{x0} \cos(\phi_0 + t_0\omega + \sqrt{\eta + v_{x0}^2}\tau\omega)}{\sqrt{\eta + v_{x0}^2}\omega} \right. \\ \left. + v_{x0}\tau \sin(\phi_0 + t_0\omega) \right) \quad (7.5)$$

$$t(\tau) = t_0 + \sqrt{\eta + v_{x0}^2}\tau + \frac{hv_{x0}^2}{(\eta + v_{x0}^2)} \left(\frac{\cos(\phi_0 + t_0\omega + \sqrt{\eta + v_{x0}^2}\tau\omega) - \cos(\phi_0 + t_0\omega)}{2\omega} \right. \\ \left. + \tau \sqrt{\eta + v_{x0}^2} \sin(\phi_0 + t_0\omega) \right) \quad (7.6)$$

to linear order in h where $\eta = g_{\mu\nu} \frac{dx^\mu}{d\tau} \frac{dx^\nu}{d\tau}$ is 0 for null geodesics and 1 for time-like geodesics. The leading order pieces of these are just the normal trajectories in flat space.

Using these trajectories, the intersection points can be calculated and the final phase shift found as in the general method laid out in [29]. Here the relevant equations are made solvable by expanding always to first order in h . Note that here the use of the local Lorentz frame to calculate the atom-light interactions is unnecessary. The interaction rules are applied at one space-time point so the local curvature of the

space is irrelevant. Further, the choice of boost (the velocity of the frame) can only make corrections of $\mathcal{O}(v^2)$ to the transferred momentum, giving a $\mathcal{O}(v^3)$ correction to the overall velocity of the atom, which is negligible.

To define the lasers' frequencies in a physically meaningful way as in [29], we take each laser to have a frequency, k , given in terms of the coordinate momenta of the light by

$$\left(g_{\mu\nu} U^\mu \frac{dx_{\text{light}}^\nu}{d\lambda} \right) \Big|_{x_L} = k \quad (7.7)$$

where $U^\mu = \frac{dx_{\text{obs}}^\mu}{d\tau}$ is the four-velocity of an observer at the position of the laser. The momenta of the light is then changed by the gravitational wave as it propagates and the kick it gives to the atom is given by its momenta at the point of interaction.

7.3.2 Results

Following the method above, the phase difference seen in the atom interferometer in metric (7.2) is shown in Table 7.1. As in Figure 6.1, the lasers are taken to be a distance D apart, with the atom initially a distance x_i from the left laser and moving with initial velocity v_L . The left laser is the control laser and the right is the passive laser, as defined above. The atom's rest mass in the lower ground state is m , the atomic energy level splitting is ω_a , the laser frequencies are k_1 and k_2 , and h , ω , and ϕ_0 are respectively the amplitude, frequency and initial phase of the gravitational wave. We will be considering a situation in which $D \sim 1$ km is much larger than the size of the interferometer region $v_r T \sim 1$ m.

The first term in Table 7.1 is the largest phase shift and the source of the gravitational wave effect we will look for in our proposed experiment:

$$\Delta\phi_{\text{tot}} = 4 \frac{\hbar k_2}{\omega} \sin^2 \left(\frac{\omega T}{2} \right) \sin(\omega(x_i - \frac{1}{2}D)) \sin(\phi_0 + \omega(x_i - \frac{1}{2}D) + \omega T) + \dots \quad (7.8)$$

This is proportional to k_2 , just as in the phase shift from Newtonian gravity [29]. This arises from the choice of laser 2 as the passive laser which is always on and laser 1 as the control laser which defines the timing of the beamsplitter and mirror interactions. As shown in [29], the laser phase from laser 1 is zero and the main effect then arises

Phase Shift	Size (rad)
$4 \frac{hk_2}{\omega} \sin^2\left(\frac{\omega T}{2}\right) \sin\left(\omega\left(x_i - \frac{D}{2}\right)\right) \sin\left(\phi_0 + \omega\left(x_i - \frac{D}{2}\right) + \omega T\right)$	3×10^{-7}
$-4hk_2v_L T \sin\left(\frac{\omega T}{2}\right) \cos\left(\phi_0 + 2\omega\left(x_i - \frac{D}{2}\right) + \frac{3\omega T}{2}\right)$	3×10^{-9}
$4 \frac{h\omega_A}{\omega} \sin^2\left(\frac{\omega T}{2}\right) \sin\left(\frac{\omega x_i}{2}\right) \sin\left(\phi_0 + \frac{\omega x_i}{2} + \omega T\right)$	10^{-12}
$8 \frac{hk_2v_L}{\omega} \sin^2\left(\frac{\omega T}{2}\right) \cos\left(\frac{\omega x_i}{2}\right) \cos\left(\phi_0 + \frac{\omega x_i}{2} + \omega T\right)$	10^{-14}

Table 7.1: A size ordered list of the largest terms in the calculated phase shift due to a gravitational wave. The sizes are given assuming $D \sim x_i \sim 1$ km, $h \sim 10^{-17}$, $\omega \sim 1$ rad/s, $k_2 \sim 10^7$ m⁻¹, $v_L \sim 3 \times 10^{-8}$, and $T \sim 1$ s.

from the laser phase of laser 2 and so is proportional to k_2 . Under certain conditions, this term is proportional to the baseline length, D , between the lasers (see Eqn. 7.9).

The effect of a gravitational wave is always proportional to a length scale. The second term in Table 7.1 is not proportional to the distance D between the lasers, but is proportional to the distance the atom travels during the interferometer $\sim v_L T$. Thus it cannot be increased by scaling the laser baseline. Instead it depends on the size of the region available for the atomic fountain, which is more difficult to increase experimentally. Thus this term will likely be several orders of magnitude smaller than the first term in a practical experimental setup, as seen in Table 7.1. This $v_L T$ term is essentially the same term that has been found by previous authors (e.g. [102]). We will not use this term for the signal in our proposed experiment as it is smaller than the first term.

The second term can be loosely understood from the intuition that the type of atom interferometer being considered is an accelerometer. In the frame in which the lasers are stationary, this atom interferometer configuration is usually said to respond to the acceleration a of the atom with a phase shift $\sim kaT^2$. In this frame, the motion of the atom in the presence of a gravitational wave (metric (7.2)) appears

to have a coordinate acceleration $a \sim h\omega v$. This would then give a phase shift $kaT^2 \sim kh\omega vT^2$ which is approximately the second term in Table 7.1. Of course, this is clearly coordinate-dependent intuition and will not work in a different coordinate system. Nevertheless, it is interesting that this ‘accelerometer’ term arises in a fully relativistic, coordinate-invariant calculation.

The third term in Table 7.1 is essentially the same as the first term, but with k_2 replaced by ω_a since it arises from the difference in rest masses between the two atomic states. We are considering a Raman transition between two nearly degenerate ground states so $\omega_a \ll k_2$. However for an atom interferometer made with a single laser driving a transition directly between two atomic states, the k_2 terms would be gone and the terms proportional to ω_a would be the leading order phase shift. In this case, ω_a would be the same size as the k of the laser in order to make the atomic transition possible. Such a configuration may be difficult to achieve experimentally.

To understand the answer for the gravitational wave phase shift in Eqn. (7.8), consider the limit where the period of the gravitational wave is longer than the interrogation time of the interferometer. Expanding Eqn. (7.8) in the small quantities ωT , ωD and ωx_i gives

$$\Delta\phi_{\text{tot}} = hk_2\omega^2T^2\left(x_i - \frac{1}{2}D\right)\left\{\sin(\phi_0) + \omega T \cos(\phi_0) - \frac{7}{12}\omega^2T^2 \sin(\phi_0) + \mathcal{O}(\omega^3T^3)\right\} + \dots \quad (7.9)$$

The phase shift is proportional to the distance of the atom from the midpoint between the two lasers. This had to be the case because the leading order phase shift does not depend on the atom’s velocity, resulting in a parity symmetry about the midpoint. The signal increases with the size of the interferometer and the interrogation time T . Of course, as we see from Eqn. (7.8) this increase stops when the size and time of the interferometer become comparable to the wavelength and period, $\frac{1}{\omega}$, of the gravitational wave. Note that in the intermediate regime where $T > \frac{1}{\omega} > D$ then we can expand in ω times the distances so

$$\Delta\phi_{\text{tot}} = 4hk_2\left(x_i - \frac{1}{2}D\right)\sin^2\left(\frac{\omega T}{2}\right)\sin\left(\phi_0 + \omega\left(x_i - \frac{1}{2}D\right) + \omega T\right) + \dots \quad (7.10)$$

When $\omega T \sim 1$, this is very similar to the phase shift in LIGO which goes as $hk\ell$.

Although we will not go through the details of the whole calculation here, we will motivate the origin of the main effect, $\Delta\phi_{\text{tot}} \propto hk_2(x_i - \frac{D}{2})$. In other words, we work in the limit of Eqn. 7.10 when $\omega T \approx 1$. We will be interested in the case where the length of the atom's paths are small compared to the distance between the lasers, $v_L T \ll D$ so the interferometer essentially takes place entirely at position x_i . The main effect comes from laser phase from the passive laser, hence from the timing of these laser pulses. The control laser's pulses are always at 0, T , and $2T$. As an example, the first beamsplitter pulse from the control laser then would reach the atom at time x_i in flat space and so the passive laser pulse then originates at $2x_i - D$. However if the gravitational wave is causing an expansion of space the control pulse is ‘delayed’ and actually reaches the atom at time $\sim x_i(1 + h)$. Then the passive laser pulse originated at $\sim (2x_i - D)(1 + h)$. Thus the laser phase from the passive laser pulse has been changed by the gravitational wave by an amount $k_2 h(2x_i - D)$. This is our signal. Although this motivation is coordinate dependent, it provides intuition for the result of the full gauge invariant calculation.

Eqn. (7.8) is the main effect of a gravitational wave in an atom interferometer. Therefore, the signal we are searching for is a phase shift in the interferometer that oscillates in time with the frequency of the gravitational wave. Note that Eqn. (7.8) and all terms in Table 7.1 are oscillatory because ϕ_0 , the phase of the gravitational wave at the time the atom interferometer begins (the time of the first beamsplitter pulse), oscillates in time. In other words, the phase shift measured by the atom interferometer changes from shot to shot because the phase of the gravitational wave changes.

One way to enhance this signal is to use large momentum transfer (LMT) beam-splitters as described in Section 7.2. This can be thought of as giving a large number of photon kicks to the atom, transferring momentum $N\hbar k$. This enhances the signal by a factor of N since laser phase is enhanced by N . The phase shift calculation is then exactly as if k of the laser is replaced by Nk .

As usual for a gravitational wave detector, this answer would be modulated by the angle between the direction of propagation of the gravitational wave and the

orientation of the detector. If the gravitational wave is propagating in the same direction as the lasers in the interferometer there will be no signal (for the results above we assumed a gravitational wave propagating perpendicularly to the laser axis). This is clear since a gravitational wave is transverse, so space is not stretched in the direction of propagation.

7.4 Terrestrial Experiment

7.4.1 Experimental Setup

We have shown that there is an oscillatory gravitational wave signal in an atom interferometer. To determine whether this signal is detectable requires examining the backgrounds in a possible experiment. Two of the most important backgrounds are vibrations and laser phase noise. As experience with LIGO would suggest, vibrational noise can be orders of magnitude larger than a gravitational wave signal. For an atom interferometer, laser phase noise can also directly affect the measurement and can be larger than the signal. Reducing these backgrounds must therefore dictate the experimental configuration.

After the atom clouds are launched, they are inertial and do not feel vibrations. The vibrations they feel while in the atomic trap do not directly affect the final measured phase shift because the first beamsplitter pulse has not been applied yet. Both vibrational and laser phase noise arise only from the lasers which run the atom interferometer. We propose a differential measurement between two simultaneous atom interferometers run with the same laser pulses to greatly reduce these backgrounds. In order to maximize a gravitational wave signal, these atom interferometers should be separated by a distance L which is as large as experimentally achievable.

On the earth, one possible experimental configuration is to have a long, vertical shaft with one interferometer near the top and the other near the bottom of the shaft. The atom interferometers would be run vertically along the axis defined by the common laser pulses applied from the bottom and top of the shaft, as shown in Fig. 7.1(b). For reference we will consider a $L \sim 1$ km long shaft, with two

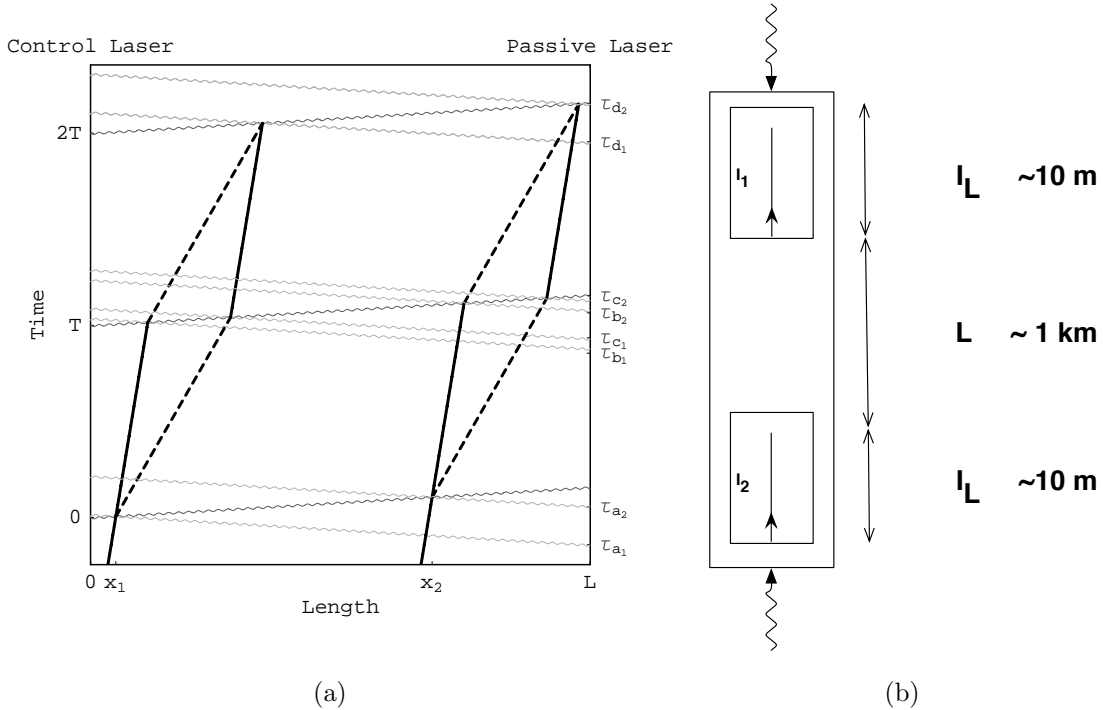


Figure 7.1: Figure 7.1(a) is a space-time diagram of two light pulse interferometers in the proposed differential configuration, as in Figure 6.1. Figure 7.1(b) is a diagram of the proposed setup for a terrestrial experiment. The straight lines represent the path of the atoms in the two $I_L \sim 10 \text{ m}$ interferometers I_1 and I_2 separated vertically by $L \sim 1 \text{ km}$. The wavy lines represent the paths of the lasers.

$I_L \sim 10 \text{ m}$ long atom interferometers I_1 and I_2 . Each atom interferometer then has $T \sim 1 \text{ s}$ of interrogation time, so such a setup will have maximal sensitivity to a gravitational wave of frequency around 1 Hz. Because the two atom interferometers are separated by a distance L , the gravitational wave signal in each will not have the same magnitude but will differ by $\sim hL\omega^2T^2$ as shown in the previous section. Such a differential measurement can reduce backgrounds without reducing the signal.

One reason to use only 10 m at the top and bottom of the shaft for the atom interferometers themselves is to reduce the cost scaling with length. There are more stringent requirements on the interferometer regions than on the region between them.

The interferometer regions should have a constant bias magnetic field applied vertically in order to fix the atomic spins to the vertical axis. This bias field must be larger than any ambient magnetic field, and this, along with the desire to reduce phase shifts from this ambient field (as will be seen later), requires magnetically shielding the interferometer regions. Further, the regions must be in ultra-high vacuum $\sim 10^{-10}$ Torr in order to avoid destroying the cold atom cloud. At this pressure and room temperature the vacuum contains $n \approx 3 \times 10^{12} \frac{1}{\text{m}^3}$ particles at an average velocity of $v \approx 500 \frac{\text{m}}{\text{s}}$. The N₂-Rb cross section is $\sigma \approx 4 \times 10^{-18} \text{ m}^2$ [63]. The average time between collisions is $\frac{1}{n\sigma v} \approx 200 \text{ s}$, so the cold atom clouds can last the required 1 to 10 s.

As discussed in section 7.3, the signal in the interferometer arises from the time dependent variation of the distance between the interferometers as sensed by the laser pulses executing the interferometry. The success of this measurement strategy requires the optical path length in the region between the interferometers to be stable in the measurement band. In order to detect a gravitational wave of strain $h_{rms} \sim \frac{10^{-19}}{\sqrt{\text{Hz}}}$ (see section 7.7), time variations in the index of refraction η of the region between the interferometers, in the 1 Hz band, must be smaller than h_{rms} . The index of refraction of air is $\eta \sim 1 + 10^{-4} \left(\frac{P}{760 \text{ Torr}} \right) \left(\frac{300 \text{ K}}{\tau} \right)$ where P is the pressure and τ is the temperature. Time variations $\delta\tau$ of the temperature cause time variations in the index of refraction $\delta\eta \sim 10^{-4} \left(\frac{P}{760 \text{ Torr}} \right) \left(\frac{300 \text{ K}}{\tau} \right) \left(\frac{\delta\tau}{\tau} \right)$. The required stability in η can be achieved if the region between the interferometers is evacuated to pressures $P \sim 10^{-7}$ Torr ($\frac{0.01 \text{ K}}{\delta\tau}$) with temperature variations $\delta\tau$ over time scales ~ 1 second.

If the entire length L of the shaft can be evacuated to $\sim 10^{-10}$ torr and magnetically shielded then the atom interferometers can be run over a much larger length $I_L \sim L$, yielding a larger interrogation time and greater sensitivity to low frequency gravitational waves. The signal sensitivity is $\propto (L - \frac{1}{2}gT^2)(\omega T)^2$ for a gravitational wave of frequency $\omega \leq T^{-1}$. For such a low frequency gravitational wave, this is maximized when $I_L = \frac{1}{2}gT^2 = \frac{1}{2}L$, so the length of each interferometer should be chosen to be equal to half the distance between the lasers. In the case of a 1 km long shaft this would give an interrogation time of $T \approx 10$ s so a peak sensitivity to 0.1 Hz gravitational waves.

In order to run an atom interferometer over such a long baseline, it is necessary to

have the laser power to drive the stimulated 2-photon transitions (Raman or Bragg) used to make beamsplitter and mirror pulses from that distance. It is possible to obtain a sufficiently rapid Rabi oscillation frequency using a $\sim 1\text{ W}$ laser with a Rayleigh range $\sim 10\text{ km}$ which is easy to achieve with a waist of $\sim 10\text{ cm}$. This will be a more restrictive requirement for the satellite based experiment and so will be considered in greater detail in Section 7.5.1.

The atom interferometer configurations discussed here are maximally sensitive to frequencies as low as $\frac{1}{T}$ and lose sensitivity at lower frequencies. However, the sensitivity is also limited at high frequencies by the data-taking rate, f_d , the frequency of running cold atom clouds through the interferometer. Gravitational wave frequencies higher than the Nyquist frequency, $\frac{f_d}{2}$, will be aliased to lower frequencies which is undesirable since we wish to measure the frequency of the gravitational wave. We will cut off our sensitivity curves at the Nyquist frequency. If only one cloud of atoms is run through the interferometer at a time, the Nyquist frequency will be below $\frac{1}{T}$. Thus it is important to be able to simultaneously run more than one cloud of atoms through the same interferometer concurrently. Using the same spatial paths for all the cold atom clouds is useful since otherwise DC systematic offsets in the phase of the different interferometers could give a spurious signal at a frequency $\sim f_d$.

It is then necessary to estimate how high a data-taking rate is achievable. We will show that it is possible to have multiple atom clouds running concurrent atom interferometers in each of the two interferometer regions. This is possible because the atom clouds are dilute and so pass through each other and also because it is possible for the beamsplitter and mirror laser pulses to interact only with a particular atom cloud even though all the atom clouds are along the laser propagation axis. This is accomplished by Doppler detuning the required laser frequencies of each atomic transition by having all the atom clouds moving with different velocities at any instant of time. We imagine having different clouds shot sequentially with the same launch position and velocity, with a time difference $\frac{1}{f_d} < T$ (see Figure 7.2). The atom clouds accelerate under gravity and so each successive atom cloud always has a velocity difference from the preceding one of $\frac{g}{f_d}$. When a beamsplitter or mirror pulse is applied along the axis, it must be tuned to the Doppler shifted atomic transition

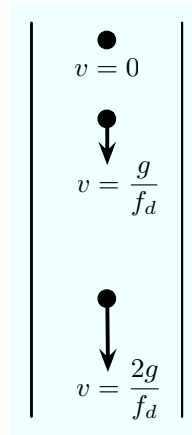


Figure 7.2: A diagram of several clouds of atoms being run through the atom interferometer sequence concurrently. The arrows indicate the velocity of each cloud of atoms at a single instant in time. Earlier shots will be moving with more downward velocity, allowing the clouds to be individually addressed with Doppler detuned laser frequencies.

frequency. The width of the two-photon transitions that make the beamsplitters and mirrors is set by the Rabi frequency and so can be roughly $\Omega^{-1} \sim 10^4$ Hz. Taking a laser frequency of 3×10^{14} Hz implies that the clouds must have velocities that differ by at least $\Delta v \sim \frac{10^4}{3 \times 10^{14}} \approx 3 \times 10^{-11} \approx 1 \frac{\text{cm}}{\text{s}}$ in order for the Doppler shift to be larger than the width of the transition. In practice, every cloud besides the one being acted upon should be many line-widths away from resonance which can be accomplished if $\frac{g}{f_d} \gg 3 \times 10^{-11}$.

While doppler detuning prevents unwanted stimulated transitions, the laser field can drive spontaneous 2-photon transitions as discussed in subsection 7.5.1. A significant fraction of the atoms should not undergo spontaneous transitions in order for the interferometer to operate with the desired sensitivity. Using the formalism discussed in subsection 7.5.1, the spontaneous emission rate R is given by $R \sim \frac{2\Omega_{\text{st}}^2}{\Gamma \frac{I}{I_{\text{sat}}}}$ where Ω_{st} is the Rabi frequency of the stimulated 2-photon transition, Γ is the decay rate of the excited state, I the intensity of the lasers at the location of the atoms and I_{sat} the saturation intensity of the chosen atomic states. With $\Omega_{\text{st}} \sim 2\pi (10^4 \text{ Hz})$, lasers of waist $\sim 3 \text{ cm}$ and power $\sim 1 \text{ W}$, atomic parameters (e.g. for Rb or Cs) $I_{\text{sat}} \approx 2.5 \frac{\text{mW}}{\text{cm}^2}$,

and $\Gamma \approx 3 \times 10^7 \frac{\text{rad}}{\text{s}}$ [101, 103] the spontaneous emission rate is $R \sim (5 \text{ s})^{-1}$. These parameters will allow for the operation of up to ~ 5 concurrent interferometers using up to $N \sim 1000$ LMT beamsplitters. This implies a data-taking rate of $f_d \sim 5 \text{ Hz}$. This number of course depends on the particular atomic species being used and the laser intensity. A more judicious choice of atom species or increased laser power will directly increase the data-taking rate. Our only desire here is to show that it should be possible to have a data-taking rate of $f_d \sim 10 \text{ Hz}$. This is the number we will use for our sensitivity plots. In the actual experiment, the data-taking rate will depend on many complex details, including the atom cooling mechanism. There is a tradeoff between the rate of cooling and the number of atoms in the cloud. Here we only assume that cooling can be done at this rate, if necessary with several different atomic traps, since this rate is not drastically higher than presently achievable rates.

In order to detect a gravitational wave it is only necessary to have one such pair of atom interferometers. However, it may be desirable to have several such devices operating simultaneously. Detecting a stochastic background of gravitational waves requires cross-correlating the output from two independent gravitational wave detectors. Even for a single, periodic source, correlated measurements would increase the confidence of a detection. Furthermore, cross-correlating the outputs of independent gravitational wave detectors will help reduce the effects of backgrounds with long coherence times. In addition, with three such single-axis gravitational wave detectors whose axes point in different directions, it is possible to determine information on the direction of the gravitational wave source. Such independent experiments could be oriented vertically in different locations on the earth, giving different axes. It is also possible to consider orienting the laser axis of such a pair of atom interferometers horizontally, though to maintain sensitivity to $\sim 1 \text{ Hz}$ gravitational waves the atom interferometers themselves would still have to be 10 m long vertically. Such a configuration would still have the same signal, proportional to the length between the interferometers, though some backgrounds could be different.

It may be desirable to operate two, non-parallel atom interferometer baselines that share a common passive laser in a LIGO-like configuration. For example, one baseline could be vertical with the other horizontal, or both baselines can be horizontal. Each

baseline consists of two interferometers. The interferometers along each baseline are operated by a common control laser. The passive laser is placed at the intersection of the two baselines with appropriate optical beamsplitters so that the beam from the passive laser is shared by both baselines. As discussed in sub section 7.4.2, laser phase noise in this configuration is significantly suppressed.

7.4.2 Backgrounds

We consider the terrestrial setup discussed in the above section with two atom interferometers separated vertically by a $L \sim 1$ km long baseline. The interferometers will be operated by common lasers and the experiment will measure the differential phase shift between the two atom interferometers. This strategy mitigates the effects of vibration and laser phase noise. Based upon realistic extrapolations from current performance levels, atom interferometers could conceivably reach a per shot phase sensitivity $\sim 10^{-5}$ rad. This will make the interferometer sensitive to accelerations $\sim 10^{-15} \frac{g}{\sqrt{\text{Hz}}} \left(\frac{1\text{s}}{T}\right)^2$ (Section 7.7). We will assume a range of sensitivities. In what follows, we will show that backgrounds can be controlled to better than the most optimistic sensitivity $\sim 10^{-5}$ rad.

A gravitational wave of amplitude h and frequency ω produces an acceleration $\sim hL\omega^2$. With an acceleration sensitivity of $10^{-15} \frac{g}{\sqrt{\text{Hz}}}$, the experiment will have a gravitational wave strain sensitivity $\sim \frac{10^{-18}}{\sqrt{\text{Hz}}} \left(\frac{1\text{ km}}{L}\right)$. This sensitivity will allow the detection of gravitational waves of amplitude $h \sim 10^{-22} \left(\frac{4\text{ km}}{L}\right)$ after $\sim 10^6$ s of integration time (Section 7.7). The detection of gravitational waves at these sensitivities requires time varying differential phase shifts in the interferometer to be smaller than the per shot phase sensitivity $\sim 10^{-5}$. In particular, time varying differential acceleration backgrounds must be smaller than the target acceleration sensitivity $10^{-15} \frac{g}{\sqrt{\text{Hz}}}$.

In addition to stochastic noise, there might be backgrounds with long coherence times in a given detector. Since these backgrounds will not efficiently integrate down, the sensitivity of any single detector will be limited by the floor set by these backgrounds. However, as discussed in sub section 7.4.1, it may be desirable to build and simultaneously operate a network of several such gravitational wave detectors.

The gravitational wave signal in a given detector depends upon the orientation of the detector relative to the incident direction, the polarization and the arrival time of the gravitational wave at the detector. If the detectors are sufficiently far away, then the gravitational wave signal in the detectors are in a well defined relationship which is different from the contribution of backgrounds with long coherence time. If the output of these detectors are cross-correlated, then the sensitivity of the network will be limited by the stochastic noise floor. In the following, we will assume that such a network of independent gravitational wave detectors can be constructed with their cross-correlated sensitivity limited by stochastic noise. We discuss these stochastic backgrounds and strategies to suppress them to the required level.

Vibration Noise

The phase shift in the interferometer is accrued by the atom during the time between the initial and final beamsplitters. In this period, the atoms are in free fall and are coupled to ambient vibrations only through gravity. In addition to this coupling, vibrations of the trap used to confine the atoms before their launch will lead to fluctuations in the launch velocity of the atom cloud. These fluctuations do not directly cause a phase shift since the initial beamsplitter is applied to the atoms after their launch. However, variations in the launch velocity will make the atoms move along different trajectories. In a non-uniform gravitational field, different trajectories will see different gravitational fields thereby producing time dependent phase shifts. But, since these effects arise from gravitational interactions, their impact on the experiment is significantly reduced. A detailed discussion of these gravitational backgrounds is contained in subsection 7.4.2.

The vibrations of the lasers contribute directly to the phase shift through the laser pulses used to execute the interferometry. The pulses from the control laser (Section 7.3) at times 0, T and $2T$ (Figure 7.1(a)) are common to both interferometers and contributions from the vibrations of this laser to the differential phase shift are completely cancelled. The vibrations of the passive laser (Section 7.3) are not completely common. The pulses from the passive laser that hit one interferometer ($\tau_{a_1}, \tau_{b_1}, \tau_{c_1}, \tau_{d_1}$) are displaced in time by L from the pulses ($\tau_{a_2}, \tau_{b_2}, \tau_{c_2}, \tau_{d_2}$) that

hit the other interferometer due to the spatial separation L between interferometers (Figure 7.1(a)).

The proposed experiment relies on using LMT beamsplitters to boost the sensitivity of the interferometer. The effect of a LMT pulse on the atom can be understood by modeling the LMT pulse as being composed of N (~ 1000) regular laser pulses. If the time duration of each regular pulse is greater than the light travel time L between the two interferometers, then all but the beginning and end of each LMT pulse will be common to the interferometers. The time duration of the pulses can be modified by changing the Rabi frequency of the transition of interest by manipulating the detuning and intensity of the lasers from the intermediate state used to facilitate the 2-photon Raman transitions. With Rabi frequencies $\sim 3 \times 10^5$ Hz ($\frac{1 \text{ km}}{L}$), the duration of a regular pulse is equal to the distance between the interferometers. The beginning and end of the LMT pulse from the passive laser that hits one interferometer is displaced in time by L from the pulse that hits the other interferometer. Vibrations δx of the passive laser position in this time interval are uncommon and result in a phase shift $\sim k\delta x$ instead of $k_{\text{eff}}\delta x$. Contributions to the phase shift from vibrations of the passive laser at frequencies smaller than $\frac{1}{L}$ are common to both interferometers and are absent in the differential phase shift.

The net phase shift $k\delta x$ is smaller than 10^{-5} if $\delta x \lesssim 10^{-12}$ m ($\frac{10^7 \text{ m}^{-1}}{k}$). Here δx is the amount by which the passive laser moves in the light travel time L between the two interferometers. A vibration at frequency ν with amplitude a contributes to the displacement δx of the laser in a time L by an amount $a\nu L$. This displacement is smaller than 10^{-12} m if $a < \left(\frac{10^{-12} \text{ m}}{\nu L}\right) = 3 \times 10^{-7} \text{ m} \left(\frac{1 \text{ Hz}}{\nu}\right) \left(\frac{1 \text{ km}}{L}\right)$. This can be achieved by placing the passive laser on vibration isolation stacks that damp its motion below $10^{-7} \frac{\text{m}}{\sqrt{\text{Hz}}} \left(\frac{1 \text{ Hz}}{\nu}\right)^{\frac{3}{2}} \left(\frac{1 \text{ km}}{L}\right)$. It is only necessary to damp the motion of the lasers below this value in the frequency band 3×10^5 Hz ($\frac{1 \text{ km}}{L}\right) \gtrsim \nu \gtrsim 1 \text{ Hz}$. The high frequency cutoff is established since contributions to the phase shift from vibrations at frequencies above 3×10^5 Hz ($\frac{1 \text{ km}}{L}\right)$ are suppressed by the size of the Rabi pulse. The low frequency cutoff arises since vibrations at frequencies below 1 Hz are irrelevant to the detection of gravitational waves at 1 Hz.

While these vibrations may have long coherence times in a single gravitational

wave detector, cross correlating multiple detectors with different vibrational noise should allow these vibrations to be reduced to the stochastic floor.

Laser Phase Noise

The gravitational wave signal in the interferometer arises from an asymmetry in the time durations between the first and second and between the second and third laser pulses. The interferometer is operated by pulsing the control laser at equal time intervals. The corresponding pulses from the passive laser that interact with the atom must then have been emitted at unequal time intervals since in the presence of a gravitational wave, pulses emitted at different times travel along different trajectories². The phase of the passive laser reflects this temporal asymmetry. This phase is impinged on the atom during the interaction between the atom and the laser field producing a phase shift in the interferometer (see Section 7.3). Noise in the evolution of the laser's phase will mimic a temporal variation and is a background to the experiment. The pulses from the control laser are common to both interferometers. Noise in the phase of this laser does not contribute to the differential phase shift as these contributions are completely cancelled.

The pulses from the passive laser that hit one interferometer $(\tau_{a_1}, \tau_{b_1}, \tau_{c_1}, \tau_{d_1})$ are displaced in time by L from the pulses $(\tau_{a_2}, \tau_{b_2}, \tau_{c_2}, \tau_{d_2})$ that hit the other interferometer (Figure 7.1(a)). Since the pulses are not completely common, phase noise in the passive laser will contribute to the differential phase shift. Phase noise in a laser operating at a central frequency k during a time interval δT can be characterized as the difference $\delta\phi = \phi_m - k\delta T$ where ϕ_m is the phase measured after δT . The pulses from the passive laser that hit the two interferometers are separated in time by L and phase noise of the laser during this period will contribute to the differential phase shift. An additional contribution arises from the drift of the central frequency of the laser in the time T between pulses. A drift, δk , in the central frequency of the laser between pulses changes the evolution of the laser phase mimicking a change in the time of emission of the laser pulse. The pulses from the passive laser that interact

²Note that the passive laser is turned on well before the control laser is pulsed, and then we are only referring to the part of the passive laser pulse which triggers the atomic transitions.

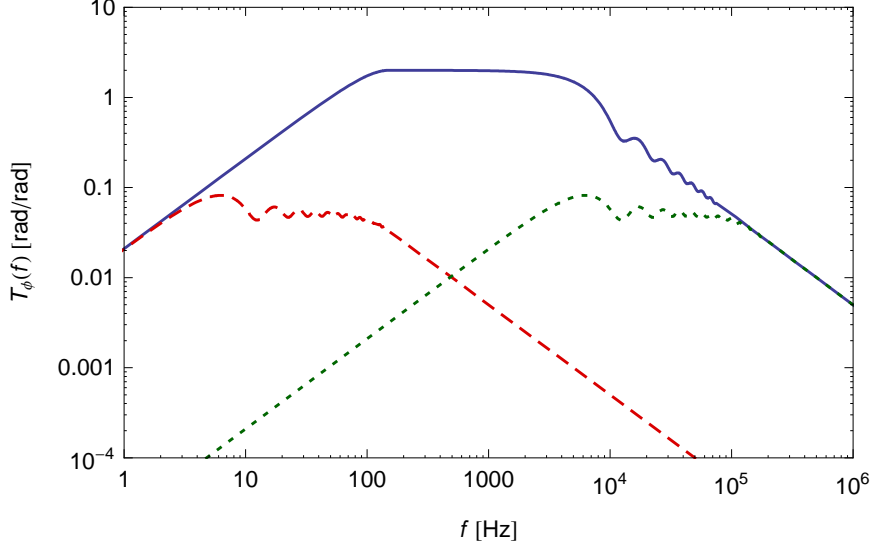


Figure 7.3: Interferometer response to laser phase noise in a single $\frac{\pi}{2}$ pulse. The dotted (green) curve represents a differential measurement strategy with $L = 1$ km and a Rabi period of 10^{-4} s. The solid (blue) curve is the same Rabi period but $L = 1000$ km. The dashed (red) curve is $L = 1000$ km and a Rabi period of 10^{-1} s. Sharp spikes in the response curves above the Rabi frequency have been enveloped.

with the two interferometers are separated by a time $L \ll T$. The contribution to the phase of these pulses from the frequency drift are common except for the additional phase accrued by the laser during the time L . This additional phase $\delta k L$ contributes to the differential phase shift in the interferometer.

The proposed experiment relies on using LMT beamsplitters to boost the sensitivity of the interferometer. As a proof of principle, we will model the LMT pulse as a sequential Bragg process. In other words, it is composed of N (~ 1000) of the regular laser pulses (those used to drive a single 2-photon Bragg transition) run consecutively with no time delay between them. Each regular laser pulse transfers a momentum $2k$ to the atom resulting in an overall momentum transfer $k_{\text{eff}} = 2Nk$. The phase of every laser pulse is registered on the atom, amplifying the phase noise transferred to the atoms to $\sqrt{N}\delta\phi \oplus N\delta k L$ (\oplus means add in quadrature). However, if the time duration of each regular pulse is greater than the light travel time L between the

two interferometers, then all but the beginning and end of each LMT pulse will be common to the interferometers. This can be achieved by setting the Rabi frequency of the transition to be $\lesssim \frac{1}{L} \sim 3 \times 10^5$ Hz ($\frac{1\text{ km}}{L}$). The Rabi frequency can be tuned by manipulating the detuning of the lasers from the intermediate state used to facilitate the 2-photon Bragg transitions. The differential phase shift will then receive contributions from the phase noise in the beginning and end of each LMT pulse alone. For example, if the light travel time L is equal to the 2-photon Rabi period, then only the first and last of the regular laser pulses making up the LMT pulse will have uncommon phase noise, all the rest will give common phase noise to the two interferometers which will cancel. In this case the laser phase noise would be reduced to $\sqrt{2}\delta\phi \oplus 2\delta k L$, independent of N . This method for reducing the laser phase noise from an LMT pulse was discussed for a sequential Bragg process as a demonstration, but similar ways of reducing the phase noise may exist for other LMT methods³.

Low frequency phase noise is suppressed by the differential measurement strategy outlined above at frequencies below $\sim \frac{1}{L}$. High frequency phase noise is reduced by averaging over the finite time length of the pulse, and will be suppressed above the Rabi frequency. To see these reductions, the calculated atom response to phase noise is shown in Fig. 7.3 for several different configurations (for a description of a similar calculation see [104], here we have also added in a time delay due to the finite speed of light). With Rabi frequencies $\sim 3 \times 10^5$ Hz ($\frac{1\text{ km}}{L}$), the contribution of the laser phase noise to the differential phase shift is $\sim \delta\phi \oplus \delta k L$. This phase shift must be smaller than 10^{-5} .

$\delta\phi$ is the phase noise in the laser at frequencies $\sim 3 \times 10^5$ Hz ($\frac{1\text{ km}}{L}$). This is smaller than 10^{-5} if the phase noise of the laser is smaller than $-140 \frac{\text{dBc}}{\text{Hz}}$ at a $\sim 3 \times 10^5$ Hz ($\frac{1\text{ km}}{L}$) offset. The $\delta k L$ term is smaller than 10^{-5} if $\delta k \lesssim 10^{-9} \text{ m}^{-1} (\frac{1\text{ km}}{L})$ which requires fractional stability in the laser frequency $\sim 10^{-15} (\frac{10^7 \text{ m}^{-1}}{k})$ over time scales $\sim T$. These requirements can be met using lasers locked to high finesse cavities [105].

Another scheme that could be employed to deal with laser phase noise is to operate

³For example, a sequential Raman process with reduced phase noise might be realizable in a similar manner if the light travel time L is set equal to twice the Rabi period and both lasers alternate between the two frequencies needed to run the Raman process with no intervening time.

interferometers along two, non parallel baselines that share a common passive laser in a LIGO-like configuration. For example, one baseline could be vertical with the other horizontal, or both baselines can be horizontal. Each baseline consists of two interferometers. The interferometers along each baseline are operated by a common control laser. The passive laser is placed at the intersection of the two baselines with appropriate optical beamsplitters so that the beam from the passive laser is shared by both baselines. The same pulses from the passive laser can trigger transitions along the interferometers in both baselines if the control lasers along the two baselines are simultaneously triggered. The laser phase noise in the difference of the differential phase shift along each baseline is greatly suppressed since phase noise from the control laser is common to the interferometers along each baseline and the phase noise from the passive laser is common to the baselines. The gravitational wave signal is retained in this measurement strategy since the gravitational wave will have different components along the two non parallel baselines. As discussed in sub section 7.5.2, laser phase noise along the two arms can be cancelled up to knowledge of the arm lengths of each baseline. With ~ 10 cm knowledge of the arm lengths, these contributions are smaller than shot noise if the frequency drift δk of the laser is controlled to better than $\sim 10^4 \frac{\text{Hz}}{\sqrt{\text{Hz}}}$ at frequencies $\omega \sim 1$ Hz.

Newtonian Gravity Backgrounds

The average gravitational field g_L along the space-time trajectory of each atom contributes to the phase shift in the interferometer. Each shot of the experiment measures the average phase shift of all the atoms in the cloud and is hence sensitive to the average value (g_L^{avg}) of g_L over all the atoms in the cloud. Time variations in g_L^{avg} are a background to the experiment. Seismic and atmospheric activity are the dominant natural causes for time variations in g_L^{avg} . The gravitational effects of these phenomena were studied in [106] and [107]. Using the interferometer transfer functions evaluated in these papers, we find that time varying gravitational accelerations will not limit the detection of gravitational waves at sensitivities $\sim \frac{10^{-17}}{\sqrt{\text{Hz}}}(\frac{1 \text{ km}}{L})$ at frequencies above 300 mHz (Figures 7.4, 7.5). Human activity can also cause time variations in g_L^{avg} . Any object whose motion has a significant overlap with the 1 Hz

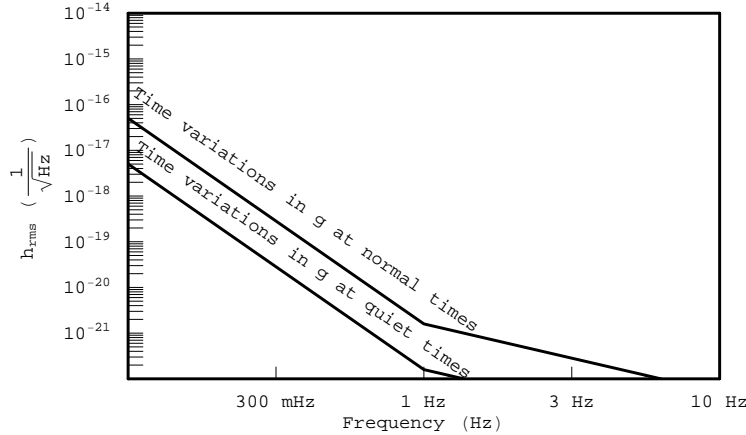


Figure 7.4: Interferometer response in strain per $\sqrt{\text{Hz}}$ to a time varying g with a 10 km baseline setup.

band is a background to the experiment. This background is smaller than $10^{-15} \frac{g}{\sqrt{\text{Hz}}}$ if such objects (of mass M) are at distances larger than $1 \text{ km} \sqrt{\frac{M}{1000 \text{ kg}}}$.

The trajectory of the atom is determined by its initial position (R_L) and velocity (v_L). Variations in R_L and v_L will change the trajectory of the atom. In a non-uniform gravitational field, different trajectories will have different values of g_L . The interferometer has to run several shots during the period of the gravitational wave source in order to detect the time varying phase shift from the gravitational wave. The average launch position and velocity of the atoms may change from shot to shot thereby changing the average gravitational field sensed by the interferometer. These variations cause time dependent phase shifts. We estimate the size of these effects by writing g_L in terms of the length $I_L \sim v_L T$ of the interferometer as:

$$g_L = g(R_L) + \nabla g(R_L)v_L T + \dots \quad (7.11)$$

where $g(R_L)$ and $\nabla g(R_L)$ are the gravitational field and its gradient at the initial position R_L of the atom. g_L^{avg} can then be expressed in terms of the average initial position (R_L^{avg}) and velocity (v_L^{avg}) of the atom cloud as:

$$g_L^{avg} = g(R_L^{avg}) + \nabla g(R_L^{avg})v_L^{avg}T + \dots \quad (7.12)$$

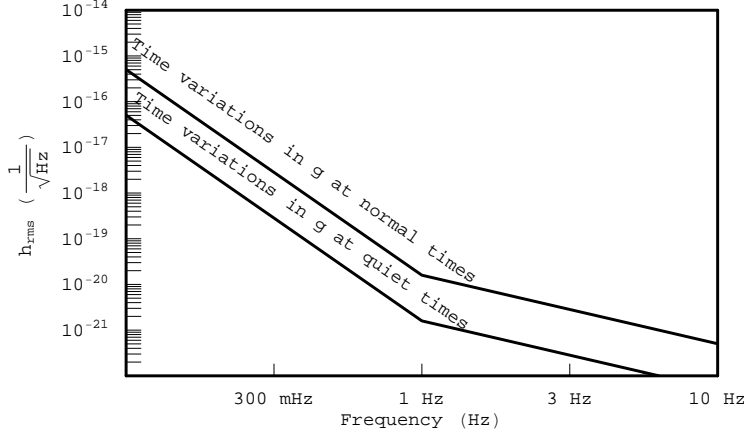


Figure 7.5: Interferometer response in strain per $\sqrt{\text{Hz}}$ to a time varying g with a 1 km baseline setup.

Shot to shot variations δR_L^{avg} and δv_L^{avg} in the average position and velocity of the atom cloud will result in accelerations $\sim \nabla g \delta R_L^{avg} + \nabla g \delta v_L^{avg} T$. These accelerations must be made smaller than $10^{-15} \frac{g}{\sqrt{\text{Hz}}}$.

The gradient of the Earth's gravitational field in a vertical interferometer is $\nabla g \sim \frac{GM_E}{R_E^3}$. The corresponding accelerations $\frac{GM_E}{R_E^2} \frac{\delta R_L^{avg}}{R_E}$ and $\frac{GM_E}{R_E^2} \frac{\delta v_L^{avg} T}{R_E}$ are smaller than $10^{-15} \frac{g}{\sqrt{\text{Hz}}}$ if δR_L^{avg} and δv_L^{avg} are smaller than $10 \frac{\text{nm}}{\sqrt{\text{Hz}}}$ and $10 \frac{\text{nm/s}}{\sqrt{\text{Hz}}}$ respectively. δR_L^{avg} and δv_L^{avg} are caused by vibrations of the atom traps used to confine the atoms and thermal effects in the atom cloud.

Vibrations of the atom traps are caused by seismic motion and fluctuations in the magnetic fields used to confine the atoms. Seismic vibrations in the 1 Hz band have been measured to be $\sim 10 \frac{\text{nm}}{\sqrt{\text{Hz}}}$ [108] at an average site on the Earth. During noisier times, these vibrations may be as large as $\sim 100 \frac{\text{nm}}{\sqrt{\text{Hz}}}$ [108]. Seismic vibrations of the trap are therefore only marginally bigger than the $10 \frac{\text{nm}}{\sqrt{\text{Hz}}}$ control required by this experiment and hence these vibrations can be sufficiently damped by vibration isolation systems.

The magnetic fields used to trap the atom will fluctuate due to variations in the currents used to produce these fields. The trap used in this experiment can be modelled as a harmonic oscillator with frequency $\omega_T = \sqrt{\frac{\kappa}{M_A}} \sim 100 \text{ Hz}$ where M_A is

the mass of the atom and the “spring constant” κ is proportional to the (curvature of) applied magnetic field. Fluctuations in the equilibrium position of this oscillator due to variations in κ are $\sim \frac{g}{\omega_T^2} \frac{\delta\kappa}{\kappa}$ and these are smaller than $10 \frac{\text{nm}}{\sqrt{\text{Hz}}}$ if $\frac{\delta\kappa}{\kappa} \lesssim \frac{10^{-5}}{\sqrt{\text{Hz}}}$. Since κ is proportional to the applied current, fractional stability $\sim \frac{10^{-5}}{\sqrt{\text{Hz}}}$ in the current source will adequately stabilize the equilibrium position of the trap.

The requirements on the control over the atom traps can be ameliorated by using a common optical lattice to launch the atoms in both interferometers. The vibrations of the lattice will then be common to both interferometers and the first non-zero contribution to the differential phase shift from the Earth’s gravitational field arises from the quadratic gradient of this field. These contributions are smaller than $10^{-15} \frac{g}{\sqrt{\text{Hz}}}$ if the vibrations of the lattice are $\lesssim \frac{10^{-4} \text{m}}{\sqrt{\text{Hz}}}$ in the 1 Hz band.

The average velocity of the atom clouds will change from shot to shot due to the random fluctuations in the thermal velocities of the atoms. These variations are smaller than 10 nm/s if the average thermal velocity of each atom cloud is smaller than 10 nm/s. In an atom cloud with $\sim 10^8$ atoms, the average thermal velocity is smaller than 10 nm/s if the thermal velocities of the atoms are $\sim 100 \mu\text{m/s}$. Such thermal velocities can be achieved by cooling the cloud to ~ 100 picokelvin temperatures. Similarly, the average position of the atom cloud changes from shot to shot due to thermal effects. These fluctuations can be made smaller than 10 nm by confining the atoms within a region of size 100 μm .

The control required over the launch parameters of the atom cloud is directly proportional to the gravity gradient ∇g . Thus these requirements may be ameliorated by reducing the local gravity gradient. We estimated these controls using the natural value of $\nabla g \sim \frac{GM_E}{R_E^3}$ on the surface of the Earth. However for a ~ 10 m atom interferometer, it may be possible to reduce gravity gradients to $\sim 1\%$ their natural value by shimming the local gravitational field using a suitably chosen local mass density. The density of the Earth varies significantly with distance below its surface. The average density of the Earth is $\bar{\rho} \sim 5.5 \text{ gm/cm}^3$ while the average density of its crust is $\rho_c \sim 3 \text{ gm/cm}^3$. The earth’s gravitational field in a vertical interferometer inside the Earth’s crust can be modeled as arising from a sphere of radius R_E with average density equal to ρ_c and a point object of mass $(\frac{4\pi}{3})(\bar{\rho} - \rho_c)R_E^3$ located at the center of

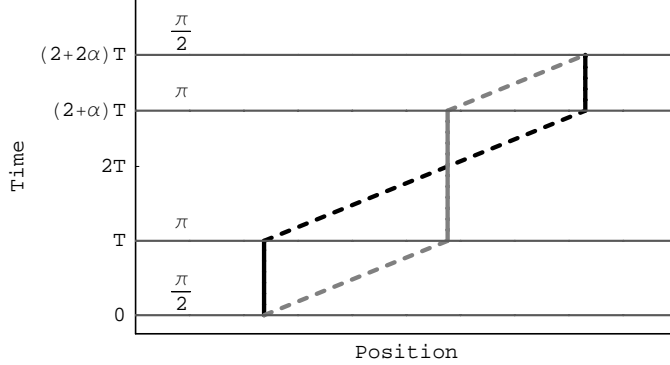


Figure 7.6: A space-time diagram of the double loop interferometer. The black and gray lines indicate the two halves of the wave function after the initial beamsplitter. The dashed and solid lines represent the two internal states of the atom. The laser light used to manipulate the atom is shown as horizontal dark gray lines. The speed of light has been exaggerated.

the Earth. The gradient of this field is $\sim G(\frac{4\pi}{3})(2(\bar{\rho} - \rho_c) - \rho_c)$ and the effect of this gradient can be cancelled by surrounding the upper end of the interferometer by a sphere of radius ~ 1 m and average density $\sim 2(\bar{\rho} - \rho_c) \sim 5$ gm/cm³ (see also Section V of [29]). The demands on the launch parameters of the experiment can be relaxed to the extent to which the local gravity gradient can be reduced. For example, if the gravity gradient in each interferometer is reduced to a percent of its natural value, the experiment can reach the target sensitivity with $1\frac{\mu\text{m}}{\sqrt{\text{Hz}}}$ control over the average position and $1\frac{\mu\text{m}/\text{s}}{\sqrt{\text{Hz}}}$ control over the average velocity of the atom clouds in the 1 Hz frequency band.

The interferometer configuration discussed above executes its control pulses in the Mach-Zender sequence $\frac{\pi}{2} - \pi - \frac{\pi}{2}$ with equal time between pulses. The interferometer can also be run in the $\frac{\pi}{2} - \pi - \pi - \frac{\pi}{2}$ double loop configuration with the atom spending a time $2T$ in the lower loop and a time $(\sqrt{5}-1)T$ in the upper loop (Figure 7.6 with $\alpha = \frac{\sqrt{5}-1}{2}$). In this configuration, the phase shift from constant accelerations is retained while the contribution from linear acceleration gradients is identically cancelled [44, 48]. In this case the only velocity-dependent contributions come from second gradients

of the gravitational field. Phase shift variations from shot to shot variations in the average velocity of the atom cloud are then smaller than the requirement if this average velocity is controlled to better than $1 \frac{\text{cm/s}}{\sqrt{\text{Hz}}}$. Since this configuration does not cancel constant accelerations, the average position of the atom clouds must still be controlled to 10 nm in order to achieve target sensitivity. The gravitational wave signal in this configuration is $\sim k_{\text{eff}} h L (\omega T)^2$ just like the Mach Zender interferometer. However, this interferometer has to run for a time $(1 + \sqrt{5})T$ instead of $2T$ in order to resonantly couple to gravitational waves of frequency $\omega \sim \frac{1}{T}$. With fixed total interferometer time, the Mach Zender configuration can probe lower frequencies than the double loop. It is therefore preferable to run the interferometer in the Mach-Zender configuration. The double loop configuration can however be used if the stringent control over the average launch velocity of the atom cloud proves to be technically challenging. The double loop configuration can also be run with the atom spending equal times in both loops (Figure 7.6 with $\alpha = 1$). Constant accelerations do not contribute to the phase shift in this configuration [44, 48]. This sequence relaxes the control required over the average launch position of the cloud but does not alleviate the control required over the average launch velocity of the cloud.

In addition to the double loop configuration, the interferometer can also be operated with the pulse sequence $\frac{\pi}{2} - \pi - \pi - \pi - \frac{\pi}{2}$ with the time between the $\frac{\pi}{2} - \pi$ and $\pi - \pi$ pulses in the ratio $\frac{1}{1+\sqrt{2}}$ (Figure 7.7). In this configuration, constant accelerations and time independent linear acceleration gradients do not contribute to the phase shift [44, 48]. The first non-zero phase shift in such an interferometer comes from the quadratic gradient $\nabla(\nabla g)$ which produces an acceleration $\sim \frac{GM_E}{R_E^2} \left(\frac{v_L^{avg} T}{R_E} \right)^2$ in a vertical terrestrial interferometer. This acceleration is orders of magnitude smaller than g and its linear gradient ∇g . Fluctuations of this acceleration due to variations in the launch position and velocity of the atom clouds can be made smaller than $10^{-15} \frac{g}{\sqrt{\text{Hz}}}$ with minimal control over these parameters. For instance, the contribution from shot to shot variations in the average velocity of the atom cloud are smaller than $10^{-15} \frac{g}{\sqrt{\text{Hz}}}$ if these variations are smaller than $1 \frac{\text{cm/s}}{\sqrt{\text{Hz}}}$. The gravitational wave signal in this multiloop configuration is $\sim k_{\text{eff}} h L (\omega T)^4$. This interferometer is equally sensitive

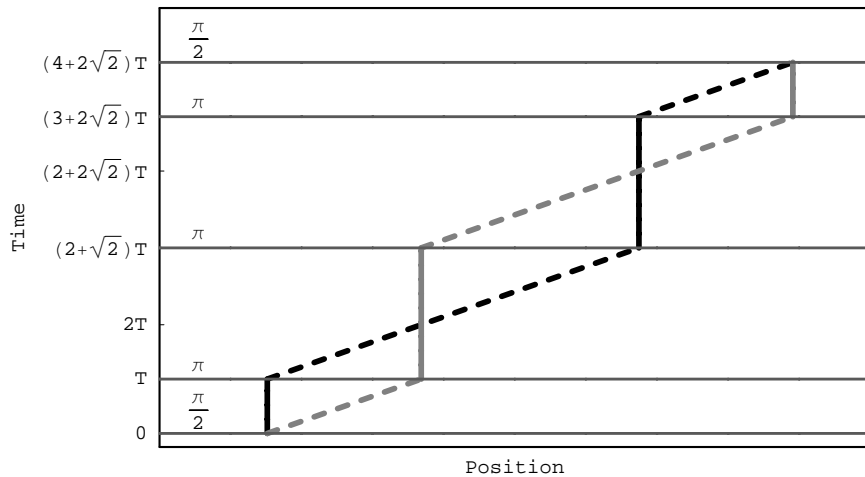


Figure 7.7: A space-time diagram of the triple loop interferometer. The black and gray lines indicate the two halves of the wave function after the initial beamsplitter. The dashed and solid lines represent the two internal states of the atom. The laser light used to manipulate the atom is shown as horizontal dark gray lines. The speed of light has been exaggerated.

to gravitational waves at the interferometer's resonant frequency ($T \sim \frac{1}{\omega}$) as the double loop configuration considered earlier but its bandwidth is suppressed by $\sim (\omega T)^2$ relative to the double loop interferometer. Furthermore, this interferometer needs to run for a time $(4 + 2\sqrt{2})T$ in order to resonantly couple to a gravitational wave of frequency $\omega \sim \frac{1}{T}$. The triple loop can be used if control over both the average launch position and velocity of the atom clouds becomes difficult.

The effects of position and velocity noise may be amplified due to the presence of local mass anomalies near the interferometer. A local anomaly is a mass distribution near the interferometer whose field changes by $\mathcal{O}(1)$ over the length of the interferometer. The phase shift from such an anomaly of mass M at a distance $R \lesssim v_R T$ from the interferometer can be calculated using the methods of [29] and was found to be

$$\Delta\phi \sim k_{\text{eff}} \left(\frac{GM}{(R v_R T)} \right) \left(1 - \left(\frac{v_L T}{R} \right) \right) T^2 + \dots \quad (7.13)$$

where v_L and $v_R = \frac{k_{\text{eff}}}{m_{\text{atom}}}$ are the launch and recoil velocity of the atoms with $v_L T \ll R$. Time varying accelerations from shot to shot variations in the average position or velocity of the atom cloud with respect to this anomaly are smaller than $10^{-15} \frac{g}{\sqrt{\text{Hz}}}$ if $\delta R_L^{avg} \lesssim 1 \frac{\mu\text{m}}{\sqrt{\text{Hz}}} \left(\frac{1000 \text{ kg}}{M} \right) \left(\frac{R}{1 \text{ m}} \right)^2$ and $\delta v_L^{avg} \lesssim 1 \frac{\mu\text{m/s}}{\sqrt{\text{Hz}}} \left(\frac{1000 \text{ kg}}{M} \right) \left(\frac{R}{1 \text{ m}} \right)^2$. The constraints on launch position and velocity demanded by local mass anomalies are less stringent than the demands imposed by the Earth's gravity gradient.

The time varying signal caused by a local mass anomaly is due to fluctuations in the relative position and velocity of the atom cloud with respect to the anomaly. Since the fractional fluctuations in these quantities can be controlled to $\sim \frac{10^{-6}}{\sqrt{\text{Hz}}}$ relatively easily, the anomaly must produce a relatively large gravitational field ($\sim 10^{-9} g$) inside the interferometer in order for these position and velocity fluctuations to cause accelerations $\sim 10^{-15} \frac{g}{\sqrt{\text{Hz}}}$. The gravitational field in the interferometer can be measured to $10^{-9} g$ using conventional gravimeters enabling the detection of mass anomalies of interest. The effects of these anomalies can then be minimized by strategically positioning mass sources that shim the gravitational field in the detector.

The measurement of g_L^{avg} can also fluctuate from shot to shot due to fluctuations δk_{eff} in the frequency of the lasers over the time scale of a second. The differential

phase shift caused by this effect is $\delta k_{\text{eff}} \nabla g L T^2$. Fractional stability in the laser frequency $\sim 10^{-11} (\frac{1 \text{ km}}{L})$ in the 1 Hz band is required to push this background below shot noise. The experiment will employ lasers with fractional stability $\sim 10^{-15}$ to tackle laser phase noise. Hence this background will be smaller than shot noise.

Timing Errors

The interferometer is initiated by the first $\frac{\pi}{2}$ pulse which hits the atom causing it to split into two arms, one moving with the original launch velocity v_L and the other with velocity $v_L + v_R$. The π pulse switches the velocities of the arms after which the final $\frac{\pi}{2}$ pulse interferes the arms. An asymmetry δT in the time between the $\frac{\pi}{2} - \pi$ and $\pi - \frac{\pi}{2}$ stages of the interferometer results in the arms spending unequal times moving with velocity $v_L + v_R$, causing a phase difference $\sim M v_R v_L \delta T = k_{\text{eff}} v_L \delta T$. In addition to the phase accrued by the atom as a result of time evolution, the atom also picks up the average phase of the laser during the atom-laser interaction. The $\frac{\pi}{2}$ and π pulses consist of $N \sim 1000$ LMT pulses each of frequency k ($k_{\text{eff}} = 2Nk$). A timing error δT changes the average laser phase of each LMT pulse by $k\delta T$ resulting in a total phase shift $\sim Nk\delta T = k_{\text{eff}}\delta T$. The net phase shift contributed by timing errors is then $\sim k_{\text{eff}}\delta T + k_{\text{eff}}v_L\delta T$. Differential measurement cancels the $k_{\text{eff}}\delta T$ term and yields a phase shift $k_{\text{eff}}\delta v_L\delta T$ where δv_L is the difference between the launch velocities of the atom clouds. We assume the shutters that control the time between the pulses can be operated with picosecond precision. With $\delta T \sim 10^{-12}$ s, this background can be made smaller than shot noise by launching the atoms such that $\delta v_L < 1 \text{ cm/s}$.

Finally, variations in the overall interrogation time of the experiment cause a time varying phase shift $\sim k_{\text{eff}}gT\delta T$ in each interferometer resulting in a differential phase shift $k_{\text{eff}}\nabla g L T \delta T$. With picosecond control over the shutters and the interrogation time of the experiment, this effect is $\sim 10^{-16} \frac{g}{\sqrt{\text{Hz}}} (\frac{L}{1 \text{ km}})$.

Effects of Rotation

For a laser fixed to the earth's surface, there is a differential Coriolis acceleration $\sim \omega_E \delta v$ between the two atom clouds where ω_E is the angular velocity of the earth

and δv is the difference between the transverse velocities of the clouds. δv is caused by thermal effects and transverse vibrations of the trap used to prepare the atom clouds. The statistical variation in the average thermal velocities of two atom clouds with $\sim 10^8$ atoms at ~ 100 picokelvin temperatures is $\lesssim 10^{-8}$ m/s. Thermal effects will cause δv to vary from shot to shot by 10^{-8} m/s. With $\omega_E \sim 10^{-4}$ rad/s, these thermal variations cause accelerations $\sim 10^{-13}g$ which is larger than shot noise.

One way to control this problem is to servo the laser's axis so that the axis remains non-rotating in an inertial frame. In this case, the only residual backgrounds arise from errors $\delta\omega$ in the servoing mechanism. The servoing apparatus can operate with nanoradian precision. With $\delta\omega \sim 10^{-9} \frac{\text{rad/s}}{\sqrt{\text{Hz}}}$, the variations in the Coriolis acceleration due to thermal effects are smaller than $10^{-15} \frac{g}{\sqrt{\text{Hz}}}$ if $\delta v \lesssim 10^{-5}$ m/s. The wobble $\delta\omega$ of the laser's axis also causes a differential centrifugal acceleration $L(\delta\omega)^2$ between the atom clouds. This acceleration is below $10^{-15} \frac{g}{\sqrt{\text{Hz}}}$ if $\delta\omega < 10^{-9} \frac{\text{rad/s}}{\sqrt{\text{Hz}}} (\frac{1 \text{ km}}{L})^{\frac{1}{2}}$.

The proposed experimental setup involves two atom interferometers vertically separated by a length $L \sim 1$ km and run by a common laser. One interferometer will then be at a distance L from the laser. The atoms in this interferometer will have a velocity $\sim L\omega \sim 10 \text{ cm/s} (\frac{L}{1 \text{ km}})$ perpendicular to the axis of the servoed laser due to the rotation of the Earth. Since these velocities have to be smaller than 10^{-5} m/s to suppress Coriolis accelerations from the jitter of the servoing apparatus, these atoms must be launched with a transverse kick that cancels the relative velocity between the laser's axis and the atom cloud to 10^{-5} m/s. These kicks could potentially be delivered using an appropriately positioned laser. The vertical vibrations of this laser will cause fluctuations in the launch velocity of the atom cloud leading to time varying accelerations as discussed in sub section 7.4.2 and these vibrations must be appropriately damped. This transverse velocity could also be cancelled by locking both atom clouds in an optical lattice and rotating the lattice itself to counter the rotation of the Earth.

The interferometer measures the component of \vec{g} along the laser's axis. Jitters $\delta\omega$ in the laser's axis will cause differential accelerations $\sim \nabla g L(\omega_E T)(\delta\omega T)$ and $\sim \nabla g L(\omega_E T)(\delta\omega_E T)$. With nanoradian stability in $\delta\omega$, $L \sim 1$ km and $T \sim 1$ s, the first term is smaller than $10^{-15} \frac{g}{\sqrt{\text{Hz}}}$. The second term is also smaller than $10^{-15} \frac{g}{\sqrt{\text{Hz}}}$

since at 1 Hz, $\delta\omega_E \ll 10^{-7} \frac{\text{rad/s}}{\sqrt{\text{Hz}}}$.

The need to servo the lasers emerged from the demand to suppress Coriolis accelerations due to thermal fluctuations in the atom cloud. The experiment can be performed without servoing the lasers if the interferometer is operated in the multiloop configurations described in sub section 7.4.2. The Coriolis acceleration caused by a laser rotating with a constant angular velocity and an atom cloud moving with a constant transverse velocity is constant. If the interferometer is run in the multiloop configurations, the phase shift due to this acceleration can be completely cancelled eliminating the need to servo the laser. In the multiloop configuration, the interferometer has a smaller bandwidth but has the same sensitivity to gravitational waves at its resonant frequency as the Mach Zender configuration. In these multiloop configurations, rotational backgrounds arise due to instabilities $\delta\omega$ in the rotation of the laser's axis leading to Coriolis and centrifugal accelerations $\sim \delta\omega\delta v + L(\delta\omega)^2$. These accelerations are smaller than $10^{-15} \frac{g}{\sqrt{\text{Hz}}}$ if $\delta\omega \lesssim 10^{-9} \frac{\text{rad/s}}{\sqrt{\text{Hz}}}$.

Due to unavoidable misalignments, the earth's gravitational field will have a component along the direction transverse to the laser's axis. This component will cause a differential velocity $\sim \nabla g L \sin(\theta)T$ between the atom clouds where θ is the angle between the local gravitational field and the laser's axis. Jitter in the lasers' axis causes an acceleration $\sim \delta\omega \nabla g L \sin(\theta)T$. The interferometer needs to be operated with $\theta \sim 0.01(\frac{1 \text{ km}}{L})$ for this acceleration to be smaller than $10^{-15} \frac{g}{\sqrt{\text{Hz}}}$.

Effects of Magnetic Fields

A magnetic field B changes the energy difference between the hyperfine ground states in the $m = 0$ sublevel of the atom by an amount $\alpha_{\text{ZC}} B^2$ where α_{ZC} is the Zeeman Clock shift of the atom. If the magnetic field varies by δB during the course of the experiment, the energy difference between the atom states during the $\frac{\pi}{2} - \pi$ stage will be different from the energy difference during the $\pi - \frac{\pi}{2}$ stage of the experiment. This produces a phase shift $\sim \alpha_{\text{ZC}} B_0 \delta B T$ which must be smaller than the per shot phase sensitivity of the interferometer $\sim 10^{-5}$. With a bias field $B_0 \sim 100 \text{ nT}$ and $\alpha_{\text{ZC}} \sim 1 \frac{\text{kHz}}{\text{G}^2}$ (for Rubidium), this phase shift can be made smaller than 10^{-5} rad if δB is smaller than $1 \frac{\text{nT}}{\sqrt{\text{Hz}}}$. Time varying magnetic fields in the interferometer are

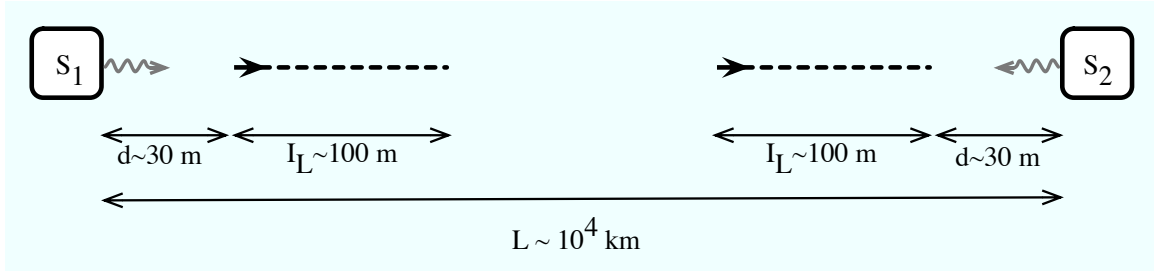


Figure 7.8: The proposed setup for a satellite experiment. Two satellites S_1 and S_2 house the lasers and atom sources. The atoms are brought a distance $d \sim 30 \text{ m}$ from the satellites at the start of the interferometer sequence. The dashed lines represent the $I_L \sim 100 \text{ m}$ path travelled by the atoms during the interferometer sequence. The gray lines represent the paths of the lasers along the axis between the satellites. In practice it is desirable to have a third satellite in a LISA-like constellation with such a pair of interferometers operated along each arm.

caused by time variations in the applied bias field and the Earth's magnetic field. The current source used to create the bias field may be made stable to 6 digits in the 1 Hz band, resulting in 1 Hz variations due to the 100 nT bias field smaller than $1 \frac{\text{nT}}{\sqrt{\text{Hz}}}$. Magnetic fields from external sources like the Earth can be shielded to the required $1 \frac{\text{nT}}{\sqrt{\text{Hz}}}$ level by following the techniques of [78].

7.5 Satellite Based Experiment

The search for gravitational waves in the sub-Hertz band on the Earth is impeded by time varying local gravitational fields due to seismic and atmospheric activity. Additionally, the atom interferometer is maximally sensitive to a gravitational wave of frequency ω when the interrogation time T of the experiment is such that $T \sim \frac{1}{\omega}$. Interrogation times larger than 10 s are difficult to achieve in a terrestrial interferometer, since the atoms are in free fall. We are thus lead to consider satellite-based interferometer configurations to search for gravitational waves in the sub-Hertz band.

7.5.1 Experimental Setup

The atom interferometer configurations discussed in section 7.3 can be realized in a satellite experiment by using two satellites (S_1 and S_2 in Figure 7.8) separated by a long baseline L . As we will show, the satellites can act as base stations (housing lasers and atom sources) to operate $I_L \sim 100$ m interferometers along the axis between the satellites. The atoms are brought a distance $d \sim 30$ m from the satellites at the start of the interferometer sequence. The atoms travel a distance $I_L \sim 100$ m during the course of the interferometry executed by the lasers in the satellites. As in the terrestrial interferometer, the experiment measures the differential phase shift $\sim k_{\text{eff}} h L$ between two interferometers separated by L and operated by common lasers in order to suppress backgrounds from low frequency vibrations and phase noise of the lasers. The satellites could be placed in heliocentric or geocentric orbits.

It is desirable to operate the atom interferometers outside the satellites. As we will show, this suppresses backgrounds, resulting in significantly reduced satellite requirements. Importantly, it ameliorates the control required over the position of the spacecraft. The gravitational force on the atom from the spacecraft will vary in time due to uncontrolled motion of the spacecraft and will mimic a gravitational wave signal. If the atoms are far from the spacecraft, the magnitude of this acceleration is reduced and makes the interferometer less sensitive to fluctuations in the position of the spacecraft. Additionally this increases the available interferometer region, improving sensitivity by allowing longer interrogation times and larger recoil velocities.

The two atom interferometers can be constructed by initially placing atoms a distance $I_L + d$ from S_2 towards S_1 (Figure 7.8) using laser manipulations. Similarly, a cloud from S_1 can be brought a distance d towards S_2 . After the clouds are appropriately positioned, the same laser pulses can be used to operate both interferometers. We will argue (see Section 7.5.1) that it should be possible to run the interferometer outside the spacecraft to distances ~ 100 m. With interrogation times $T \sim 100$ s, the length of the interferometer region limits $k_{\text{eff}} \sim 10^9$ m $^{-1}$.

In order to detect a gravitational wave it is only necessary to have one such baseline containing a pair of atom interferometers. However, it may be desirable to have a third satellite in a LISA-like constellation with a pair of atom interferometers operated

along each baseline. The addition of the third satellite provides another gravitational wave channel. As discussed in sub section 7.4.2, since the gravitational wave signal in each detector depends upon the orientation of the detector relative to the incident direction and the polarization of the gravitational wave, the cross-correlated sensitivity of the constellation will be set by the stochastic noise floor. The addition of the third satellite can be useful in further suppressing laser phase noise (see Section 7.5.2). Additionally, independent correlated measurements would increase the confidence of detection. Detecting a stochastic background of gravitational waves requires cross-correlating the output from two independent gravitational wave detectors. Furthermore, with three such single-axis gravitational wave detectors whose axes point in different directions, it is possible to determine information on the direction of the gravitational wave source.

The signal in the interferometer is directly proportional to the size of the baseline L and the effective momentum k_{eff} transferred by the atom optics. The transfer of a large momentum will impart a large recoil velocity to the atom. The operation of the interferometer with a large recoil velocity requires the interferometer region I_L to be long and hence the limit on I_L imposed by the satellite will limit k_{eff} . The detection of a time varying signal from a gravitational wave of frequency f requires a data taking rate $f_d \gtrsim 2f$. As discussed in sub section 7.4.1, this requires the operation of concurrent atom interferometers along the common satellite axis. In the following, we examine the limits imposed on these quantities in a satellite experiment.

Baseline Limit from Atom Optics

Gravitational wave experiments benefit from long baselines since the signal increases linearly with the baseline. The most stringent limit on the baseline is imposed by the need to drive the atomic transitions that create the beamsplitter and mirror pulses using a laser that is a large distance away on the far satellite. The laser field from the nearby satellite can be intense, but at large distances the laser field from the far satellite will necessarily spread and lose intensity.

To find this limit, consider an atom in the presence of the laser field from the nearby satellite with intensity I_n and from the far satellite with intensity I_f . The

Rabi frequency Ω_{st} of stimulated 2-photon transitions in Fig. 2.3(a) is [109]

$$\Omega_{\text{st}} = \left| \frac{\langle e | \mathbf{d} \cdot \mathbf{E}_n | 1 \rangle \langle e | \mathbf{d} \cdot \mathbf{E}_f | 2 \rangle}{2\Delta} \right| \approx \frac{\Gamma^2}{4\Delta} \sqrt{\frac{I_n I_f}{I_{\text{sat}}^{(e1)} I_{\text{sat}}^{(e2)}}} \quad (7.14)$$

where Δ is the detuning from the intermediate state $|e\rangle$ and Γ is the decay rate of the excited state. The saturation intensity, I_{sat} is defined by $\frac{I}{I_{\text{sat}}^{(e1)}} = 2 \left(\frac{\Omega_{e \rightarrow 1}}{\Gamma} \right)^2$ where $\Omega_{e \rightarrow 1}$ is the resonant two-level Rabi frequency between the excited state and state $|1\rangle$ [109]. Note that I_{sat} is an atomic property independent of laser intensity. For simplicity we assume that the decay rate and dipole matrix element are independent of the choice of state $|1\rangle$ or $|2\rangle$, i.e. $I_{\text{sat}}^{(e1)} \approx I_{\text{sat}}^{(e2)}$. The intensity I_f of the far satellite decreases as the baseline is increased, decreasing Ω_{st} . The width of the 2-photon atomic transition is set by Ω_{st} and if Ω_{st} becomes too small, the transitions can become very velocity selective due to Doppler detuning. To avoid loss of SNR, the initial thermal velocity spread of the atoms must be smaller than the velocity selection imposed by Ω_{st} . Thus the lowest attainable temperature sets a lower limit on Ω_{st} . With cloud temperatures ~ 0.1 nK, the Rabi frequency Ω_{st} must be $\gtrsim 2\pi (10^2 \text{ Hz})$.

To maximize sensitivity, a significant fraction of the atoms should not undergo spontaneous 2-photon transitions during the time the atom is in the presence of the light. A spontaneous 2-photon transition can occur when one laser field (in practice the more intense one) drives the atom up to the intermediate state and this state then decays due to spontaneous emission. In this case the atom gets a momentum kick in an arbitrary direction and will be lost from the interferometer. The spontaneous transition rate due to the near laser is [101, 103]

$$R = \frac{\frac{\Gamma}{2} \frac{I_n}{I_{\text{sat}}}}{1 + 4 \left(\frac{\Delta}{\Gamma} \right)^2 + \frac{I_n}{I_{\text{sat}}}}. \quad (7.15)$$

The detuning can be eliminated using Eqn. (7.14). The total time for which the atom is in the presence of the light must be smaller than $\frac{1}{R}$. Since we wish to use LMT beamsplitters that deliver N photon kicks to the atom, the atom will be in the presence of the transition light for time $\sim \frac{N}{\Omega_{\text{st}}}$. The need to suppress spontaneous

emission yields $R \lesssim \frac{\Omega_{\text{st}}}{N}$.

With stimulated Rabi frequency $\Omega_{\text{st}} \sim 2\pi(10^2 \text{ Hz})$ and spontaneous emission rate $R \sim (10 \text{ s})^{-1}$, we find that baselines $L \sim 10^3 \text{ km}$ can be achieved with lasers of waist $\sim 0.5 \text{ m}$ and power $\sim 1 \text{ W}$. We have assumed atomic parameters (e.g. for Rb or Cs) $\lambda \approx 1 \mu\text{m}$, $I_{\text{sat}} \approx 1 \frac{\text{mW}}{\text{cm}^2}$, and $\Gamma \approx 3 \times 10^7 \frac{\text{rad}}{\text{s}}$ [101, 103], thus requiring a detuning $\Delta \approx 20 \text{ GHz}$ to reach this limit. This configuration would allow the interferometer to use $N \sim 100$ LMT beamsplitters. This is the main limitation on the distance between the satellites. Improvements on this limit, either through higher laser power, an optimized choice of atom transitions or improved cooling techniques that can allow the transitions to proceed at smaller Rabi frequencies should allow direct enhancements in the final sensitivity.

Environmental Constraints on the Interferometer Region

The length of each interferometer must be at least $v_r T$ (where v_r is the recoil velocity of the atom) since the two arms of the interferometer will separate by $v_r T$ during the course of the experiment. The recoil velocity v_r is equal to $\left(\frac{k_{\text{eff}}}{M_a}\right)$, where k_{eff} is the momentum transferred to the atom and M_a is the mass of the atom. For a fixed length I_L , an interrogation time T requires $v_r < \frac{I_L}{T}$. Since the signal scales linearly with k_{eff} , we would like to make I_L as large as possible. If the atom trajectories are restricted to lie within the spacecraft, then I_L has to be smaller than the typical dimensions of spacecraft $\sim 1 \text{ m}$. The atom interferometer requires the laser and the atom source be placed inside the satellite, near their power sources. However, the diffuse atom cloud trajectories that form the arms of the interferometer need not be inside the satellite.

Collisions of the atoms with background gas (e.g. solar wind) and photons are the major problem posed by the environment to the atom interferometer. These collisions cause decoherence and atoms that undergo such interactions cannot engage in quantum interference. Collisions are therefore not a source of noise since they do not cause phase shifts. However, by knocking atoms away from the atom cloud, collisions reduce the number of atoms available to do the experiment, thereby decreasing the sensitivity of the instrument.

Solar photons are a source of decoherence. The interaction cross section of the

photon with the atom is appreciable only if the frequency of the photon is within the width of an atomic transition. For example, for Rubidium the most important transition in this band is the 780 nm line with a width of a few MHz. At a distance of 1 AU, the solar spectral intensity around 780 nm is $\sim 1 \frac{\text{W}}{\text{m}^2 \text{nm}}$. Thus the intensity within the atomic linewidth is $\sim 10^{-5} \frac{\text{W}}{\text{m}^2}$. The number density of photons within this line is then $n \sim 10^5 \text{ m}^{-3}$. The resonant photon-atom scattering cross section is $\sigma \sim \lambda^2 = (780 \text{ nm})^2$. The mean photon scattering rate for an atom in the sun's light is then $n\sigma c \sim 10 \text{ s}^{-1}$. This is a severe limit on the possible interrogation time for the atom interferometer and so must be avoided. There are several possible solutions.

Satellite experiments like the James Webb Space Telescope (JWST) mission rely on the use of large $\sim 200 \text{ m}^2$ ultra-light sunshields ($\sim 2.5 \text{ kg}$) to protect the satellite from solar radiation. These shields can reduce the solar intensity from $\sim 1000 \frac{\text{W}}{\text{m}^2}$ to $\sim 10 \frac{\text{mW}}{\text{m}^2}$ [110, 111]. The decoherence time scale due to the residual solar flux is $\sim 10^{-4} \text{ s}^{-1}$ which is significantly longer than the time scales of interest to this experiment. In this case the size of the shield would be one limit on the size of the atom path. Another possibility is to place the satellites in a lunar or geocentric orbit. If the experiment is done in such an orbit, then the satellites will spend an order one fraction of the time on the dark side of the moon/earth where there is no problem (a similar estimate for a 300 K blackbody spectrum gives a very low scattering rate). This leads to an order one loss of duty cycle and a small loss of statistical sensitivity. It might also be possible to perform the experiment farther from the sun to reduce the solar intensity, though this would presumably increase the difficulty and expense while still limiting interrogation times.

The environment outside the satellite is dominated by the solar wind composed of protons and electrons with a number density $\sim 10^7 \frac{\text{particles}}{\text{m}^3}$ moving at velocities $\sim 500 \text{ km/s}$. The typical interaction cross-section of these particles with the atom is $\sim 10^{-18} \text{ m}^2$ leading to mean collision times $\gg 10^3 \text{ s}$. The local environment near the spacecraft is less pristine than the space vacuum due to emissions from the spacecraft. In order to make use of the local space environment to run the interferometer, the craft must be designed so that such emissions are not in the direction of the atom trajectories.

The atom will be subjected to the interplanetary magnetic field if the experiment is done outside the spacecraft. In order to suppress phase shifts from magnetic fields, the atom must be placed in a magnetically insensitive $m = 0$ state in the direction set by the field. The Rabi frequency of the atomic transition is set by the internal state of the atom and the laser must be tuned to match this frequency. Since, in the random interplanetary magnetic field, the atom's spin precesses rapidly, the spin of the atom will change as the direction of the magnetic field changes. If the direction of the magnetic field changes over the length of the interferometer, the atom will evolve away from the original $m = 0$ state. The laser's frequency is however tuned to the original $m = 0$ state. The interaction between the laser and the atom will excite, for example, $m = \pm 1$ states along the new axis of quantization. Pollution into these states will cause phase shifts that are a background to the experiment.

The interplanetary planetary magnetic field at 1 AU is ~ 5 nT and has a correlation length ~ 0.01 AU. The drift in the direction of the field is smaller than 5° over 10 minutes during an average time interval but can be as large as 10° over 10 minutes during noisier times [112]. The phase shift due to these direction changes in the magnetic field are smaller than the shot noise requirements of this experiment (see subsection 7.5.2). In addition to this slow drift, the magnetic field also exhibits sharp discontinuities in its direction. These sharp directional discontinuities are separated by periods of an hour [112] and are not a problem to an interferometer with interrogation time smaller than 100 s. The direction of the magnetic field in the interferometer region can be further stabilized by attaching a permanent magnet to the spacecraft, coaxial to the atomic trajectory. A bar magnet of size $1\text{ m} \times 10\text{ cm} \times 10\text{ cm}$ with magnetization $\sim 10^7$ A/m can provide magnetic fields ~ 20 nT out to distances ~ 100 m. This field is larger than the interplanetary magnetic field ~ 5 nT and can enhance the stability of the direction of the magnetic field in the interferometer. The experiment relies on differential measurement strategies which requires both interferometers to be operated by the same set of lasers. The correlation length of the interplanetary magnetic field is significantly larger than the baseline $L \sim 10^3$ km of this experiment. With the addition of the ~ 20 nT bias field, the magnetic field direction in the two interferometers can be sufficiently aligned to enable the same lasers to operate both

interferometers.

The torque on the spacecraft from the action of the interplanetary magnetic field on the external magnet is $\sim 10^{-4}$ Nm, which is of the same order of magnitude as the torque produced by solar pressure on the satellite. Since the forces on the spacecraft due to the external magnet are comparable to the force from solar pressure, the addition of the magnet will not significantly alter the dynamics of the spacecraft control system. With the addition of the bias field from the permanent magnet, the interferometer can be run over at least $I_L \sim 100$ m. Interferometer lengths longer than 100 m may be achievable when the interplanetary magnetic field is quiet.

The hardware required to measure the phase shift in the interferometer has to be housed in the spacecraft. A normalized measurement of the phase shift is done by counting the number of atoms in each final state of the atom after the interferometer pulse sequence. If the experiment is performed outside the spacecraft, the counting must be performed with detectors located on the spacecraft. Remote detection of an atom in a given internal state can be done using absorption imaging wherein a light beam, whose frequency is tuned to an atomic resonance accessible from the internal state of interest, is pulsed from one spacecraft to the other. The atoms that are in the internal state of interest will absorb these photons. A photodetector on the other spacecraft will measure the change in the intensity of the initial beam measuring the number of absorbed photons and hence the number of atoms in the internal state of interest.

The absorption detection technique must be sufficiently sensitive to detect the required phase sensitivity $\sim 10^{-4}$ (see section 7.7) of this experiment. With $N_a \sim 10^8$ atoms in the cloud, a phase sensitivity $\sim 10^{-4}$ requires the detection scheme to measure changes in the number as small as $\sqrt{N_a} \sim 10^4$ atoms. The absorption cross-section of the atom with the resonant laser light of wavelength λ is $\sigma_{\text{abs}} \sim \lambda^2 \sim (1\mu\text{m})^2$. If the detection is done over a period $\delta\tau$, then the total number of photons scattered by $\sqrt{N_a} \sim 10^4$ atoms is $N_s \sim \sqrt{N_a} \left(\frac{I_f}{k} \right) \sigma_{\text{abs}} \delta\tau$ where $k \sim 10^{-19}$ J is the energy of the detection photon. This number must be larger than the photoelectron shot noise $\sim \sqrt{\left(\frac{I_f}{k} \right) A \delta\tau}$ over the detection area A . The size of the detection area (e.g. the size of a lens) must be as big as the typical size of the

atom clouds used in this experiment $A \sim (10\text{ cm})^2$. With these parameters, a satellite experiment with a baseline $L \sim 10^3\text{ km}$ and a detection laser with intensity $\sim 10^{-8}\frac{\text{W}}{\text{cm}^2}$ laser and a $\sim 1\text{ m}$ waist housed on the distant satellite can image the atom cloud with the necessary precision in a detection time $\delta\tau \sim 0.1\text{ s}$. Each atom undergoes $\left(\frac{I_f}{k}\right)\sigma_{\text{abs}}\delta\tau \sim 10^2$ absorptions during this imaging time. Since the atom undergoes rapid spontaneous emission upon excitation, absorption imaging must be performed between atomic states that have ~ 100 cycling transitions to prevent loss of atoms through spontaneous emission into other atomic states.

These arguments suggest that it should be possible to run the interferometer outside the spacecraft to distances $\sim 100\text{ m}$.

Limit on Data Taking Rate

The detection of a time varying signal from a gravitational wave of frequency f requires a data taking rate $f_d \gtrsim 2f$. As discussed in sub section 7.4.1, this requires the operation of concurrent atom interferometers along the common satellite axis. Concurrent operation of atom interferometers requires that the laser fields that trigger interferometry in one interferometer not cause transitions in the other interferometers in the common beam axis. This can be achieved by launching the interferometers with different launch velocities so that the interferometers are all doppler detuned from one another. The width of a 2-photon transition is equal to the Rabi frequency Ω_{st} of the transition. Two interferometers are doppler detuned if the relative velocity between them is $\sim 10^{-4}\text{ m/s} \left(\frac{\Omega_{\text{st}}}{2\pi(10^2\text{ Hz})}\right)$. While doppler detuning prevents unwanted stimulated transitions, the laser field can drive spontaneous 2-photon transitions, as discussed in subsection 7.5.1. Following the discussion in subsection 7.5.1, the spontaneous emission rate is $R \sim (10\text{ s})^{-1}$ in a configuration with baseline $L \sim 10^3\text{ km}$, with $\sim 1\text{ W}$ lasers and stimulated Rabi frequency $\Omega_{\text{st}} \sim 2\pi(10^2\text{ Hz})$. The operation of q concurrent atom interferometers with transition times $\sim \frac{N}{\Omega_{\text{st}}}$ requires $q\frac{N}{\Omega_{\text{st}}} \lesssim \frac{1}{R}$. With the beam parameters described above, we can operate $q \sim 10$ concurrent interferometers.

The interferometers will be operated outside the satellites with the phase shift in

each interferometer measured through absorption detection. The process of measuring the phase shift in one interferometer through this technique should not affect the other interferometers operating in the beam line. This can be achieved by initially performing a velocity selective stimulated Raman transition that takes the atom state at the end of the interferometer (the ‘interferometer state’) into another long lived ground state of the system (the ‘detection state’), detuned from the original interferometer state. The phase shift can be measured by imaging the detection state. For example, in Rubidium, the hyperfine interaction splits the ground state into states separated by $\sim 2\pi$ (6.8 GHz). One of these states could be used to run the interferometer (the interferometer state) and velocity selective stimulated Raman transitions can be used to populate the other state (the detection state) prior to detection. A Rabi frequency $\sim 2\pi(10^2 \text{ Hz})$ for this stimulated Raman process can be achieved through laser and beam features described in the preceding paragraph. The spontaneous emission rate induced by this process is then $\sim (10 \text{ s})^{-1}$ which is not a problem for the operation of the interferometers since this light will be on for only $\sim 0.01 \text{ s}$ during detection. The spontaneous emission rate for the atoms in the interferometer state due to the $\sim 10^{-8} \frac{\text{W}}{\text{cm}^2}$ detection light tuned to the detection state is $\sim (10^5 \text{ s})^{-1}$ and is also not a problem for the experiment.

With this configuration, the data taking rate f_d can be $\lesssim 1 \text{ Hz} \left(\frac{10 \text{ s}}{T}\right)$ where T is the interrogation time of the experiment, limited by spontaneous emission caused by the laser light used to operate the interferometers. This is the main limitation on the data taking rate of the experiment. Improvements on this limit, either through higher laser power, an optimized choice of atom transitions or improved cooling techniques that can allow the transitions to proceed at smaller Rabi frequencies should allow direct enhancements to this rate.

7.5.2 Backgrounds

Our configuration consists of two satellites in orbit separated by $L \sim 10^3 \text{ km}$. The satellites act as base stations and run the atom interferometers along their axis using common laser pulses. With a stabilizing magnetic field $\gtrsim 20 \text{ nT}$ provided by a

permanent magnet housed in the spacecraft, the satellite environment permits the operation of the atom interferometer out to distances $I_L \sim 100$ m from the satellite and for interrogation times ~ 100 s. Prior to launch, the atoms are positioned at distances $d \sim 30$ m and $d + I_L$ from their base stations S_1 and S_2 respectively using laser manipulations (Figure 7.8). The atoms are then launched with a common launch velocity and the interferometry is performed using common laser pulses.

The differential acceleration caused by a gravitational wave of amplitude h and frequency ω is $hL\omega^2$ causing a phase shift $k_{\text{eff}}hL\omega^2T^2$. A $L \sim 10^3$ km long baseline interferometer can detect gravitational waves of amplitude $h \sim 10^{-23}$ with $\sim 10^6$ s of integration time if it is sensitive to accelerations $\sim 10^{-19}g(\frac{\omega}{10^{-2}\text{ Hz}})^2$. The strain sensitivity of such a configuration would be $\sim \frac{10^{-20}}{\sqrt{\text{Hz}}}$. The proposed experiment could reach target sensitivity using $200k$ LMT beamsplitters and atom statistics phase sensitivity $\frac{1}{\sqrt{N_a}} \sim 10^{-4}$ using ensembles of $N_a \sim 10^8$ atoms and interrogation times $T \sim \frac{1}{\omega}$. Phase shifts from noise sources must be made smaller than 10^{-4} . In particular, acceleration backgrounds should be less than $\sim 10^{-19}g(\frac{\omega}{10^{-2}\text{ Hz}})^2$. We will assume that a LISA-like three satellite atom interferometer constellation is placed in orbit. As discussed in sub section 7.5, the cross-correlated sensitivity of the gravitational wave channels thus produced is limited by the stochastic noise floor. Thus we can assume that the noise in the entire set of detectors is stochastic, even if certain noise sources have long correlation times in any individual detector. In the following, we discuss these stochastic noise sources and strategies to suppress them to the level required to detect gravitational waves with strain sensitivity $\sim \frac{10^{-20}}{\sqrt{\text{Hz}}}$ in the 10^{-2} Hz - 1 Hz band.

Vibrations and Laser Phase Noise

Vibration and laser phase noise issues were discussed in Section 7.4.2. The solutions proposed to address these issues in the terrestrial interferometer can also be used for the space based experiment. Following the analysis in that section, contributions from the vibration of the lasers to the phase shift are smaller than shot noise if these vibrations are smaller than $10^{-5}\frac{\text{m}}{\sqrt{\text{Hz}}} \left(\frac{10^{-2}\text{ Hz}}{\nu}\right)^{\frac{3}{2}} \left(\frac{10^3\text{ km}}{L}\right)$ at frequencies $300\text{ Hz} \left(\frac{10^3\text{ km}}{L}\right) \gtrsim \nu \gtrsim 10^{-2}\text{ Hz}$.

Additionally, in space, an alternate strategy to handle laser phase noise is to use the same passive laser to run interferometers along two non parallel baselines in a LISA-like three satellite configuration. Each baseline consists of two interferometers. The interferometers along each baseline are operated by a common control laser. The passive laser is placed at the intersection of the two baselines with appropriate optical beamsplitters so that the beam from the passive laser is shared by both baselines. The same pulses from the passive laser can trigger transitions along the interferometers in both baselines if the control lasers along the two baselines are simultaneously triggered. The laser phase noise in the difference of the differential phase shift along each baseline is greatly suppressed since phase noise from the control laser is common to the interferometers along each baseline and the phase noise from the passive laser is common to the baselines. The gravitational wave signal is retained in this measurement strategy since the gravitational wave will have different components along the two non parallel baselines.

The contribution to the differential phase shift along each baseline due to a drift δk in the frequency of the laser is suppressed by the arm length of the baseline (see Section 7.4.2). The residual contribution of this frequency drift to the difference of the differential phase shift along each baseline is $\delta k \delta L$ where δL is the difference in the length of the two baselines. The effect of this contribution can be cancelled to the extent to which the arm length difference δL is known. With ~ 1 m knowledge of the arm lengths, these contributions are smaller than shot noise if the frequency drift δk of the laser is controlled to better than $\sim 10^4 \frac{\text{Hz}}{\sqrt{\text{Hz}}}$ at frequencies $\omega \sim 10^{-2}$ Hz. In addition to this effect, differences δT between the timing of the control lasers that operate the interferometer will also change the phase of the passive laser that is imprinted along the interferometers in the two baselines. The phase shift due to this effect is $\sim \delta k \omega \delta T L$. With $\delta k \lesssim 10^4 \frac{\text{Hz}}{\sqrt{\text{Hz}}}$ at frequencies $\omega \sim 10^{-2}$ Hz, this phase shift is smaller than the per shot phase sensitivity 10^{-4} of this experiment if the two control lasers are synchronized with $\delta T \lesssim 100\mu\text{s}$.

In addition to classical sources of phase noise discussed above, the quantum nature of the laser field will contribute to noise in the imprinted phase. This quantum noise was computed in [113] and was found to be $\sim \frac{1}{\sqrt{N_\gamma}}$ where N_γ is the total number of

photons that form the coherent state of the laser field. The interferometers in this experiment are operated with ~ 1 Watt lasers with transition times $\sim 10^{-2}$ s leading to $N_\gamma \sim 10^{17}$. Phase noise in the interferometer from the quantum nature of light is negligibly small.

Newtonian Gravity Backgrounds

The gravitational field of the satellite will cause a phase shift in the interferometer. Since the gravitational field of the spacecraft changes by $\mathcal{O}(1)$ over the length of the interferometer, the spacecraft is a local mass anomaly of mass M at a distance $d_I \lesssim v_R T$ from the interferometer (subsection 7.4.2). The phase shift in the interferometer due to the spacecraft is given by [29]

$$\Delta\phi \sim k_{\text{eff}} \left(\frac{GM}{(d_I v_R T)} \right) \left(1 - \left(\frac{v_L T}{d_I} \right) \right) T^2 + \dots \quad (7.16)$$

when the launch velocity v_L of the atom cloud satisfies $v_L T \ll d_I$ and the recoil velocity v_R is such that $d_I \lesssim v_R T$.

The relative distance between the spacecraft and the atom will change due to random motions of the spacecraft. Additionally, the average initial position of the atom clouds with respect to the spacecraft will also change from shot to shot due to thermal variations in the atom clouds and vibrations of the trap. A variation δR in this distance due to these effects will cause an acceleration $\sim \frac{GM}{d_I v_R T} \frac{\delta R}{d_I}$. This acceleration is smaller than $\sim 10^{-19} g (\frac{\omega}{10^{-2} \text{ Hz}})^2$ if $\delta R(\omega) \lesssim 10 \frac{\mu\text{m}}{\sqrt{\text{Hz}}} (\frac{\omega}{10^{-2} \text{ Hz}})^{\frac{3}{2}} (\frac{d_I}{30 \text{ m}})^2 (\frac{1000 \text{ kg}}{M})$. With $N_a \sim 10^8$ atoms, shot to shot variations in the central position of the atom clouds due to thermal fluctuations can be made smaller than $10 \frac{\mu\text{m}}{\sqrt{\text{Hz}}}$ by confining the atoms within traps of size $\sim 1 \text{ cm} \sqrt{\frac{N_a}{10^8}}$. The atom trap and the spacecraft must be engineered so that their vibrations at frequency ω are smaller than $10 \frac{\mu\text{m}}{\sqrt{\text{Hz}}} (\frac{\omega}{10^{-2} \text{ Hz}})^{\frac{3}{2}} (\frac{d_I}{30 \text{ m}})^2 (\frac{1000 \text{ kg}}{M})$.

The average launch velocity v_L of the atom cloud will change from shot to shot due to thermal variations in the atom clouds. These variations δv_L will change the trajectory of the atoms in the gravitational field of the spacecraft. Due to the non-zero gradient of this field, these trajectories will experience different gravitational fields resulting in time varying accelerations $\sim \frac{GM}{d_I v_R T} \frac{\delta v_L T}{d_I}$. This acceleration is smaller than

$10^{-19} g (\frac{\omega}{10^{-2} \text{ Hz}})^2$ if $\delta v_L(\omega) \lesssim 100 \frac{\text{nm/s}}{\sqrt{\text{Hz}}} (\frac{\omega}{10^{-2} \text{ Hz}})^{\frac{5}{2}} (\frac{d_I}{30 \text{ m}})^2 (\frac{1000 \text{ kg}}{M})$. The atom cloud used in this experiment will contain $N_a \sim 10^8$ atoms. Thermal fluctuations in the average velocity of this cloud are smaller than $100 \frac{\text{nm/s}}{\sqrt{\text{Hz}}}$ if the cloud is cooled to temperatures $\sim 100 \text{ pK} \sqrt{\frac{N_a}{10^8}}$. Thus the thermal velocity of the atoms do not limit the detection of gravitational waves in the frequency band and sensitivities of interest in this paper.

We note that the control over the position and velocity of the spacecraft required by this experiment are weaker than the requirements of the LISA mission. LISA's inertial masses need to be placed inside the spacecraft since these masses must be shielded from the external environment. This increases the gravitational force of the spacecraft on the inertial masses making the inertial masses more sensitive to fluctuations in the position of the spacecraft. In the atom interferometer, the inertial atoms do not require the protection of the spacecraft and the experiment can be performed at distances $d_I \sim 30 \text{ m}$ from the spacecraft thereby decreasing the gravitational acceleration of the atoms by a factor of 10^4 relative to LISA [114]. The decreased gravitational acceleration makes the interferometer less sensitive to vibrations of the spacecraft.

Timing Errors

The effect of asymmetries in the time between the $\frac{\pi}{2} - \pi$ and $\pi - \frac{\pi}{2}$ pulses were discussed earlier under backgrounds for the terrestrial interferometer. A timing error δT causes a differential phase shift $\sim k_{\text{eff}} \Delta v_L \delta T$ where Δv_L is the relative launch velocity between the atom clouds. This phase shift must be smaller than the per shot phase sensitivity of the instrument $\sim 10^{-4}$. With picosecond control over δT , this background is smaller than shot noise if the atoms are launched such that $\Delta v_L < 10 \text{ cm/s}$. If the spacecrafts are in solar orbits separated by a distance $L \sim 10^3 \text{ km}$, then the relative velocity between the spacecrafts is $\sim 10 \text{ cm/s} (\frac{L}{10^3 \text{ km}})$. But, this velocity is transverse to the interferometer baselines and hence the atoms can be launched with relative velocities smaller than 10 cm/s along the baseline.

Effects of Rotation

The angular velocity of one spacecraft relative to the other is equal to its orbital angular velocity $\omega_S \sim 10^{-7}$ rads/s around the sun at ~ 1 AU. The atom clouds are also in orbits around the sun and will therefore rotate around the passive laser housed in the spacecraft S_2 with the same angular velocity ω_S . The laser axis will always be kept along the line between the satellites. If this axis rotates with angular velocity ω_S , transverse velocities v_T of the atom cloud result in Coriolis accelerations $\sim \omega_S v_T$. In an atom cloud with $N_a \sim 10^8$ atoms cooled to $100 \text{ pK} \sqrt{\frac{N_a}{10^8}}$ temperatures, the average transverse velocity of the clouds will change from shot to shot by $\sim 10^{-8}$ m/s. These thermal variations cause accelerations $\sim 10^{-16}g$ which are higher than the required $\sim 10^{-19}g(\frac{\omega}{10^{-2} \text{ Hz}})^2$ acceleration tolerance of this experiment.

This problem can be tackled by fixing the direction of the laser's axis with respect to an inertial reference. The Coriolis acceleration due to the thermal velocity $v_T \sim 10^{-8}$ m/s of the atom cloud is smaller than the shot noise $10^{-19}g(\frac{\omega}{10^{-2} \text{ Hz}})^2$ of this experiment if the residual rotational velocity $\delta\omega$ of the laser axis is smaller than 10^{-10} rads/s. Control over the rotation axis at the level of 10^{-14} rads/s has been achieved [115]. However, if the laser axis is inertial, the satellite at distance L away from it will have a transverse velocity $L\omega_S \sim 10 \text{ cm/s} (\frac{L}{10^3 \text{ km}})$ with respect to the laser axis. The residual rotational velocity $\delta\omega$ of the laser axis couples to this transverse velocity and causes a Coriolis acceleration $\sim L\omega_S\delta\omega$ which is smaller than $10^{-19}g(\frac{\omega}{10^{-2} \text{ Hz}})^2$ if $\delta\omega$ is smaller than 10^{-17} rads/s ($\frac{L}{10^3 \text{ km}}$). The control required over the rotation axis can however be relaxed by applying forces on one satellite while using the other as an inertial reference to cancel the relative rotation between them. The gravitational tidal force on the satellites due to the Sun is $\sim 10^{-4} \text{ N} \left(\frac{M}{1000 \text{ kg}} \right) \left(\frac{L}{10^3 \text{ km}} \right)$ while the force on the satellites due to solar radiation pressure $\sim 10^{-5} \text{ N}$. These forces are small enough to be compensated by FEEP and colloid thrusters [114]. The application of these forces cancels the relative transverse velocity between the laser's axis and the distant satellite. The residual transverse velocity v_T of the atom clouds due to their thermal velocity and vibrations of the atom trap can also cause Coriolis accelerations. If the atoms are cooled to $\sim 100 \text{ pK} \sqrt{\frac{N_a}{10^8}}$ temperatures, their thermal velocities are smaller than 10^{-8} m/s. The Coriolis acceleration is then smaller than $10^{-19}g(\frac{\omega}{10^{-2} \text{ Hz}})^2$ if $\delta\omega$

is controlled better than 10^{-10} rad/s and the transverse vibrations of the atom clouds are smaller than $10 \text{ nm/s} (\frac{\omega}{10^{-2} \text{ Hz}})^2$.

In addition to the Coriolis acceleration, any instability $\delta\omega$ in the laser's angular velocity (e.g. in the rotation servoing mechanism) causes a differential centrifugal acceleration $\sim L(\delta\omega)^2$. This acceleration is smaller than $10^{-19} g (\frac{\omega}{10^{-2} \text{ Hz}})^2$ if $\delta\omega \lesssim 10^{-11} \frac{\text{rad/s}}{\sqrt{\text{Hz}}} \sqrt{(\frac{10^3 \text{ km}}{L})} (\frac{\omega}{10^{-2} \text{ Hz}})^{\frac{1}{2}}$ at frequency ω . The control over the rotation of the laser's axis can be potentially further relaxed by tuning the radius of curvature of the laser beam. Since the atom senses the local phase of the laser beam, the atoms will not sense rotations of the laser's axis if the phase fronts are appropriately curved. If the radius of curvature R of the beam is equal to the distance L between the atom and the laser then the atom is insensitive to centrifugal accelerations $\sim L(\delta\omega)^2$. The control over the rotation of the laser's axis can be relaxed to the extent to which the radius of curvature of the beam at the distant interferometer can be tuned to equal the distance between that interferometer and the laser. The differential setup proposed in this experiment requires one interferometer to be close to the laser at a distance $I_L \sim 100 \text{ m}$ while the other is at a distance $L \sim 10^3 \text{ km}$. The centrifugal acceleration of the atoms near the laser will produce accelerations $\sim I_L (\delta\omega)^2$. These accelerations set the minimal control required over the laser's rotation to $\delta\omega \lesssim 10^{-9} \frac{\text{rad/s}}{\sqrt{\text{Hz}}} \sqrt{(\frac{100 \text{ m}}{I_L})} (\frac{\omega}{10^{-2} \text{ Hz}})^{\frac{1}{2}}$.

In this configuration, due to the finite radius of curvature of the laser beam, the interferometer is sensitive to transverse vibrations of the lasers. The effects of these vibrations on the two interferometers will not be entirely common if the radii of curvature of the laser beams that interact with the two interferometers are not equal. The phase shift from a transverse vibration δy to a single interferometer is $\sim k_{\text{eff}} \frac{\delta y^2}{R}$ where R is the radius of curvature of the beam. This phase shift can be made smaller than shot noise even without relying on common mode cancellation by damping the transverse vibrations of the laser below $100 \mu\text{m} \sqrt{\frac{R}{10^3 \text{ km}}}$ over the frequencies of interest.

The need to reference the axis of the laser to an inertial reference emerged from the demand to suppress Coriolis accelerations due to the thermal velocity of the atom cloud. Another way to deal with this problem is to operate the interferometer in the multiloop configurations described in sub section 7.4.2. The Coriolis acceleration

caused by a laser rotating with a constant angular velocity and an atom cloud moving with a constant transverse velocity is constant. The phase shift due to such a constant acceleration is completely cancelled in these multiloop configurations. In this configuration, the interferometer has a smaller bandwidth but has the same sensitivity to gravitational waves at its resonant frequency as the Mach Zender configuration.

Rotational backgrounds in this multi-loop setup can be controlled by servoing the laser to track the rotation of the satellites. An instability $\delta\omega$ in the angular velocity of the axis will cause a centrifugal acceleration $L(\delta\omega)^2$. Moreover, the transverse velocity v_T of the atom cloud caused by the thermal velocity of the atom and vibrations of the trap used to confine the atoms will cause accelerations $\delta\omega v_T$. These backgrounds can be made smaller than $10^{-19}g(\frac{\omega}{10^{-2}\text{ Hz}})^2$ by making $\delta\omega$ smaller than 10^{-10} rads/s as discussed earlier in this section.

Effects of Magnetic Fields

A time variation δB in the magnetic field B_0 produces a phase shift $\sim \alpha_{ZC}B_0\delta BT$ in the interferometer as discussed in sub section 7.4.2. This phase shift must be smaller than 10^{-4} . Time variations in the interplanetary magnetic field at ~ 1 AU have been measured to be $\sim 0.1\frac{\text{nT}}{\sqrt{\text{Hz}}}(\frac{10^{-2}\text{ Hz}}{\omega})$ [116]. The applied bias magnetic field B_0 is ~ 100 nT over the interferometer region I_L and $\alpha_{ZC} \sim 1\frac{\text{kHz}}{\text{G}^2}$ (for Rubidium). With these values, $\alpha_{ZC}B_0\delta BT \sim 10^{-5}$ for $T \lesssim 100$ s.

Note this is true only if the atom interferometer is operated using Raman transitions, so the atom is in different internal levels during the course of the interferometer. This phase shift will be absent if the interferometer is operated using Bragg transitions, since the phase accrued along each arm is the same. However, there will still be a phase shift that goes like $\sim \alpha_{ZC}\nabla(B_0\delta B)(v_R T)T$.

The atoms are in magnetically insensitive ($m = 0$) states and they move through a non-uniform magnetic field. The gradient ∇B of the magnetic field causes a force $\sim \alpha_{ZC}B\nabla B$ on the atom due to the second order Zeeman effect. The atom experiences a gradient $\nabla B \sim \frac{100\text{ nT}}{30\text{ m}}$ from the external bias magnet in the configuration considered in this experiment. With this gradient, time variations $\delta B \sim 0.1\frac{\text{nT}}{\sqrt{\text{Hz}}}(\frac{10^{-2}\text{ Hz}}{\omega})$ [116] in the interplanetary magnetic field cause accelerations $\sim 10^{-19}g$ which is equal to

the shot noise requirement of the experiment. The time varying acceleration caused by fluctuations in the position of the bias magnet are smaller than $\sim 10^{-19}g$ if these fluctuations are smaller than $\sim 1 \frac{\text{mm}}{\sqrt{\text{Hz}}}$ in the 10^{-2} Hz band.

The atom is placed in a $m = 0$ state with respect to the external magnetic field at the start of the interferometer to minimize the effects of accelerations from time dependent magnetic fields. The Rabi frequency of the atomic transition is set by the internal state of the atom and the laser is tuned to match this frequency. Changes to the direction of the external magnetic field during the interrogation time of the experiment are adiabatic compared to the rapid precession rate of the atom's spin. If the direction of the magnetic field changes, the quantization axis of the atom's spin will track this direction change. Since the laser is tuned to the original $m = 0$ state, the atom-laser interaction will excite $m = \pm 1$ states along the new axis of quantization. The phase shift from these states is a background.

The $m = \pm 1$ components developed by the atom as a result of a misalignment by an angle θ between the magnetic field and the quantization axis are proportional to $\sin(\theta)$. The probabilities induced by this mixing are therefore proportional $\sin^2(\theta)$. The contributions of this mixing to the phase shift in the interferometer are smaller than 10^{-4} when $\theta \lesssim 10^{-2}$. The direction of the interplanetary magnetic field was characterized by [112]. During an average time, the drift in the direction of the magnetic field was found to be smaller than 5° over 10 minutes. In the presence of a ~ 100 nT bias field over the interferometer region, these angular variations of the ~ 5 nT interplanetary magnetic field will change the overall direction of the magnetic field in the interferometer by less than 10^{-2} in 100 seconds.

The above arguments indicate that the effects of time varying interplanetary electromagnetic fields on the atom interferometer are naturally small and close to the shot noise floor of the experiment. The effects of these fields can be additionally suppressed to the extent to which these fields can be measured. The response of the atom interferometer to a given electromagnetic field is determined by known quantities like the magnetic moment of the atom and its polarizability. Since these quantities are known to several digits, a measurement of the electromagnetic fields will enable us to predict the effect of these fields on the atom interferometer. These effects can then

be subtracted out from the measured phase shift.

We note that the effects of electromagnetic forces on the atom interferometer are significantly suppressed compared to their effects on LISA's inertial test masses. Spurious electromagnetic forces on the test masses due to charge transfer between the test masses and the satellite environment is a major background for LISA. The test mass acquires a random charge from its environment and its response to time varying electromagnetic fields cannot be predicted even if the electromagnetic fields themselves are measured. Since the atom interferometer is operated using magnetically insensitive atomic states, electromagnetic forces on the atom are greatly diminished. The response of the atom interferometer to electromagnetic fields can be predicted to the extent to which these fields are measured providing additional immunity to the atom interferometer from time varying electromagnetic fields.

The Radius of Curvature of the Beam

The temperature of the atom cloud will cause the atom to have thermal velocities along the direction transverse to the laser fields propagating along the interferometer axis. This velocity will cause the atoms to move in a direction transverse to the laser beam. Owing to the finite radius of curvature R of the beam, an atom that is slightly off-axis by δy from the center of the beam will see an additional phase $k_{\text{eff}}(\frac{\delta y^2}{R})$. With $N_a \sim 10^8$ atoms in the cloud, shot to shot variations in this phase are $\sim \frac{1}{\sqrt{N_a}} k_{\text{eff}}(\frac{\delta y^2}{R})$ and these must be smaller than $\sim 10^{-4}$. With thermal velocities $\sim 100\mu\text{m/s}$, the maximum transverse distance travelled by the clouds is $\delta y \sim 1\text{cm}$ over an interrogation time $T \sim 100\text{ s}$. The phase shift $\frac{1}{\sqrt{N_a}} k_{\text{eff}}(\frac{\delta y^2}{R})$ is then smaller than 10^{-4} if the radius of curvature R of the beam is greater than $\sim 100\text{ km} \left(\frac{10^9\text{ m}^{-1}}{k_{\text{eff}}} \right)$.

Blackbody Clock Shift

Black body radiation shifts the hyperfine transition frequency of the atom by $\sim 10^{-4}\text{ Hz} \left(\frac{\tau}{300\text{ K}} \right)^4$ [117]. The ambient temperature τ at 1 AU is $\sim 300\text{ K}$. Time variations $\delta\tau$ in the temperature of the interferometer region during the interrogation time T of the experiment will change the hyperfine transition frequency by $\delta\nu \sim 4 \times$

10^{-4} Hz $(\frac{\tau}{300 \text{ K}})^4 (\frac{\delta\tau}{\tau})$ causing a phase shift $\delta\nu T \sim 10^{-2} (\frac{\tau}{300 \text{ K}})^4 (\frac{\delta\tau}{\tau}) (\frac{\omega}{10^{-2} \text{ Hz}})$. This phase shift is smaller than 10^{-4} if the temperature fluctuations $\delta\tau$ in the frequency band ω are smaller than $\sim 1 \text{ K} (\frac{\omega}{10^{-2} \text{ Hz}})$. Time dependence in the temperature of the interferometer is caused by variations in the solar output and fluctuations of the spacecraft temperature. Time variations of the solar output typically occur over the time scale of a day at distances $\sim 1 \text{ AU}$ [118]. The solar output changes by $\sim 1 \text{ Watt}$ during this period leading to a temperature change $\sim 0.05 \text{ K}$ in the time scale of a day. These variations are therefore not a problem for the interferometer.

The effects of the thermal variation of the satellite on the interferometer are suppressed since the interferometer is operated at a distance $d_I \sim 30 \text{ m}$ away from the satellite. Temperature variations of the satellite at frequency ω have to be larger than $\sim 10 \text{ K} (\frac{\omega}{10^{-2} \text{ Hz}}) (\frac{d_I}{30 \text{ m}})^{\frac{1}{2}}$ in order to change the temperature of the interferometer region by 1 K. The spacecraft receives heat from the Sun and the solar wind. As discussed above, variations in the solar output are small over the time scale of interest. The solar wind is composed of 2 keV protons and electrons with density $\sim \frac{5}{\text{cm}^3}$ moving at speeds $\sim 400 \text{ km/s}$. The change in temperature of the satellite from an order one change in the flux of the solar wind is $\sim 1 \text{ mK}$. The environment of the satellite will therefore not cause its temperature to fluctuate at levels of interest to this experiment.

The satellite will also establish a spatial thermal gradient over the interferometer region due to its shadow. This spatial gradient will contribute to the phase shift in the interferometer. The natural time scale for the variation of this phase shift is equal to the orbital period of the satellite $\sim 1 \text{ year}$ and is therefore not a problem for the current experiment. Time variations of this spatial gradient are also created by random motions of the satellite during the interrogation time of the experiment. However, these motions need to be well controlled to suppress Newtonian gravity backgrounds which are much larger than the small phase shift produced by the spatial thermal gradient. The variations in this phase shift due to the residual random motions of the spacecraft will therefore be smaller than shot noise.

7.5.3 Comparison with LISA

The detection of gravitational waves requires techniques that are sensitive to the minuscule effects of gravitational waves and can simultaneously suppress noise in the measurement bandwidth to permit the extraction of the signal. The atom interferometer configurations discussed in this paper can probe the same frequency spectrum as satellite based light interferometers like LISA with comparable sensitivity (see Section 7.7). However, as discussed in subsection 7.5.2, these configurations may naturally permit significant suppression of several serious backgrounds faced by LISA, see Table 7.2.

LISA aims to detect gravitational waves by measuring the relative distance between two inertial proof masses separated by an arm length ~ 5 million kilometers. Position noise of these masses is a background for LISA. The significant gravitational coupling between random motions of the satellite and the proof mass is a dominant cause of this position noise. In order to sufficiently suppress this noise, LISA requires satellite position control at $\sim 1 \frac{\text{nm}}{\sqrt{\text{Hz}}}$ in its measurement bandwidth [114]. However, as argued in subsections 7.5.1 and 7.5.2, since the atom interferometer can be operated outside the satellite over a ~ 100 m region from the satellite, the effects of position noise of the satellite on the interferometer are significantly suppressed. For gravitational wave sensitivity similar to LISA, our atom interferometer setup would require satellite position control at $\sim 10 \frac{\mu\text{m}}{\sqrt{\text{Hz}}}$ in the measurement bandwidth.

In addition to random motions of the satellite, spurious electromagnetic forces on the LISA proof mass also contribute to its position noise. These forces are caused by direct collisions between the proof mass and the background gas and due to charge accumulation on the proof mass from interactions with cosmic rays and the solar wind. The test mass acquires a random charge from its environment and its response to time varying electromagnetic fields cannot be predicted even if the electromagnetic fields themselves are measured. Since the atoms are neutral and the atom interferometer is operated using magnetically insensitive ($m = 0$) states, electromagnetic forces on the atom clouds are naturally small. The response of the atom interferometer to electromagnetic fields can be predicted to the level at which these fields are measured.

This provides additional immunity from time varying electromagnetic fields. Collisions of the atoms with background particles from the solar wind or cosmic rays lead to particle deletion from the cloud and not charging of the cloud. These deletions result in a minor reduction in the sensitivity (for interrogation times $\lesssim 1000$ s) but do not cause phase shifts to the remaining atoms and hence are not a background for this experiment.

Laser phase noise is another major background for gravitational wave detectors. This noise can be suppressed by the simultaneous operation of interferometers along the arms of a three-satellite constellation. In this configuration, the effects of laser phase noise are cancelled up to knowledge of the arm lengths (see subsection 7.5.2). Both LISA and the atom interferometer can benefit by exploiting this idea. However, due its long (~ 5 million km) arm length, LISA faces unique challenges in determining the absolute distance between its satellites [119, 120]. Owing to these difficulties, LISA requires control over the frequency drift of its lasers at $\sim 1 \frac{\text{Hz}}{\sqrt{\text{Hz}}}$ at 10^{-2} Hz. The atom interferometer setup considered in this paper can reach sensitivities comparable to LISA with significantly smaller arm lengths $\sim 10^3$ km. The compactness of this baseline might allow for the determination of the arm lengths of the atom interferometer constellation with better precision than LISA. If these arm lengths are known to within ~ 1 m, our experiment can reach sensitivities similar to LISA with control over laser frequency $\sim 10^4 \frac{\text{Hz}}{\sqrt{\text{Hz}}}$ at 10^{-2} Hz.

The atom interferometer setup discussed in this paper might significantly relax the requirements on several major backgrounds faced by light interferometers like LISA while achieving comparable sensitivity. We have attempted to consider the relevant backgrounds introduced by the atom interferometer setup in section 7.5.2 and show that they could be controlled with practical technology in a realistic setup. Since many of these backgrounds require careful engineering, further study is necessary. However, the experiment appears to be feasible and exciting enough to merit more serious consideration.

Attribute	AGIS	LISA
baseline	10^3 km	5×10^6 km
satellite control (at $\sim 10^{-2}$ Hz)	10^4 nm/ $\sqrt{\text{Hz}}$	1 nm/ $\sqrt{\text{Hz}}$
laser frequency control (at $\sim 10^{-2}$ Hz)	10^4 Hz/ $\sqrt{\text{Hz}}$	1 Hz/ $\sqrt{\text{Hz}}$
rotational control (at $\sim 10^{-2}$ Hz)	10^{-2} nrad/ $\sqrt{\text{Hz}}$	1 nrad/ $\sqrt{\text{Hz}}$
electromagnetic forces	atoms neutral, EM forces naturally small, predictable response to measured EM field	cosmic ray charging of proof mass
collisions with background gas	delete atoms, not a noise source	cause acceleration noise

Table 7.2: A comparison between specifications for a three satellite AGIS configuration that could potentially allow comparable sensitivity to LISA, and the LISA requirements. There are many caveats and details that cannot be captured in a table and are discussed in Sections 7.5.2 and 7.5.3 and in the LISA papers (see e.g. [114, 121]).

7.6 Gravitational Wave Sources

There are many known and potential sources for gravitational waves from astrophysics and cosmology. Here we will discuss only a few, including the well-known compact object binaries, which give a coherent oscillatory gravitational wave signal, and more speculative cosmological sources, which give a stochastic background of gravitational waves. There are many reviews of this subject that discuss other sources including gamma-ray bursts, supernovae, and spinning neutron stars (see, for example, [28, 122]).

7.6.1 Compact Object Binaries

One of the most promising sources of observable gravitational waves is a binary star where both components are compact objects such as white dwarfs, neutron stars, or black holes [28]. These compact binaries emit strongly in gravitational waves because they contain large mass stars relatively close to each other. The amplitude of the

gravitational waves emitted is

$$h \sim G\mu \frac{(GM\Omega)^{\frac{2}{3}}}{r} \sim \frac{(GM_1)(GM_2)}{rR} \quad (7.17)$$

where $M_{1,2}$ are the masses of the components, $M = M_1 + M_2$ and $\mu = \frac{M_1 M_2}{M}$ are the total and reduced masses, R is the radius of the binary, Ω is the orbital frequency of the binary, and r is the distance from the binary at which the wave is observed. As neutron stars and white dwarfs are both roughly 1 solar mass, M_\odot , we will primarily be interested in compact binaries composed of two $1 M_\odot$ mass components as sources. The amplitude of the emitted gravitational waves then depends only on the orbital period and the distance to the star. For a binary with $\Omega = 1$ s in our galaxy we expect $h \sim 10^{-18}$, in our local cluster $h \sim 10^{-21}$, and in a Hubble volume (i.e. out to redshifts $z \sim 1$) $h \sim 10^{-23}$.

The main frequency component of the emitted gravitational wave is at twice the binary's orbital frequency, $\omega \propto 2\Omega$ [123]. This is clear for equal mass stars, and can also be seen for unequal masses from the fact that gravitational radiation arises from the second time derivative of the quadrupole moment of the binary.

Near the end of its life, the dominant energy loss mechanism for a compact binary is gravitational radiation. As a compact binary loses energy, the stars spiral inward, increasing the orbital frequency. This can bring the emitted gravitational waves into the observable part of the spectrum for gravitational wave detectors. This process ends when the two compact objects collide. Thus, the highest gravitational wave frequency emitted depends on the radii of the compact objects. A neutron star binary can reach frequencies of over 100 Hz while a white dwarf binary can only reach roughly 0.5 Hz before collision. The power emitted in gravitational waves is $P \sim M_{\text{planck}}^2 h^2$. Because this power depends mainly on a few variables like the masses and orbital period of the binary, the inspiral of a compact binary near the end of its life is consistent and predictable and therefore so is the waveform of the emitted gravitational waves. Using the power emitted in gravitational waves, the remaining

lifetime of a compact binary is [123]

$$\tau \sim \frac{1}{50G\mu(GM)^{\frac{2}{3}}\Omega^{\frac{8}{3}}}. \quad (7.18)$$

As the orbital frequency increases, the rate of energy loss increases and the remaining lifetime decreases rapidly. This means that at any given Ω most of the remaining life of the binary will occur near that frequency.

There are thus two main advantages to being able to observe gravitational waves at lower frequencies. First, the population of binary stars that are potentially observable is increased, both because new classes of stars such as white dwarf or high-mass black hole binaries are observable and because a greater fraction of any given class, such as neutron star binaries, is at lower frequencies than at higher ones. Indeed, for a gravitational wave detector such as LISA which can observe waves with frequencies as low as 10^{-3} Hz, the large number of white dwarf binaries creates a stochastic background of gravitational waves for the detector in this frequency band [124]. Second, a lower frequency binary has a longer time left to live which increases the observation time and thus the sensitivity of the detector for this source.

7.6.2 Stochastic Sources

In addition to a large number of white dwarf binaries, several potential cosmological sources can produce a stochastic background of gravitational waves including inflation and reheating, a network of cosmic strings, or phase transitions in the early universe.

A period of inflation can produce a fairly flat (scale-invariant) stochastic gravitational wave background [125]. This could be as high as $\Omega_{\text{GW}}(f) \approx 10^{-13}$, as limited by the COBE bound [126], though slow-roll inflation models probably give a smaller value and a tilted spectrum [122]. This is fairly difficult for planned experiments to detect, but reheating after inflation can give a more peaked spectrum of gravitational waves with a higher value of Ω_{GW} . For example, reheating after hybrid inflation [127] or preheating [128, 129], can give a spectrum of gravitational waves with Ω_{GW} several orders of magnitude higher than that from the period of inflation itself. The frequency of the peak is model-dependent, proportional to the scale of reheating. It

probably lies within a range from roughly 1 Hz to 10^9 Hz. There is then a possibility that this enhanced strength of gravitational waves from reheating will allow a detection by interferometers. There are also other possibilities such as pre-big bang [130] or extended [131] inflation that can lead to much higher values of $\Omega_{\text{GW}}(f)$ in the phenomenologically interesting frequency range for interferometers.

A first-order phase transition in the early universe can produce gravitational waves through bubble nucleation and turbulence [132, 133]. The frequency of the gravitational waves today is given by redshifting the frequency at which they were produced, which is proportional to the Hubble scale at the phase transition. There are, however, significant uncertainties in the calculations of these frequencies (see [122]). The best expectation is that a phase transition at the electroweak scale is likely to produce gravitational waves with a frequency today in a range near 10^{-3} Hz. Earlier phase transitions at higher temperatures produce gravitational waves with proportionally higher frequencies. In some models with new physics at the weak scale [134], including some supersymmetric [135] and warped extra-dimensional [136] models, the electroweak phase transition can produce gravitational waves with very large Ω_{GW} , well above the threshold for detection by atom interferometers.

A network of cosmic strings produces a stochastic background of gravitational waves from vibrations of the strings. Cusps and kinks in the strings produce bursts of gravitational waves which could be seen individually or as a stochastic background. Unfortunately, even in the simplest models there are large uncertainties in the calculation of the formation and subsequent gravitational radiation of such string networks. Thus, it is very difficult to get a precise prediction from theory about the strength of gravitational waves coming from a network of cosmic strings. Using the current understanding of cosmic string networks, the sensitivities of atom interferometers on earth and in space to a stochastic gravitational wave background (see Figs. 7.12 and 7.13) could allow detection of cosmic strings with $G\mu \sim 10^{-8}$ to 10^{-11} (μ is the string tension) or lower, depending on the sensitivity achieved and the uncertainties in the cosmic string calculations. For a recent review of this subject see for example [137].

There are many other possible sources for gravitational waves from fundamental physics in the early universe including Goldstone modes of scalar fields [138], or radion

modes and fluctuations of our brane in an extra dimensional scenario [139, 140]. There are also other astrophysical sources that may lead to an interesting stochastic gravitational wave background (for a review see [122]).

The possibility of accessing these cosmological and astrophysical sources makes gravitational waves a very interesting avenue for exploring the universe and probing fundamental physics. Indeed, observing gravitational waves could be one of our only ways of getting information about the universe before the last scattering surface.

7.7 Sensitivities

In this Section we find projected sensitivity curves for the terrestrial and satellite experiments. There is always significant uncertainty in projecting the sensitivity of a proposed experiment. We have attempted to give a range of sensitivities to show more conservative and more aggressive assumptions about what may be experimentally achievable. There is also some uncertainty in these sensitivity curves because we have not attempted to perform a careful statistical study of the exact sensitivity for a particular configuration. Especially in the case of the stochastic gravitational wave background, this can make important differences that have been worked out carefully by many authors for laser interferometers. We leave such considerations to future work.

7.7.1 Binary Sources

The inherent limit on the sensitivity to a gravitational wave due to shot noise can be found from Eqn. (7.8). This limit, equivalently the power spectrum of the shot noise in the experiment $h_n(f)$, is shown in Figure 7.9 for an example configuration, as described in Sections 7.5.1 or 7.4.1. Here we have taken the two atom interferometers to be a distance $L = 1$ km apart, with interrogation time $T = 1$ s, $100\hbar k$ LMT beamsplitters, and a per shot phase sensitivity of 10^{-5} rad. We have also assumed a data-taking rate of 10 Hz. The plot is cutoff at the Nyquist frequency of 5 Hz. There would in actuality be some sensitivity to higher frequencies but they will be aliased

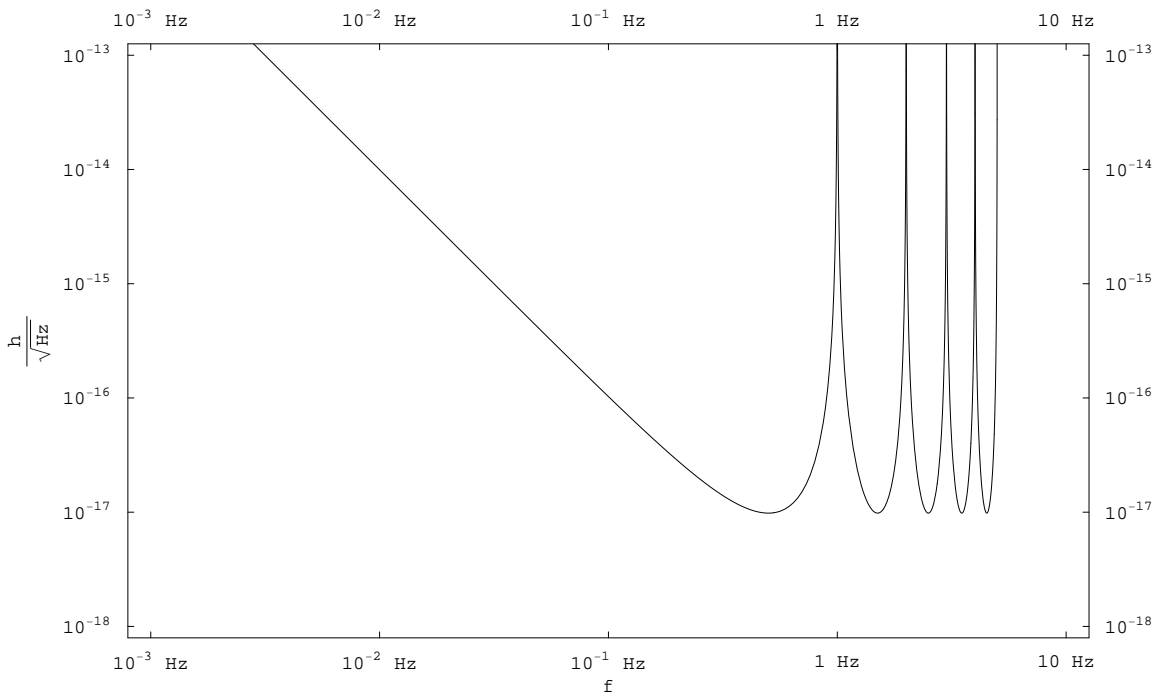


Figure 7.9: An example sensitivity curve to a gravitational wave of frequency f . It is a shot noise power spectrum in the response of the atom interferometer to a gravitational wave of amplitude h . Here we have taken the two atom interferometers to be a distance $L = 1$ km apart, with interrogation time $T = 1$ s, $100\hbar k$ LMT beamsplitters, a per shot phase sensitivity of 10^{-4} rad, and a data-taking rate of 10 Hz.

to look like lower frequencies potentially also leading to confusion with backgrounds.

At low frequencies the sensitivity rises as f^{-2} as is clear from Eqn. (7.9). For higher frequencies, the sensitivity flattens out because a longer interrogation time does not increase the response of the interferometer once it is longer than the period of the gravitational wave $T > f^{-1}$. The sensitivity then reaches its maximum when $\sin^2\left(\frac{\omega T}{2}\right) = 1$, i.e. when there are an odd number of periods of the gravitational wave in the entire time $2T$ of the interferometer. This agrees with the intuition that the interferometer is sensitive to changes in the relative timing of the laser pulses caused by the stretching of the metric and therefore maximally sensitive when there is the greatest change in the distance to the laser (the clock) between each successive laser pulse.

The singularities in the sensitivity curve in Figure 7.9 come at frequencies which are integral multiples of $f = T^{-1}$, when an integral number of periods of the gravitational wave fit in the interrogation time T . Roughly the periods when the gravitational wave is causing a ‘stretch’ exactly equal the periods when it is causing a ‘squeeze’. The net integrated effect of the gravitational wave is then zero and the phase shift response of the atom interferometer goes to zero. Thus the atom interferometer has no sensitivity to such frequencies.

Note that the best sensitivities in Figure 7.9 come at frequencies halfway between the singularities, when there are an odd, integral number of periods of the gravitational wave in the entire atom interferometer (a time of $2T$). This can be understood since the atom interferometer is essentially taking the difference between the phases accrued by the atom in the first and second halves of the sequence. The maximal difference arises when the ‘stretch’ part of the gravitational wave (which is when the coefficient of the dx^2 term in Eqn (7.2) is greater than 1) occurs during one of the halves and the ‘squeeze’ during the other. These are the frequencies to which the atom interferometer responds maximally.

A longer interrogation time for the experiment does not actually improve the peak sensitivity in the sense of lowering the curve in Figure 7.9. Instead, it slides the curve left, lowering the frequency at which the maximum sensitivity is reached. Of course, a larger length L or higher momentum beamsplitters improves the entire

Setup	L	k_{eff}	T	I_L	Phase Sensitivity	f_d
Terrestrial 1	1 km	$1.6 \times 10^9 \text{ m}^{-1}$	1.4 s	10 m	10^{-4} rad	10 Hz
Terrestrial 2	4 km	$1.6 \times 10^{10} \text{ m}^{-1}$	4.5 s	100 m	10^{-5} rad	10 Hz
Satellite 1	100 km	$1.6 \times 10^9 \text{ m}^{-1}$	10 s	100 m	10^{-4} rad	1 Hz
Satellite 2	10^3 km	$3.2 \times 10^9 \text{ m}^{-1}$	100 s	200 m	10^{-4} rad	1 Hz
Satellite 3	10^4 km	$1.6 \times 10^9 \text{ m}^{-1}$	100 s	100 m	10^{-5} rad	1 Hz

Table 7.3: The experimental parameters chosen for the benchmark sensitivity curves in Figures 7.10 and 7.11. The phase sensitivity is the per shot sensitivity. L is the length of the baseline, f_d is the data-taking or shot repetition rate, k_{eff} is the effective momentum transfer of the beamsplitters, T is the interrogation time of each shot, I_L is the length of each interferometer region.

sensitivity curve linearly. We have cut off the sensitivity curve above the Nyquist frequency. In reality there will be a slightly more gradual loss of sensitivity before this frequency and even some sensitivity to higher frequencies, although they will be aliased. Assuming a constant number of atoms per second that can be cooled and run through the interferometer, a faster data-taking rate does not improve sensitivity. It would merely improve the high frequency cutoff. Thus it seems unnecessary to strive for a data-taking rate faster than $\mathcal{O}(10 \text{ Hz})$. The sensitivity would also decrease as the frequency of the gravitational wave approached the light travel time (or really the gravitational wave travel time) across the whole experiment, namely L . However this frequency is much higher than the frequency of maximal sensitivity for an atom interferometer. This would not be true for a light interferometer where the light travel time across the device is also the time length of a ‘shot’, the analogue of the interrogation time. For example, this explains why LISA loses sensitivity above $\sim 0.05 \text{ Hz}$ while the atomic interferometer’s sensitivity curve remains flat (see, for example, Figure 7.10).

The projected sensitivities for two possible configurations of the proposed earth-based experiments are shown in Figure 7.10. The choice of experimental parameters for these two configurations, shown in Table 7.3, is meant to illustrate the range of possible sensitivities that could be achievable. These are the envelopes of curves similar to the one in Figure 7.9. We have chosen to remove the singularities that

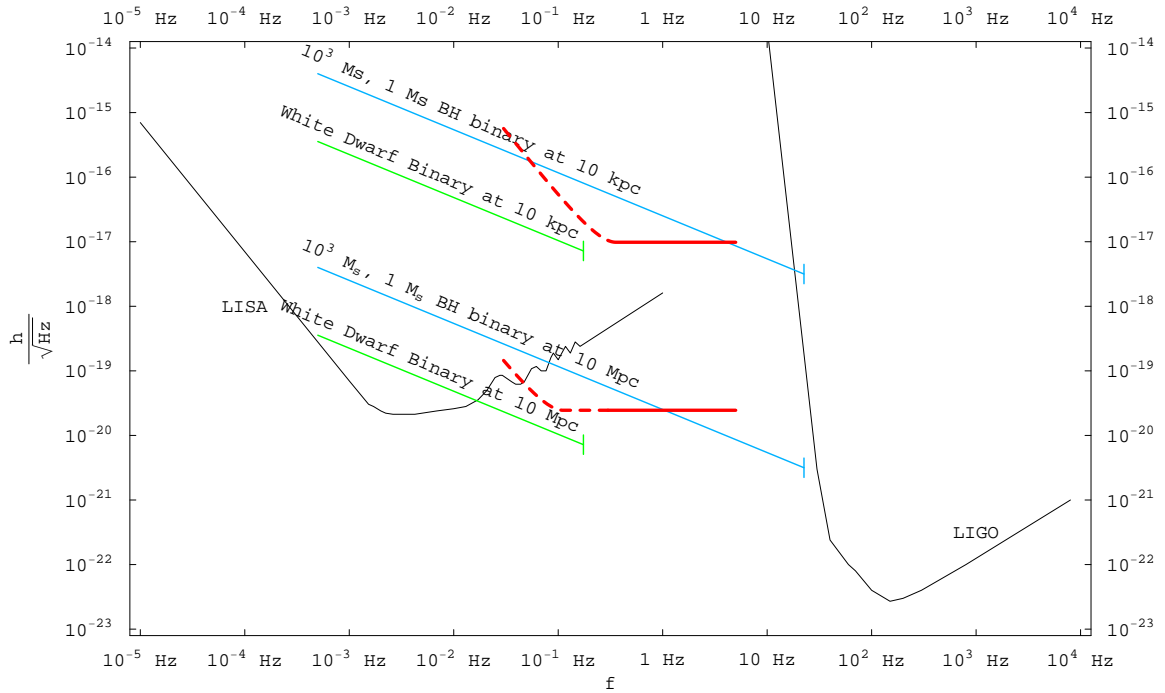


Figure 7.10: The thick (red) curves show projected sensitivities of our proposed terrestrial experiments to a gravitational wave of frequency f . The choices of experimental parameters for these two configurations are shown in Table 7.3. These are only projected shot noise power spectra in the response to a gravitational wave of amplitude h . They do not include other backgrounds, since as we have argued, these may be reduced below shot noise. Possible sources are shown. Expected noise curves are shown for initial LIGO and LISA.

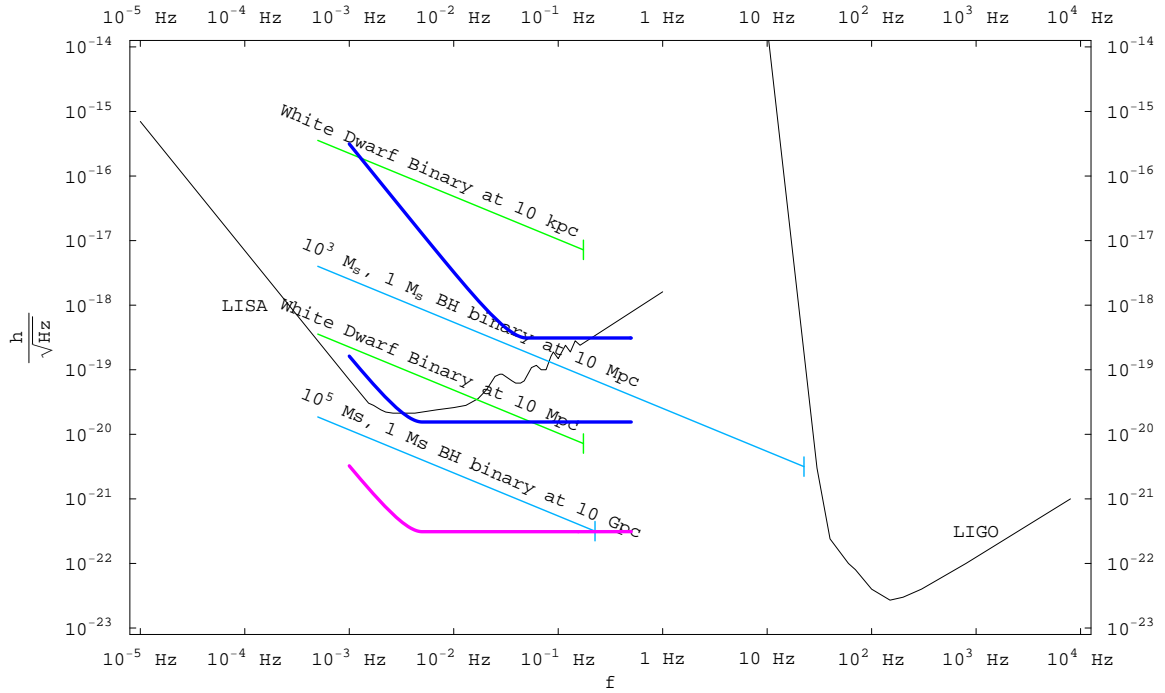


Figure 7.11: The thick (blue and purple) curves show the projected sensitivities of our proposed satellite experiments to a gravitational wave of frequency f . The choices of experimental parameters for these three configurations are shown in Table 7.3. The lowest (purple) curve, satellite 3 in Table 7.3, is an aggressive possibility that might be realizable in the future. These are just projected shot noise power spectra in the response to a gravitational wave of amplitude h . Possible sources are shown. Expected noise curves are shown for initial LIGO and LISA.

appear in Figure 7.9 to emphasize the frequency scaling for a general AI detector. In an actual experiment, the entire area of the envelope curve can be swept out by increasing the interrogation time T by a factor of roughly two. The sensitivities plotted are only the inherent sensitivity of the atom interferometer, i.e. the power spectra of the expected shot noise. We have argued in Section 7.4.2 that other backgrounds are smaller than this level. The one exception is time-varying gravity gradient noise and so the sensitivity curves are shown dashed below the frequency at which we expect gravity gradient noise to become the dominant noise source (see Figures 7.4 and 7.5). The upper sensitivity curve assumes a $L = 1$ km distance between two 10 m atom interferometers, with, therefore, an interrogation time of $T = 1.4$ s. Each interferometer has $100\hbar k$ LMT beamsplitters, a per shot phase sensitivity of 10^{-4} rad, and a data-taking rate of 10 Hz. The more aggressive curve assumes $L = 10$ km, $1000\hbar k$ LMT beamsplitters, 100 m interferometers with $T = 4.5$ s, a per shot phase sensitivity of 10^{-5} rad and the same data-taking rate. The curves are cut off at the Nyquist frequency. The sensitivity of initial LIGO [141] and the projected sensitivity of LISA [142] are also shown.

Figure 7.11 shows the projected sensitivities for three possible configurations of the proposed satellite experiment, with parameters shown in Table 7.3. The most conservative curve assumes $L = 100$ km, $100\hbar k$ LMT beamsplitters, $T = 10$ s, per shot phase sensitivity of 10^{-4} rad and data-taking rate of 10 Hz. The middle curve is the same except it assumes $L = 10^4$ km, $100\hbar k$ LMT beamsplitters, and $T = 100$ s. The most aggressive curve assumes the same length, beamsplitters, and interrogation time as the middle curve but assumes an extra factor of 10 in the per shot phase sensitivity, either from a larger number of atoms or from squeezed states.

7.7.2 Stochastic Gravitational Wave Backgrounds

A stochastic background of gravitational waves would be undistinguishable from any other background noise in a single gravitational wave detector. A single detector means for example one of the LIGO sites or one AGIS configuration (i.e. two atom interferometers with a long laser baseline in between as in Figures 7.1 or 7.8). With

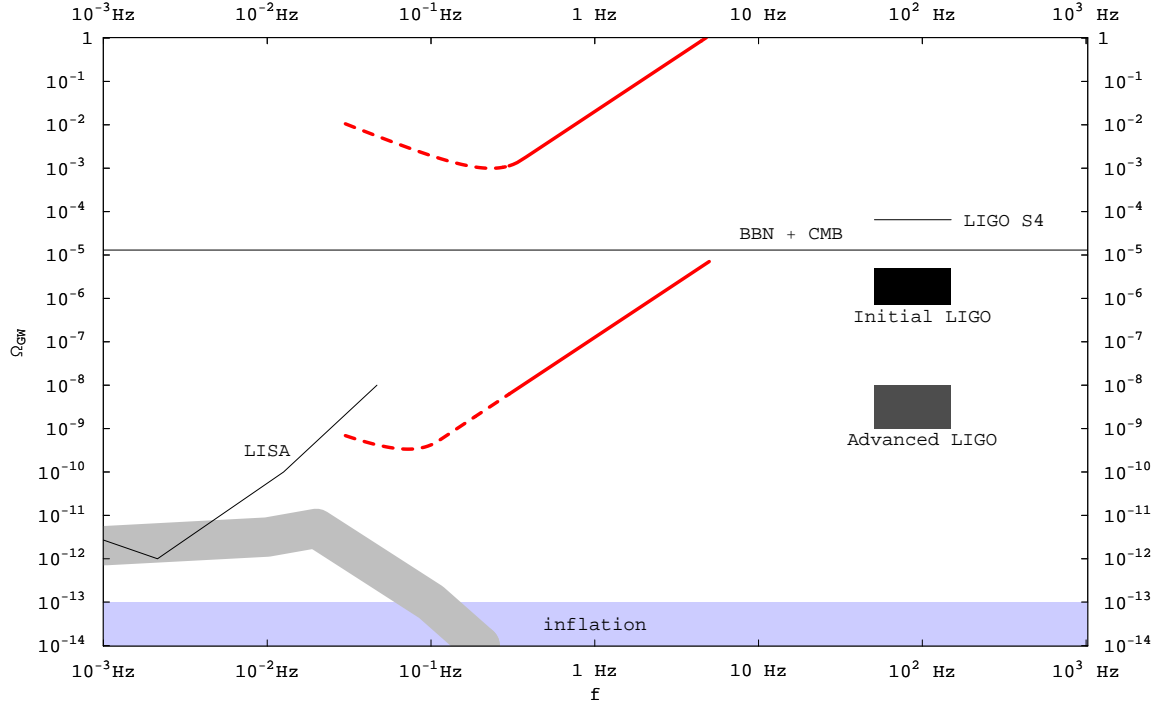


Figure 7.12: The projected sensitivity in Ω_{GW} of our proposed Earth based experiments, thick (red) curves, to a stochastic background of gravitational waves. The parameter choices are as in Fig. 7.10. These curves only take into account shot noise. The limit from LIGO Science Run 4 and the projected limits from initial and advanced LIGO are shown [143]. The limits from BBN [144] and the CMB [145] apply to the integral of the stochastic gravitational wave background over frequency. The possible region of gravitational waves produced by a period of inflation (not including reheating) is shown. The upper limit on this region is set by the COBE bound [126]. The gray band shows a prediction for the stochastic gravitational wave background from extragalactic white dwarf binaries; its width shows an expected error [124].

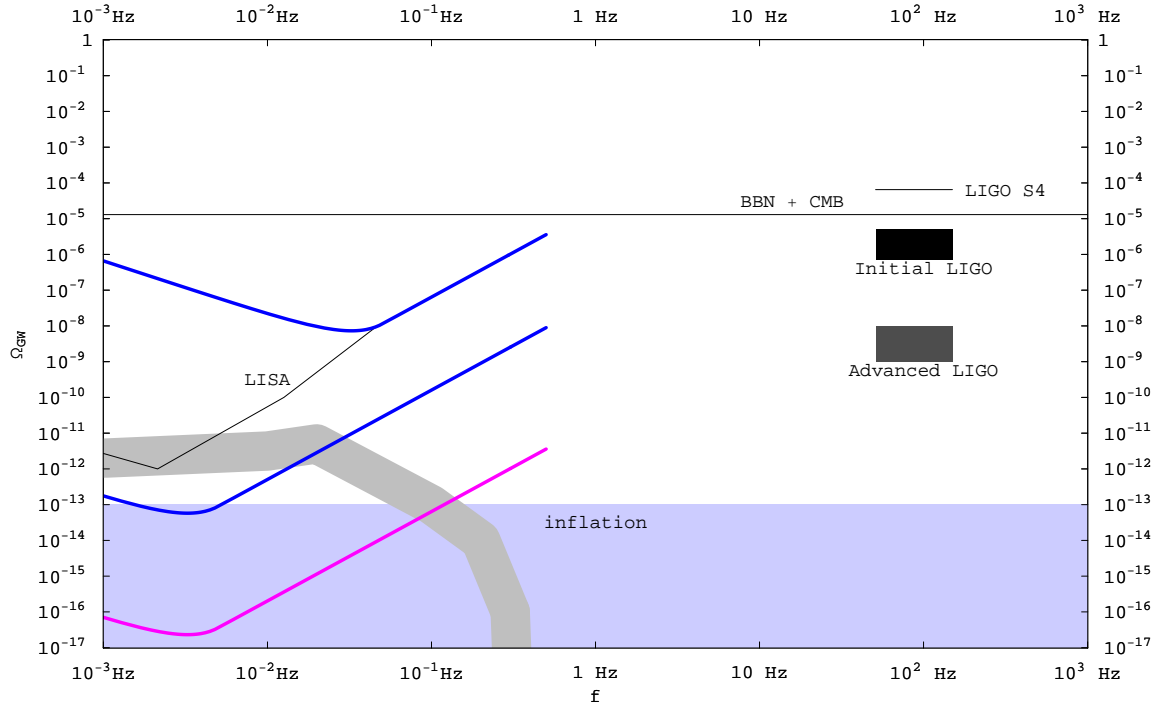


Figure 7.13: The projected sensitivity in Ω_{GW} of our proposed satellite experiments, thick (blue and purple) curves, to a stochastic background of gravitational waves. The parameter choices are as in Fig. 7.11. These curves only take into account shot noise. The limit from LIGO Science Run 4 and the projected limits from initial and advanced LIGO are shown [143]. The limits from BBN [144] and the CMB [145] apply to the integral of the stochastic gravitational wave background over frequency. The possible region of gravitational waves produced by a period of inflation (not including reheating) is shown. The upper limit on this region is set by the COBE bound [126]. The gray band shows a prediction for the stochastic gravitational wave background from extragalactic white dwarf binaries; its width shows an expected error [124].

two gravitational wave detectors it is possible to cross-correlate the measurements and obtain sensitivity to a stochastic background of gravitational waves. It is preferable if these two detectors are far apart either on the earth or in space since a stochastic background of gravitational waves coming from astrophysical or cosmological sources would be common to both detectors, but other sources of noise (nearby motions of the earth for example) would not. Thus a single gravitational wave detector can never detect a stochastic background of gravitational waves (or at least can never prove that is what is being detected) but more than one detector allows sensitivity to a stochastic background of gravitational waves. This standard strategy is also employed by LIGO and is described for example in [143].

As is standard, the sensitivity to such gravitational waves is shown in Figures 7.12 and 7.13, plotted in the variable

$$\Omega_{\text{GW}}(f) = \frac{f}{\rho_c} \frac{d\rho_{\text{GW}}}{df} \quad (7.19)$$

where ρ_c is the critical energy density of the universe and ρ_{GW} is the local energy density in gravitational waves. These curves follow from the standard analysis, so we plot the 95% confidence limit on the spectrum of stochastic gravitational waves. Following [146] (but see also [147, 148]) we estimate this limit by

$$\Omega_{\text{GW}}(f) = \frac{\pi c^2 f^3}{\rho_c G |\gamma(\vec{x}_1, \vec{x}_2, f)|} \sqrt{\frac{2}{\tau_{\text{int}} \Delta f}} (1.645) h_n^2(f) \quad (7.20)$$

where τ_{int} is the total time length of the experiment, γ is a geometric factor taking into account the positions of the two detectors which we take equal to its maximum value $\frac{8\pi}{5}$ (it will probably be slightly smaller in a real configuration), and h_n is the power spectrum of the noise in the gravitational wave detector as plotted for example in Figure 7.9. To produce the curves in Figures 7.12 and 7.13 we use the h_n from Figures 7.10 and 7.11, respectively. As is standard, we assume a $\tau_{\text{int}} \sim 1$ yr integration time for the experiment. This is only a benefit if two detectors can be cross-correlated. Otherwise, the sensitivity to a stochastic background is no better than the noise on each shot and it is only possible to place limits on and not to detect such a background.

It is advantageous to measure at lower frequencies to gain sensitivity in the variable Ω_{GW} because it scales favorably with low f . Further, there is a cutoff in γ and thus the sensitivity when the two gravitational wave detectors are farther apart than the wavelength of the gravitational waves, f^{-1} . For frequencies below $\mathcal{O}(10 \text{ Hz})$ this is not a problem for our detectors, but for LIGO this is an issue. The sensitivity of LIGO to stochastic gravitational waves is reduced because of the large distance between their two detectors, $\sim 3000 \text{ km}$ [147].

There is predicted to be a stochastic background of gravitational waves from the large number of galactic and extragalactic close binaries, mainly white dwarf binaries. There are significant uncertainties in the calculation of the spectrum from this source due to uncertainty in stellar population models. Figures 7.12 and 7.13 show one prediction [124] for this background with the approximate uncertainty represented by the size of the band. This background is reduced to some extent by the ability to measure and subtract known binary sources. It can limit the ability of gravitational wave detectors to see other, cosmological sources of gravitational waves in this low frequency band.

New Physics Signals

Figure 7.14 shows several possible new physics sources of gravitational waves. An example spectrum from the TeV scale phase transition in RS1 taken from [136] is shown to illustrate roughly what the spectrum from an electroweak scale phase transition might look like. It shows a peak at frequencies around 10^{-2} Hz and can certainly be strong enough to be visible in these interferometric detectors. Of course there is much model dependence in this spectrum; for example, only a first order weak scale phase transition will produce gravitational waves at all.

Two example spectra are shown for cosmic strings with tensions $G\mu = 10^{-10}$ and 10^{-16} from [149]. It is important to note that not only is there model dependence in the spectrum from cosmic strings, but there is also much uncertainty in the calculation and so these should probably be considered to be upper limits on the spectrum of gravitational waves from such cosmic string networks. However, given these optimistic assumptions, it may be possible to detect a network of cosmic strings with tension

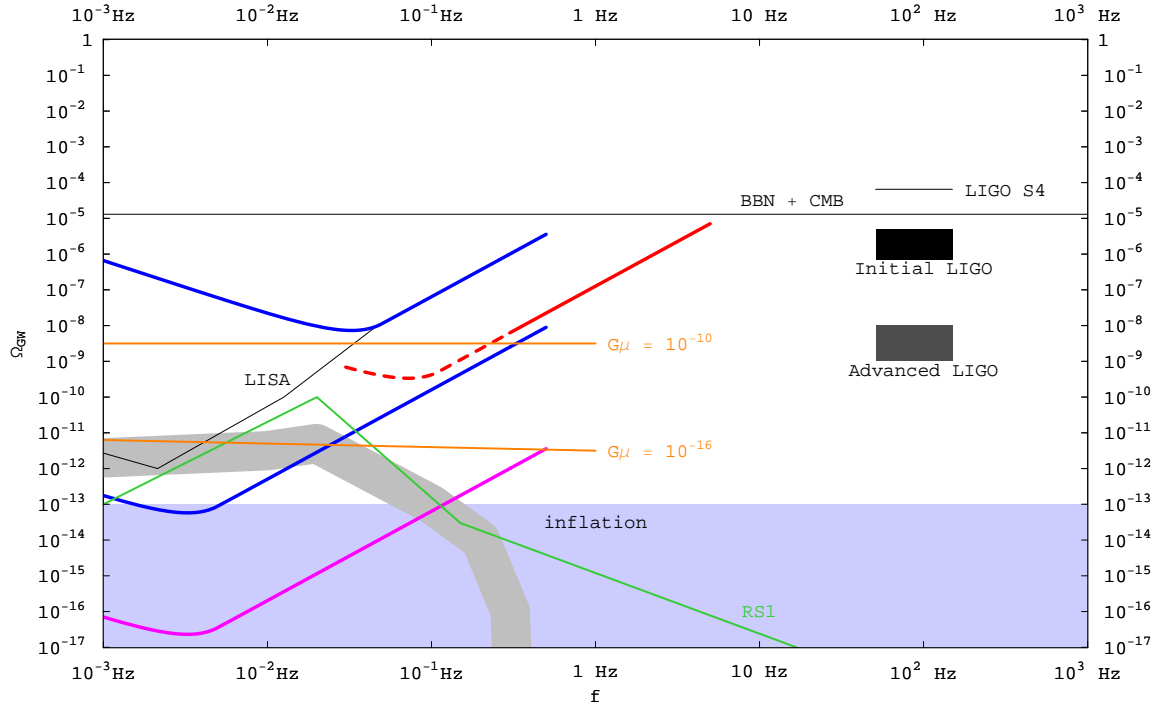


Figure 7.14: The same plot as in Figures 7.12, 7.13 with possible new physics sources of stochastic gravitational waves. The (green) curve labeled RS1 corresponds to an example spectrum of gravity waves from a TeV scale phase transition, in this case in RS1 [136]. The (orange) lines labeled with $G\mu$ correspond to one prediction for a network of cosmic strings with tensions $G\mu = 10^{-10}$ and 10^{-16} (with $\alpha = 0.1$ and $\gamma = 50$) [149]. Note that these cosmic string estimates have large uncertainties and may be optimistic assumptions.

as low as $G\mu = 10^{-16}$ using these interferometers. This is becoming limited by the white dwarf background, whose calculation itself has large uncertainties.

The region labeled ‘inflation’ in the figure is really the upper limit on the possible inflation spectrum assuming it is perfectly flat from the low frequency CMB bound. However, realistic models of inflation give $\Omega \lesssim 10^{-15}$ in our frequency band with the highest values of Ω from the highest scale models of inflation. Low scale inflation models will not directly give observable gravitational wave spectra, but could give observable gravitational waves from reheating (see e.g. [129]).

7.8 Conclusion

7.8.1 Comparison with Previous Work

Previous studies on the role of atom interferometers in gravitational wave detection concluded that they would be of limited use in probing the gravitational wave spectrum. Our proposal differs significantly from these efforts owing to the central role played by light pulse interferometry in our setup.

The work of [150], [151] and [152] used material mirrors like diffraction gratings to execute the interferometer. The gravitational wave signal in the configurations considered in these papers is $\sim khd$ where k is the momentum of the atom, h the amplitude of the gravitational wave and d the distance between the mirrors. It is experimentally difficult to make the distance between these mirrors bigger than ~ 1 m. Even if the distance between the mirrors were to be increased, the experiment would still be difficult since the separation between the two arms of the atom’s wave function must also be equally scaled. These considerations forced the authors to conclude that an unrealistic atom flux would be needed to see a gravitational wave. The use of material mirrors suffers from the additional drawback that the mirrors would be subject to vibration noise. The mirrors would have to be placed on vibration isolation stacks so this interferometer would be subject to the same limitations as light based interferometers like LIGO.

The work of [153] and [102] described atom interferometers which used light pulse

interferometry. However, these authors did not consider the effect of the gravitational wave on the light pulses used to execute the interferometry. Without this effect, the phase shift in the interferometer is $\sim khd$ where d is the separation between the two arms of the interferometer (see discussion in Section 7.3.2). Since the separation between the two arms of the interferometer cannot be easily scaled, these authors were also forced to consider unrealistic atom fluxes. Moreover, these papers did not discuss strategies to handle crucial backgrounds to gravitational wave detection like vibration and laser phase noise.

In this paper, we point out that the effect of the gravitational wave on the light pulses used to execute the interferometer is crucial and can be easily scaled to increase the signal. When the interferometer is operated by a laser at a distance L , a gravitational wave of amplitude h causes a phase shift $\sim khL$. This signal increases as long as L is smaller than the wavelength of the gravitational wave. Unlike the separation between the two arms of the atom's wave function, the distance between the atom and the laser can be easily scaled. With $L \sim 10$ km, the signal in this interferometer is 10^4 larger than the signal in the configurations previously considered. In addition to boosting the signal, the configuration considered in this paper offers an effective way to deal with vibration and laser phase noise. By using the same laser to run two widely separated interferometers and measuring the differential phase shift between the two interferometers, this setup drastically suppresses the effects of vibrations and laser phase noise. Our setup thus achieves a large, scaleable enhancement in the signal while simultaneously suppressing backgrounds thereby making it possible to search for gravitational waves with current technology.

The SAGAS [154] project that uses atom interferometry and ion clock techniques to explore gravity in the outer solar system was proposed. SAGAS will improve current bounds on stochastic gravitational waves in the frequency band 10^{-5} Hz – 10^{-3} Hz but is not expected to be sensitive to known sources of gravitational radiation. In contrast, our proposal will search for gravitational waves in the 10^{-3} Hz – 10 Hz band at sensitivities that can detect gravitational waves from expected sources.

7.8.2 Summary

We have proposed two experiments, terrestrial and satellite-based, to observe gravitational waves using atom interferometry. Both experiments rely on similar underlying ideas to achieve a large, scaleable enhancement to the gravitational wave signal while naturally suppressing many backgrounds. A differential measurement is performed between two atom interferometers run simultaneously using the same laser pulses. The lasers provide a common ‘ruler’ for comparison of the two interferometers. The distance between the interferometers can be large because only the light travels over this distance, not the atoms. The signal still scales with this distance and so can be competitive with light interferometers. In a sense, the atom interferometers are the analogue of the mirrors in a light interferometer and it is the distance between them that determines the size of the signal.

Further, many backgrounds are naturally suppressed by this method. Laser phase noise, which must be cancelled between the two arms of a light interferometer, is here cancelled by the differential measurement between the two atom interferometers. Since this subtraction is between two interferometers along the same laser axis with only vacuum in between, vibrations of the lasers (and any optics) are cancelled as well. The atoms themselves, the analogues of the mirrors in a light interferometer, are in free fall and are unaffected by vibrations. This removes one of the major backgrounds which prohibits terrestrial light interferometers from achieving sensitivity to lower frequencies. For example, Advanced LIGO will lose sensitivity below ~ 10 Hz due to direct (non-gravitational) coupling to vibrations (see e.g. [107]). Similarly, in the satellite-based experiment the atoms can be far from the satellite, greatly reducing the engineering requirements on the control of the satellites. Satellite position control and laser noise are two of the major hurdles for an experiment such as LISA. For similar gravitational wave sensitivity, these requirements are significantly reduced for our atom interferometer proposal.

Of course, new backgrounds may enter in an atomic experiment. We have attempted to consider all the relevant backgrounds and show that they are controllable with practical technology in a realistic setup. Many backgrounds will require careful engineering, just as for any gravitational wave detector. We are certainly not experts

in every relevant area of expertise necessary for such experiments, but this experiment seems possible and exciting enough to merit more serious consideration.

An interesting consequence of having a differential measurement between two interferometers along the same baseline is that this setup would have sensitivity to scalar-type perturbations, that would, for example, change the length of the perimeter of the LISA triangle. LIGO lacks sensitivity to these signals since two perpendicular laser arms are used to remove backgrounds including laser phase noise. Our setup confers sensitivity to overall changes in the length of a single arm since each arm is a laser phase noise free combination. In LISA these Sagnac channel events would be vetoed. One interesting signal of this type would arise from large mass dark matter particles passing near the detector [155, 156].

There are many avenues for improvement of these proposals in the future. The atom statistics may be improved with improved cooling techniques, ultimately limited only by the limit on the density of the cloud from atom-atom interactions and on the total number of atoms from opacity of the cloud. The use of squeezed atom states may also allow significant improvements in atom statistics beyond the standard quantum limit. Improved sensitivities could also come from better classical and atom optics including multi-photon LMT beamsplitters, higher laser powers and larger laser waist sizes. There may also be clever ideas for improved atomic systems, for example which suppress the spontaneous 2-photon transition rate without suppressing the stimulated rate. It is difficult to predict what advances will be made in the future. Nevertheless, the rapid advance of atom interferometry motivates us to consider a range of sensitivity curves that illustrate the possibilities not just for current but also near future technology.

The proposed gravitational wave detectors may allow the observation of low frequency sources in the band $10^{-3} - 10$ Hz. This is a very exciting range for astrophysical and cosmological sources. Compact binaries including black holes, neutron stars, and white dwarfs live for a long period in this band. Such low frequencies also allow enhanced sensitivity to a stochastic background of gravitational waves, assuming at least two such AGIS detectors are built. Many cosmological sources arising from physics beyond the Standard Model could be present in this range including inflation

and reheating, early universe phase transitions, or cosmic strings. The observation of gravitational waves has the potential to reveal significant information about new physics at both the shortest and longest length scales.

Chapter 8

Conclusion

This work has made great strides towards an ambitious new class of fundamental physics tests. A 10-meter tall atomic fountain gravimeter has been designed and built that is expected to reach record levels of acceleration sensitivity. In the near future, this apparatus will enable a test of the Equivalence Principle at the $10^{-15}g$ level.

There are many systematic errors that must be controlled and characterized at this previously unexplored sensitivity which this work has addressed in great detail. We created a comprehensive error model for the experiment and then used it to design the critical aspects of the apparatus. We developed viable strategies for suppressing the most challenging perturbations, including the coriolis force, magnetic fields, gravity inhomogeneities, and laser wavefront non-uniformity.

In addition to our experimental effort to test the Equivalence Principle, we have theoretically analyzed the potential impact of atom interferometry in other tests of general relativity. For instance, the current generation apparatus will have the sensitivity to measure non-trivial GR effects – such as velocity dependent forces and non-linear gravity – in a laboratory environment. We also proposed a new configuration for the detection of gravitation waves using atom interferometry, including a detailed, realistic consideration of the experimental backgrounds. Gravity wave sensors using atom interferometry offer access to a new, astrophysically interesting frequency band that complements the range accessible to LIGO-like sensors. These

theoretical studies represent a serious effort to explore the potential science applications that will soon be possible with atom interferometry.

While our initial test of the Equivalence Principle remains very important in its own right, we also see the EP apparatus developed in this work as the prototype for a series of exciting new experiments. Since its inception, atom interferometry has promised to advance gravitational science, and we now appear even closer to seeing that promise realized.

Appendix A

Testing Atom and Neutron Neutrality

A.1 Introduction

Charge quantization and atom neutrality in the Standard Model (SM) are mysteries which are automatically solved when the theory is embedded in a Grand Unified group. Even then, Witten has shown [157] that in the presence of CP non-conservation magnetic monopoles acquire an electric charge that is proportional to the amount of CP violation, a non-quantized quantity. This suggests that we have to rethink our notion of atom neutrality even in the presence of a unifying group.

The first experiments to test charge cancelation between the constituents of the atom came at the turn of the twentieth century [158]. These experiments placed a bound on $\frac{e+p}{e}$ of 10^{-21} , a value that is only an order of magnitude larger than the bound set by recent experiments [158, 159]. Experiments to detect individual neutron charges independently required different technology, took longer to develop, and have eventually reached a sensitivity of $10^{-21}e$, similar to that of atom neutrality experiments [158, 159]. Over eighty years after the first precision experiment on atom neutrality was performed, atom interferometry pushes the precision frontier, and provides a new tool for testing fundamental physics by measuring effects on individual atoms [109]. An experiment to test the equivalence principle and modifications of

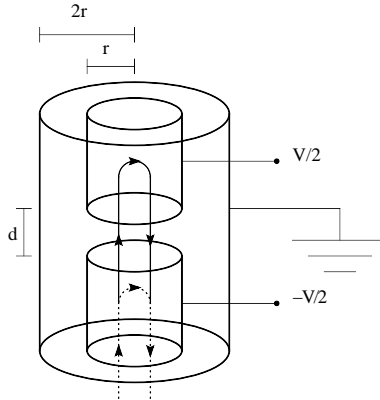


Figure A.1: The experimental setup including particle trajectories. The upper and lower electrode tubes are operated at potentials $V/2$ and $-V/2$ respectively, as described in the text.

gravity is already under construction [34]. In this Letter, we propose a modification of that experiment based on the scalar Aharonov-Bohm effect [160] that can detect atom and, independently, neutron charges down to $10^{-28}e$.

Because of the topological nature of the Aharonov-Bohm effect, the atoms are under the influence of pure gauge electromagnetic potentials; all electric and magnetic fields are zero. As a result, there are ideally no forces acting on the atoms, and systematics from the finite atom polarizability are avoided. If the atom carries a small charge ϵe , its wave-function will acquire a phase $\frac{\epsilon e}{\hbar} V t$, where e is the electron charge, t is the time spent in the region of electric potential V , and ϵ is the ratio of atom charge compared to the electron charge.

We begin with the experimental setup, and analyze possible systematics as well as the ultimate sensitivity of the experiment with different upgrades. We end with a discussion on the theoretical motivation behind infinitesimally charged atoms.

A.2 Experimental Setup

The proposed apparatus is based on a 10 m interferometer designed to test the equivalence principle [34]. Evaporatively cooled ^{87}Rb atoms are launched vertically with

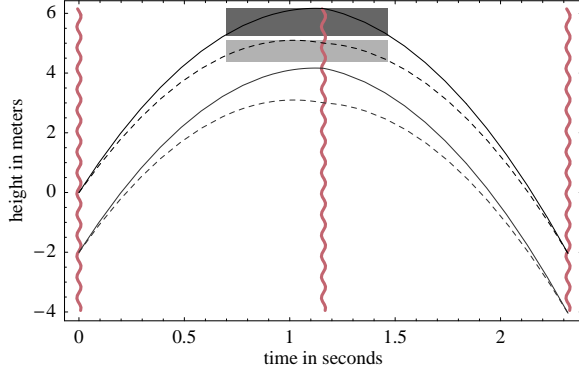


Figure A.2: The atom wave function trajectories as a function of time. The areas in dark and light gray indicate when the fast and slow atom wavefunctions are traveling in a region of voltage $V/2$ and $-V/2$, respectively. Below are shown the trajectories for a second atom cloud launched at the same time, in order to control systematics from laser phase noise.

an initial velocity $v_L \sim 10 \frac{\text{m}}{\text{s}}$. A series of laser pulses ($\frac{\pi}{2} - \pi - \frac{\pi}{2}$ sequence) acts as beamsplitters and mirrors for the atoms, splitting the atom wave-function into a superposition of space-time trajectories with momentum difference $\hbar k_{\text{eff}}$, and then recombining them in order to interfere. This momentum difference also sets the maximum spatial separation of the wave-packets at the maxima of their trajectories. Within the next few years, the application of Large Momentum Transfer (LMT) beamsplitters [36, 44, 161] in atom interferometry will likely be realized. With LMT, a velocity splitting of $\frac{\hbar k_{\text{eff}}}{m_{\text{atom}}} \sim 1 \frac{\text{m}}{\text{s}}$ may be possible and would result in a separation of 1.07 m between the fast and the slow wave-function component at the highest points of their trajectories.

Taking advantage of this large spatial separation, we can introduce regions of potential $V/2$ and $-V/2$ in the trajectories of the fast and slow components respectively, as illustrated in Fig. A.1. Both the fast and slow trajectories extend vertically along the axis of the lower cylindrical electrode of radius r . Only the fast-component trajectory extends upwards into a second cylindrical electrode of radius r . An axial gap d separates the two cylindrical electrodes, and the trajectory of the slow-component does not extend into the gap region. Assuming $d \sim \text{cm}$, strong electric fields of order

$V/d \sim 10^7 \frac{V}{m}$ are present in the gap. To avoid these, the voltage is applied only when the atoms are well inside the electrode tubes.

A.3 Sensitivity

If the atom carries a small charge ϵe , the phase difference between the fast and slow component of the atom wave-function is:

$$\epsilon e \int \frac{V}{\hbar} dt. \quad (\text{A.1})$$

For $V = 10^5$ Volts and an interaction time of 0.7 s, the phase shift becomes $\sim 10^{20}\epsilon$. With 10^6 atoms, assuming shot-noise limited phase sensitivity of 10^{-3} rad per trial and integrating over 10^6 trials, the experiment can probe phase shifts of 10^{-6} rad and measure atom charges down to $\epsilon \sim 10^{-26}$. These bounds are usually expressed in terms of the average charge per nucleon, $\eta \equiv \frac{\epsilon}{A}$, where A is the total number of nucleons in the atom. In this language, the experimental reach is $\eta \sim 10^{-28}$. The current laboratory limit is $\eta = 10^{-22}$ [159].

Future prospects for atom interferometry involve increasing the number of atoms per trial to $10^7 - 10^8$ and/or using entangled states of atoms. In experiments with entangled atoms, the atom phases add coherently in each shot and the sensitivity becomes Heisenberg-limited [162, 40, 41]. These prospects combined could allow an improvement of at least two orders of magnitude, bringing the experimental reach down to $\eta \sim 10^{-30}$.

A measurement of ϵ determines a linear combination of the proton, electron and neutron charges. An independent bound on the charge of the neutron can be placed by performing a differential measurement between ^{87}Rb and ^{85}Rb atoms in the same atom cloud. In this case, the ultimate sensitivity is $10^{-28}e$, an approximate 7 orders of magnitude improvement on current bounds. This experiment, combined with the measurement of the individual Rb atom charges, will give independent measurements of the neutron charge and the sum of the proton and electron charges. Measuring the charges of different atoms will improve the neutron charge measurement, but is

always sensitive to the sum of the proton and electron charges.

To obtain the desired experimental sensitivity, other stochastic sources of interferometer phase noise must be kept below the fundamental atom noise limit. Examples of such sources include laser phase noise and the fluctuating initial positions z_i of the atomic clouds, which couple to gravity gradients T_{zz} and lead to a phase shift $-k_{\text{eff}}T^2T_{zz}z_i \approx 7 \frac{\text{rad}}{\text{mm}}$, where $T = 1.16$ s is the interrogation time of the experiment, the time interval between the laser pulses in the $\frac{\pi}{2} - \pi - \frac{\pi}{2}$ sequence. To suppress laser phase noise, we consider operating a second interferometer in the same tube, vertically separated from the primary interferometer by approximately 2 meters to avoid the high voltage electrodes, and subject to the same laser pulses. We then compare the differential phase shift between the two interferometers as a function of the tube voltage in the primary interferometer; laser phase noise is the same for both interferometers and cancels as common mode. For the neutron charge measurement, the differential measurement is between the two collocated Rb isotopes and there is no need for the additional interferometer. Assuming the local gravitational gradient can be reduced to 10% by an engineered local mass distribution, the initial position fluctuations between the interferometers must be controlled at the $1 \mu\text{m}$ level to allow shot-noise-limited sensitivity, and at the 10 nm level for a Heisenberg-limited interferometer. Also, variations in the initial launch velocity can contribute to the noise through a gravity gradient phase shift $-k_{\text{eff}}T^3T_{zz}v_L \approx 10^4 \text{ rad}$. The launch velocity v_L must therefore be maintained consistent at the level of $1 \frac{\mu\text{m}}{\text{s}}$ for shot-noise limited sensitivity and $10 \frac{\text{nm}}{\text{s}}$ to reach the Heisenberg-limit.

A.4 Systematics

The potential is a control parameter that distinguishes the scalar Aharonov-Bohm effect from other systematic phase shifts. Assuming stochastic noise sources can be controlled at the shot-noise level, only systematic phase shifts that depend on the voltage can potentially limit sensitivity. Such an effect comes from the electric field gradient near the openings of the tube electrodes, which induces a dipole force on the atoms. To reduce this effect below detection, the voltage is turned on when the atoms

are at least 10 radii inside the tube electrodes. Since the atoms spend most of their time at the highest point of their trajectories, this procedure does not significantly affect the experimental sensitivity.

Turning the potential on and off involves transient currents which result in transient magnetic fields. We consider a linear voltage ramp to $V_0 = 100$ kV in a time $\tau = 0.1$ s. For a 1-meter long electrode of radius $r = 1$ cm surrounded by the coaxial grounded tube of radius $2r$, the transient current flowing during the charging process is approximately 8×10^{-5} A. Any asymmetry in the transient currents creates a magnetic field inside the tube. Assuming complete asymmetry the magnitude of the field along the axis of the tube is at most $B_{tr} \sim \frac{\mu_0}{2r} I_{tr} \sim 50 \mu\text{G}$. Since the atoms are in the $m_F = 0$ state along the z axis, they interact to second order with magnetic fields along z: $-\frac{1}{2}\alpha_m \vec{B}^2 = -\frac{1}{2}\alpha_m (\vec{B}_{tr} + \vec{B}_0)^2$, where $\vec{B}_0 = (1 \text{ mG}) \hat{z}$ is a constant bias magnetic field used to define the axis of quantization for the atoms. The transient field produces an additional acceleration along the direction of motion:

$$a = \alpha_m \frac{\partial_z (2\vec{B}_{tr} \cdot \vec{B}_0 + \vec{B}_{tr}^2)}{m} \sim 10^{-11} \frac{\text{m}}{\text{s}^2}, \quad (\text{A.2})$$

assuming significant variation of the transient field over 1 cm and $\alpha_m = 2\pi \times 575 \frac{\text{Hz}}{\text{G}^2}$ for ^{87}Rb .

One of the advantages of the aforementioned voltage-symmetric ($V/2$ and $-V/2$) design is that, as long as both the fast and slow atoms experience similar transient field gradients, the induced magnetic phase shift will partially cancel. To make a quantitative estimate, we separately consider the following set of magnetic fields and their gradients: the background bias field B_0 , the additional transient magnetic fields present in the upper ($V/2$) and lower ($-V/2$) electrodes while the voltage is being ramped up (B_{t1} and B_{t2} , respectively), and the additional transient magnetic field present in the upper and lower electrodes while the voltage is being brought back to ground (B_{t3} and B_{t4} , respectively).

To properly estimate the transient field effects we conduct the full phase calculation, as [47]:

$$\Delta\phi_{\text{total}} = \Delta\phi_{\text{propagation}} + \Delta\phi_{\text{laser}} + \Delta\phi_{\text{separation}}. \quad (\text{A.3})$$

Aharonov-Bohm Signal	phase shift(rad)	Scaling
$\epsilon eV(t_{\text{off}} - t_{\text{on}})/\hbar$	$10^{20}\epsilon$	V
Systematic	phase shift(rad)	Scaling
Magnetic (symmetric)		
$-\frac{1}{3\hbar}gt_{\text{off}}v_L\alpha_m\tau_2^3(\frac{\partial B_{t4}}{\partial z})^2$	-1×10^{-3}	$V^2\tau_2$
$\frac{1}{3\hbar}gt_{\text{off}}v_L\alpha_m\tau_2^3(\frac{\partial B_{t3}}{\partial z})^2$	1×10^{-3}	$V^2\tau_2$
$\frac{1}{6\hbar}g^2t_{\text{off}}^2\alpha_m\tau_2^3(\frac{\partial B_{t4}}{\partial z})^2$	7×10^{-4}	$V^2\tau_2$
$-\frac{1}{6\hbar}g^2t_{\text{off}}^2\alpha_m\tau_2^3(\frac{\partial B_{t3}}{\partial z})^2$	-7×10^{-4}	$V^2\tau_2$
$-\frac{1}{3\hbar}gt_{\text{on}}v_L\alpha_m\tau_1^3(\frac{\partial B_{t2}}{\partial z})^2$	-5×10^{-4}	$V^2\tau_1$
$\frac{1}{3\hbar}gt_{\text{on}}v_L\alpha_m\tau_1^3(\frac{\partial B_{t1}}{\partial z})^2$	5×10^{-4}	$V^2\tau_1$
Magnetic (non-symmetric)		
$-\frac{1}{3m}gk_{\text{eff}}(t_{\text{off}} - t_{\text{on}})\alpha_m\tau_1^3(\frac{\partial B_{t1}}{\partial z})^2$	-5×10^{-5}	$V^2\tau_1$
$-\frac{1}{m}B_0k_{\text{eff}}\alpha_m\tau_1^2\frac{\partial B_{t1}}{\partial z}$	-9×10^{-5}	$VB_0\tau_1$
Electric polarizability	10^{-14}	V^2

Table A.1: Estimated voltage-dependent signal and systematic phase shifts. V is the voltage applied on the tubes. t_{on} and t_{off} are the times when the voltage is turned on and off, respectively. The magnetic systematics are divided into terms that vanish for perfect upper-lower symmetry ($\partial_z B_{t1} = \partial_z B_{t2}$, $\partial_z B_{t3} = \partial_z B_{t4}$) and equal ramping times ($\tau_1 = \tau_2$) and terms that do not.

The primary voltage-dependent contributions to the phase shift are listed in Table A.1. Terms of order 10^{-4} rad may persist even with perfect upper-lower symmetry and equal ramp times. These terms may be present even when using two collocated Rb isotopes, since their respective α_m values are significantly different.

Both the symmetric and non-symmetric terms are suppressed by reducing the ramp times τ_i , and improving the symmetry of the electrode geometry so that the transient fields B_{ti} and their gradients are reduced. The transient magnetic fields vanish for current flow uniform on the tube surface and parallel to the tube axis during the charging process. In our estimate appearing in Table A.1 we have maximally exaggerated the asymmetry to demonstrate the most conservative case. \vec{B}_{tr}^2 and

There is another potential source of voltage dependent systematics: the walls of the high-voltage tube electrode experience a small deformation that depends on voltage due to electrostatic pressure. This deformation affects the diffraction of the laser from the walls of the tube and creates a small spurious voltage dependent phase

shift. This systematic can be pushed below the Heisenberg statistics sensitivity level, by reducing the laser beam waist below 5 mm for an electrode tube of 1 cm radius.

An earlier proposal to test matter neutrality [163] already employs the scalar Aharonov-Bohm effect. The apparatus is based on a Mach-Zehnder atom interferometer and the design sensitivity is $\eta \sim \frac{10^{-21}}{\sqrt{\text{Hz}}}$, compared to $\eta \sim \frac{10^{-27}}{\sqrt{\text{Hz}}}$ for the current proposal.

Appendix B

Gravity Inhomogeneities

Gravity inhomogeneities are an important background for the Equivalence Principle (EP) measurement. For this experiment, we use two Rb isotopes to measure the local gravitational acceleration g of the Earth. We simply drop the atoms and then perform atom interferometry as they freely fall, thereby precisely measure the acceleration of each isotope. Then we compare the two acceleration measurements derived from the isotopes to test the Equivalence Principle. This conceptually simple technique is unfortunately complicated by the fact that g varies with position in the lab. Therefore, it is easy to measure two different values of g simply by starting the two isotopes at different locations, resulting in an apparent EP violation. To combat this potential source of systematic error, the two isotope clouds must precisely follow the same trajectories so that they experience the same position dependent gravitational acceleration. The purpose of this appendix is to quantify how sensitive the interferometer is to gravitation perturbations at different length scales. This ultimately helps determine how well the isotope trajectories must coincide in order to suppress this background.

To proceed, we must calculate the sensitivity of an atom interferometer to gravity inhomogeneities. The observable quantity in an atom interferometer is the phase shift $\Delta\Phi$ that accumulates between its two arms. This phase shift depends on the local gravitational field that each arm experiences as it propagates. To a significant extent, the response of the interferometer is dominated by the constant piece of the

the gravitational field. This effect gives the main signal for the EP measurement and is calculated in Chapter 4. However, for this analysis, we are instead concerned with the small ripples in the gravitational field that are superimposed on this large constant piece. Since the gravitational inhomogeneities considered here are small, we can use perturbation theory to calculate the phase shift that they induce in the atom interferometer.

The next two sections deal with calculating the response of the atom interferometer to these ripples in the gravitational field. In order to make the analysis more general, we compute the response in the Fourier domain (\mathbf{k} -space). Our main result is a transfer function for gravity inhomogeneities. Conceptually, this transfer function gives the phase shift response of the interferometer to gravity perturbations as a function of the spatial wavelength of the perturbation. Quantitatively, the transfer function then provides a general mechanism for computing the phase shift caused by any arbitrary gravitational perturbation simply by summing up the contributions from each spatial frequency component of the perturbation weighted by the value of the transfer function at that frequency.

B.1 Perturbation theory phase shifts

We model gravitational inhomogeneities as a small position-dependent potential energy $\delta U(\mathbf{r})$. The presence of this perturbation modifies the atom's Lagrangian so that it becomes

$$L = L_0 - \epsilon \delta U(\mathbf{r}) \quad (\text{B.1})$$

where L_0 is the unperturbed Lagrangian. Here the dimensionless parameter ϵ is used to keep track of the order of the perturbation. To first order in ϵ ,[46] the phase shift is found by integrating the perturbing part of the Lagrangian over the *unperturbed* path of the interferometer:

$$\Delta\Phi = -\frac{\epsilon}{\hbar} \left\{ \int_{t_i}^{t_f} \delta U(\mathbf{r}_u) dt - \int_{t_i}^{t_f} \delta U(\mathbf{r}_l) dt \right\} + O(\epsilon^2) \quad (\text{B.2})$$

Here $\mathbf{r}_u(t)$ and $\mathbf{r}_l(t)$ are the upper and lower paths, respectively, of the unperturbed ($\epsilon = 0$) interferometer. The limits of the integral run from the first beamsplitter pulse of the interferometer at time t_i to the final beamsplitter at time t_f . In this formalism, the paths $\mathbf{r}_u(t)$ and $\mathbf{r}_l(t)$ are piecewise functions representing the entire trajectory during the interval $\{t | t_i \leq t \leq t_f\}$ which spans all of the beamsplitter and mirror pulses of the interferometer.

Note that the perturbation introduced here will in fact modify the interferometer paths at $O(\epsilon)$, but it just so happens that the resulting contributions to the phase shift are only $O(\epsilon^2)$. This approximation allows for a tremendous simplification of the calculation which holds up as long as the perturbation $\delta U(\mathbf{r})$ remains sufficiently small such that $O(\epsilon^2)$ terms can be neglected. This condition is easily met by the small gravitational ripples we consider here.

B.2 Transfer function for gravity inhomogeneities

The gravitational perturbation for an atom of mass m may be written

$$\delta U(\mathbf{r}) = m \delta\phi(\mathbf{r}) \quad (\text{B.3})$$

with $\delta\phi(\mathbf{r})$ the gravitational potential. The first order phase shift formula from above then becomes

$$\Delta\Phi = -\frac{1}{\hbar} \int_{t_i}^{t_f} m (\delta\phi(\mathbf{r}_u) - \delta\phi(\mathbf{r}_l)) dt \quad (\text{B.4})$$

where we dropped the parameter ϵ to simplify the notation. Consider the Fourier decomposition of the potential:

$$\delta\phi(\mathbf{r}) = \int \frac{d^3k}{(2\pi)^3} \widetilde{\delta\phi}(\mathbf{k}) e^{i\mathbf{k}\cdot\mathbf{r}} \quad (\text{B.5})$$

$$\widetilde{\delta\phi}(\mathbf{k}) = \int d^3r \delta\phi(\mathbf{r}) e^{-i\mathbf{k}\cdot\mathbf{r}} \quad (\text{B.6})$$

Here $\widetilde{\delta\phi}(\mathbf{k})$ is the amplitude of the Fourier component with spatial wavevector \mathbf{k} . The functions $\delta\phi(\mathbf{r})$ and $\widetilde{\delta\phi}(\mathbf{k})$ form a Fourier transform pair. Substituting Eq. B.5 into

Eq. B.4 gives

$$\Delta\Phi = -\frac{m}{\hbar} \int_{t_i}^{t_f} dt \int \frac{d^3k}{(2\pi)^3} (e^{i\mathbf{k}\cdot\mathbf{r}_u} - e^{i\mathbf{k}\cdot\mathbf{r}_l}) \widetilde{\delta\phi}(\mathbf{k}). \quad (\text{B.7})$$

We can then exchange the order of these integrals and define the transfer function response to gravitational potential perturbations:

$$T_\phi(\mathbf{k}) \equiv -\frac{m}{\hbar} \int_{t_i}^{t_f} dt (e^{i\mathbf{k}\cdot\mathbf{r}_u(t)} - e^{i\mathbf{k}\cdot\mathbf{r}_l(t)}) \quad (\text{B.8})$$

The phase shift can then be expressed as

$$\Delta\Phi = \int \frac{d^3k}{(2\pi)^3} \widetilde{\delta\phi}(\mathbf{k}) T_\phi(\mathbf{k}) \quad (\text{B.9})$$

which is just a sum over all spatial frequencies of the response transfer function times the size of the perturbation of the potential at that frequency.

The above formula (Eq. B.9) is conceptually the main result of this section. Although Eq. B.9 encompasses all of the physics necessary to study the effect of gravitational ripples on the interferometer, we will find it useful to develop several additional versions of this result. In particular, the main shortcoming of Eq. B.9 is that it is expressed in terms of the gravitational potential. While computationally convenient, the potential is conceptually less useful than the gravitational field. We will therefore reexpress this result in terms of the field instead of the potential. This will allow for more intuitive comparisons to other known acceleration backgrounds.

We begin with the standard definition of the gravitational field in terms of the gradient of the potential:

$$\delta\mathbf{g}(\mathbf{r}) \equiv -\nabla\delta\phi(\mathbf{r}) = -\int \frac{d^3k}{(2\pi)^3} (i\mathbf{k}) e^{i\mathbf{k}\cdot\mathbf{r}} \widetilde{\delta\phi}(\mathbf{k}) \quad (\text{B.10})$$

Notice that the gradient brings down an ($i\mathbf{k}$) in the frequency domain representation. The gravitational field $\delta\mathbf{g}(\mathbf{r})$ forms a Fourier transform pair with its \mathbf{k} -space

representation $\widetilde{\delta\mathbf{g}}(\mathbf{k})$:

$$\delta\mathbf{g}(\mathbf{r}) = \int \frac{d^3k}{(2\pi)^3} \widetilde{\delta\mathbf{g}}(\mathbf{k}) e^{i\mathbf{k}\cdot\mathbf{r}} \quad (\text{B.11})$$

$$\widetilde{\delta\mathbf{g}}(\mathbf{k}) = \int d^3r \delta\mathbf{g}(\mathbf{r}) e^{-i\mathbf{k}\cdot\mathbf{r}} \quad (\text{B.12})$$

Comparison of Eqs. B.10 and B.11 allows for the identification

$$\widetilde{\delta\mathbf{g}}(\mathbf{k}) = -i\mathbf{k}\widetilde{\delta\phi}(\mathbf{k}) \quad (\text{B.13})$$

which relates the Fourier components of the potential to the gravitational field. Inverting this expression yields

$$\widetilde{\delta\phi}(\mathbf{k}) = \frac{i\mathbf{k}}{k^2} \cdot \widetilde{\delta\mathbf{g}}(\mathbf{k}) \quad (\text{B.14})$$

which can now be substituted into Eq. B.9:

$$\Delta\Phi = \int \frac{d^3k}{(2\pi)^3} \left(\frac{i\mathbf{k}}{k^2} \cdot \widetilde{\delta\mathbf{g}}(\mathbf{k}) \right) T_\phi(\mathbf{k}). \quad (\text{B.15})$$

Finally we arrive at the gravitational field version of Eq. B.9

$$\Delta\Phi = \int \frac{d^3k}{(2\pi)^3} \widetilde{\delta\mathbf{g}}(\mathbf{k}) \cdot \mathbf{T}_g(\mathbf{k}) \quad (\text{B.16})$$

where the field transfer function is given by

$$\mathbf{T}_g(\mathbf{k}) \equiv \frac{i\mathbf{k}}{k^2} T_\phi(\mathbf{k}). \quad (\text{B.17})$$

It is worth reiterating that Eqs. B.9 and B.16 express the same physics and are simplify different formulations of the same result. Also notice that while this analysis so far has been very general, our result is somewhat cumbersome due to the three-dimensional nature of the problem. To gain further insight, it is useful to consider a one-dimensional version of the problem.

In this case, the atom interferometer configurations we are interested in are intrinsically one-dimensional. Ideally, the atoms should be freely-falling along the $\hat{\mathbf{z}}$ direction in order to maximize sensitivity to gravity. In any real experiment there will be unavoidable transverse motion arising from imperfect initial conditions and small transverse forces present during the interferometer. However, these effects are usually quite small. In a typical experiment, motion in the $\hat{\mathbf{z}}$ direction spans many meters while motion in the transverse direction is limited to the millimeter scale. Thus the dominate contribution to Eq. B.16 comes from $\hat{\mathbf{z}}$ component of the path.

Consider a perfectly one-dimensional interferometer along the $\hat{\mathbf{z}}$ -direction with $\mathbf{r}_u(t) \equiv z_u(t)\hat{\mathbf{z}}$ and $\mathbf{r}_l(t) \equiv z_l(t)\hat{\mathbf{z}}$ being the upper and lower paths, respectively. The transfer function for the potential is then reduced to

$$T_\phi(\mathbf{k}) \stackrel{1D}{=} -\frac{m}{\hbar} \int_{t_i}^{t_f} dt (e^{ik_z z_u(t)} - e^{ik_z z_l(t)}) = T_\phi(k_z) \quad (\text{B.18})$$

which only depends on k_z , the $\hat{\mathbf{z}}$ -component of the spatial wavevector. The phase shift for the one-dimensional problem is

$$\Delta\Phi_{1D} = \int \frac{d^3k}{(2\pi)^3} \widetilde{\delta\phi}(\mathbf{k}) T_\phi(k_z) \quad (\text{B.19})$$

$$= \int \frac{dk_z}{2\pi} T_\phi(k_z) \iint \frac{dk_x dk_y}{(2\pi)^2} \left(\int d^3r \delta\phi(\mathbf{r}) e^{-i\mathbf{k}\cdot\mathbf{r}} \right) \quad (\text{B.20})$$

where in the second line we have inserted the transform of $\widetilde{\delta\phi}(\mathbf{k})$ using Eq. B.6. Next, we can evaluate the k_x and k_y integrals since T_ϕ only depends on k_z :

$$\Delta\Phi_{1D} = \int \frac{dk_z}{2\pi} T_\phi(k_z) \int d^3r \delta\phi(\mathbf{r}) e^{-ik_z z} \left(\int \frac{dk_x}{2\pi} e^{-ik_x x} \right) \left(\int \frac{dk_y}{2\pi} e^{-ik_y y} \right) \quad (\text{B.21})$$

$$= \int \frac{dk_z}{2\pi} T_\phi(k_z) \int d^3r \delta\phi(\mathbf{r}) e^{-ik_z z} \delta(x) \delta(y). \quad (\text{B.22})$$

Here the Dirac delta function is given by

$$\delta(x) \equiv \int \frac{dk_x}{2\pi} e^{-ik_x x}. \quad (\text{B.23})$$

The integrals over x and y are now trivial and we are left with

$$\Delta\Phi_{1D} = \int \frac{dk_z}{2\pi} T_\phi(k_z) \left(\int dz \delta\phi(0, 0, z) e^{-ik_z z} \right) \quad (\text{B.24})$$

where the term in parenthesis is just the Fourier transform of the potential along the $\hat{\mathbf{z}}$ axis. Defining the one-dimensional scalar potential Fourier transform pair,

$$\widetilde{\delta\phi}(k_z) = \int dz \delta\phi(0, 0, z) e^{-ik_z z} \quad (\text{B.25})$$

$$\delta\phi(0, 0, z) = \int \frac{dk_z}{2\pi} \widetilde{\delta\phi}(k_z) e^{ik_z z} \quad (\text{B.26})$$

we then arrive at the one-dimensional analog of Eq. B.9,

$$\Delta\Phi_{1D} = \int \frac{dk_z}{2\pi} T_\phi(k_z) \widetilde{\delta\phi}(k_z). \quad (\text{B.27})$$

To convert this result from the potential to the field, we once again begin with the definition of the field but consider only the $\hat{\mathbf{z}}$ component:

$$\delta g_z(z) \equiv \hat{\mathbf{z}} \cdot \delta\mathbf{g}(0, 0, z) = -\partial_z \delta\phi(0, 0, z) \quad (\text{B.28})$$

In this case the derivative brings down a factor of (ik_z) in the Fourier domain giving

$$\delta g_z(z) = - \int \frac{dk_z}{2\pi} (ik_z) \widetilde{\delta\phi}(k_z) e^{ik_z z}. \quad (\text{B.29})$$

As before, the one-dimensional field can be written as a Fourier transform pair:

$$\delta g_z(z) = \int \frac{dk_z}{2\pi} \widetilde{\delta g_z}(k_z) e^{ik_z z} \quad (\text{B.30})$$

$$\widetilde{\delta g_z}(k_z) = \int dz \delta g_z(z) e^{-ik_z z}. \quad (\text{B.31})$$

Combining Eq. B.29 and B.30 gives the one-dimensional analog of Eq. B.13

$$\widetilde{\delta g_z}(k_z) = -ik_z \widetilde{\delta\phi}(k_z) \quad (\text{B.32})$$

The one-dimensional phase shift expressed in terms of the field is then given by

$$\Delta\Phi_{1D} = \int \frac{dk_z}{2\pi} T_{g_z}(k_z) \widetilde{\delta g_z}(k_z) \quad (\text{B.33})$$

where the one-dimensional field transfer function is

$$T_{g_z}(k_z) \equiv \frac{i}{k_z} T_\phi(k_z) = \hat{\mathbf{z}} \cdot \mathbf{T}_g(0, 0, k_z). \quad (\text{B.34})$$

We conclude this section by expressing the above result for the one-dimensional phase shift in terms of the spatial wavelength λ which is related to the wavevector by $k_z = \frac{2\pi}{\lambda}$. This conversion requires a simple change of variables for the integral in Eq. B.33. It can be shown that for an integral over any function $f(k_z)$ that this substitution gives

$$\int_{-\infty}^{\infty} \frac{dk_z}{2\pi} f(k_z) = \int_{-\infty}^{\infty} \frac{d\lambda}{\lambda^2} f(2\pi/\lambda). \quad (\text{B.35})$$

Applying this identity results in

$$\Delta\Phi_{1D} = \int \frac{d\lambda}{\lambda^2} T_{g_z}(2\pi/\lambda) \widetilde{\delta g_z}(2\pi/\lambda). \quad (\text{B.36})$$

We now make the following definition for the spectral components of the field as a function of wavelength:

$$\delta g_z^{(\lambda)}(\lambda) \equiv \frac{1}{\lambda^2} \widetilde{\delta g_z}(2\pi/\lambda). \quad (\text{B.37})$$

The field $\delta g_z(z)$ and $\delta g_z^{(\lambda)}(\lambda)$ then form a transform pair given by

$$\delta g_z^{(\lambda)}(\lambda) = \frac{1}{\lambda^2} \int dz \delta g_z(z) e^{-i\frac{2\pi z}{\lambda}} \quad (\text{B.38})$$

$$\delta g_z(z) = \int d\lambda \delta g_z^{(\lambda)}(\lambda) e^{i\frac{2\pi z}{\lambda}} \quad (\text{B.39})$$

which has the desirable property that $\delta g_z^{(\lambda)}(\lambda)$ is the amplitude of the Fourier coefficient with wavelength λ . The final result expressed in terms of wavelength is then

$$\Delta\Phi_{1D} = \int d\lambda T_{g_z}^{(\lambda)}(\lambda) \delta g_z^{(\lambda)}(\lambda) \quad (\text{B.40})$$

where the field transfer function versus wavelength is defined as

$$T_{g_z}^{(\lambda)}(\lambda) \equiv T_{g_z}(2\pi/\lambda) = \frac{i\lambda}{2\pi} T_\phi(2\pi/\lambda). \quad (\text{B.41})$$

B.3 Applications to specific interferometer configurations

The phase shift response of an atom interferometer depends critically on the space-time trajectories of the interfering paths. For the light-pulse atom interferometers that we consider here, these paths depend on the laser pulses used to manipulate each atom during the interferometer. These light pulses are used to implement the atom beamsplitters and mirrors. During each interaction with the laser, an atom can exchange momentum with the light, resulting in either an increase or decrease in velocity. This light-induced velocity change is called the recoil velocity and is given by

$$\mathbf{v}_R = \hbar \mathbf{k}_{\text{eff}} / m \quad (\text{B.42})$$

where \mathbf{k}_{eff} is the effective wavevector of the light. The specific value of \mathbf{k}_{eff} depends on the details of the atom-light interaction that implements the atom optics. For example, in the commonly used two-photon Raman or Bragg atom optics we have $\mathbf{k}_{\text{eff}} = 2\mathbf{k}$ where $k = 2\pi/\lambda$ is the normal wavevector of the light with wavelength λ . However, in the case of large momentum transfer (LMT) beamsplitters we have $\mathbf{k}_{\text{eff}} = N\mathbf{k}$ where N may be 10 or even 100.

B.3.1 Three pulse sequence

The simplest version of an atom-interferometer accelerometer that we consider is based on a three pulse sequence $(\frac{\pi}{2} - \pi - \frac{\pi}{2})$. The sequence consists of a beamsplitter $(\frac{\pi}{2})$ pulse at time $t = t_0$ followed by a mirror (π) pulse at $t = t_0 + T$ and finishes with a final beamsplitter $(\frac{\pi}{2})$ at $t = t_0 + 2T$. As a result, the three-pulse sequence is the atom equivalent of a Mach-Zehnder interferometer. The dominate phase shift of this

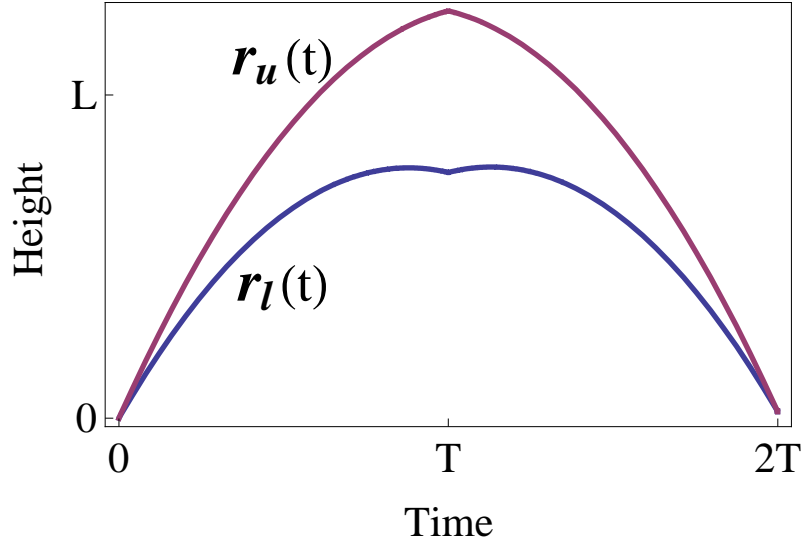


Figure B.1: Atom trajectory for a $(\frac{\pi}{2}, \pi, -\frac{\pi}{2})$ three pulse sequence.

sequence is the accelerometer response, which for acceleration \mathbf{g} is

$$\Delta\Phi_{3\text{ pulse}}^{(0)} = \mathbf{k}_{\text{eff}} \cdot \mathbf{g} T^2 \quad (\text{B.43})$$

Figure B.1 shows the space-time trajectories of the upper and lower paths in a three-pulse sequence. At each of the three times when light pulses occur, the velocity of the atom changes discontinuously due to the recoil velocity.

The field transfer function for the three pulse sequence is shown in Fig. B.2. At very long wavelengths ($\lambda \rightarrow \infty$) the response asymptotes to the constant gravity phase shift given by Eq. B.43. For short wavelengths ($\lambda \lesssim L$), the response is cutoff since the interferometer effectively averages over many oscillations of those perturbations with wavelength smaller than its characteristic size L .

For the EP experiment, we are interested in the differential response between the two isotopes of Rubidium. The differential field transfer function versus wavelength is defined as

$$\Delta T_{g_z}^{(\lambda)}(\lambda) \equiv [T_{g_z}^{(\lambda)}(\lambda)]_{^{85}\text{Rb}} - [T_{g_z}^{(\lambda)}(\lambda)]_{^{87}\text{Rb}} \quad (\text{B.44})$$

Figure B.3 shows the differential gravity transfer function for the EP measurement.

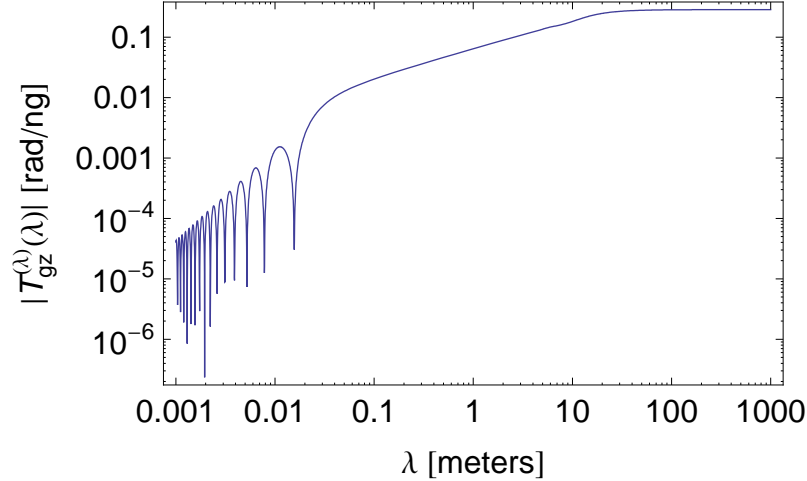


Figure B.2: Magnitude of the gravity transfer function as a function of wavelength for ^{87}Rb . The plot is for a symmetric interferometer in which the launch velocity $v_L = gT = 13 \text{ m/s}$ (see Fig. B.1).

Notice that the long wavelength differential response is suppressed since both interferometers have the same response to a constant acceleration (assuming the EP holds). The residual differential response is due to differences in the trajectories of the two isotopes during the interferometers. Their trajectories vary both as a result of differences in initial conditions (launch kinematics) and because of the different recoil velocity of each isotope due to their unequal mass.

B.3.2 Four pulse sequence

More complicated interferometer sequences can be used to suppress certain systematic errors. For example, a four pulse $(\frac{\pi}{2} - \pi - \pi - \frac{\pi}{2})$ sequence suppresses phase shifts due to a linear gravity gradient.[48] As discussed in Chapter 4, the differential gravity gradient phase shift in the EP measurement is a challenging systematic error to control because it requires nm-level overlap of the isotope trajectories. A four pulse sequence can reduce these requirements by rendering the interferometer insensitive to the gravity gradient perturbation.

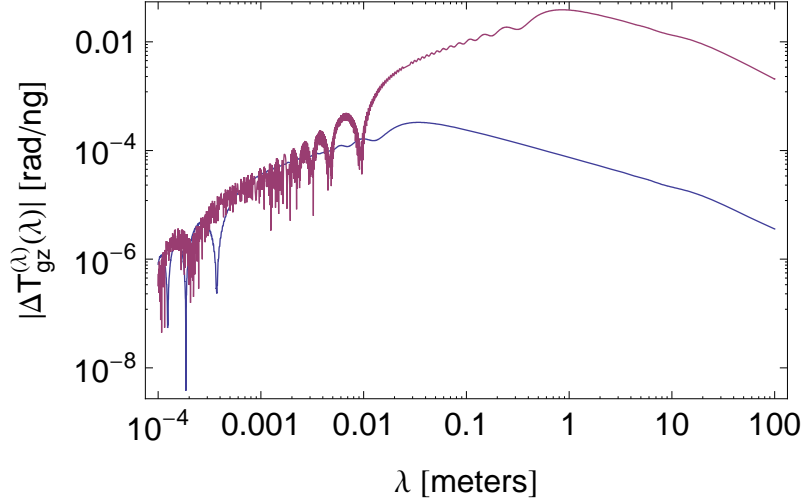


Figure B.3: Magnitude of the differential gravity transfer function as a function of wavelength for the EP measurement using a three-pulse sequence. The blue curve assumes conventional $2\hbar k$ atom optics while the red curve assumes $50\hbar k$ LMT atom optics.

The four pulse sequence consists of a beamsplitter ($\frac{\pi}{2}$) pulse at time $t = t_0$, a mirror (π) pulse at $t = t_0 + T_1$, another mirror (π) pulse at $t = t_0 + T_2$, and a final beamsplitter ($\frac{\pi}{2}$) at $t = t_0 + 2T$, where $0 < T_1 < T_2 < 2T$. The specific choice of T_1 and T_2 determines the shape of the interferometer which affects its phase response. For example, the symmetric case $T_1 = T/2$ and $T_2 = 3T/2$ results in an interferometer that is insensitive to uniform acceleration.

The gravity gradient phase shift¹ is suppressed for the choice $T_1 = \frac{(\sqrt{5}-1)}{2}T$ and $T_2 = \frac{(\sqrt{5}+1)}{2}T$. The trajectories that result from this choice are shown in Fig. B.4. In this case, the uniform acceleration response is reduced to[48]

$$\Delta\Phi_{4 \text{ pulse}}^{(0)} = (\sqrt{5} - 2)\mathbf{k}_{\text{eff}} \cdot \mathbf{g}T^2 \approx 0.24 \Delta\Phi_{3 \text{ pulse}}^{(0)} \quad (\text{B.45})$$

which means that the insensitivity to the gravity gradient comes at the expense of a reduced sensitivity to uniform acceleration compared to the three pulse sequence.

¹More precisely, this choice for T_1 and T_2 eliminates all phase shifts that are proportional to T^3 .

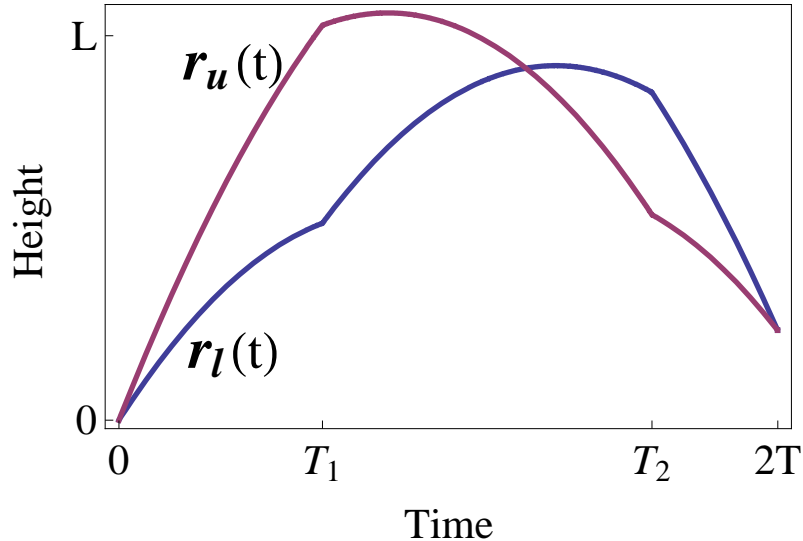


Figure B.4: Atom trajectory for a $(\frac{\pi}{2}-\pi-\pi-\frac{\pi}{2})$ four pulse sequence. The choice of $T_1 = \frac{(\sqrt{5}-1)}{2}T$ and $T_2 = \frac{(\sqrt{5}+1)}{2}T$ shown here makes the interferometer insensitive to gravity gradient induced phase errors.

Figure B.5 shows the differential gravity transfer function for the EP measurement for the case of a four pulse sequence with T_1 and T_2 chosen to eliminate the gravity gradient response. Notice that, as expected, the sensitivity of the four pulse sequence is smaller at long wavelengths than the three pulse sequence. This reflects the fact that a linear gravity gradient acts like a $\lambda \gtrsim L$ wavelength perturbation within the interferometer region.

B.4 Phase shift response for a discrete source spectrum

The theoretical treatment developed here so far has been limited to working with continuous functions for the gravitational field. This model is only directly applicable in the rare case when the gravitational field is known analytically. In the physically relevant case that the gravitational field is experimentally measured, $\mathbf{g}(\mathbf{r})$ will only be known at a discrete set of points limited by the necessarily finite spatial separation

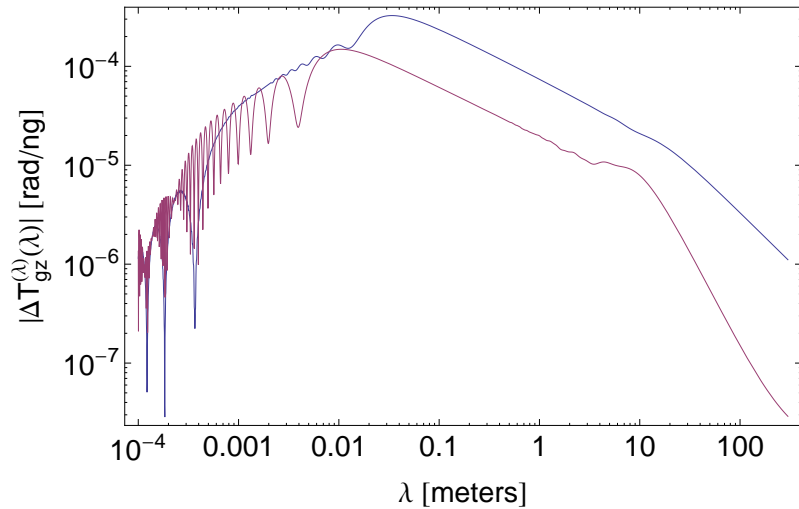


Figure B.5: Magnitude of the EP differential gravity transfer function using a four pulse sequence with π pulse times chosen to cancel gravity gradients (red). The blue curve is the three pulse sequence EP response shown for reference. Both curves assume equal launch kinematics for ^{85}Rb and ^{87}Rb , with $v_L = 13 \text{ m/s}$ and $2\hbar k$ atom optics. The response of the four pulse sequence to wavelengths $\lambda \gtrsim L \approx 10 \text{ m}$ is suppressed because these long wavelengths approximate a linear gravity gradient in the interferometer region.

between each measurement. This same situation applies for a numerically modeled gravitational field since the field can only be calculated on a finite grid of points, e.g. in a finite-element model(FEM). In both cases we must adapt the result of Eq. B.40 for a gravitational field that is only known at discrete points.

To begin, it is convenient to work with the single-sided spectrum:

$$\Delta\Phi_{1D} = \int_{-\infty}^{\infty} d\lambda T_{g_z}^{(\lambda)}(\lambda) \delta g_z^{(\lambda)}(\lambda) \quad (\text{B.46})$$

$$= \int_0^{\infty} d\lambda T_{g_z}^{(\lambda)}(\lambda) \delta g_z^{(\lambda)}(\lambda) + \int_0^{\infty} d\lambda T_{g_z}^{(\lambda)}(-\lambda) \delta g_z^{(\lambda)}(-\lambda) \quad (\text{B.47})$$

Here we split the integral into a positive and negative half and then changed variables so that the range of each integral is the same. Next, direct inspection of the definitions of $T_{g_z}^{(\lambda)}(\lambda)$ and $\delta g_z^{(\lambda)}(\lambda)$ lead to the identities

$$T_{g_z}^{(\lambda)}(-\lambda) = T_{g_z}^{(\lambda)*}(\lambda) \quad (\text{B.48})$$

$$\delta g_z^{(\lambda)}(-\lambda) = \delta g_z^{(\lambda)*}(\lambda) \quad (\text{B.49})$$

where the asterisk indicates the complex conjugate. Combining the two integrals,

$$\Delta\Phi_{1D} = \int_0^{\infty} (T_{g_z}^{(\lambda)}(\lambda) \delta g_z^{(\lambda)}(\lambda) + T_{g_z}^{(\lambda)*}(\lambda) \delta g_z^{(\lambda)*}(\lambda)) d\lambda \quad (\text{B.50})$$

$$= 2 \int_0^{\infty} \text{Re}[T_{g_z}^{(\lambda)}(\lambda) \delta g_z^{(\lambda)}(\lambda)] d\lambda \quad (\text{B.51})$$

where we used $\text{Re}[z] = (z + z^*)/2$. Now the phase shift is expressed in terms of an integral over only the positive half of the spectrum.

The above integral can be approximated by a Riemann sum over a finite set of N points. Let $\lambda_n \equiv \frac{L}{n}$ for $1 \leq n \leq N$ be the points where the integrand is evaluated. The integral is then approximately given by

$$\Delta\Phi_{1D} \approx 2 \sum_{n=1}^N \text{Re}[T_{g_z}^{(\lambda)}(\lambda_n) \delta g_z^{(\lambda)}(\lambda_n)] (\lambda_n - \lambda_{n+1}) \quad (\text{B.52})$$

where $\lambda_1 = L$ is chosen to be large enough so that the contribution to the integral

from the range $[L, \infty)$ can be safely ignored. Also, the number of discrete sampling points N must be sufficiently large to ensure that the Riemann sum converges to the integral within some allowable error. This essentially requires that the Nyquist wavelength $\lambda_N = L/N$ is small enough so that all the significant frequency content of the integrand is properly sampled. The final result for the discrete version of the phase shift response is

$$\Delta\Phi_{1D} = 2 \sum_{n=1}^N \operatorname{Re}[T_{g_z n}^{(\lambda)} \delta g_{zn}^{(\lambda)}] \quad (\text{B.53})$$

where we have made the following definitions:

$$T_{g_z n}^{(\lambda)} \equiv T_{g_z}^{(\lambda)}(\lambda_n) \quad (\text{B.54})$$

$$\delta g_{zn}^{(\lambda)} \equiv \delta g_z^{(\lambda)}(\lambda_n) \cdot (\lambda_n - \lambda_{n+1}) \quad (\text{B.55})$$

Notice that $g_{zn}^{(\lambda)}$ has the units of gravitational acceleration and should be interpreted as the amplitude of the Fourier component at wavelength λ_n in the sampling bandwidth $(\lambda_n - \lambda_{n+1})$.

Next, Eq. B.38 can also be approximated by a Riemann sum over the discrete values of the gravitational field:

$$\delta g_{zn}^{(\lambda)} = \frac{(\lambda_n - \lambda_{n+1})}{\lambda_n^2} \sum_{j=1}^N (z_{j+1} - z_j) \delta g_z(z_j) e^{-i(2\pi z_j / \lambda_n)} \quad (\text{B.56})$$

Here $z_j \equiv \Delta z \cdot j$ are the positions where the field is known and $L \equiv N\Delta z$ is chosen to be the size of the measurement region. Thus we have $\lambda_n = \frac{N\Delta z}{n}$ which finally leads to

$$\delta g_{zn}^{(\lambda)} = \frac{1}{N} \frac{n}{n+1} \sum_{j=1}^N \delta g_z(z_j) e^{-2\pi i j n / N} \quad (\text{B.57})$$

where the sum is just the usual formula for the discrete Fourier transform of the measured field.

Appendix C

Broadband Optical Serrodyne Frequency Shifting

Optical frequency shifting has broad commercial and scientific applications. For example, optical telecommunication FSK protocols can be implemented using single-sideband (SSB) frequency shifters[164]. In spectroscopy and laser cooling experiments, agile frequency shifts from the MHz through the GHz range are often required[165, 166].

Acousto-optic modulators (AOMs) are commonly used for MHz-level shifts, but a given AOM has a limited tuning range which is only a small fraction of its fixed center frequency. AOMs that can deliver GHz-level shifts typically offer this increased bandwidth by sacrificing diffraction efficiency. Broadband electro-optic phase modulators (EOMs) avoid many of the bandwidth and tuning range limitations of AOMs. Commercially available fiber phase modulators can have modulation bandwidths > 10 GHz. However, typical sinusoidal phase modulation is an inherently inefficient method of frequency shifting. At best, the fraction of the power in the first-order sideband is $\eta = (J_1(\beta_{\max}))^2 \approx 0.34$, where $J_n(\beta)$ are the Bessel functions of the first kind. Also, the presence of large undesirable frequency spurs at other harmonics can cause problems in some applications.

In this appendix, we use a serrodyne phase modulation signal[167] to demonstrate broadband electro-optic frequency shifting with high efficiency into the desired

sideband and correspondingly small undesirable spurs.

We briefly review the theory of serrodyne phase modulation[168]. The electric field for the light exiting the EOM is $E(t) = E_0 \cos(\omega t + \phi(t))$ where ω is the optical frequency and $\phi(t)$ is the phase imprinted by the modulator. A direct frequency shift can be imparted by applying a linear phase ramp,

$$\phi(t) = (m\delta) \cdot t \bmod 2\pi m \quad (\text{C.1})$$

where $\dot{\phi} = m\delta$ is the desired shift and m is an integer. This phase ramp need only extend from 0 to $2\pi m$ before resetting since cosine is 2π -periodic. The resulting waveform is a sawtooth with angular frequency δ and amplitude $2\pi m$. The first order ($m = 1$) condition results in a frequency shift δ , but higher order shifts ($m > 1$) are also possible. Although a serrodyne signal can theoretically mimic a linear phase ramp within a finite tuning range, it requires a high bandwidth to faithfully reproduce the discontinuities at the end of each period.

The usefulness of the serrodyne technique is limited by the quality of the sawtooth waveform that can be produced within an experimentally accessible bandwidth, and this gets increasingly difficult for higher frequency shifts. Early work was done with MHz-level frequency shifts[167, 169], and more recently improved spur suppression has been demonstrated at these frequencies[168, 170, 171, 172]. Higher frequency serrodyne shifts were achieved with photonic arbitrary waveform generation (PAWG) using mode-locked lasers[173, 174], but these techniques are complicated and have limited tunability. In addition, PAWG based on spatial-spectral holography[175, 176] as well as commercially available conventional arbitrary wave generators with > 10 GS/s sampling rates could conceivably be used to produce high-quality GHz sawtooth waves.

Here we generate high frequency (200 MHz - 1.6 GHz) sawtooth waveforms with good fidelity by using a Non-Linear Transmission Line (NLTL). In an NLTL, an electronic signal experiences an amplitude-dependent propagation speed[177]. This effect results in a steepening of the input waveform as the higher amplitude components

catch up with the lower amplitude components. A sinusoidally driven NLTL therefore outputs an approximate sawtooth waveform at the drive frequency. The NLTLs that we use are commercially available, passive components and generate harmonic content out to > 20 GHz.

We directly drive a LiNbO₃ fiber phase modulator (Photline Technologies NIR-MPX850-LN08, > 8 GHz bandwidth) with the serrodyne signal generated by an NLTL and analyze the resulting spectrum with a Coherent model 240 Fabry-Perot spectrometer (Fig. C.1a). We drive the NLTLs by amplifying the output of a signal generator (HP83712A) with a broadband RF amplifier (Mini-Circuits ZHL-42W). The NLTLs produce high output power serrodyne signals, and since the fiber phase modulators have a low $V_\pi \simeq 8$ V, we can directly drive the modulator without post-amplifying, and thus further bandwidth limiting, the NLTL output.

We generate 780 nm narrow-linewidth (~ 1 MHz) laser light using a MOPA laser setup (New Focus Vortex injecting an Eagleyard Tapered Amplifier). A small fraction of the light (30 mW) is coupled into the fiber phase modulator, providing up to 14 mW of output light. We couple a fraction of this power into the Fabry-Perot cavity (FSR 7.5 GHz, resolution ~ 25 MHz).

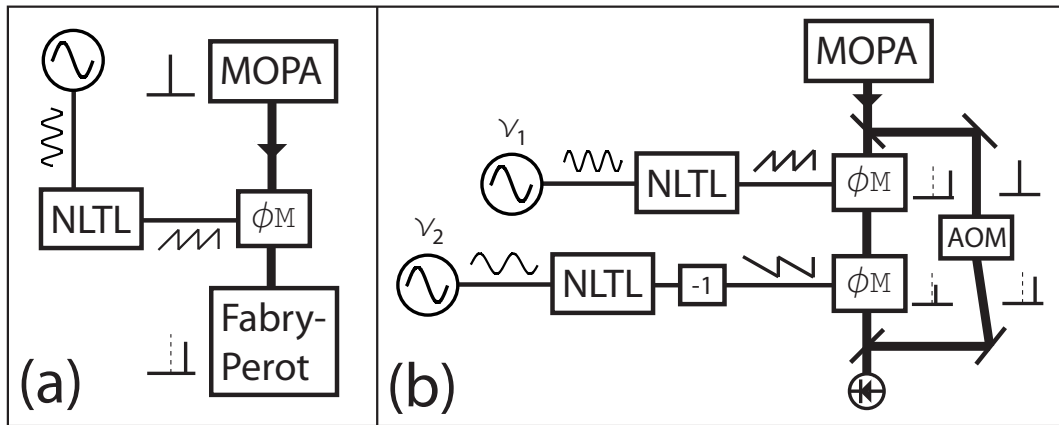


Figure C.1: Experimental setup. (a) A single phase modulator (ϕM) measured with a Fabry-Perot cavity. (b) Two phase modulators in a push-pull configuration measured via a heterodyne beat with the reference beam shifted 194 MHz by an AOM.

The serrodyne output of the NLTL varies with input frequency and amplitude.

We characterized three NLTLs manufactured by Picosecond Pulse Labs with different frequency ranges and rated input powers: 7112-110 (300 – 700 MHz @ 29 dBm), 7113-110 (600 – 1600 MHz @ 29 dBm) and 7102-110 (300 – 700 MHz @ 24 dBm, requiring a ZHL-42W post-amplifier). Each NLTL was swept through its frequency range, and the input amplitude was varied at each point to determine the optimum serrodyne signal. We captured a data spectrum and a reference spectrum (no RF drive applied to the NLTL) at each drive frequency with a digital oscilloscope. Example traces are shown in Fig. C.2. Note that since the fiber phase modulator is electrically floating, we can reverse the signal and ground connections to apply a minus sign to the serrodyne signal (a balun could also be used).

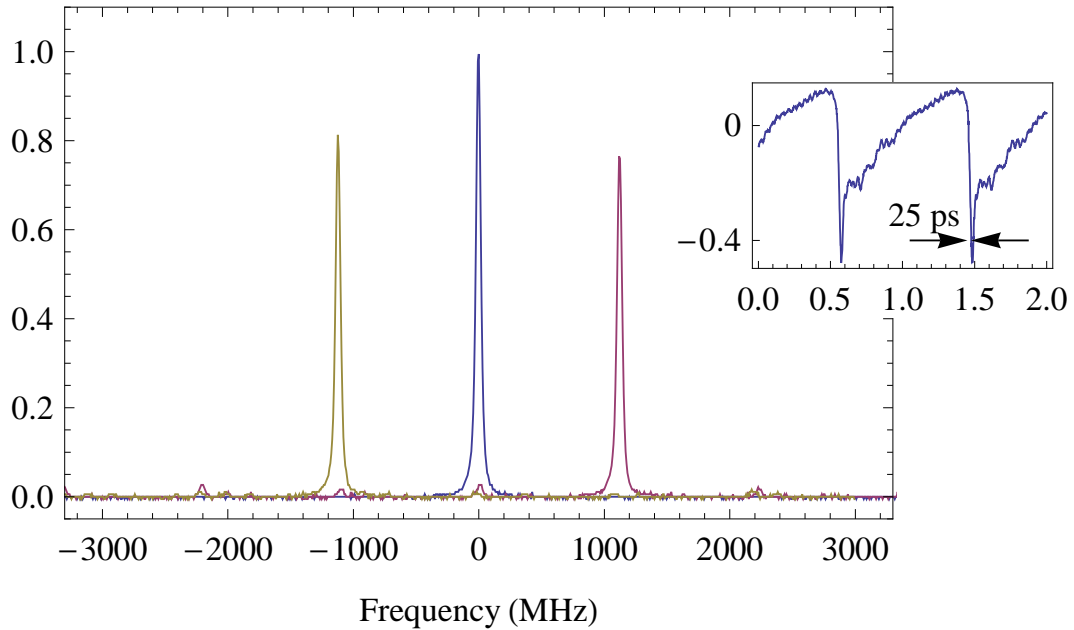


Figure C.2: Optical spectrum with and without serrodyne modulation normalized to the unmodulated carrier. The center (blue) curve shows the optical spectrum with no RF modulation. The right (red) and left (yellow) curves are the spectrum with a serrodyne modulation of +1.1 GHz and -1.1 GHz, respectively. The inset shows the applied 1.1 GHz serrodyne waveform in volts versus time in nanoseconds as measured by a 63 GHz oscilloscope.

The efficiency η of the serrodyne is the fraction of the unmodulated carrier power shifted into the desired sideband. Our serrodyne frequency shift has $\eta > 0.6$ from

200 MHz to 1.2 GHz as shown in Fig. C.3. Of particular interest are the regions from 400 – 500 MHz and from 1 – 1.1 GHz which maintain $\eta \sim 0.8$. This is comparable to a well-aligned single pass AOM. Similarly, we also characterize the cleanliness of the resulting spectrum by its spurious sideband fraction SF, defined as the ratio of the largest spurious frequency component to the desired signal. We measure SF < 0.2 from 200 MHz to 1.2 GHz as shown in Fig. C.3. In the region from 700 MHz to 1.1 GHz we find SF < 0.1. Figure C.2 (left trace) shows a shift with $\eta = 0.82$ and SF = -16 dB.

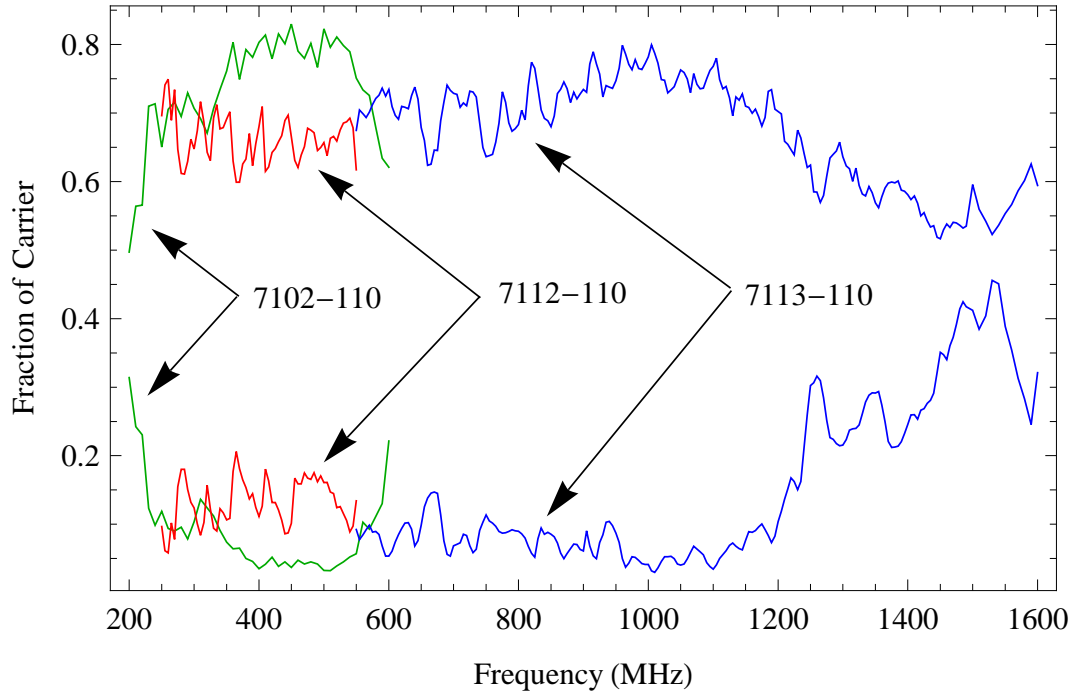


Figure C.3: Serrodyne modulation efficiency. The upper and lower curves show η and SF, respectively.

As a consistency check of the observed spectra, we made a time domain measurement of the applied sawtooth waveform $V(t)$ using a 63 GHz Agilent Infiniium DCA 86100B oscilloscope (Fig. C.2 inset). We then calculated the implied serrodyne spectrum using $\phi(t) = \alpha V(t)$ and fit the result to the observed spectrum shown in Fig. C.2 with a single free parameter α . The predicted spectrum matches the observations very well, with an RMS peak height difference of < 2% relative to the carrier.

In addition to the first order serrodyne results, we demonstrated second order shifts ($m = 2$ in Eq. C.1) by increasing the amplitude of the sawtooth waveform using the post-amplified 7102-110. This allows for a larger serrodyne frequency shift of 2δ without exceeding the frequency range of the NLTL. We observed second order shifts with $\eta_2 > 0.5$ and $SF_2 < 0.25$ for a frequency shift range of 800 MHz to 1 GHz. These results were likely limited by the 4.2 GHz bandwidth of the post-amplifier.

To obtain smaller frequency shifts, we arranged two identical fiber phase modulators in a push-pull configuration (Fig. C.1b). The two modulators are driven by NLTLs supplied by independently tunable amplified function generators running at frequencies ν_1 and ν_2 , respectively. With this flexible setup we can continuously scan the serrodyne output at $\Delta\nu = \nu_1 - \nu_2$ from positive to negative frequencies out to the maximum frequencies of the NLTLs. We used a heterodyne measurement to characterize the push-pull spectrum for $\Delta\nu$ smaller than the linewidth of the Fabry-Perot (Fig. C.4). An AOM in the reference arm of the interferometer shifted the carrier by a fixed frequency of 194 MHz so that we could distinguish positive frequency beat notes from negative frequency beat notes with respect to the unshifted carrier. We find that higher-order harmonics of $\Delta\nu$ are suppressed by at least 25 dB compared to the desired shifted signal.

We investigated the phase noise of the serrodyne-shifted light by comparing the unmodulated heterodyne beat note signal to that of the push-pull signal out to 1 MHz with a resolution bandwidth of 1 kHz. The phase noise of the unmodulated signal was -95 dBc/Hz at 150 kHz offset. During serrodyne modulation we observe no increase in phase noise above this noise floor.

Optical SSB modulation using a dual Mach-Zehnder geometry[178] is another well-known solution for frequency shifting in the GHz range. However the maximum efficiency is $\eta_{SSB} = (J_1(\beta_{max}))^2 \approx 0.34$, at which point the -3δ spur is only suppressed by $SF_{SSB} = \left(\frac{J_3(\beta_{max})}{J_1(\beta_{max})}\right)^2 \approx -15$ dB. Our measured efficiency is better than this limit, and in some frequency ranges the spur suppression is better as well. Additionally, the NLTL serrodyne scheme needs only a single phase modulator compared to the four that must be integrated into an SSB modulator. Finally, the multiple path Mach-Zehnder geometry is a potential source of low-frequency drift.

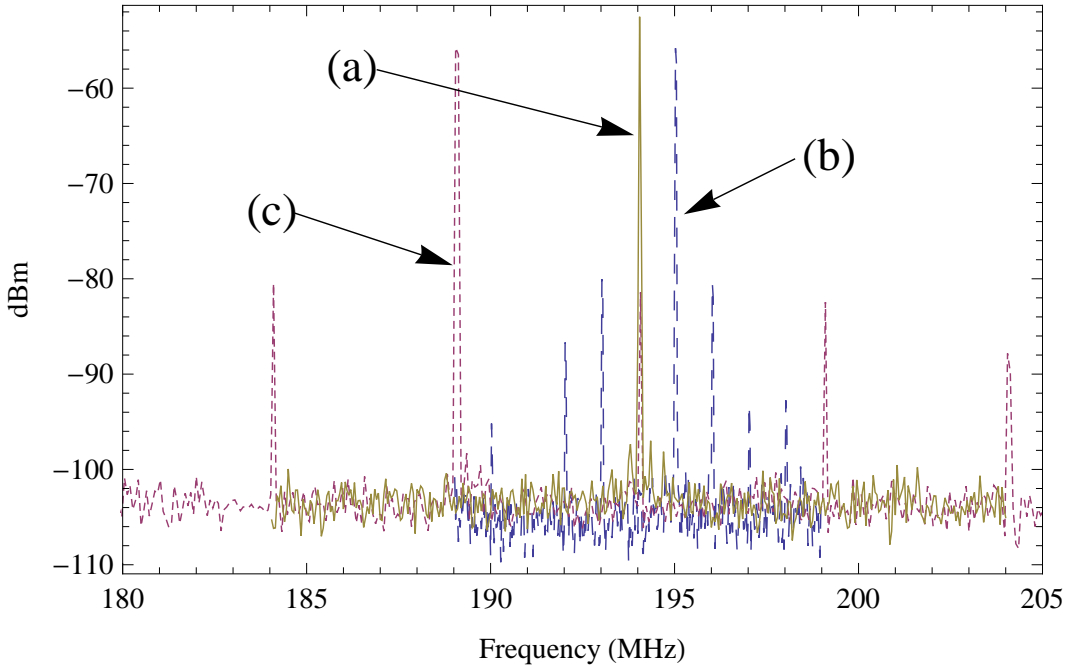


Figure C.4: Heterodyne spectra of push-pull frequency shift. (a) No modulation (b) $\Delta\nu = +1$ MHz (c) $\Delta\nu = -5$ MHz.

The serrodyne technique can potentially be improved to offer cleaner frequency shifts and a larger tuning range. The fall time is the principle performance driver[168], and NLTLs can generate sub-picosecond transients[179]. This is more than 50 times faster than our measured fall time. Additionally, the serrodyne could be improved by adding a passive network to adjust the phase and amplitude of the existing frequency components.

Although the dual modulator push-pull configuration allows for a much larger tuning range, it does so at the expense of an additional modulator. In principle, the two serrodyne drive signals could be subtracted using a high-frequency balun and then applied to a single modulator.

It is interesting to compare these NLTL results to what could be achieved with state-of-the-art commercially available AWGs. An AWG with a 24 GS/s sampling rate can in principle generate sawtooth waveforms with fall times as short as 35 ps which would allow for GHz serrodyne shifts with spurious sideband fraction and

phase noise similar to what we observe with the NLTLs¹. However, an AWG-based scheme would most likely require high-power, broadband (~ 1 W, $BW \approx 10$ GHz) post-amplification to achieve efficient phase modulation, and the cost and overhead associated with high frequency arbitrary synthesis is a disadvantage.

Serrodyne frequency shifting using NLTLs offers several advantages over traditional optical frequency manipulation. Unlike an AOM, the serrodyne phase modulator does not spatially shift the beam and is thus immune to temperature induced alignment changes. An NLTL-driven phase modulator offers a greater than three octave dynamic tuning range, and using a push-pull configuration we have demonstrated continuous tuning from -1.6 GHz to $+1.6$ GHz. This is more flexible than previous frequency shifting techniques in this band.

A similar implementation of the serrodyne technique recently appeared in [180]. Many thanks to the Fejer group for lending us the Infinium oscilloscope.

¹Tektronix AWG7122B, 35 ps fall time @ 1 Vpp, phase noise -85 dBc/Hz @ 10 kHz offset.

Appendix D

Picosecond Optical Switching using RF Non-Linear Transmission Lines

To keep pace with the demand for digital content, optical data rates are being pushed toward 1 Tb/s. High speed Optical Time Division Multiplexing (OTDM) using a single wavelength is an attractive option to achieve these transmission speeds. OTDM requires fast optical switches and short pulse generators, and these elements have been implemented in a variety of manners [181]. Electro-optic[182] and electroabsorptive[183, 182] modulators can directly apply an electronic switching signal to an optical carrier. Alternatively, non-linear effects have been used to modulate a short clock pulse to implement an all-optical mux and demux at 160 Gb/s [184]. A variety of OTDM schemes use an interferometer as an intensity modulator by inducing a phase shift between the arms via some non-linear interaction (*e.g.*, cross phase modulation)[185, 186]. These require short (~ 1 ps) optical gate pulses, typically generated by mode-locked laser diodes (MLLD). These schemes are either complicated, or have not been shown to be capable of sub-psec switching speeds.

In this appendix, we propose a novel switching scheme that is simple and robust and has the potential to be competitive with current technology and could conceivably support a Tb/s OTDM network. Our proposed sub-picosecond optical switch is composed of an interferometer in which the phase difference between the arms is controlled by a pair of electro-optic modulators (EOMs) driven by a non-linear

transmission line (NLTL). An NLTL can passively generate the THz-level harmonic content needed for sub-ps switching, and as a result we do not need a fast control pulse.

In an NLTL, an electronic signal experiences an amplitude-dependent propagation speed that causes an input sinusoidal wave with period T to steepen as it propagates[177]. The output approximates a sawtooth wave that periodically grows linearly for a time $(T - t_F)$ and then returns to zero in a short fall time t_F at the end of each cycle. Commercially available NLTLs have fall times in the picosecond range which are necessary for sawtooth generation in the GHz range[33]. When this signal is used to drive an electro-optic phase modulator, the short fall time is imprinted on the light as a phase shift $\phi(t)$ provided that the modulator RF bandwidth is larger than $\sim t_F^{-1}$.

In order to implement an optical switch, we apply NLTL-generated phase shifts to both arms of an interferometer using two independent phase modulators ϕM_1 and ϕM_2 (Fig. D.1). The interferometer output depends on the phase difference between the two arms given by

$$\delta\theta = \phi(t - \Delta T) - \phi(t) + \delta\theta_0 \quad (\text{D.1})$$

where ΔT is an added time delay between the drive signals and $\delta\theta_0$ is any (slowly varying) phase difference not induced by the modulators. The intensity at the output port is then proportional to $\sin^2(\delta\theta/2)$. For $\Delta T = 0$, the $\phi(t)$ signals are temporally overlapped and cause no phase shift. Choosing $\Delta T = t_F$ results in a narrow window of time $2t_F$ at the end of each sawtooth period during which the two waveforms do not cancel, leading to a rapid variation in $\delta\theta$. The output intensity of the interferometer then depends on $\delta\theta_0$. Setting $\delta\theta_0 = 0$ gives a dark port condition for all times except during the interval $2t_F$ when light can emerge as a short pulse.

NLTLs with fall times around 500 fs have already been demonstrated in GaAs[179, 177], and sub-300 fs fall times should be possible[177]. However, phase modulators are limited by their finite RF bandwidth, which typically can be no greater than 100–200 GHz due to the dielectric loss tangent[187] or electrode surface resistance[188].

It may be possible to mitigate these RF coupling losses by directly integrating an NLTL into the traveling-wave modulator instead of putting them in series. This could be accomplished by periodically loading the modulator waveguide with Schottky diodes. If the modulator's RF waveguide acts as an NLTL in the region where the light and RF co-propagate, then the rapidly falling edge that develops on the RF signal should be directly imprinted on the light, avoiding any coupling loss. This could allow for sub-picosecond phase modulation features that would enable Tb/s optical switching. Note that the performance of GaAs-based traveling wave EOMs is comparable to the LiNbO₃ modulators employed here[189, 190], and waveguide dimensions and doping profiles of GaAs modulators[191] are very similar to state-of-the-art NLTL designs[192].

We implement this scheme in a proof-of-concept experiment where we demonstrate 70 ps optical switching using commercially available NLTLs driving LiNbO₃ traveling wave EOMs. Previously, the output of a silicon-based NLTL driven at 10 GHz followed by a pulse forming network (PFN) was applied to a LiNbO₃ modulator, resulting in a 27 ps optical pulse train[193]. This corresponds to a time reduction of 3.7 as compared to the factor of 30 that we demonstrate here. In addition, our switch operates by subtracting two sawtooth modulation signals optically instead of differentiating the NLTL output electronically, thereby avoiding the need for a PFN and any bandwidth limits that it may impose.

We built optical switches based on both Mach-Zehnder and Sagnac interferometer geometries (Figs D.1a and D.1b, respectively). The Mach-Zehnder interferometer (MZI) has the advantage that both its output ports are accessible. Therefore the MZI can be used as a directional switch allowing input light to transfer to either of its output ports. However, the spatially separated arms of the Mach-Zehnder make the interferometer sensitive to uncontrolled drifts in the optical phase $\delta\theta_0$ and so it must be actively stabilized. The Sagnac interferometer geometry is intrinsically insensitive to drifts in $\delta\theta_0$ since all optical elements are common to both arms. Furthermore the output port of the Sagnac is naturally dark. Since the Sagnac interferometer only has one output port distinct from its input, it acts as a toggle switch. If both ports are required, a non-reciprocal element (*e.g.*, an optical isolator) can be used to access

the other port.

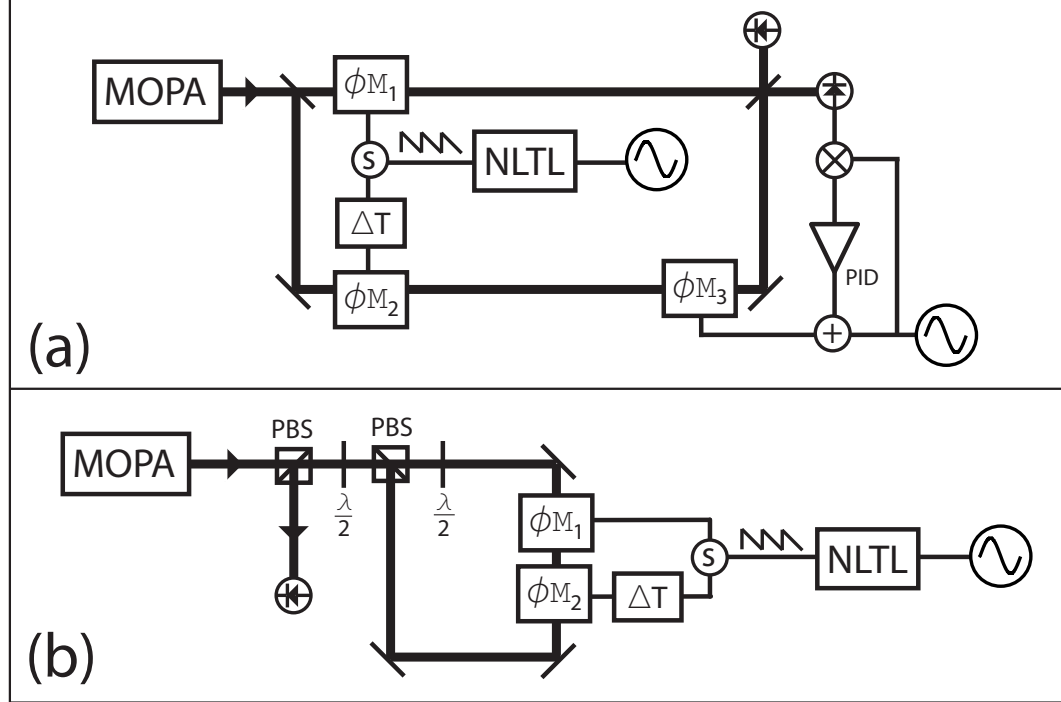


Figure D.1: Experimental setup. (a) Mach-Zehnder interferometer. Each arm contains a phase modulator (ϕM). An additional phase modulator ϕM_3 applies PID feedback to actively stabilize the interferometer. The sawtooth RF signal is split (S) and then goes through a delay line (ΔT). (b) Sagnac interferometer. The two phase modulators are connected back-to-back with a fiber-fiber coupler to form a Sagnac loop. The symmetry of the Sagnac loop allows for stable operation without active feedback. PBS: polarizing beam-splitter; $\lambda/2$: half waveplate.

We demonstrate these two switches using a sinusoidal RF drive to create an optical pulse train from a CW laser source. The pulse spacing is then given by the period T of the input RF signal and the pulse width is determined by the time delay ΔT .

For the MZI switch, we generate the sawtooth waveform with an NLTL (Picosecond Pulse Labs 7102-110) driven with a 450 MHz RF signal at 26 dBm from an amplified (Mini-Circuits ZHL-1W) function generator. We divide the NLTL output using a power splitter (Mini-Circuits ZN2PD2-50), send one signal through a tunable RF delay line, and then apply the two resulting 20 dBm sawtooth waves to separate fiber phase modulators (Photline Technologies NIR-MPX850-LN08, > 8 GHz

bandwidth).

For the input light, we use a 780 nm narrow-linewidth (1 MHz) MOPA laser setup (New Focus Vortex injecting an Eagleyard tapered amplifier). A small fraction of the light (25 mW - this power level is set by technical limitations of our setup and it is not fundamental) is coupled into each fiber phase modulator and the outputs are then overlapped and interfered on a beam splitter. We detect the intensity modulated light at the dark port of the interferometer using a 25 GHz-bandwidth photodiode (New Focus 1431 VIS-IR).

Mechanical and thermal noise cause phase variations in $\delta\theta_0$. In order to remain at the dark port we actively stabilize the relative phase between the two arms using a dither lock. An additional phase modulator ϕM_3 in one interferometer arm serves as a feedback actuator. We generate the error signal by dithering ϕM_3 at 10 MHz with small modulation depth and then demodulating the bright port response at the dither frequency. This error signal is sent through a PID controller, combined with the dither signal using a bias-tee and applied to ϕM_3 .

We measure the time domain photodiode signal of the stabilized MZI using a 63 GHz Agilent Infinium DCA 86100B oscilloscope. The measured pulses were averaged 64 times. By optimizing the time delay ΔT for short pulses, we obtained a 70 ps pulse train at a repetition rate of 450 MHz as shown in Fig. D.2. Choosing ΔT correctly is crucial for generating short pulses. In Fig. D.2, the optimized MZI pulse train is shown in comparison to the case where $\Delta T = \Delta T_{\text{optimal}} + 130$ ps. Not only are the resulting pulses longer, they are also asymmetric due to ripple on the sawtooth time-domain waveform [33].

We built a Sagnac interferometer by placing two phase modulators back-to-back as shown in Fig. D.1b. The Sagnac geometry relies on the direction-dependent modulation efficiency of the traveling wave EOMs to impart a differential phase shift to the counter-propagating arms. Since the modulators rely on phase velocity matching between the RF signal and light for efficient phase-modulation, ϕM_1 and ϕM_2 are arranged with opposite RF propagation directions so that each modulator predominately affects only one direction of the Sagnac loop. Still, even with this phase velocity

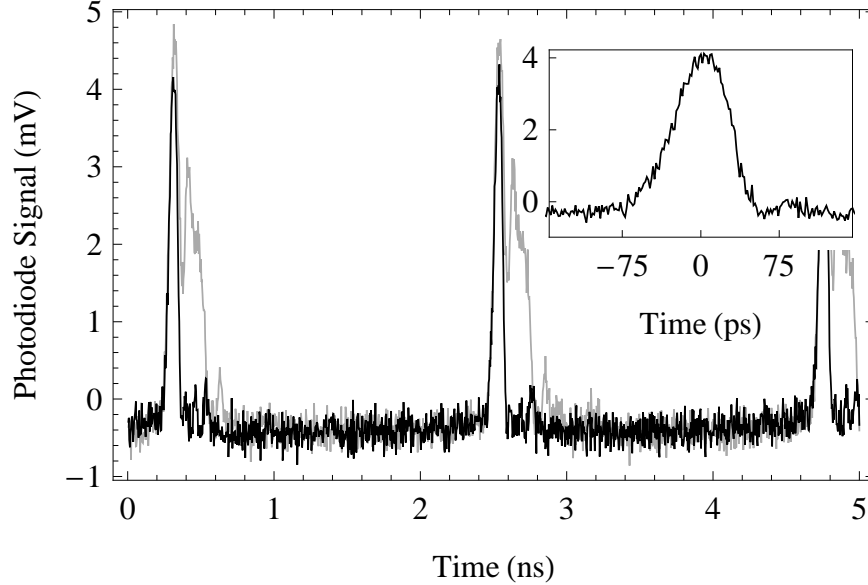


Figure D.2: MZI pulse train. A 450 MHz repetition rate, 70 ps FWHM pulse train generated by subtracting two sawtooth waveforms with an MZI (black). Appropriate choice of ΔT is required to obtain these short pulses. The longer (150 ps) pulses (gray) have $\Delta T = \Delta T_{\text{optimal}} + 130$ ps.

mismatch, each modulator imprints an undesired phase shift on the non-phase velocity matched arm. However, the counter-propagating modulator is not efficient above the corner frequency $f_c = \frac{c}{2\pi nL} \approx 680$ MHz, and its modulation is completely suppressed whenever $f = \pi m f_c$ for positive integer m , where n is the index of refraction and L is the length of the electro-optic crystal[194]. This allows for asymmetric RF modulation between the two directions.

Again we optimized the time delay ΔT and NLTL drive frequency for short pulses, obtaining a 100 ps pulse train at a repetition rate of 617.9 MHz as shown in Fig. D.3. To avoid damage to the phase modulators, the light power in either direction of the Sagnac is less than in either arm of the MZI. The data in Fig. D.3 is averaged 256 times.

The power reduction in the Sagnac configuration is not fundamental and can conceivably be improved. In principle, a single phase modulator with RF propagating in

both directions could reduce fiber coupling and insertion losses by up to ~ 3 dB. Appropriate choice of NLTL drive frequency and electro-optic crystal length can further suppress modulation crosstalk from the non-phase-velocity-matched direction.

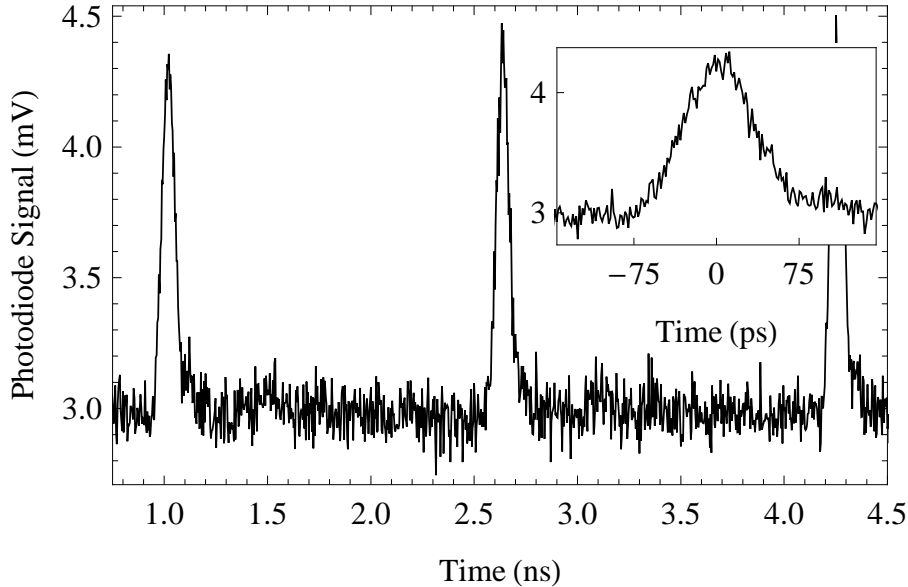


Figure D.3: Sagnac interferometer pulse train. A 617.9 MHz repetition rate, 100 ps FWHM pulse train generated by subtracting two sawtooth waveforms with a Sagnac interferometer.

With appropriate RF control over the input to the NLTL, the switches demonstrated here can be incorporated into an OTDM system. Although the data shown in Figs. D.2 and D.3 was taken using a continuous RF drive signal, in principle the switch only requires a single RF cycle to operate. The NLTL passively reduces the pulse length of the RF waveform from the initial period T to the fall time t_F . In our case, a 2.2 ns period sine wave is converted into a 70 ps pulse train, corresponding to a time reduction of ~ 30 . In an OTDM system, this would allow the electronic data rate to be 30 times slower than the optical data rate, allowing many channels to be multiplexed using the same wavelength.

Bibliography

- [1] Clifford Will. *Theory and Experiment in Gravitational Physics*. Cambridge University Press, Cambridge, 1993.
- [2] C. Brans and R. H. Dicke. Mach's principle and a relativistic theory of gravitation. *Phys. Rev.*, 124(3):925–935, Nov 1961.
- [3] T. Damour and A. M. Polyakov. The string dilation and a least coupling principle. *Nuclear Physics B*, 423(2-3):532 – 558, 1994.
- [4] Gia Dvali, Gregory Gabadadze, and Massimo Porrati. 4d gravity on a brane in 5d minkowski space. *Physics Letters B*, 485(1-3):208 – 214, 2000.
- [5] Nima Arkani-Hamed, Savas Dimopoulos, Gia Dvali, and Gregory Gabadadze. Non-local modification of gravity and the cosmological constant problem. (arXiv:hep-th/0209227), 2002.
- [6] Nima Arkani-Hamed, Hsin-Chia Cheng, Markus A. Luty, and Shinji Mukohyama. Ghost condensation and a consistent infrared modification of gravity. *Journal of High Energy Physics*, 2004(05):074, 2004.
- [7] M. Milgrom. A modification of the Newtonian dynamics as a possible alternative to the hidden mass hypothesis. *Astrophys. J.*, 270:365–370, July 1983.
- [8] Jacob D. Bekenstein. Relativistic gravitation theory for the modified newtonian dynamics paradigm. *Phys. Rev. D*, 70(8):083509, Oct 2004.
- [9] G. M. Clemence. The relativity effect in planetary motions. *Rev. Mod. Phys.*, 19(4):361–364, Oct 1947.

- [10] R. V. Pound and G. A. Rebka. Apparent weight of photons. *Phys. Rev. Lett.*, 4(7):337–341, Apr 1960.
- [11] Mark Kasevich and Steven Chu. Atomic interferometry using stimulated raman transitions. *Phys. Rev. Lett.*, 67(2):181–184, Jul 1991.
- [12] T. L. Gustavson, P. Bouyer, and M. A. Kasevich. Precision rotation measurements with an atom interferometer gyroscope. *Phys. Rev. Lett.*, 78(11):2046–2049, Mar 1997.
- [13] M. J. Snadden, J. M. McGuirk, P. Bouyer, K. G. Haritos, and M. A. Kasevich. Measurement of the earth’s gravity gradient with an atom interferometer-based gravity gradiometer. *Phys. Rev. Lett.*, 81(5):971–974, Aug 1998.
- [14] G. Biedermann. *Gravity Tests, Differential Accelerometry and Interleaved Clocks with Cold Atom Interferometers*. PhD thesis, Stanford University, 2007.
- [15] A Peters, K Y Chung, and S Chu. High-precision gravity measurements using atom interferometry. *Metrologia*, 38(1):25, 2001.
- [16] Holger Müller, Sheng-wey Chiow, Sven Herrmann, Steven Chu, and Keng-Yeow Chung. Atom-interferometry tests of the isotropy of post-newtonian gravity. *Phys. Rev. Lett.*, 100(3):031101, Jan 2008.
- [17] J. B. Fixler, G. T. Foster, J. M. McGuirk, and M. A. Kasevich. Atom Interferometer Measurement of the Newtonian Constant of Gravity. *Science*, 315(5808):74–77, 2007.
- [18] Clifford M. Will. The confrontation between general relativity and experiment. *Living Rev. Rel.*, 9:3, 2005.
- [19] James G. Williams, Slava G. Turyshev, and Dale H. Boggs. Progress in lunar laser ranging tests of relativistic gravity. *Phys. Rev. Lett.*, 93(26):261101, Dec 2004.

- [20] S. Schlamminger, K.-Y. Choi, T. A. Wagner, J. H. Gundlach, and E. G. Adelberger. Test of the equivalence principle using a rotating torsion balance. *Phys. Rev. Lett.*, 100(4):041101, Jan 2008.
- [21] J. Mester, R. Torii, P. Worden, N. Lockerbie, S. Vitale, and C. W. F. Everitt. The STEP mission: principles and baseline design. *Classical and Quantum Gravity*, 18:2475–2486, July 2001.
- [22] P. Touboul, B. Foulon, L. Lafargue, and G. Metris. The microscope mission. *Acta Astronautica*, 50:433–443, April 2002.
- [23] Sebastian Fray, Cristina Alvarez Diez, Theodor W. Hänsch, and Martin Weitz. Atomic interferometer with amplitude gratings of light and its applications to atom based tests of the equivalence principle. *Phys. Rev. Lett.*, 93(24):240404, Dec 2004.
- [24] E. Fischbach, G. T. Gillies, D. E. Krause, J. G. Schwan, and C. Talmadge. Non-Newtonian Gravity and New Weak Forces: an Index of Measurements and Theory. *Metrologia*, 29:213–260, January 1992.
- [25] E. G. Adelberger, B. R. Heckel, and A. E. Nelson. Tests of the gravitational inverse-square law. *Annual Review of Nuclear and Particle Science*, 53(1):77–121, 2003.
- [26] S. Schlamminger, K.-Y. Choi, T. A. Wagner, J. H. Gundlach, and E. G. Adelberger. Test of the equivalence principle using a rotating torsion balance. *Phys. Rev. Lett.*, 100(4):041101, Jan 2008.
- [27] D. B. Kaplan and M. B. Wise. Couplings of a light dilaton and violations of the equivalence principle. *Journal of High Energy Physics*, 8:37, August 2000.
- [28] C. Cutler and K. S. Thorne. An Overview of Gravitational-Wave Sources. (arXiv:gr-qc/0204090), April 2002.

- [29] Savas Dimopoulos, Peter W. Graham, Jason M. Hogan, and Mark A. Kasevich. General relativistic effects in atom interferometry. *Phys. Rev. D*, 78(4):042003, Aug 2008.
- [30] J. M. Hogan, D. M. S. Johnson, and M. A. Kasevich. Light-pulse atom interferometry. In E. Arimondo, W. Ertmer, and W. P. Schleich, editors, *Proceedings of the International School of Physics "Enrico Fermi" on Atom Optics and Space Physics*, pages 411–447, Amsterdam, 2009. IOS Press.
- [31] Savas Dimopoulos, Peter W. Graham, Jason M. Hogan, Mark A. Kasevich, and Surjeet Rajendran. An Atomic Gravitational Wave Interferometric Sensor (AGIS). *Phys. Rev. D*, 78:122002, 2008.
- [32] Asimina Arvanitaki, Savas Dimopoulos, Andrew A. Geraci, Jason Hogan, and Mark Kasevich. How to test atom and neutron neutrality with atom interferometry. *Phys. Rev. Lett.*, 100(12):120407, Mar 2008.
- [33] D. M. S. Johnson, J. M. Hogan, S. w. Chiow, and M. A. Kasevich. Broadband optical serrodyne frequency shifting. *Opt. Lett.*, 35(5):745–747, 2010.
- [34] Savas Dimopoulos, Peter W. Graham, Jason M. Hogan, and Mark A. Kasevich. Testing general relativity with atom interferometry. *Phys. Rev. Lett.*, 98(11):111102, Mar 2007.
- [35] C. Pethick and H. Smith. *Bose-Einstein Condensation in Dilute Gases*. Cambridge University Press, New York, 2002.
- [36] J. H. Denschlag, J. E. Simsarian, H. Häffner, C. McKenzie, A. Browaeys, D. Cho, K. Helmerson, S. L. Rolston, and W. D. Phillips. A Bose-Einstein condensate in an optical lattice. *Journal of Physics B: Atomic, Molecular and Optical Physics*, 35(14):3095, 2002.
- [37] G. Santarelli, Ph. Laurent, P. Lemonde, A. Clairon, A. G. Mann, S. Chang, A. N. Luiten, and C. Salomon. Quantum projection noise in an atomic fountain:

- A high stability cesium frequency standard. *Phys. Rev. Lett.*, 82(23):4619–4622, Jun 1999.
- [38] J. M. McGuirk, G. T. Foster, J. B. Fixler, and M. A. Kasevich. Low-noise detection of ultracold atoms. *Opt. Lett.*, 26(6):364–366, 2001.
- [39] S. Bize, et al. Cold atom clocks and applications. *Journal of Physics B: Atomic, Molecular and Optical Physics*, 38(9):S449, 2005.
- [40] D. Leibfried, M. D. Barrett, T. Schaetz, J. Britton, J. Chiaverini, W. M. Itano, J. D. Jost, C. Langer, and D. J. Wineland. Toward Heisenberg-Limited Spectroscopy with Multiparticle Entangled States. *Science*, 304(5676):1476–1478, 2004.
- [41] A. K. Tuchman, R. Long, G. Vrijen, J. Boudet, J. Lee, and M. A. Kasevich. Normal-mode splitting with large collective cooperativity. *Phys. Rev. A*, 74(5):053821, Nov 2006.
- [42] Holger Müller, Sheng-wei Chiow, Sven Herrmann, and Steven Chu. Atom interferometers with scalable enclosed area. *Phys. Rev. Lett.*, 102(24):240403, Jun 2009.
- [43] Tim Kovachy, Jason M. Hogan, David M. S. Johnson, and Mark A. Kasevich. Optical lattices as waveguides and beam splitters for atom interferometry: An analytical treatment and proposal of applications. (arxiv:0910.3435), Oct 2009.
- [44] J. M. McGuirk, M. J. Snadden, and M. A. Kasevich. Large area light-pulse atom interferometry. *Phys. Rev. Lett.*, 85(21):4498–4501, Nov 2000.
- [45] Holger Müller, Sheng-wei Chiow, Quan Long, Sven Herrmann, and Steven Chu. Atom interferometry with up to 24-photon-momentum-transfer beam splitters. *Phys. Rev. Lett.*, 100(18):180405, May 2008.
- [46] Pippa Storey and Claude Cohen-Tannoudji. The Feynman path integral approach to atomic interferometry. a tutorial. *J. Phys. II France*, 4(11):1999–2027, November 1994.

- [47] K. Bongs, R. Launay, and M. A. Kasevich. High-order inertial phase shifts for time-domain atom interferometers. *Applied Physics B: Lasers and Optics*, 84:599–602, September 2006.
- [48] B. Dubetsky and M. A. Kasevich. Atom interferometer as a selective sensor of rotation or gravity. *Phys. Rev. A*, 74(2):023615, Aug 2006.
- [49] C. J. Bordé. Quantum Theory of Atom-Wave Beam Splitters and Application to Multidimensional Atomic Gravito-Inertial Sensors. *General Relativity and Gravitation*, 36:475–502, March 2004.
- [50] Jae-Hoo Gweon and Jeong-Ryeol Choi. Propagator and geometric phase of a general time-dependent harmonic oscillator. *J. Korean Phys. Soc.*, 42(3), 2003.
- [51] C. Antoine. Matter wave beam splitters in gravito-inertial and trapping potentials: generalized ttt scheme for atom interferometry. *Applied Physics B: Lasers and Optics*, 84:585–597, September 2006.
- [52] M. Jansen. *Atom interferometry with cold metastable helium*. PhD thesis, Technische Universiteit Eindhoven, 2007.
- [53] Kathryn Moler, David S. Weiss, Mark Kasevich, and Steven Chu. Theoretical analysis of velocity-selective Raman transitions. *Phys. Rev. A*, 45(1):342–348, Jan 1992.
- [54] A. F. Bernhardt and B. W. Shore. Coherent atomic deflection by resonant standing waves. *Phys. Rev. A*, 23(3):1290–1301, March 1981.
- [55] L. Allen and J.H. Eberly. *Optical Resonance and Two-Level Atoms*. Dover Publications, Inc., New York, 1987.
- [56] J. M. Obrecht, R. J. Wild, M. Antezza, L. P. Pitaevskii, S. Stringari, and E. A. Cornell. Measurement of the temperature dependence of the Casimir-Polder force. *Phys. Rev. Lett.*, 98(6):063201, Feb 2007.

- [57] J. M. McGuirk, D. M. Harber, J. M. Obrecht, and E. A. Cornell. Alkali-metal adsorbate polarization on conducting and insulating surfaces probed with bose-einstein condensates. *Phys. Rev. A*, 69(6):062905, Jun 2004.
- [58] Marco Pisani and Milena Astrua. Angle amplification for nanoradian measurements. *Appl. Opt.*, 45(8):1725–1729, 2006.
- [59] J. H. Müller, O. Morsch, D. Ciampini, M. Anderlini, R. Mannella, and E. Arimondo. Atomic micromotion and geometric forces in a triaxial magnetic trap. *Phys. Rev. Lett.*, 85(21):4454–4457, November 2000.
- [60] I. Bloch, M. Greiner, O. Mandel, T. W. Hänsch, and T. Esslinger. Sympathetic cooling of ^{85}Rb and ^{87}Rb . *Phys. Rev. A*, 64(2):021402, August 2001.
- [61] T. Bitter, et al. A large volume magnetic shielding system for the ILL neutron-antineutron oscillation experiment. *Nuclear Instruments and Methods in Physics Research A*, 309:521–529, November 1991.
- [62] T. Kurosu, Y. Fukuyama, K. Abe, and Y. Koga. Measurement of a Weak Magnetic Field Using Cold Atoms. *Japanese Journal of Applied Physics*, 41:L586–L588, May 2002.
- [63] Umakant D. Rapol, Ajay Wasan, and Vasant Natarajan. Loading of a Rb magneto-optic trap from a getter source. *Phys. Rev. A*, 64(2):023402, Jun 2001.
- [64] W. G. Wadey. Magnetic shielding with multiple cylindrical shells. *Review of Scientific Instruments*, 27(11):910–916, 1956.
- [65] Nir Davidson, Heun Jin Lee, Mark Kasevich, and Steven Chu. Raman cooling of atoms in two and three dimensions. *Phys. Rev. Lett.*, 72(20):3158–3161, May 1994.
- [66] Mark Kasevich and Steven Chu. Laser cooling below a photon recoil with three-level atoms. *Phys. Rev. Lett.*, 69(12):1741–1744, September 1992.

- [67] A. Aspect, E. Arimondo, R. Kaiser, N. Vansteenkiste, and C. Cohen-Tannoudji. Laser cooling below the one-photon recoil energy by velocity-selective coherent population trapping. *Phys. Rev. Lett.*, 61(7):826–829, August 1988.
- [68] Wolfgang Petrich, Michael H. Anderson, Jason R. Ensher, and Eric A. Cornell. Stable, tightly confining magnetic trap for evaporative cooling of neutral atoms. *Phys. Rev. Lett.*, 74(17):3352–3355, Apr 1995.
- [69] S. G. Cox, P. F. Griffin, C. S. Adams, D. DeMille, and E. Riis. Reusable ultrahigh vacuum viewport bakeable to 240 C. *Review of Scientific Instruments*, 74(6):3185–3187, 2003.
- [70] K. J. Weatherill, J. D. Pritchard, P. F. Griffin, U. Dammalapati, C. S. Adams, and E. Riis. A versatile and reliably reusable ultrahigh vacuum viewport. *Review of Scientific Instruments*, 80(2):026105, 2009.
- [71] K. Dieckmann, R. J. C. Spreeuw, M. Weidemüller, and J. T. M. Walraven. Two-dimensional magneto-optical trap as a source of slow atoms. *Phys. Rev. A*, 58(5):3891–3895, Nov 1998.
- [72] S. Dimopoulos, P. W. Graham, J. M. Hogan, M. A. Kasevich, and S. Rajendran. Gravitational wave detection with atom interferometry. *Physics Letters B*, 678:37–40, July 2009.
- [73] S. Weinberg. *Gravitation and Cosmology*. John Wiley & Sons, New York, 1972.
- [74] A. Peters. *High Precision Gravity Measurements Using Atom Interferometry*. PhD thesis, Stanford University, 1998.
- [75] D. S. Weiss, B. C. Young, and S. Chu. Precision measurement of \hbar/m_{Cs} based on photon recoil using laser-cooled atoms and atomic interferometry. *Applied Physics B: Lasers and Optics*, 59:217–256, September 1994.
- [76] H. Müller, S.-W. Chiow, Q. Long, C. Vo, and S. Chu. A new photon recoil experiment: towards a determination of the fine structure constant. *Applied Physics B: Lasers and Optics*, 84:633–642, September 2006.

- [77] Marco Pisani and Milena Astrua. Angle amplification for nanoradian measurements. *Appl. Opt.*, 45(8):1725–1729, 2006.
- [78] T. Bitter, et al. A large volume magnetic shielding system for the ILL neutron-antineutron oscillation experiment. *Nuclear Instruments and Methods in Physics Research Section A: Accelerators, Spectrometers, Detectors and Associated Equipment*, 309(3):521 – 529, 1991.
- [79] S. Kokkelmans, B. J. Verhaar, K. Gibble, and D. J. Heinzen. Predictions for laser-cooled Rb clocks. *Phys. Rev. A*, 56(6):R4389–R4392, Dec 1997.
- [80] Y. Sortais, S. Bize, C. Nicolas, A. Clairon, C. Salomon, and C. Williams. Cold collision frequency shifts in a ^{87}Rb atomic fountain. *Phys. Rev. Lett.*, 85(15):3117–3120, Oct 2000.
- [81] Karl-Peter Marzlin and Jürgen Audretsch. “Freely” falling two-level atom in a running laser wave. *Phys. Rev. A*, 53(2):1004–1013, Feb 1996.
- [82] G. C. McVittie. The mass-particle in an expanding universe. *Mon. Not. R. Astron. Soc.*, 93:325–339, March 1933.
- [83] John D. Anderson, Philip A. Laing, Eunice L. Lau, Anthony S. Liu, Michael Martin Nieto, and Slava G. Turyshev. Indication, from Pioneer 10/11, Galileo, and Ulysses data, of an apparent anomalous, weak, long-range acceleration. *Phys. Rev. Lett.*, 81(14):2858–2861, Oct 1998.
- [84] C. Lammerzahl, (ed.), C. W. F. Everitt, (ed.), and F. W. Hehl, (ed.). Gyros, clocks, interferometers...: Testing relativistic gravity in space. Proceedings, 220th WE-Heraeus Seminar, Bad Honnef, Germany, August 21-27, 1999. Prepared for 220th WE-Heraeus Seminar on Gyros, Clocks, and Interferometers: Testing General Relativity in Space, Bad Honnef, Germany, 22-27 Aug 1999.
- [85] I. Ciufolini and E. Pavlis. On the measurement of the Lense-Thirring effect using the nodes of the LAGEOS satellites, in reply to On the reliability of the so-far performed tests for measuring the Lense-Thirring effect with the LAGEOS satellites by L. Iorio. *New Astronomy*, 10(8):636 – 651, 2005.

- [86] L. Iorio. *Testing frame-dragging with the Mars Global Surveyor spacecraft in the gravitational field of Mars*, pages 183–186. November 2007.
- [87] K. Nordtvedt. Existence of the Gravitomagnetic Interaction. *International Journal of Theoretical Physics*, 27:1395–1404, November 1988.
- [88] M.-C. Angonin-Willaime, X. Ovidio, and P. Tourrenc. Gravitational Perturbations on Local Experiments in a Satellite: The Dragging of Inertial Frame in the HYPER Project. *General Relativity and Gravitation*, 36:411–434, February 2004.
- [89] R. J. Warburton and J. M. Goodkind. Search for evidence of a preferred reference frame. *Astrophysical Journal*, 208:881–886, September 1976.
- [90] C. J. Bordé, J.-C. Houard, and A. Karasiewicz. Relativistic Phase Shifts for Dirac Particles Interacting with Weak Gravitational Fields in Matter-Wave Interferometers. In C. Lämmerzahl, C. W. F. Everitt, & F. W. Hehl, editor, *Gyros, Clocks, Interferometers ...: Testing Relativistic Gravity in Space*, volume 562 of *Lecture Notes in Physics*, Berlin Springer Verlag, page 403, 2001.
- [91] Katalin Varjú and Lewis H. Ryder. Comparing the effects of curved space and noninertial frames on spin 1/2 particles. *Phys. Rev. D*, 62(2):024016, Jun 2000.
- [92] Shigeru Wajima, Masumi Kasai, and Toshifumi Futamase. Post-Newtonian effects of gravity on quantum interferometry. *Phys. Rev. D*, 55(4):1964–1970, Feb 1997.
- [93] J. Anandan. Curvature effects in interferometry. *Phys. Rev. D*, 30(8):1615–1624, Oct 1984.
- [94] Jürgen Audretsch and Karl-Peter Marzlin. Ramsey fringes in atomic interferometry: Measurability of the influence of space-time curvature. *Phys. Rev. A*, 50(3):2080–2095, Sep 1994.
- [95] B F Schutz. Gravitational wave astronomy. *Classical and Quantum Gravity*, 16(12A):A131, 1999.

- [96] B. F. Schutz. Determining the Hubble constant from gravitational wave observations. *Nature*, 323:310, September 1986.
- [97] P Astone, et al. The 2003 run of the explorernautilus gravitational wave experiment. *Classical and Quantum Gravity*, 23(8):S169, 2006.
- [98] J.-P. Zendri, et al. Status report and near future prospects for the gravitational wave detector AURIGA. *Classical and Quantum Gravity*, 19(7):1925, 2002.
- [99] R. Ballantini, et al. Microwave apparatus for gravitational waves observation. (arXiv:gr-qc/0502054), February 2005.
- [100] W. H. Oskay, et al. Single-atom optical clock with high accuracy. *Phys. Rev. Lett.*, 97(2):020801, Jul 2006.
- [101] H.J. Metcalf and P. Straten. *Laser Cooling and Trapping*. Springer, New York, 1999.
- [102] G M Tino and F Vetrano. Is it possible to detect gravitational waves with atom interferometers? *Classical and Quantum Gravity*, 24(9):2167, 2007.
- [103] Daniel A. Steck. Rubidium 87 D line data. (<http://steck.us/alkalidata>), August 2009.
- [104] P. Cheinet, B. Canuel, F. Pereira Dos Santos, A. Gauguet, F. Leduc, and A. Landragin. Measurement of the sensitivity function in time-domain atomic interferometer. (arXiv:physics/0510197), October 2005.
- [105] A. D. Ludlow, X. Huang, M. Notcutt, T. Zanon-Willette, S. M. Foreman, M. M. Boyd, S. Blatt, and J. Ye. Compact, thermal-noise-limited optical cavity for diode laser stabilization at 1×10^{-15} . *Opt. Lett.*, 32(6):641–643, 2007.
- [106] Peter R. Saulson. Terrestrial gravitational noise on a gravitational wave antenna. *Phys. Rev. D*, 30(4):732–736, Aug 1984.
- [107] Scott A. Hughes and Kip S. Thorne. Seismic gravity-gradient noise in interferometric gravitational-wave detectors. *Phys. Rev. D*, 58(12):122002, Nov 1998.

- [108] James E. Fix. Ambient earth motion in the period range from 0.1 to 2560 sec. *Bulletin of the Seismological Society of America*, 62(6):1753–1760, 1972.
- [109] P. Berman, editor. *Atom Interferometry*. Academic Press, San Diego, 1997.
- [110] J. P. Gardner. The James Webb space telescope white paper. (<http://www.stsci.edu/jwst/science/SRD.pdf>).
- [111] C. R. Sandy. Next generation space telescope inflatable sunshield development. (<http://ieeexplore.ieee.org/iel5/7042/18960/00877925.pdf?arnumber=877925>).
- [112] L. F. Burlaga. Directional Discontinuities in the Interplanetary Magnetic Field. *Solar Physics*, 7:54–71, April 1969.
- [113] J. Jacobson, G. Björk, and Y. Yamamoto. Quantum limit for the atom-light interferometer. *Applied Physics B: Lasers and Optics*, 60:187–191, February 1995.
- [114] <http://www.srl.caltech.edu/lisa/documents/FTR.pdf>.
- [115] W. J. Bencze, Y. Xiao, D. N. Hipkins, G. F. Franklin, and B. W. Parkinson. Gyroscope spin axis direction control for the Gravity Probe B satellite. *IEEE CONFERENCE ON DECISION AND CONTROL*, 1:480–485, 1996.
- [116] J. W. Sari and N. F. Ness. Power Spectra of the Interplanetary Magnetic Field. *Solar Physics*, 8:155–165, July 1969.
- [117] S. Bize, Y. Sortais, M. S. Santos, C. Mandache, A. Clairon, and C. Salomon. High-accuracy measurement of the ^{87}Rb ground-state hyperfine splitting in an atomic fountain. *Europhysics Letters*, 45(5):558, 1999.
- [118] G. Rottman. Measurement of Total and Spectral Solar Irradiance. *Space Science Reviews*, 125:39–51, August 2006.
- [119] Daniel A. Shaddock, Massimo Tinto, Frank B. Estabrook, and J. W. Armstrong. Data combinations accounting for LISA spacecraft motion. *Phys. Rev. D*, 68(6):061303, Sep 2003.

- [120] Neil J Cornish and Ronald W Hellings. The effects of orbital motion on LISA time delay interferometry. *Classical and Quantum Gravity*, 20(22):4851, 2003.
- [121] P. Bender, et al. LISA Pre-Phase A Report. (http://maxim.gsfc.nasa.gov/documents/Mission_Concept_Work/ISAL_January_2002_SST/Astrometry/LISA-prephaseA.pdf), 1998.
- [122] Michele Maggiore. Gravitational wave experiments and early universe cosmology. *Physics Reports*, 331(6):283 – 367, 2000.
- [123] R. D. Blandford and K. S. Thorne. *Applications of Classical Physics*. (<http://www.pma.caltech.edu/Courses/ph136/yr2006/text.html>), 2005.
- [124] A. J. Farmer and E. S. Phinney. The gravitational wave background from cosmological compact binaries. *Mon. Not. Roy. Astron. Soc.*, 346:1197–1214, December 2003.
- [125] Alexei A. Starobinsky. Spectrum of relict gravitational radiation and the early state of the universe. *JETP Lett.*, 30:682–685, 1979.
- [126] Bruce Allen and Scott Koranda. Temperature fluctuations in the cosmic background radiation from inflationary cosmological models. *Phys. Rev. D*, 50:3713, 1994.
- [127] Juan García-Bellido, Daniel G. Figueroa, and Alfonso Sastre. Gravitational wave background from reheating after hybrid inflation. *Phys. Rev. D*, 77(4):043517, Feb 2008.
- [128] Richard Easther, John T. Giblin, and Eugene A. Lim. Gravitational wave production at the end of inflation. *Phys. Rev. Lett.*, 99(22):221301, Nov 2007.
- [129] Jean-François Dufaux, Amanda Bergman, Gary Felder, Lev Kofman, and Jean-Philippe Uzan. Theory and numerics of gravitational waves from preheating after inflation. *Phys. Rev. D*, 76(12):123517, Dec 2007.

- [130] M. Gasperini and G. Veneziano. The pre-big bang scenario in string cosmology. *Phys. Rept.*, 373:1–212, January 2003.
- [131] Michael S. Turner and Frank Wilczek. Relic gravitational waves and extended inflation. *Phys. Rev. Lett.*, 65(25):3080–3083, Dec 1990.
- [132] Marc Kamionkowski, Arthur Kosowsky, and Michael S. Turner. Gravitational radiation from first-order phase transitions. *Phys. Rev. D*, 49(6):2837–2851, Mar 1994.
- [133] Chiara Caprini, Ruth Durrer, and Géraldine Servant. Gravitational wave generation from bubble collisions in first-order phase transitions: An analytic approach. *Phys. Rev. D*, 77(12):124015, Jun 2008.
- [134] Christophe Grojean and Geraldine Servant. Gravitational Waves from Phase Transitions at the Electroweak Scale and Beyond. *Phys. Rev. D*, 75:043507, 2007.
- [135] Riccardo Apreda, Michele Maggiore, Alberto Nicolis, and Antonio Riotto. Gravitational waves from electroweak phase transitions. *Nuclear Physics B*, 631(1-2):342 – 368, 2002.
- [136] Lisa Randall and Graldine Servant. Gravitational waves from warped spacetime. *Journal of High Energy Physics*, 2007(05):054, 2007.
- [137] Joseph Polchinski. Cosmic String Loops and Gravitational Radiation. (arXiv:0707.0888), 2007.
- [138] Craig J. Hogan. Cosmological gravitational wave backgrounds. (arXiv:astro-ph/9809364), 1998.
- [139] Craig J. Hogan. Gravitational waves from mesoscopic dynamics of the extra dimensions. *Phys. Rev. Lett.*, 85:2044–2047, 2000.
- [140] Craig J. Hogan. Scales of the extra dimensions and their gravitational wave backgrounds. *Phys. Rev. D*, 62:121302, 2000.

- [141] <http://www.ligo.caltech.edu/>.
- [142] Shane L. Larson, William A. Hiscock, and Ronald W. Hellings. Sensitivity curves for spaceborne gravitational wave interferometers. *Phys. Rev. D*, 62(6):062001, Aug 2000.
- [143] B. Abbott, et al. Searching for a stochastic background of gravitational waves with the laser interferometer gravitational-wave observatory. *The Astrophysical Journal*, 659(2):918, 2007.
- [144] Bruce Allen. The stochastic gravity-wave background: Sources and detection. 1996.
- [145] Tristan L. Smith, Elena Pierpaoli, and Marc Kamionkowski. New cosmic microwave background constraint to primordial gravitational waves. *Phys. Rev. Lett.*, 97(2):021301, Jul 2006.
- [146] Nelson Christensen. Measuring the stochastic gravitational-radiation background with laser-interferometric antennas. *Phys. Rev. D*, 46(12):5250–5266, Dec 1992.
- [147] Eanna E. Flanagan. Sensitivity of the laser interferometer gravitational wave observatory to a stochastic background, and its dependence on the detector orientations. *Phys. Rev. D*, 48(6):2389–2407, Sep 1993.
- [148] Bruce Allen and Joseph D. Romano. Detecting a stochastic background of gravitational radiation: Signal processing strategies and sensitivities. *Phys. Rev. D*, 59(10):102001, Mar 1999.
- [149] Matthew R. DePies and Craig J. Hogan. Stochastic gravitational wave background from light cosmic strings. *Phys. Rev. D*, 75(12):125006, Jun 2007.
- [150] R. Y. Chiao and A. D. Speliotopoulos. Towards MIGO, the matter-wave interferometric gravitational-wave observatory, and the intersection of quantum mechanics with general relativity. *Journal of Modern Optics*, 51:861–899, June 2004.

- [151] Stefano Foffa, Alice Gasparini, Michele Papucci, and Riccardo Sturani. Sensitivity of a small matter-wave interferometer to gravitational waves. *Phys. Rev. D*, 73(2):022001, Jan 2006.
- [152] Albert Roura, Dieter R. Brill, B. L. Hu, Charles W. Misner, and William D. Phillips. Gravitational wave detectors based on matter wave interferometers (MIGO) are no better than laser interferometers (LIGO). *Phys. Rev. D*, 73(8):084018, Apr 2006.
- [153] P. Delva, M.-C. Angonin, and P. Tourrenc. A comparison between matter wave and light wave interferometers for the detection of gravitational waves. *Physics Letters A*, 357(4-5):249 – 254, 2006.
- [154] P. Wolf et al. Quantum Physics Exploring Gravity in the Outer Solar System: The Sagas Project. *Exper. Astron.*, 23:651–687, 2009.
- [155] A. W. Adams and J. S. Bloom. Direct detection of dark matter with space-based laser interferometers. (arXiv:astro-ph/0405266), 2004.
- [156] Naoki Seto and Asantha Cooray. Search for small-mass black hole dark matter with space- based gravitational wave detectors. *Phys. Rev. D*, 70:063512, 2004.
- [157] E. Witten. Dyons of charge $e\theta/2\pi$. *Physics Letters B*, 86(3-4):283 – 287, 1979.
- [158] C S Unnikrishnan and G T Gillies. The electrical neutrality of atoms and of bulk matter. *Metrologia*, 41(5):S125, 2004.
- [159] S. Eidelman, et al. Review of particle physics. *Physics Letters B*, 592(1-4):1 – 5, 2004. Review of Particle Physics.
- [160] Y. Aharonov and D. Bohm. Significance of electromagnetic potentials in the quantum theory. *Phys. Rev.*, 115(3):485–491, Aug 1959.
- [161] Martin Weitz, Brenton C. Young, and Steven Chu. Atomic interferometer based on adiabatic population transfer. *Phys. Rev. Lett.*, 73(19):2563–2566, Nov 1994.

- [162] C. Orzel, A. K. Tuchman, M. L. Fenselau, M. Yasuda, and M. A. Kasevich. Squeezed States in a Bose-Einstein Condensate. *Science*, 291(5512):2386–2389, 2001.
- [163] C. Champenois, M. Buechner, R. Delhuille, R. Mathevet, C. Robilliard, C. Rizzo, and J. Vigue. Matter Neutrality Test Using a Mach-Zehnder Interferometer. In S. G. Karshenboim, F. S. Pavone, G. F. Bassani, M. Inguscio, & T. W. Hänsch, editor, *The Hydrogen Atom: Precision Physics of Simple Atomic Systems*, volume 570 of *Lecture Notes in Physics*, Berlin Springer Verlag, page 554, 2001.
- [164] Tetsuya Kawanishi, Takahide Sakamoto, and Masayuki Izutsu. High-speed control of lightwave amplitude, phase, and frequency by use of electrooptic effect. *Selected Topics in Quantum Electronics, IEEE Journal of*, 13(1):79–91, Jan-Feb 2007.
- [165] J. L. Hall, L. Hollberg, T. Baer, and H. G. Robinson. Optical heterodyne saturation spectroscopy. *Applied Physics Letters*, 39(9):680–682, 1981.
- [166] Steven Chu, L. Hollberg, J. E. Bjorkholm, Alex Cable, and A. Ashkin. Three-dimensional viscous confinement and cooling of atoms by resonance radiation pressure. *Phys. Rev. Lett.*, 55(1):48–51, Jul 1985.
- [167] K. K. Wong, R. M. De La Rue, and S. Wright. Electro-optic-waveguide frequency translator in LiNbO₃ fabricated by proton exchange. *Opt. Lett.*, 7(11):546–548, 1982.
- [168] L.M. Johnson and III Cox, C.H. Serrodyne optical frequency translation with high sideband suppression. *Journal of Lightwave Technology*, 6(1):109–112, Jan 1988.
- [169] L. Thylen, P. Sjoberg, and G.E. Lindqvist. Electro-optical serrodyne frequency translator for $\lambda = 1.3 \mu\text{m}$. *Optoelectronics, IEE Proceedings J*, 132(2):119–121, April 1985.

- [170] C. Laskoskie, H. Hung, T. El-Wailly, and C.L. Chang. Ti-LiNbO₃ waveguide serrodyne modulator with ultrahigh sideband suppression for fiber optic gyroscopes. *Lightwave Technology, Journal of*, 7(4):600–606, Apr 1989.
- [171] Sarper Ozharar, Sangyoun Gee, Frank Quinlan, and Peter J. Delfyett. Heterodyne serrodyne with high sideband suppression via time division multiplexing for arbitrary waveform generation. volume 5814, pages 79–83. SPIE, 2005.
- [172] S. Ozharar, S. Gee, F. Quinlan, I. Ozdur, and P.J. Delfyett. Ultra-high spur-free dynamic range RF synthesis using optical homodyne serrodyne technique. *Electronics Letters*, 43(5):65 –66, March 2007.
- [173] M. Shen and R.A. Minasian. Serrodyne optical frequency translation using photonics-based waveforms. *Electronics Letters*, 40(24):1545 – 1547, 2004.
- [174] I.Y. Poberezhskiy, B. Bortnik, J. Chou, B. Jalali, and H.R. Fetterman. Serrodyne frequency translation of continuous optical signals using ultrawideband electrical sawtooth waveforms. *IEEE Journal of Quantum Electronics*, 41(12):1533–1539, Dec. 2005.
- [175] R. Reibel, T. Chang, M. Tian, and W. R. Babbitt. Optical linear sideband chirp compression for microwave arbitrary waveform generation. In *IEEE Microwave Photonics Conference Proceedings*, pages 197–200. IEEE, 2004.
- [176] R. R. Reibel, Z. W. Barber, J. A. Fischer, M. Tian, and W. R. Babbitt. Broadband demonstrations of true-time delay using linear sideband chirped programming and optical coherent transients. *Journal of Luminescence*, 107(1-4):103 – 113, 2004.
- [177] M. J. W. Rodwell, et al. Active and nonlinear wave propagation devices in ultrafast electronics and optoelectronics [and prolog]. *Proceedings of the IEEE*, 82(7):1037–1059, July 1994.

- [178] S. Shimotsu, S. Oikawa, T. Saitou, N. Mitsugi, K. Kubodera, T. Kawanishi, and M. Izutsu. Single side-band modulation performance of a LiNbO₃ integrated modulator consisting of four-phase modulator waveguides. *Photonics Technology Letters, IEEE*, 13(4):364–366, apr 2001.
- [179] D. W. van der Weide. Delta-doped Schottky diode nonlinear transmission lines for 480-fs, 3.5-V transients. *Applied Physics Letters*, 65:881–883, August 1994.
- [180] Rachel Houtz, Cheong Chan, and Holger Müller. Wideband, efficient optical serrodyne frequency shifting with a phase modulator and a nonlinear transmission line. *Opt. Express*, 17(21):19235–19240, 2009.
- [181] Masatoshi Saruwatari. High-speed all-optical technologies for photonics. In Nadir Dagli, editor, *High-Speed Photonic Devices*, pages 217–248. Taylor & Francis, 2007.
- [182] Lothar Moeller, Yikai Su, Chongjin Xie, Jurgen Gripp, Xiang Liu, and Roland Ryf. 640-Gb/s OTDM RZ-DQPSK signal enabling 2.4-Bit/s/Hz spectral efficiency and its detection with an EAM-based receiver. In *Asia Optical Fiber Communication and Optoelectronic Exposition and Conference*, page SaA2. Optical Society of America, 2008.
- [183] Hsu-Feng Chou, John E. Bowers, and Daniel J. Blumenthal. Compact 160-Gb/s add-drop multiplexer with a 40-Gb/s base rate using electroabsorption modulators. *IEEE Photon. Technol. Lett.*, 16:1564–1566, 2004.
- [184] T. Ohara, et al. 160-Gb/s OTDM Transmission Using Integrated All-Optical MUX/DEMUX With All-Channel Modulation and Demultiplexing. *IEEE Photonics Technology Letters*, 16:650–652, February 2004.
- [185] I. Glesk and P.R. Prucnal. 250-Gb/s self-coded optical TDM with a polarization-multiplexed clock. *Fiber and Integrated Optics*, 14:71–82, 1995.
- [186] Andrei I. Siahlo, Anders T. Clausen, Leif K. Oxenløwe, Jorge Seoane, and Palle Jeppesen. 640 Gb/s OTDM transmission and demultiplexing using a NOLM

- with commercially available highly nonlinear fiber. In *Conference on Lasers and Electro-Optics/Quantum Electronics and Laser Science and Photonic Applications Systems Technologies*, page CTuO1. Optical Society of America, 2005.
- [187] M. Lee. Dielectric constant and loss tangent in LiNbO₃ crystals from 90 to 147 GHz. *Applied Physics Letters*, 79:1342, August 2001.
 - [188] M. Lee, H. E. Katz, C. Erben, D. M. Gill, P. Gopalan, J. D. Heber, and D. J. McGee. Broadband Modulation of Light by Using an Electro-Optic Polymer. *Science*, 298:1401–1404, November 2002.
 - [189] J. Shin, S. Wu, and N. Dagli. 35-GHz Bandwidth, 5-V-cm Drive Voltage, Bulk GaAs Substrate Removed Electrooptic Modulators. *IEEE Photonics Technology Letters*, 19:1362–1364, September 2007.
 - [190] A. Kuver, J. M. Heaton, A. Miller, G. Murdoch, Y. Zhou, P. Jiang, and D. R. Wight. Development of GaAs electro-optic modulators with improved linearity. In *Proceedings of the 2nd EMRS DTC Technical Conference-Edinburgh*, 2005.
 - [191] Y. Cui and P. Berini. Modeling and Design of GaAs Traveling-Wave Electrooptic Modulators Based on the Planar Microstrip Structure. *Journal of Lightwave Technology*, 24:2368, June 2006.
 - [192] C. J. Madden, M. J. W. Rodwell, R. A. Marsland, D. M. Bloom, and Y. C. Pao. Generation of 3.5-ps fall-time shock waves on a monolithic GaAs nonlinear transmission line. *IEEE Electron Device Letters*, 9:303–305, June 1988.
 - [193] M. Birk, L.M. Lunardi, A.H. Gnauck, H. Schumacher, and D. Behammer. 10-Gbit/s RZ pulses using an all-silicon nonlinear transmission line integrated circuit. In *Optical Fiber Communication Conference, 2000*, volume 1, pages 248–250 vol.1, 2000.
 - [194] A. Yariv. *Optical Electronics in Modern Communications*. Oxford University Press, New York, 1997.